Using quasar absorption lines to probe cold gas in high redshift galaxies

Siwei Zou

École Doctorale d'Astronomie et Astrophysique d'Île-de-France
SORBONNE UNIVERSITÉ

Ph.D. Thesis

to obtain the title of Doctor in Astrophysics
of the University Pierre et Marie Curie

Presented by

Siwei Zou

Using quasar absorption lines to probe cold gas at high redshift

---

Thesis Advisor: Prof. Patrick Petitjean and Dr. Pasquier Noterdaeme

Presented and publicly defended on the 26th of September, 2018 to a jury consisting of

Reviewers:	Denis Puy	-	Univ Montpellier, France
	Roser Pello	-	Toulouse, France
Advisor:	Patrick Petitjean	-	IAP, Paris, France
Advisor:	Pasquier Noterdaeme	-	IAP, Paris, France
President:	Marie-Christine Angonin	-	UPMC, Paris, France
Examiner:	Christophe Yeche	-	CEA, Paris, France

To my beloved family and friends.
In memory of my uncle Fulian.

Abstract

Quasar absorption lines are powerful tool to study the ISM in the galaxies and the CGM and IGM around galaxies. We study a sample of 66 $z > 1.5$ absorbers selected based on the presence of strong C I absorption lines in SDSS spectra and observed with the ESO-VLT spectrograph X-shooter/UVES. I study 17 systems that are re-observed by X-shooter. I derive metallicities, depletion onto dust, extinction by dust and analyse the absorption from Mg II, Mg I, Ca II and Na I that are redshifted into the near infrared wavelength range. I detect 9 Ca II absorptions with W(Ca IIλ3934) > 0.23 Å out of 14 systems where we have appropriate wavelength coverage. I detect 10 Na I absorptions in the 11 systems where we could observe this absorption. The median equivalent width (W(Na Iλ5891) = 0.68 Å) is larger than what is observed in local clouds with similar H I column densities but also in $z < 0.7$ Ca II systems detected in the SDSS. The systematic presence of Na I absorption in these C I systems strongly suggests that the gas is neutral and cold, maybe part of the diffuse molecular gas in the ISM of high-redshift galaxies.

Most of the systems (12 out of 17) have W(Mg IIλ2796) > 2.5 Å when six of them have log N(H I) < 20.3 with the extreme case of J1341+1852 which has log N(H I) = 18.18. The Mg II absorptions are spread over more than $\Delta v \sim 400$ km s^{-1} for half of the systems; three absorbers have $\Delta v > 500$ km s^{-1}. The kinematics is strongly perturbed for most of these systems which probably do not arise in quiet disks and must be close to regions with intense star formation activity and/or are part of interacting objects. All this suggests that a large fraction of the cold gas at high redshift arises in disturbed environments. There is also a peculiar system without Lyα trough in the spectrum. We detect molecular hydrogen in all the systems within the detection limit.

This thesis is organised as below. I will introduce the background knowledge about quasar absorption lines and DLA systems in Chapter 1. I will present the work done for the subsample in Chapter 2 and two individual systems in Chapter 3. The molecular gas results is presented in Chapter 4. Then I will summarize the results and discuss the future work in Chapter 5 and 6.

Résumé

Contents

Chapter 1

Introduction

Contents

1.1 QSO

1.1.1 What is a quasar?

Quasi-stellar objects (hereafter QSOs), also called quasars, are extremely bright point sources in the Universe. They provide unique targets used to probe the medium along the line-of-sight. The emission given of a quasar covers a substantial wavelength ranges from radio to X-ray. Most of quasars ($\geq$ 90%) are radio-quiet. A quasar is normally regarded as one kind of active galactic nucleus (AGN). It is powered by the accretion of matter onto a central supermassive black hole (SMBH), see Fig. 1.1. The accretion disk surrounding the SMBH has a size of about 0.1 pc. The tremendous energy released from the ultraviolet(UV) to the near-infrared corresponds to what is called the continuum in an AGN spectrum. The region surrounding the accretion disk is called the broad line region (BLR) because it produces the broad emission lines with a width of a few thousands of km s^{-1}. The input energy is from photoionization by a central non-thermal continuum source. Around the BLR there is a much larger region called the narrow line region (NLR) with dimensions $\geq$ 10 pc. It produces emission lines with a few hundreds of km s^{-1}. The hydrogen in the host galaxy is easily excited by collisions from the n=1 level the to n=2 level and generates the Ly-α lines (1215.67Å). Unlike the spectrum of most stars, a quasar's spectrum is close to a power-law shape with additional emission lines. Figure 1.2 is an example of a quasar spectrum. The easily differentiated strong emission peak is the Ly-α line, the red line is the observed continuum in a quasar spectrum. There are several other broad metal absorption lines redwards of the Lyα emission lines, such as O I, Si IV, C IV lines.

1.1.2 Detection and population

The discovery of quasars revolutionized the field of extragalactic astronomy. The first quasars 3C 48 and 3C 273 were detected in the 1950's as radio sources. Later on, their optical spectra were obtained. It was the first time that a radio source was associated to an optical object. After the first identification of quasars, a wealth of surveys have been undertaken to find quasars from the local to the high-redshift Universe. Sloan Digital Sky Survey (SDSS York et al. 2000) Data Release 7 (DR7, Schneider et al. 2010) presents 105,783 quasars from SDSS I and II, which covers 9380 deg^2. The quasar redshift range is $0.065 < z < 5.46$. The Baryon Oscillation Spectroscopic Survey (BOSS) maps the distribution of quasar at $2.15 < z < 3.5$. BOSS DR9 Quasar Catalog (DR9Q) contains 87,822 quasars spread over 3275 deg^2 at $z > 2.15$ (Pâris et al. 2012). DR10Q contains

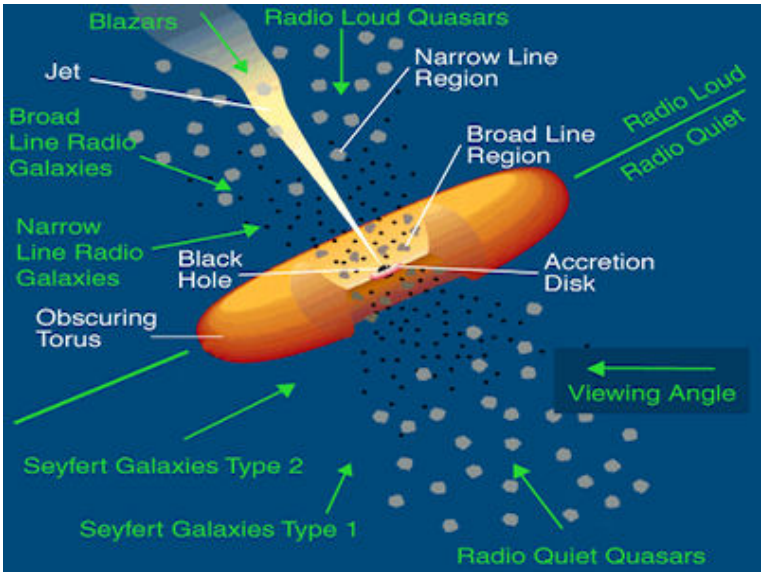

FIGURE 1.1: AGN structure, in the center is SMBH and its accretion disk, outside is the BLR and NLR. (Credit: C.M. Urry and P. Padovani)

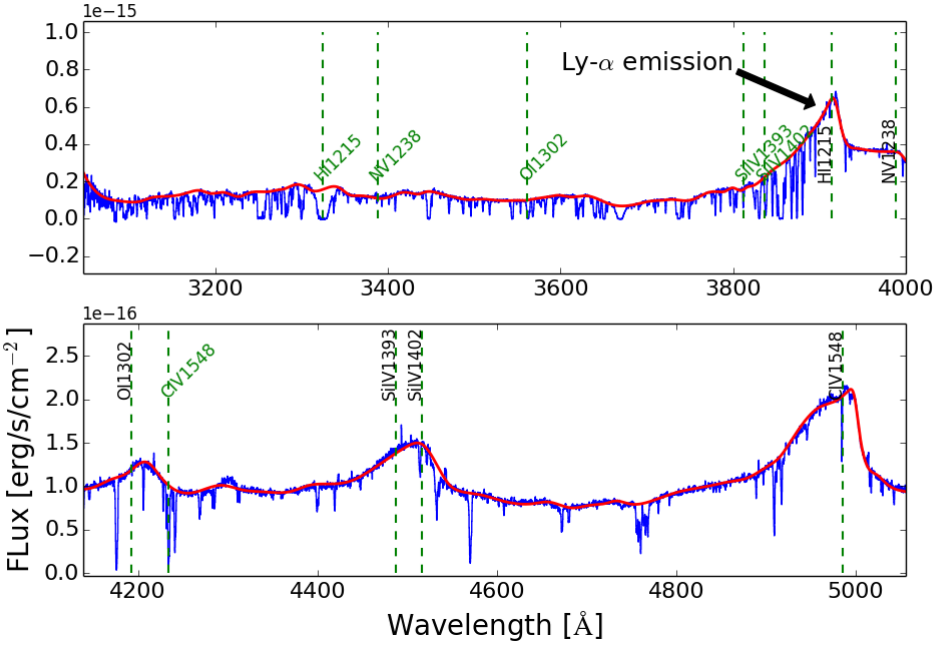

FIGURE 1.2: UV QSO spectrum of J0216 - 0021. Black labels are part of emission lines of of the quasar at $z_{em} = 2.22$. The green labels are some absorption lines at $z_{abs} = 1.737$. The peak around 3900Å is the Lyα emission. Blueward of the Lyα emission liens is Lyα forest, and redward of the Lyα line there are some typical metal absorption lines.

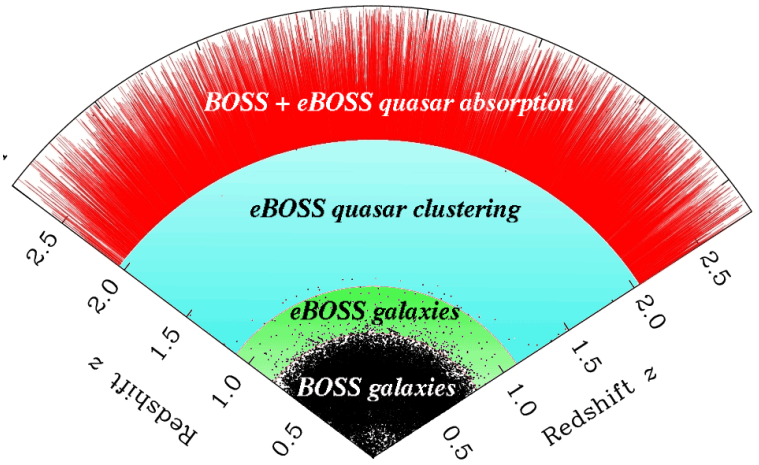

FIGURE 1.3: Different missions in SDSS to search for galaxies and quasars. BOSS and eBOSS search for the quasars at $z > 2$. BOSS searches for the galaxies between $z = 0.3$ and $z = 0.55$, eBOSS searches for red galaxies over 7500 deg^{2}at $0.6 < z < 0.8$, emission line galaxies over 1000 deg^2 at $0.6 < z < 1.0$, and quasars over 7500 deg^2 at $0.9 < z < 3.5$. (Credit: SDSS)

166,583 quasars spread over 6373 deg^2(Pâris et al. 2014). DR12Q added 272,026 new quasars from SDSS-III (Pâris et al. 2017b). The newest catalog of SDSS from SDSS-IV The Extended Baryon Oscillation Spectroscopic Survey (eBOSS) presents 144,046 new discoveries at $0.9 < z < 2.2$ Pâris et al. (2017a). Thanks to SDSS, there are already more than 500,000 quasars have been detected.

Though not as numerous as the quasars detected at $z < 5$, quasars have been detected at redshift 6 or even higher. Until recently the most distant QSO has been detected is at $z = 7.54$ by UKIDSS (Bañados et al. 2017). QSO at $z > 6$ are important for us to understand the Epoch of Reionization (EoR). After the Big Bang, the temperature of the gas decreases rapidly until $\sim$ 3000 K at $z \sim 1089$, allowing the recombination of free electrons and protons into neutral hydrogen. The first objects (first stars, quasars, galaxies) formed at $20 < z < 6$. The ultraviolet emission from these objects re-ionizes the neutral hydrogen. This period is called the re-ionization epoch. Studies on this epoch will provide important information to the structure evolution of the universe (see Fig. 1.4). More than 40 quasars at $z \sim 6$ have been detected in SDSS survey (Fan et al. 2003, 2006; Wu et al. 2015).

The number of quasars increases with redshift from z= 0 to $z \sim 3$ and reaches the peak around redshift 3. This trend implies the massive stars take over quasar to contribute to the radiation background at $z > 3$. Some models on the quasar population evolution are constructed. Heisler & Ostriker (1988) used a simple three-parameter model to describe the quasar luminosity evolution and the luminosity-dependent density evolution.

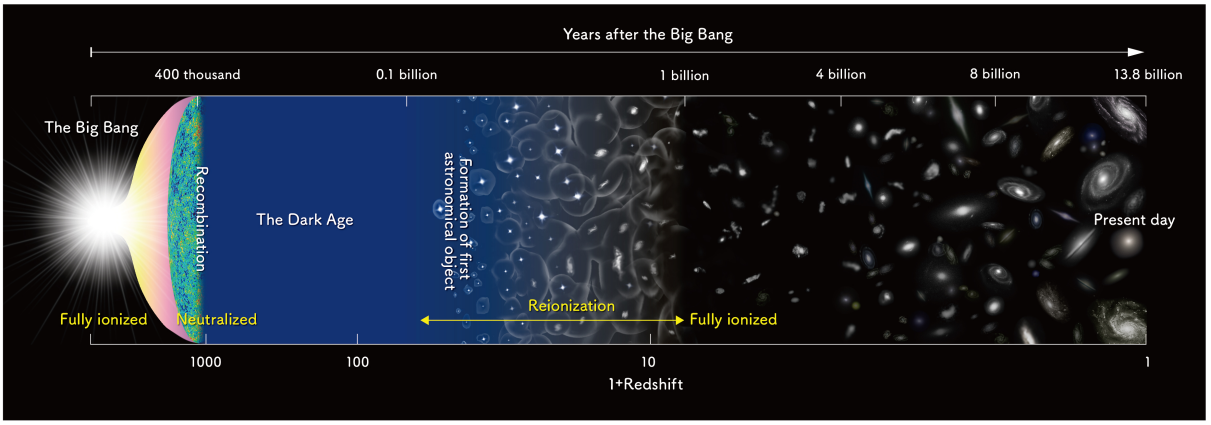

FIGURE 1.4: Different epoch in the Universe evolution. (Credit: Atacama Large Millimeter/submillimeter Array)

In combination with a corrected redshift distribution function, this model fits the apparent magnitude distribution of observed quasars well at $z < 3$. Cavaliere & Vittorini (2000) built a model to explain the fall of the quasar population around redshift 2.5.

1.2 QSO absorption lines

Different objects are located by chance along the line-of-sight between a distant QSO and the observer (see Fig 1.5). These objects absorb the quasar emission and generate absorption lines. QSO absorption lines can be divided into two categories: the intrinsic absorption lines and the intervening absorption lines. The former ones are generated by the gas around the QSO host galaxy. The latter ones are generated by the intervening objects. We focus on the intervening absorption lines in this work . By studying a QSO spectrum, we can obtain tremendous information about the structure and composition of the intervening systems. The absorption lines give us plentiful information about the inter-galactic-medium (IGM), especially when the light goes through a galaxy, the circum-galactic-medium(CGM), inter-stellar-medium (ISM). Thus the absorption lines are widely used as a powerful tool to study the physical conditions of the gas (kinematics, ionization state, temperature and chemical abundances, etc.) in the intervening systems. They can also be used to study the large-scale structures in the universe and their evolution.

1.2.1 Lyα absorbers

When the quasar photons hit intervening hydrogen clouds at different redshifts by chance, neutral hydrogen in each cloud will generate absorption lines at rest-wavelengths in the

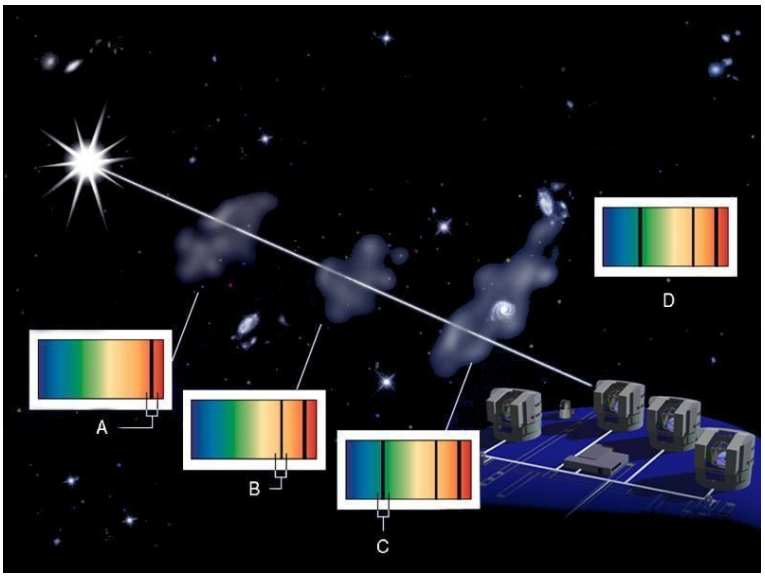

FIGURE 1.5: Illustration of the use of quasar spectroscopy to study intervening systems seen in absorption. The quasar, shown as a bright object on the left, emits light that can be absorbed by intervening gas at different redshifts (A, B, C). C indicate the emission goes through the gas around a galaxy. Each absorbing system leaves its imprints onto the quasar spectrum. (Credit: from Ed Janssen, ESO).

Lyman series (Lyα 1215.67Å, Lyβ 1025.72Å, etc). The Lyα absorption lines have a rest-wavelength 1215.67Å. The distribution of H I column density ranges from $10^{12.5} \sim$ to 10^{22} cm^{-2} (Petitjean et al. 1993; Kim et al. 2013). The frequency f(N) is described by a double power law with the break in log N(H I) $\sim$ 16 in Petitjean et al. (1993). In Kim et al. (2013), the result is in agreement with that in Petitjean et al. (1993) in the [12.75,14] range. Then the frequency becomes steeper when log N(H I) $>$ 15 cm^{-2} and shallower at high log N(H I), as in Fig 1.6. Historically, H I absorption systems are classified according to their different hydrogen column densities. Systems with N(H I) smaller than $10^{17.2}$ cm^{-2} are called 'Lyα forest absorbers'. As N $\sim 10^{17}$ cm^{-2} corresponds to a unity optical depth (Wolfe et al. 2005), therefore the Lyα forest systems are optically thin. The hydrogen in these systems is highly ionized. The forest is generated by IGM gas. Optically thick systems with $10^{17.2} <$ N(H I) $< 10^{20.3}$ cm^{-2} are called 'Lyman Limit Systems ' (LLS). They usually are located around the outer halo of galaxies or the CGM. Systems with N(H I) $> 10^{20.3}$ cm^{-2} are called 'damped Lyman-α' absorbers or DLAs. They are usually found in the ISM of galaxies where the gas is mostly neutral. Details about each system are discussed below and in Section 1.4.

• Lyα forest

In a quasar spectrum, the numerous Lyα λ1215 absorption lines seen bluewards of the Lya emission are called the Ly-α forest (Weymann et al. 1981; Gunn & Peterson 1965), see Fig 1.2. It is produced by the optically thin and highly photoionized IGM with

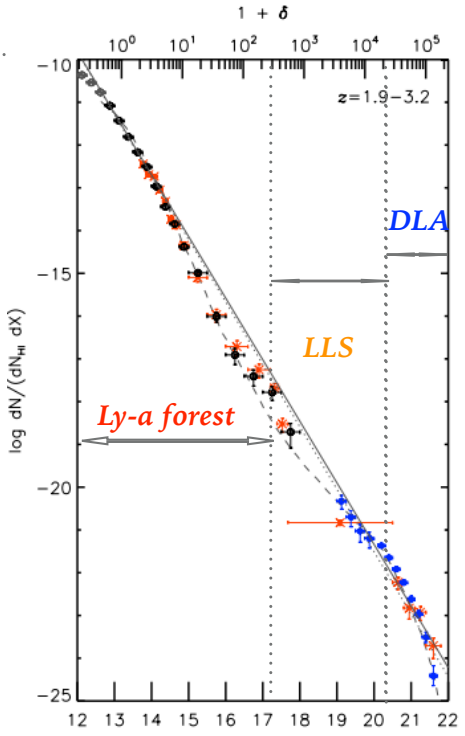

FIGURE 1.6: N(H I) frequency distribution at $1.9 < z < 3.2$, the turnover point at N $< 10^{12.75}$ cm^{-2} is due to the observation sensitivity. Adapted from Kim et al. (2013). The black and grey circles are the data in Kim et al. (2013), the red stars are the data from Petitjean et al. (1993), the blue filled circles are the data for log N(H I) > 20.1 is from Noterdaeme et al. (2009), the filled circles at $19 <$ log N(H I) < 20.1 are from O'Meara et al. (2007) at $\langle z \rangle = 3.1$, respectively. The solid line gives the power law fit to our data for log N(H I) = [12.75, 14]. The dotted line represent the fit obtained by Hu et al. (1995), the dashed line represents a theoretical prediction at z > 3 by Altay et al. (2011).

n(H I)/n(H) $\sim 10^{-5}$, where n(H) is the hydrogen volume density. The first Ly-α forest observations were conducted in the late 1970s by 4m ground-based telescopes (e.g., the AAT, KPNO, MMT, Palomar). The recent BOSS survey aims at detecting the baryon acoustic oscillations (BAO) relic in the high-z Universe. BOSS survey provides excellent Lyα forest samples for BAO studies (Eisenstein et al. 2011; Busca et al. 2013; Slosar et al. 2013; Delubac et al. 2015; Aubourg et al. 2015). BOSS used 20% of its fibers to obtain Lyα forest absorptions along the line-of-sight out of 150,000 distant quasars spectra (Eisenstein et al. 2011). BAO is a distinct effect on the anisotropies of the cosmic microwave background (CMB) in the pre-recombination time. BAOs are seen at $z \sim 0.3$ at the BAO peak in the galaxy-galaxy pair correlation function. This peak at redshift z is seen at an angular separation $\Delta\theta = r_s/(1+z)D_A(z)$ and a redshift separation $\Delta z = r_s H(z)/c$, where r_s is the co-moving distance of the sound horizon at recombination.

Once the BAO peak is measured, it can be used to constrain the cosmological parameters $H(z)$ and $D_A(z)$ at different redshift. McDonald & Eisenstein (2007) initiated the idea of using the 3D Lyα forest flux correlation function to constrain the BAO signal. Busca et al. (2013) applied this technique to study the BAO peak with Lyα forest spectra from SDSS quasars at redshift 2.3. Lee et al. (2013) selected a Lyα fiducial sample from the BOSS DR9 which comprises 54468 quasar spectra.

With the observation and simulation of the Ly-α forest, we can study the structure of the IGM and therefore dark matter fluctuations and dark matter filamentary structures (Muecket et al. 1996; Petitjean et al. 1995). Both numerical and semi-analytical simulations are conducted to reproduce the Lyα forest and its correlation with cosmology (Cen et al. 1994; Bi et al. 1995; Zhang et al. 1995; Hernquist et al. 1996; Miralda-Escudé et al. 1996; Bi & Davidsen 1997; Hui et al. 1997; Theuns et al. 1998). In the diffuse highly-ionized IGM, gravitational forces are much stronger than pressure gradients. This ensures that gas overdensities in the IGM can be used to trace the dark matter overdensity well.

Hernquist et al. (1996) simulated the Lyα forest with a numerical Lagrangian, Smoothed Particle Hydrodynamics (SPH) Cold Dark Matter (CDM) model ($\Omega = 1$, $H_0 = 50$ km s^{-1}). They assumed a uniform radiation field and included the gas heating and cooling. Haehnelt et al. (1996) give a typical hydrogen density - temperature relation of the Lyα forest at redshift ~ 3.1 from their SPH simulation (see Fig 1.7). They indicate that when $n_H > 10^{-3}$ cm^{-3}. The simulation shows large deviations from the equilibrium temperature, which is the result of the compressional heating. A recent work by Ozbek et al. (2016) uses the Ly-α forest to map the IGM in 3D on large-scale structure at redshifts 2-4.

Weinberg et al. (2003) review previous simulations that have used the Ly-α forest as a cosmological probe. The basic scenario is to include gravity, gas dynamics and photo-ionization by the UV background in 3-D boxes with 128^3 dark matter particles and 128^3 gas particles. The reason for conducting this simulation is that the Ly-α optical depth is strongly related to the local gas and dark matter densities. There is a tight relation between the density and the temperature of the gas, which is $T \approx T_0(\rho/\ \bar{\rho})^{\alpha}$. This is due to the balance between photo-ionization heating and adiabatic cooling. As the Lyα optical depth is proportional to the gas density, the Lyα forest optical depth can be seen as the 1-d map of the gas overdensity. One can constrain the cosmological model by comparing the simulated Lyα forest to observations.

• Lyman-Limit-Systems

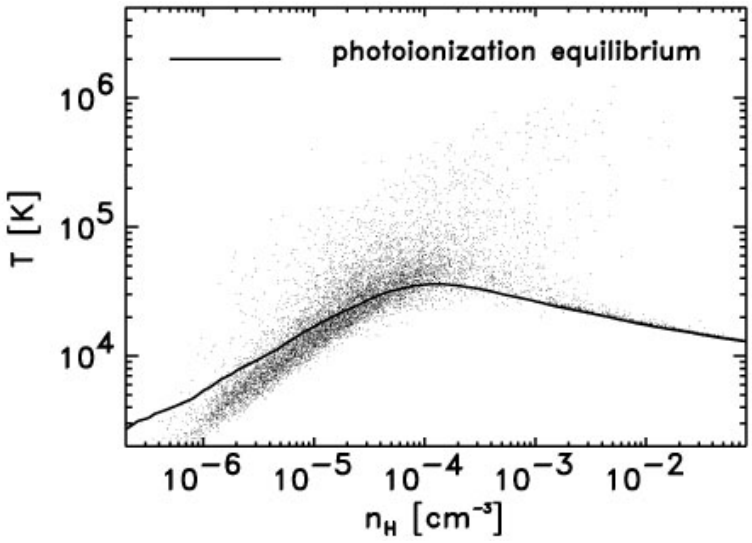

FIGURE 1.7: Density-Temperature relation in the Lyα forest at $z = 3.1$ from SPH simulations from Haehnelt et al. (1996). The dots show the n_H-T relation in the simulation. The solid curve is the thermal photo-ionization equilibrium.

The most obvious observational feature of LLS is the Lyman-limit bluewards of the Lyα emission. The rest-frame wavelength of the Lyman-limit (912Å) corresponds to the energy needed to expel a hydrogen electron from the ground-state. All the photons with energies greater than this value can be absorbed by the hydrogen. In a quasar spectrum, this feature is seen as a sharp discontinuity bluewards of the Lyman-limit. The optical depth at the Lyman limit is proportional to the column density of H I.

$$\tau_{LL}(\lambda \leq \lambda_{912}) \frac{N(H\text{I})}{10^{17.2} cm^{-2}} \times \left(\frac{\lambda}{\lambda_{912}}\right)^{-3}$$

The first Lyman limit feature in a QSO spectrum was detected by Carswell et al. (1975) with the 2.2-m telescope at the Steward Observatory. A sharp Lyman discontinuity was detected in a distant radio source OH471(0642+44) at $z_{em} = 3.40$. Because of this easy-detected feature, LLS can be identified using low/moderate resolution instrumentation. Sargent et al. (1988) initiated the first LLS-focused survey. They discovered 37 LLSs from 59 high signal-to-noise ratio (SNR) and low resolution QSO spectra. The mean emission redshift is 3. All the LLSs are found to be optically thick with optical depth $\tau \geq 1.5$. Afterwards, a set of surveys were conducted based on different sets of data from different instrumentations (Lanzetta et al. 1991; Storrie-Lombardi et al. 1994; Stengler-Larrea et al. 1995). However, due to the varying instrumentation SNR, resolutions and the selection methods of the quasars samples, the incidences of LLS evolution from these survey are not consistent with each other. Until recently, Prochaska et al. (2010) conducted a survey to select LLS with $\tau_{912} \geq 2$ from SDSS-DR7. 190 LLSs with redshift $z \geq 3.3$ are detected. Prochaska et al. (2010) reveals that the incidence of LLS between $0< z < 5$ roughly

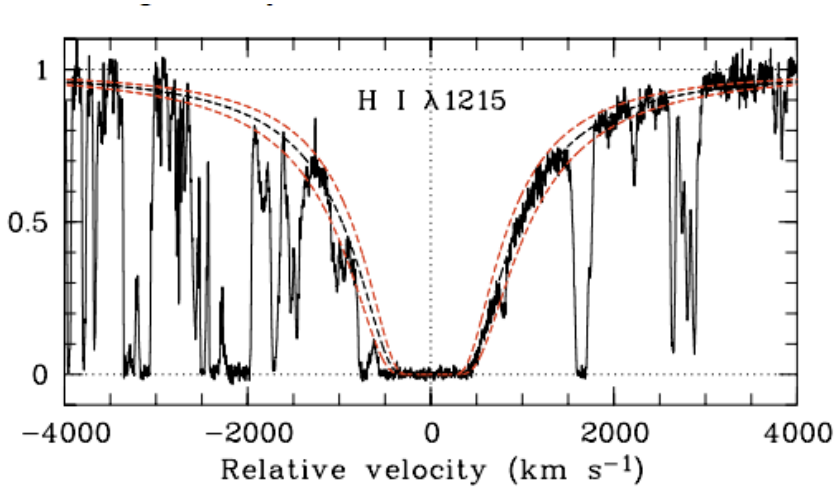

FIGURE 1.8: Adapted from Noterdaeme et al. (2007), DLA at $z = 2.431$ toward quasar Q 2343+125. The derived neutral hydrogen column density is log N(H I) = 20.40 ± 0.07. The dashed curves correspond to the best fitted Voigt profile (black) and the associated errors (red).

follows a power law: $\ell_z \propto (1+z)^{1.5}$. This result is confirmed by (Songaila & Cowie 2010; Ribaudo et al. 2011; Fumagalli et al. 2013; O'Meara et al. 2013)

• Damped Lyα systems

When the column density is large (log N(H I)>19), damped wings appear in the spectrum, allowing an accurate determination of the column density. Above N(H I) > $10^{20.3}$ cm^{-2}, these systems are called damped Lyα systems. Because of the high column density, the gas is mostly neutral. Therefore research on DLAs open the most important window to trace the neutral gas from local to high redshift. It has been widely used as a powerful tool to study: the ISM properties in the halo/disk of galaxies; the formation and evolution of galaxies; the chemical enrichment of the universe and its evolution over cosmic time. Details will be discussed in Section 1.4. Fig. 1.8 shows a typical DLA absorption profile from Noterdaeme et al. (2007).

1.2.2 Metal absorptions

The metal composition and distribution in the IGM, CGM and ISM provides key information on the physical properties of the gas, its origin and evolution. Metallicity in this work is defined as the metal to hydrogen column density ratio:

$$[\mathrm{X/H}] = (\mathrm{logN(X)} - \mathrm{logN(H)}) - (\mathrm{logN(X)} - \mathrm{logN(H)})_{\odot}$$

To determine the metallicity, column densities of both metals and hydrogen of different ionization states need to be measured. For highly ionized systems (Lyα forest and LLS), ionization correction is needed. While for DLAs, most of the gas is neutral and we can use only the dominant ionization state to represent this species. Ellison et al. (2000) claim that the appearance of metals in Lyα forest results from : 1) star formation in the local H I clouds or nearby galaxies ; 2) the early enrichment by Pop-III star formation at very high redshift. Therefore C IV systems in IGM have received a lot of attention in previous works. It is found that C IV absorptions are seen in $\sim$ 50% of the clouds where log N(H I) $>$ 14.5 and in $\sim$ 90% of the clouds with log N(H I) $>$ 15 (Cowie et al. 1995; Ellison et al. 1999; Songaila & Cowie 1996). For systems with log N(H I) $<$ 14, the detection of metals are challenging due to the SNR and resolution of the instruments. Ellison et al. (2000) concluded the N(C IV) distribution can be fitted by a power law which goes down to log N(C IV) = 12.2: $f(N)dN \propto N^{-\alpha}$ with $\alpha = 1.44 \pm 0.05$.

T.S.Kim et al. (2005) studied the metallicity of 17 Lyα systems with N(H I) = 10^{15-19} cm^{-2}. In this work, they define three types of C IV systems: C IV free systems; C IV-only systems and systems with both C IV and other ions such as Si II, SiIV and O VI. The results show that both the N(C IV)/N(H I) ratio and [C/H] are not redshift-dependent. The hydrogen density $n_{\rm H_I}$ in the C IV+ions systems is 10 times higher than that in the C IV-only systems ($10^{-2.5}$ cm^{-3} and $10^{-3.5}$ cm^{-3} respectively). [C/H] for these two kinds of systems are -1.96 and -3.03 respectively. The O VI doublet ($\lambda\lambda$ 1032,1037) has also been observed in the IGM in previous studies (Carswell 2003; Bergeron et al. 2002; Simcoe et al. 2004; Cen & Chisari 2011). Cen & Chisari (2011) pointed out that due to the higher ionization energy needed and higher relative abundance of oxygen compared to carbon, we can use O VI instead of C IV to probe low density IGM. However, the location and formation mechanism of O VI is not clear yet. Based on the simulations, O VI systems exhibits a strong correlation with redshift. D'Odorico et al. (2016) investigate the IGM at z $\sim$3 with a high Signal-to-Noise (SNR) ratio UVES spectrum of the background quasar HE0940-1050. Log N(H I) has been derived down to 13.5. In their metallicity simulation at z = 2.8, as Fig1.10 shows, between the 14$\leq$ log NH I $\leq$ 14.8, 60% C IV-traced absorbers have metallicity in the range of [-3,-1]. For the O VI absorbers, 88% of them have metallicities smaller than -2.

LLSs are found to be strongly associated with heavy element systems e.g. MgII and C IV systems. Charlton & Churchill (1996) have studied on the kinematic structure of 51 MgII absorbers between 0.4 $\leq$ z $\leq$ 1.4 and with EW$_r$ $>$ 0.3Å. All the systems are found to be LLSs. The number density of strong MgII absorbers with rest-frame equivalent width (hereafter EW) EW$_r$ $>$ 0.3Å, are found to be consistent with the LLS number density. When z $>$ 1.2, EW$_r$(C IV) absorbers are found to decrease with redshift. Presumably,

LLSs are the possible large metals reservoir in the Universe (Prochaska et al. 2015). Galaxies solely can not provide enough metals, large fraction of metals must exist in the intermediate region between the IGM and the galaxies. Prochaska et al. (2015) study 157 LLSs in the redshift range [1.76,4.39] and observed by the Keck and Magellan telescopes. They found there is no system at $z \sim 3$ with the metallicity -3. 10% of systems exhibit solar or super solar abundances. Also, based on different metals column densities ratio (Si^+/Fe^+ and O^0/Fe^+), an α enhancement characteristic is found. This likely shows LLSs are the most enriched gas reservoir in the high redshift Universe.

In LLS, hydrogen is partially ionized and should be in ionization equilibrium. In order to obtain the metallicity, the ionization state is vital to be constrained. Prochaska (1999) presents a specific LLS Q2231-00 observed by the 10m W.M.Keck I telescope. In this case, they applied the technique of determining the ionization state by measuring column densities of different elements at different ionization states. The results show a high hydrogen ionization fraction $\chi \equiv H^+/H = 0.97$. In Prochaska et al. (2015), an empirical relation of increasing ionization state with decreasing N(H I) is reported. The relation can be applied to all the species: C^{+3}/C^+, Si^{+3}/Si^+, and Al^{++}/Al^+. Even for absorbers with N(H I) $\sim 10^{20}$ cm^{-2}, a high ionization ratio ($Si^{+3}/Si^+ \simeq$ -0.5 dex) is measured. Fumagalli et al. (2015) study a sample containing 157 optically-thick LLSs with the absorption redshift ranging from 1.8 to 4.4. Contrary to previous work, they use a Bayesian inference model to derive the posterior probability of the chemical composition and physical conditions of these systems (gas-phase metallicity, density, temperature and dust content). The results indicate that a single-phase ionization model is enough for most of the LLSs in their sample, and the ionization parameter $U \equiv n_{\gamma,i} / n_H$ (where $n_{\gamma,i}$ is the ionizing photon density and n_H is the hydrogen density) is in the range of $10^{-3.5}$ - 10^{-2}. In their sample, 70% of the LLSs are metal-poor with metallicities of log $(Z/Z_\odot) \leq$ -1.5. They claim that the study of LLS opens a window to constrain the metal-poor cold gas in the CGM and the ejection of metal-rich galactic winds.

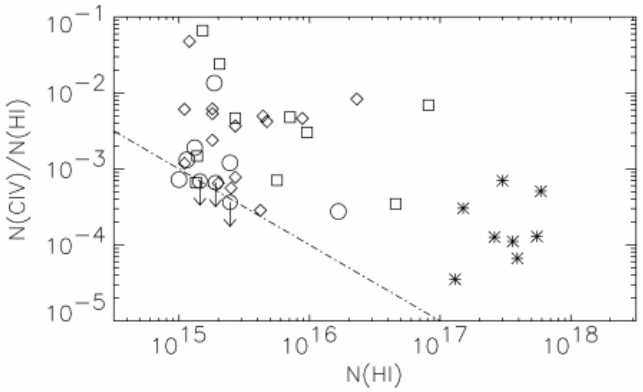

FIGURE 1.9: N(C IV)/N(H I) against N(H I) in T-S.Kim et al. 2005, the open squares are the C IV-only systems, the open circles with arrows are the upper limits. The stars and diamonds are the data from Songaila & Cowie (1996), which indicate the Lyman-limit system and Lyα forest at z$\sim$3. The dashed line is the 3σ detection limit.

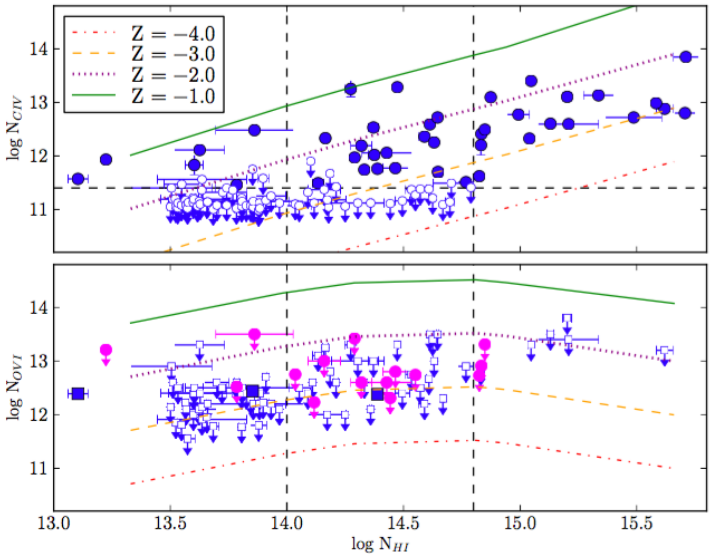

FIGURE 1.10: The column density of C IV and O VI versus N(H I) in D'Odorico et al. (2016). Different color lines denote different metallicities in the simulation. Two vertical dashed lines indicate the column density range 14.0 $\leq$ log N(H I) $\leq$ 14.8. The dots are the real detections, open circles and squares are upper limits. The dashed horizontal line in the upper panel is the C IV sensitivity limit. They empirically identify three possible regimes: At log N(H I) $\geq$ 14.8, the metals with -3 < log$Z/Z_{\odot}$ < -1, likely tracing the CGM close to galaxies. The range 14.0 $\leq$ log N(H I) < 14.8 is where 60 percent of absorbers are enriched to metallicities 3 < log$Z/Z_{\odot}$ < -1, (considering upper limits as measurements); while 40 percent of absorbers are characterized by metallicities log$Z/Z_{\odot}$ $\leq$ -3, , mostly traced by C IV upper limits. When log N(H I) < 14.0 the measurements of C IV lines are no longer sensitive to metallicities log$Z/Z_{\odot}$ $\leq$ -3.

1.3 Techniques

Here we introduce several definitions which are used in the absorption line analysis.

• Equivalent width

As the atoms in the intervening systems can move both towards the observer and away from him, so the observed absorption line has a profile covering the continuum covering some wavelength range. As seen in Fig 1.11, the observed absorption profile area (solid curve) is equal to the area of the square (hashed rectangle) with the width W_λ. This width is called **equivalent width**. One point to bear in mind is that EW is independent of the spectral resolution. EW_λ is the observed equivalent width, equal to $\mathrm{EW}_\lambda \times (1+\mathrm{z}_{abs})$, where EW_r is the rest-frame equivalent width, z_{abs} is the absorption redshift.

$$EW_\lambda = \int (1 - I_\lambda / I_0)\ d\lambda$$

where I_0 is the continuum intensity.

• Optical depth

The optical depth is the logarithmic ratio of the incident flux to the transmitted flux of a material.

$$\tau_\lambda = \mathrm{In}\frac{\Phi_\lambda^{\mathrm{i}}}{\Phi_\lambda^{\mathrm{t}}}$$

where Φ_λ^i is the incident flux at wavelength λ and Φ_λ^t is the trasmitted flux at wavelength λ.

• Doppler parameter

Due to the Doppler effect, the central frequency ν_0 of an absorption line becomes

$$\nu = \nu_0(1 + v_r/c)$$

where v_r is the atom velocity along the line of sight. It is positive when the atom moves away from the observer. The Doppler parameter is defined as b = FWHM / 2 $\sqrt{\mathrm{In}2}$. **FWHM** is the full width at half maximum of the absorption. When considering about Doppler broadening, not only the microscopic thermal motion of atoms should be included, but also the macroscopic bulk turbulence should be taken into account. Therefore the Doppler parameter becomes:

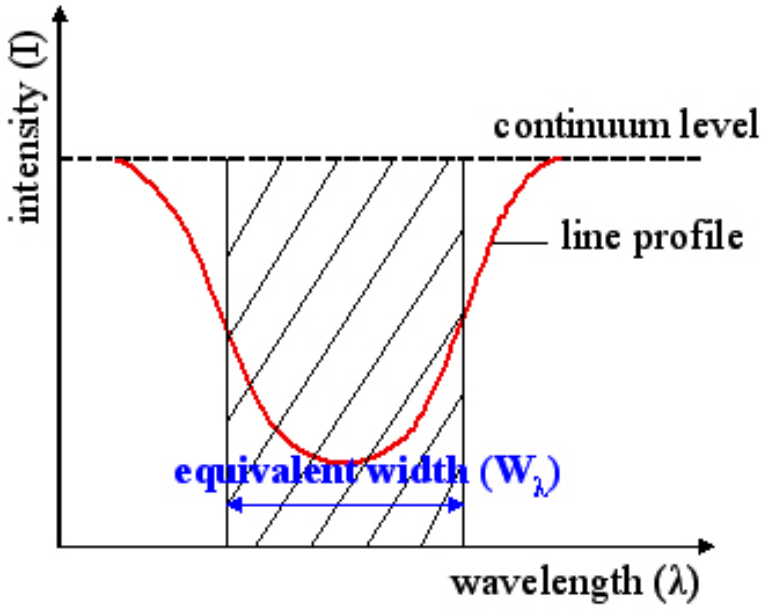

FIGURE 1.11: Definition of equivalent width. The intensity of the absorption profile depends on the number of photons that are absorbed at a particular wavelength. In order to compare the strengths of different absorption lines from a source, or the same absorption line from several different sources, we can use the equivalent width. The the area below continuum level equals to the rectangle with the width W_λ. (Credit:Wikipedia)

$$b = \sqrt{2kT/m + v_{turb}^2}$$

1.3.1 Voigt profile

The absorption lines are described by a Voigt profile which is the convolution of a Gaussian function and a Lorentzian function:

$$V(x, \sigma, \gamma) = \int_{-\infty}^{\infty} G(x', \sigma) L(x - x'; \gamma) dx'$$

where G(′,σ) is the Gaussian function and L(x - x′;γ) is the Lorentzian function, σ and γ are the FWHM. Figure 1.12 gives an example of Gaussian and Lorentzian functions with same widths. In the center of an absorption line, the Gaussian profile . In the wings of the absorption profile, pressure broadening is dominant.

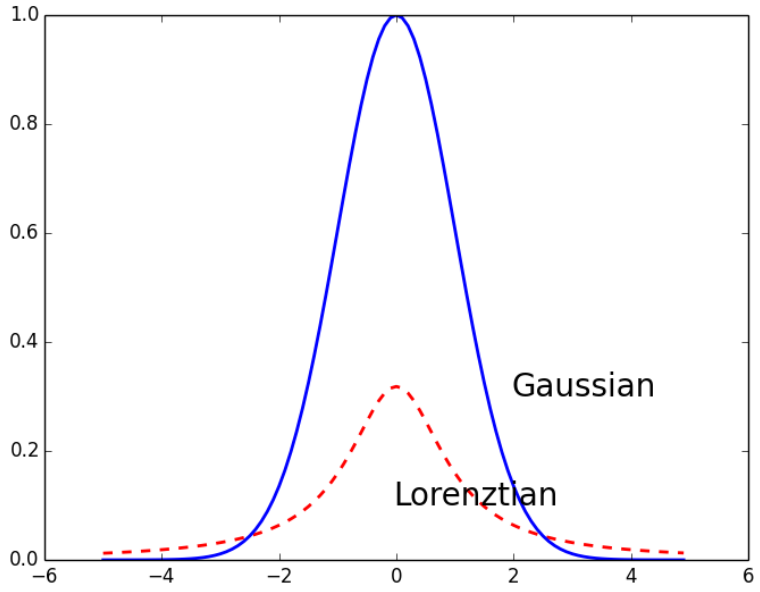

FIGURE 1.12: Gaussian function (blue curve) and Lorenztian function (red curve) with the same FWHM = 2.

1.3.2 Curve of growth

For an absorber, the column density and Doppler parameter are the two major parameters to be measured. The amount of light absorbed is related to the optical depth, which is proportional to the number of hydrogen in the path and the cross section. The relation between the optical depth and the column density of neutral hydrogen is shown in Figure 1.13. The relation between optical depth and column density can be expressed as

$$\tau(\nu) = \mathrm{N}\ \frac{1}{\sqrt{\pi}\mathrm{b}} \int_{-\infty}^{+\infty} \sigma(\nu')\mathrm{e}^{-\frac{\mathrm{v}-\mathrm{v}_0{}^2}{\mathrm{b}^2}}\mathrm{dv}$$

where the cross section of atomic transitions is

$$\sigma = f \times \frac{1}{4\pi\epsilon_0}\frac{\pi e^2}{m_e c} \times \frac{1}{\pi}\frac{\frac{\gamma}{4\pi}}{(\nu-\nu_0)^2 + (\frac{\gamma}{4\pi})^2}$$

hence Eq.1.3.2 simplifies as

$$\tau(\lambda) = 1.498 \times 10^{-2}\frac{Nf\lambda}{b}H(a,u)$$

where H (a,u) is Voigt function, $\mathrm{H(a,u)} = \frac{a}{\pi}\int_{-\infty}^{+\infty}\frac{e^{-y^2}}{(u-y)^2+a^2}\mathrm{dy}$, $\mathrm{a} = \frac{\lambda\gamma}{4\pi b}$, $\mathrm{u} = \text{-}\ \frac{c}{b}\left((1+\frac{v}{c}) - \frac{\lambda}{\lambda_0}\right)$

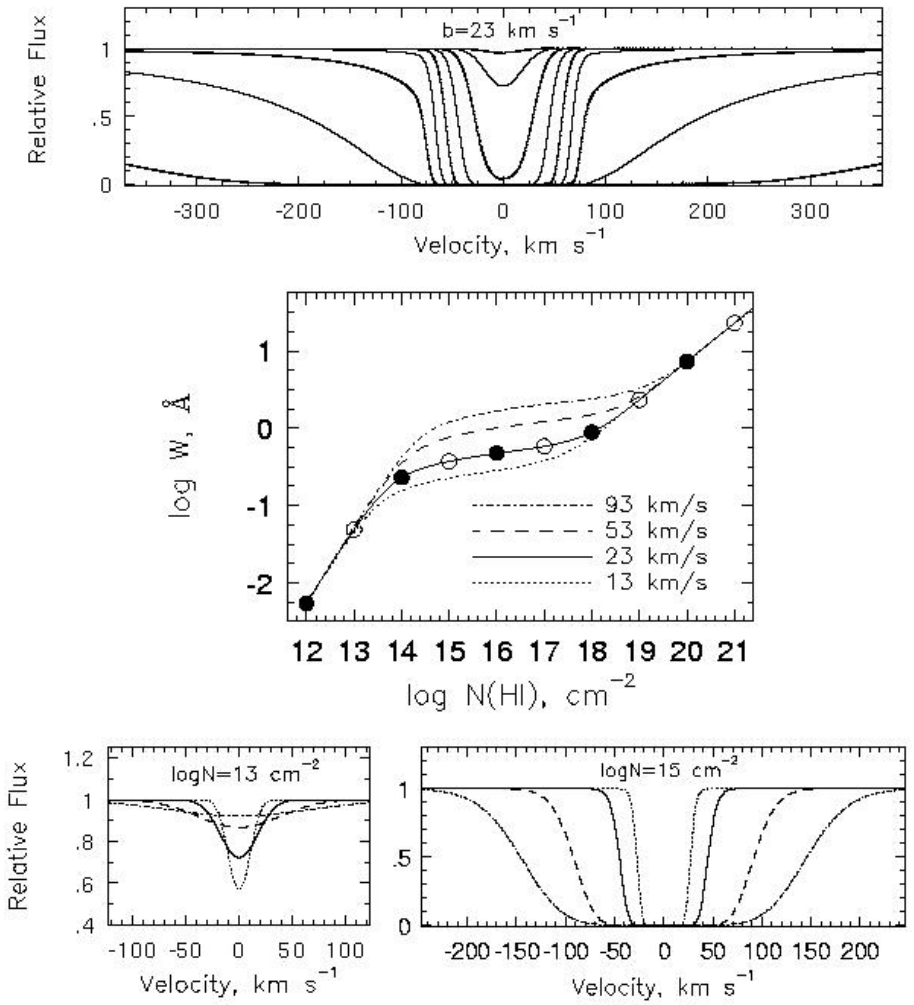

FIGURE 1.13: Curve of growth adapted from Charlton & Churchill (2000). The upper panel shows absorption profiles with Doppler parameter b = 23 km s^{-1} for the series of neutral hydrogen column densities N(H I) = 10^{12} – 10^{20} cm^2. The middle panel shows the curve of growth for the Lyα transition, relating the equivalent width, W, of the absorption profile to the column density, N(H I). The different curves represent four different values of the Doppler parameter: b = 13, 23, 53, and 93 km s^{-1}. The lower left panel shows that, at fixed N(Hi), the depth of the profile is smaller for large b, such that the equivalent width remains constant. On the flat part of the curve of growth, profiles are saturated and the equivalent width increases with b for constant N(Hi). For N(H I) > 10^{20} cm^2 , the profile develops damping wings, which dominate the equivalent width.

In the optically thin region($\tau < 0.1$), log N(H I) < 13 in Figure 1.13 middle panel, the absorption EW linearly increases with hydrogen column density. In this region, EW does not depend on b, see Figure 1.13 lower panel left plot. When N is given, whatever the b value is, the EW does not change.

$$N = 1.13 \times 10^{20} \frac{w_r}{\lambda^2 f}$$

In the middle rather flat regime of the curve-of-growth, both N and b are important to define EW. Therefore in this regime, it is impossible to derive b and N from fitting one line only.

$$\frac{w}{\lambda_0} = 2\frac{b}{c}\sqrt{In\tau_0}$$

After the line gets strongly saturated and damped, EW is again independent of b. As seen in Figure 1.13 lower panel right plot, N can be derived directly from the measure of EW.

$$\frac{w}{\lambda_0} = 2.64\frac{b\sqrt{a}}{c} \times \sqrt{\tau_0}$$

1.3.3 Fitting the absorption profiles

VPFIT (Carswell et al. 1992) is a code used to fit absorption features with Voigt profiles. It is publicly available and is widely used. If the line-of-sight crosses a medium with multiple clouds, the absorption profile is made of several components. Assuming the number and position of the components, Doppler parameters b and column densities N are constrained via VPFIT.

• Single line

When the line is highly saturated and is in the damped regime, the N measurement is reliable. This is normally the case for the H I measurements in DLAs. Figure 1.14 is an example of H I fit of one DLA.

•Multiple absorption lines for one species

If the column density of one species is in regime II of the curve-of-growth, b and N can not be determined from one line only. This is illustrated in Fig 1.15 left panel where we show the result of the Fe IIλ1608 fit only. It is apparent that the fit of other transitions (Fe IIλ2344, Fe IIλ2586, Fe IIλ2600) is not good. Therefore we fit all transitions together

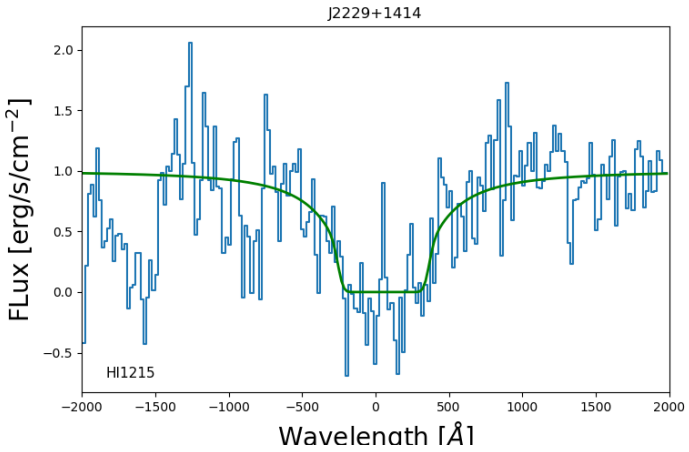

FIGURE 1.14: The Lyα absorption profile of a DLA system J2229+1414 with z_{abs} = 1.585 in this work, the green line indicates the Voigt profile fit, blue curve is the normalized spectrum.

and obtain the fit shown in Fig 1.15 right panel. The results is much better than when only one line is used.

•Tie different species

Different species from the same phase can be used. In that case, we tie together the positions of the components and their Doppler parameter. This is reasonable because due to similar ionization energy of the species used such as Fe II, Si II, ZnII, CrII we can assume they are located in the same phase. See Fig 1.16 for an example.

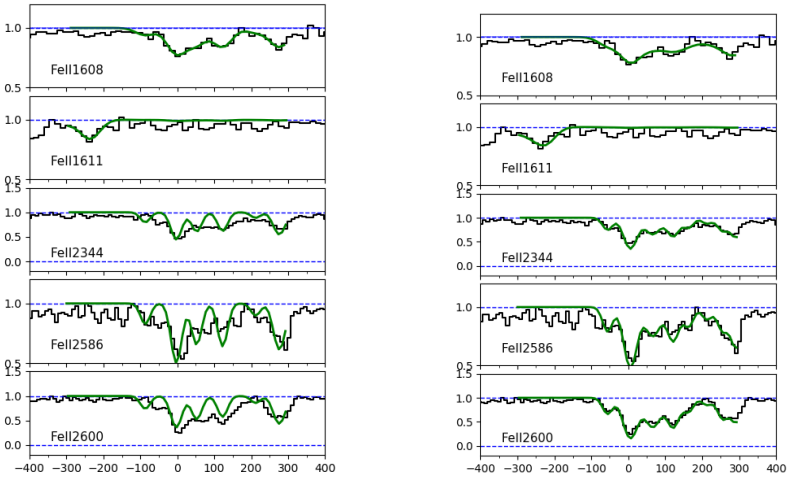

((A)) ((B))

FIGURE 1.15: Fe absorption lines at z = 1.585 towards quasar J2229+1414. (a) Fe II λ1608 only. (b) Multiple lines Fe IIλ1608,Fe IIλ2344, Fe IIλ2586, Fe IIλ2600).

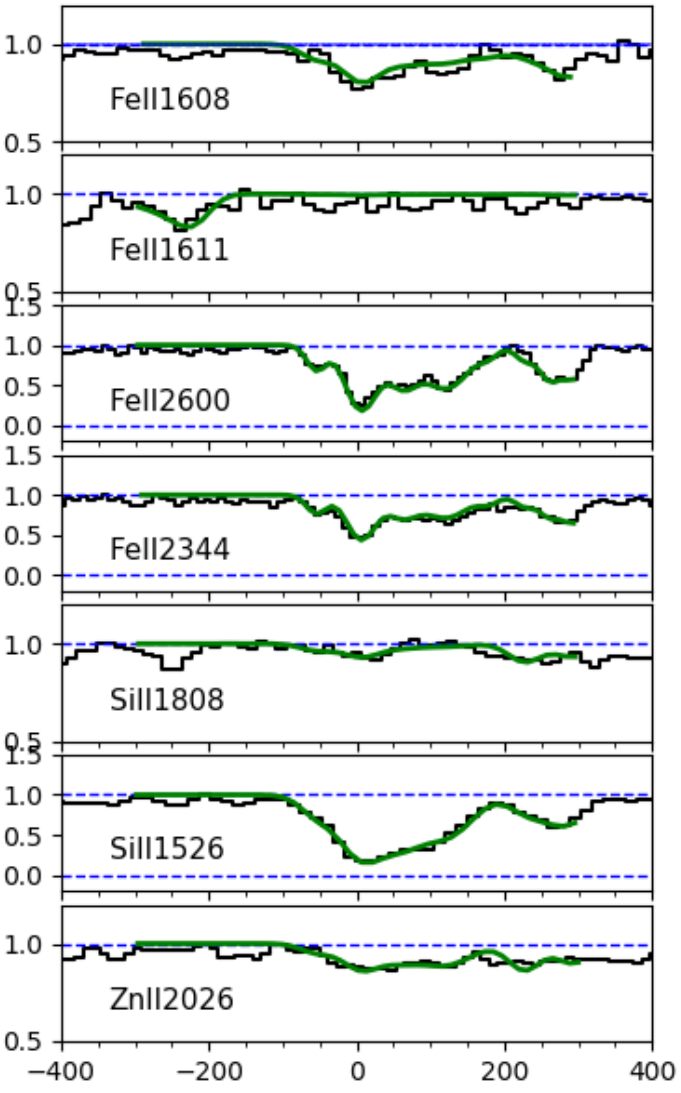

FIGURE 1.16: Quasar absorption line at $z = 1.585$ towards quasar J2229+1414. Fit results of Fe and Si and Zn lines.

1.4 Damped Lyα (DLA) systems

In this section, we will briefly review previous studies on DLAs. We will discuss the neutral hydrogen mass function derived from DLA observations. We will introduce the main physical properties of DLAs: kinematic structure, metal abundances and dust content. Finally we will describe their association with galaxies and with the star formation activities nearby.

1.4.1 DLA surveys

Wolfe et al. (2005) review the historical context of DLA detection. Until early 1980's, only four DLAs had been found accidentally (Beaver et al. 1972; Carswell et al. 1975; Smith et al. 1979; Wright et al. 1979). Wolfe et al. (1986) initiated the first systematic survey of DLAs. 68 background QSOs have been used in this sample. Details are presented in Turnshek & Grillmair (1986). After the initial survey, more samples are selected from large sky surveys of QSO spectra at different redshifts (Lanzetta et al. 1991; Prochaska & Wolfe 2009; Noterdaeme et al. 2009, 2012b; López et al. 2016). Prochaska & Wolfe (2009) selected a sample from SDSS DR5 which includes 738 DLAs at redshift $2.2 \leq z \leq 5$. Noterdaeme et al. (2009) analysed a DLA sample selected from SDSS DR7, which contains 1426 DLAs in the redshift range $2.15 < z < 5.2$. XQ-100 survey (López et al. 2016) is a legacy quasar absorption lines survey from VLT/XShooter which contains 100 background quasars with emission redshift $3.5 < z < 4.5$. The DLA sample is presented in Sánchez-Ramírez et al. (2016). 38 DLA systems are detected between $1.6 < z_{abs} < 4.5$.

When $z < 1.5$, the Lyα absorption line is located below the atmospheric limit. Thus other selection methods are applied in selecting DLA systems, in particular the associated with strong MgII $\lambda\lambda$2798,2803 doublets and 21cm absorption.

- MgII systems

The strong MgII doublet is thought to be a characteristic of large amount of neutral gas (Bergeron & Stasińska 1986). Previous studies have shown that strong MgII systems are tightly associated with DLAs. Actually, it is found that every DLA shows strong MgII$\lambda\lambda$ 2796,2803 doublets. In the range of $0.3 < z < 1.65$, the MgII doublet is redshifted into the optical range. It is much therefore easier and cheaper to study MgII system than to detect DLA with UV telescopes. Therefore to search strong MgII systems are conducted to study DLA systems instead. Several MgII surveys have been conducted at low redshift (Lanzetta et al. 1987; Rao & Turnshek 2000; Rao et al. 2006). Rao et al. (2006) selected

11 strong MgII-Fe II systems from SDSS and re-observed them with the Hubble Space Telescope (HST). They derived a relation between N(HI) and $W(\lambda2796)$-$W(\lambda2600)$. The statistical results indicate that systems with $W(\lambda2796) > 2$Å are associated with N(H I) $> 10^{19}$ cm^{-2} systems. With increasing EW of MgII λ 2796, the N(HI) also increases. No DLA system has been found with $W(\lambda2796) < 0.3$Å. Conversely, all the systems with $W(\lambda2796) > 0.6$Å are DLAs. Moreover, they found that strong MgII systems are also associated with strong Fe II systems. When the absorber with $1<W_{2796}/W_{2600}<2$Å and $W_{2852} > 0.1$Å , it is found to be a DLA.

• 21cm observations

Apart from Lyα absorbing profile, H I is also detectable in the 21 cm spin-flip transition line, which traces the cool phase of the neutral gas. Brown & Roberts (1973) detected 21-cm absorptions in DLAs at z < 1. Wolfe & Davis (1979); Wolfe et al. (1981) detected 21-cm absorption in DLAs at z ∼ 2 but detections of 21-cm at z > 2 are relatively rare. The total number of detections is less than 20 up to now (Wolfe et al. 1985; Kanekar et al. 2007, 2009; York et al. 2007; Srianand et al. 2012). In Srianand et al. (2012), ten absorptions are found using the Green Bank Telescope and Giant Metrewave Radio Telescope.

1.4.2 Ω_{HI}

One of the key purpose of DLA survey is to investigate the neutral gas distribution in ISM and its cosmic evolution. Here we start with several terms which will be used to describe the neutral gas in the ISM survey later. The incidence of DLA system is denoted as ℓ_{DLA}; the H I distribution function $f(NH_I, X)$ and the combining cosmological mass density Ω_g^{DLA}. Where X is the comoving absorption path length (Bahcall & Peebles 1969) defined as:

$$X(z) = \int_0^z (1+z)^2[(1+z)^2(1+z\Omega_M) - z(2+z)\Omega\Lambda]^{-1/2}dz$$

The definition of Ω_g^{DLA} and its relation with the DLA frequency distribution is below(Péroux et al. 2001; Prochaska & Wolfe 2009; Noterdaeme et al. 2009):

$$\Omega_g^{DLA} = \frac{H_0 \mu m_H}{c\rho_{crit}} \int_{N_{min}}^{\infty} N f(N,z) dN$$

where μ is the mean molecular mass, the value is 1.3. ρ_{crit} is the critical density, m_H is the hydrogen mass. This is what we are interested to derive in order to connect the

H I content of DLAs with the star formation and galaxy evolution. The relation between ℓ_{DLA} and $f(N_{HI}, X)$ is

$$\ell_{DLA}(X)dX = \int_{N_{DLA}}^{\infty} f(N_{H_I}, X)dNdX$$

• Shape of the $f(N_{HI}, X)$

Prochaska & Wolfe (2009) fit the frequency of H I column density $f(N_{H_I}, X)$ with a double power law:

$$f(N_{HI}, X) \sim N_{H_I}^{\alpha}$$

In the regime where N(H I) < 21.5, the function is approximately fitted by $f(N_{H_I}, X) \sim N_{H_I}^{-2}$. For N(H I) > 21.5, they derive α = -6.39. Noterdaeme et al. (2009, 2012b) derived the relation from SDSS DR9 with a double power law and a Γ function (the green-dashed line and red solid line if Fig. 1.17 respectively). The Γ function is defined as below:

$$f(N_{H_I}, X) = k_g \left(\frac{N}{N_g}\right)^{\alpha_g} e^{(-N/N_g)}$$

A much flatter slope has been found for the higher N(H I) systems ($\sim$ -3.5) and a similar slope but slightly flatter ($\sim$ -1.6) for the systems N(H I) < 21.4, when comparing the results in Prochaska & Wolfe (2009). The slope for the Γ function is -1.27. The cumulative comoving mass converges when N(H I) > 22. As initiated in Prochaska & Wolfe (2009), it is surprising to find that the shape of projected neutral hydrogen cumulative frequency distribution is nearly consistent between z=0 and z=2, in terms of there is no evolution of $f(NH_I, X)$. The possible reason can be that H I disks at galaxies at z $\sim$ 3 have the same gas distribution as the present-day galaxies. Though clear physical simulation/explanation on this has not been done yet.

• H I mass density evolution with cosmic time

Prochaska et al. (2005) and Prochaska & Wolfe (2009) combined the data from SDSS DR1, DR3 and DR5 that they found that the H I mass density Ω_g^{DLA} decreases sharply from $z = 4$ to $z = 2$. Prochaska & Wolfe (2009) claim the possible reasons for the sharp decrease of H I mass density from z =4 to z =2 can be: (i) the conversion of H I into molecular gas; (ii) the neutral gas is driven into dense star-forming regions and consumed there; (iii) the "violent" feedback processes. It is found that the first assumption can not provide an enough efficient consumption of neutral gas. By applying the Schmidt law, $\Sigma_{SFR} = K \times \Sigma_g^{1.4}$. The unchanging shape $f(N_{H_I}, X)$ provides only 1/10

TABLE 1.1: Different DLA observations to derive the H I comoving mass.

Paper	redshift	data	N(H I)
Noterdaeme+ 2009	$2 < z < 3.5$	SDSS DR7	DLA
Noterdaeme+ 2012	$2 < z < 3.5$	SDSS DR9	DLA
Prochaska+ 2012	$2.2 < z < 4$	SDSS DR5	DLA
Neeleman+ 2016	$0.01 < z < 1.6$	HST	DLA
Péroux+2003	$z > 3.5$	William Hershel	LLS+ DLA

star formation efficiency than the local galaxies. Thus it is possible that the neutral gas in DLAs is driven by secular process into dense star-forming regions in the redshift range $z = [2.5,4.5]$. Furthermore, strong processes such as AGN activity, galactic winds, tidal effects remove neutral hydrogen gas from galaxies at z$\sim$ 3. This feature is confirmed but corrected in Noterdaeme et al. (2012c) who studied a sample consists of 6839 DLAs from SDSS DR9. Noterdaeme et al. (2012c) present a correction for systematics (over/under-estimate of N(H I), incompleteness, and contribution of false positives) as a function of redshift at $z \sim 2.2$. The value of neutral gas cosmological mass at $z \sim 2.2$ is significantly higher than that in Prochaska & Wolfe (2009). They point out that the overestimation in Prochaska & Wolfe (2009) at high redshift is caused by the denser Lyα forest with increasing false positive identifications. At $z < 2.3$, the correction is upwards owing to higher incompleteness and a slight underestimation of N(H I).

Due to the detection limit of SDSS, wether there is evolution of Ω_g^{DLA} between $0 < z < 2$ is not clear. Noterdaeme et al. (2009) found that Ω_g^{DLA} at $z \sim 2.2$ is higher than the value at $z = 0$. Neeleman et al. (2016) derived the H I mass density at lower redshift. They chose the UV spectroscopic data from Hubble Space Telescope (HST) to conduct a blind survey of DLAs at $z < 1.6$ (see the black squares in Fig.1.18). The sample contains 47 DLAs with a mean redshift of 0.476. In this work, mass density of H I in DLA is expressed as $\rho_{H\ I}^{DLA}$, which is very similar to the definition of Ω_g^{DLA} introduced before. These two terms can be converted into each other with only a factor of μ / ρ_c. In Fig. 1.18, Neeleman et al. compared their results with the results Rao et al. (2006). They corrected the result to 0.25×10^8 M$\odot$ Mpc^{-3} to take into account of the missing of high column density DLAs. There is an big difference between the resuls of Neeleman et al. (2016) and Rao et al. (2006). The corrected value is still different with the Rao et al. ($\sim 1.1 \times 10^8$ M$\odot$ Mpc^{-3}). But the value in Neeleman et al. (2016) agrees with that of Zwaan & Prochaska (2006) in the local universe. The most likely reason for this is that Rao et al. overestimate the H I mass density. Finally there is a mild evolution of $\Omega_{H\ I}^{DLA}$ between $z = 0$ to the $z \sim 2$.

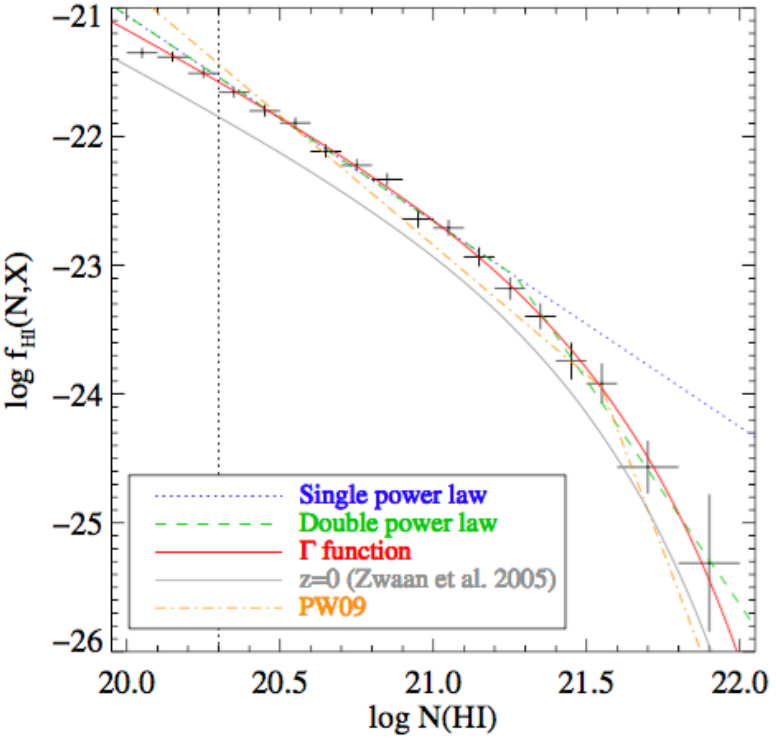

FIGURE 1.17: N(H I) frequency distribution of DLA systems in SDSS-DR7. The observations are fitted by a single power law (dotted blue line), a double power law (dashed green line) and a gamma function (the solid red line). The double-power law fit to the PW09 sample is indicated by the dashed orange line. The Γ-function fit to the frequency distribution are from the 21-cm observations at $z = 0$ in Zwaan et al. (2005) as a solid grey line for direct comparison. Adapted from Noterdaeme et al. (2009).

1.4.3 Metallicities

Metallicities in DLA systems have been explored extensively in previous works. For one DLA system, generally both low and high ionized metal lines are detected. This indicates the multiphase structure of the DLA. The usual low ionization metal lines observed are Fe II, Si II, Zn II, Cr II lines etc. High ionization lines such as C IV and Si IV lines are also typically detected and are usually strongly saturated. O I is the most accurate indicator of metallicity in both neutral and ionized gas. Because it is linked to hydrogen by an efficient charge exchange reaction. Then we have the relation of N(O)/N(H) = N(O I)/N(H I). However, the column density of O I is not easy to obtain since the line is normally strongly saturated. Alternatively, low-ionized unsaturated metal lines such as some lines of Zn II, Si II and Fe II can be used. When calculating the metallicity, we should also take the dust depletion into account. Different species are depleted onto dust grains in the ISM to different degree. For instance, Fe is depleted more compared to Zn and Si. Therefore, Zn and Si abundances are the common indicators to represent the

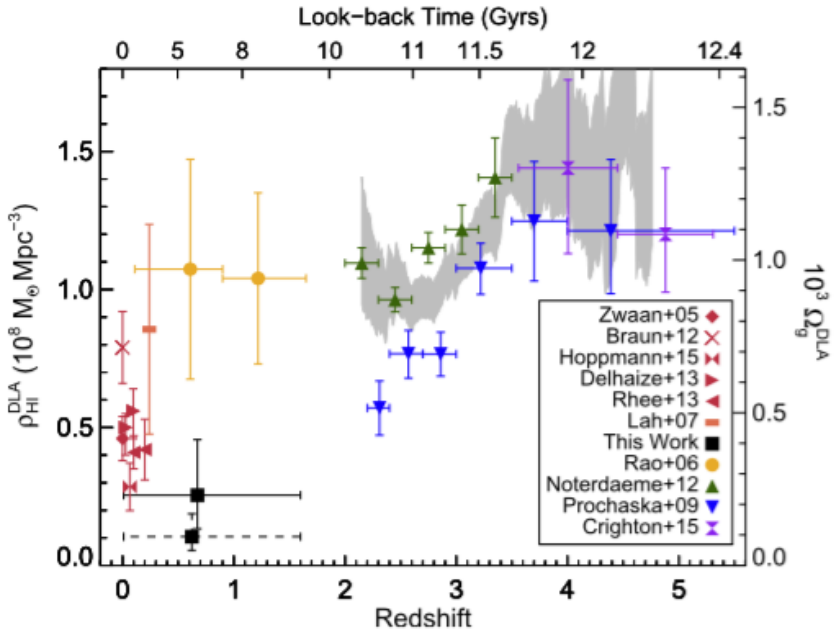

FIGURE 1.18: Neutral hydrogen mass density distribution in DLA against redshift. The black points is the corrected value in Neeleman et al. (2016). Other data are from the literature. The gray area marks the 68% confidence level for the sample compiled by Sánchez-Ramírez et al. (2016). The line density of DLAs over the redshift interval z $\simeq$ 0.01 to z $\simeq$ 1.6 is lower than the measured line density at redshift z $\simeq$ 2 at greater than 2-σ significance, indicating that ℓ_{DLA} (X) has evolved over the past 10 Gyr. Adapted from Neeleman et al. (2016).

DLA intrinsic metallicity. The most-used metal lines in this work are listed in Table 1.2 With moderate and high resolution instrumentations, these low-ionized lines generally exhibit complicated multi-component structure.

The cosmic metallicties of DLAs at different redshifts are important for us to reveal the metal enrichment history in the Universe. Previous studies have shown that typical DLA systems are metal-poor when comparing to the Sun. Pettini et al. (1997b) study 34 DLAs at $z > 2.5$ and find a mean metallicity of [Zn/H]) is -1.13 $\pm$ 0.3. Kulkarni et al. (2005) combine four intervening DLA systems observed by HST with the observations from the literature. They find a mean metallicity of -0.86 $\pm$ 0.11 for $0.09 < z < 1.37$. The new detections at $z < 0.6$ has a meaningful effect on constraining the metallicity at lower redshift. They find that the metallicity in DLA does not appear to rise up to solar at z=0. The reason can be that DLA-associated galaxies do not represent the general population of galaxies at low redshift.

A clear evolution of the mean metallicity in DLAs has been seen by many works. The mean metallicity in DLA systems decreases with redshift linearly up to $z \sim 5$. This has

TABLE 1.2: Most-used metal transition lines in this work. The second column is the rest-frame wavelength, the third column is the oscillation strength of this line.

Metals	wavelength	Oscillation strength
O I	1302.1685	0.048
C I	1328.8333	0.089
C I	1656.9284	0.149
C I	1280.1353	0.048
C I	1277.1328	0.131
C I	1560.3092	0.077
Mg II	2026.4768	0.113
Mg II	2852.9633	1.830
Mg II	2796.3543	0.616
Mg II	2803.5315	0.306
Fe II	1611.2003	1.38×10^{-3}
Fe II	1608.4509	0.058
Fe II	2344.2130	0.114
Fe II	2374.4603	0.031
Fe II	2382.7642	0.320
Fe II	2586.6490	0.070
Fe II	2600.1720	0.239
Si II	1206.5000	1.180
Si II	1526.7070	0.133
Si II	1808.0129	0.002
Si II	1304.3702	0.086
Zn II	2026.1371	0.501
Zn II	2062.6605	0.246
Na II	5891.5833	0.641
Na II	5897.5581	0.320
Ca II	3934.7750	0.627
Ca II	3969.5901	0.311
Cr II	2062.2361	0.076
Cr II	2056.2570	0.103
Cr II	2066.1640	0.051

been derived by Prochaska et al. (2003), which studied 125 damped DLA systems at $0.5 < z < 5$. The relation is given by:

$$Z = (-0.26 \pm 0.07) \times z - (0.59 \pm 0.18)$$

This is also confirmed by Kulkarni et al. (2005, 2007, 2012). Because of the Prochaska et al. (2003) sample contains only 10 DLAs with $z > 4$, the relation is poorly determined at high redshifts. Therefore, Rafelski et al. (2012) aim to determine whether this trend continues up to $z \sim 5$. Rafelski et al. (2012) measured DLA systems metallicity up to ~ 5 from 47 DLA systems using the Echellette Spectrograph and Imager and the High Resolution Echelle Spectrometer on the Keck telescope. They combined the 47 DLAs with another 194 measurements from the literature. As seen in Fig 1.19, each redshift

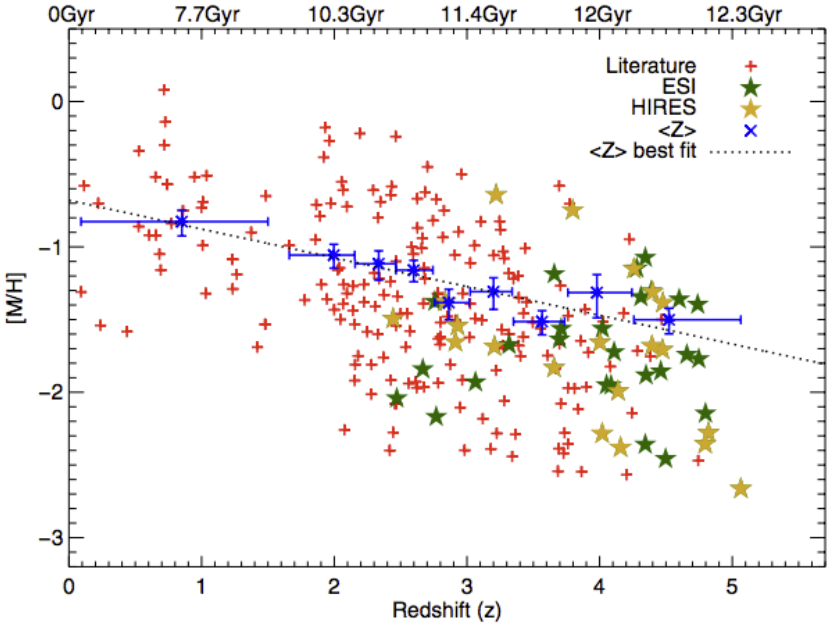

FIGURE 1.19: DLA metal abundances evolution. The mean metallicity decreases with redshift until $z = 5$. The grey-dashed line is the fit of all DLA systems. The red crosses are from literature, the green stars are the observations from ESI; yellow stars are from HIRES observations. The blue crosses are obtained in each DLA bin. Adapted from Rafelski et al. (2012).

bin contains 26 DLAs, on an average. The mean metallicity in each bin is used to fit the function of mean cosmic DLA metallicity against redshift. The mean metallicity is defined as:

$$< Z > \equiv log(\sum_i 10^{[M/H]_i} N(H_I)_i / \sum_i N(H_I)_i)$$

where i is each bin of DLAs as a function of redshift. The results indicate that (1) the average metallicity drops when $z > 4.5$, this is also confirmed in Rafelski et al. (2014); (2) there is no DLA with [M/H] < -3 even though the detection sensitivity can go down to [M/H] < -4. The limit is called the "metallicity floor". The grey-dashed line is the fit of the relation, the slope is 0.22 ± 0.03.

• **Relative abundances**

The relative metallicity is the ratio of different element column densities. For metals X and Y, the relative metallicity is defined as below:

$$[X/Y] = log_{10}(N(X)/N(Y)) - log_{10}(N(X) - N(Y))_{\odot} = [X/H] - [Y/H]$$

In one DLA, due to star formation feedback, nucleosynthesis history and dust content, different elements have different abundances in both gas and dust phases. Among the abundant species, S is the element which is least depleted on dust grains, Fe, Cr and Ca are easily depleted, Si and Zn are slightly depleted when comparing with Fe. Thus the relative abundances of S, Fe, Zn and Si can provide strong constraints on the dust content. In Fig 1.20, each panel describes different relative metal column density ratio against the different metal abundances (Rafelski et al. 2012). Panels (a), (b) shows the relative abundances [S/Si] and [S/Zn] against [Zn/H] respectively, panel (c) is the relation of [Fe/Zn] against [Zn/H]. It is found a 2σ–3σ an anti-correlation between [S/Zn] and [Zn/H]. There seems to be an anti-correlation between [Si/Zn] and [Zn/H]. The most obvious relation is the depletion of Fe, as seen in panel (c).

From the plot it is clear that that the depletion increases with metallicity. This relation is also found in Vladilo et al. (2011) and De Cia et al. (2016). De Cia et al. (2016) selected 70 DLAs from VLT-UVES to study the depletion-metallicity relation. They found [Zn/Fe] in DLAs is consistent with that in Galactic clouds, which suggests that in their sample, dust depletion is mainly related to ISM processes rather than star formation history. On the other hand, works have been done to show that star formation history has ineligible effet on [Fe/Zn]. Berg et al. (2016) correct the Fe abundances for the dust effect and find that the corrected [Fe/Zn] is subsolar in DLA systems. As the alpha process is important during star formation history, it could impact the relative metallicities measured in DLAs.

1.4.4 Dust extinction

Dust is ubiquitous in the ISM of galaxies. It has prominent effect on absorption and scattering of the emission, cooling of the gas and the star formation. Meanwhile, the properties of the dust such as the type of grains, content of the dust and the dust-to-gas ratio are still unclear. Whether it strongly affect the galaxy formation is also not clear yet and models of galaxy formation rarely take dust into consideration. Therefore derivation of the association between the gas and the dust is necessary.

The most obvious dust effect on an object is to make it looks redder, this is called reddening. The reddening is described by the color excesses, which is the difference

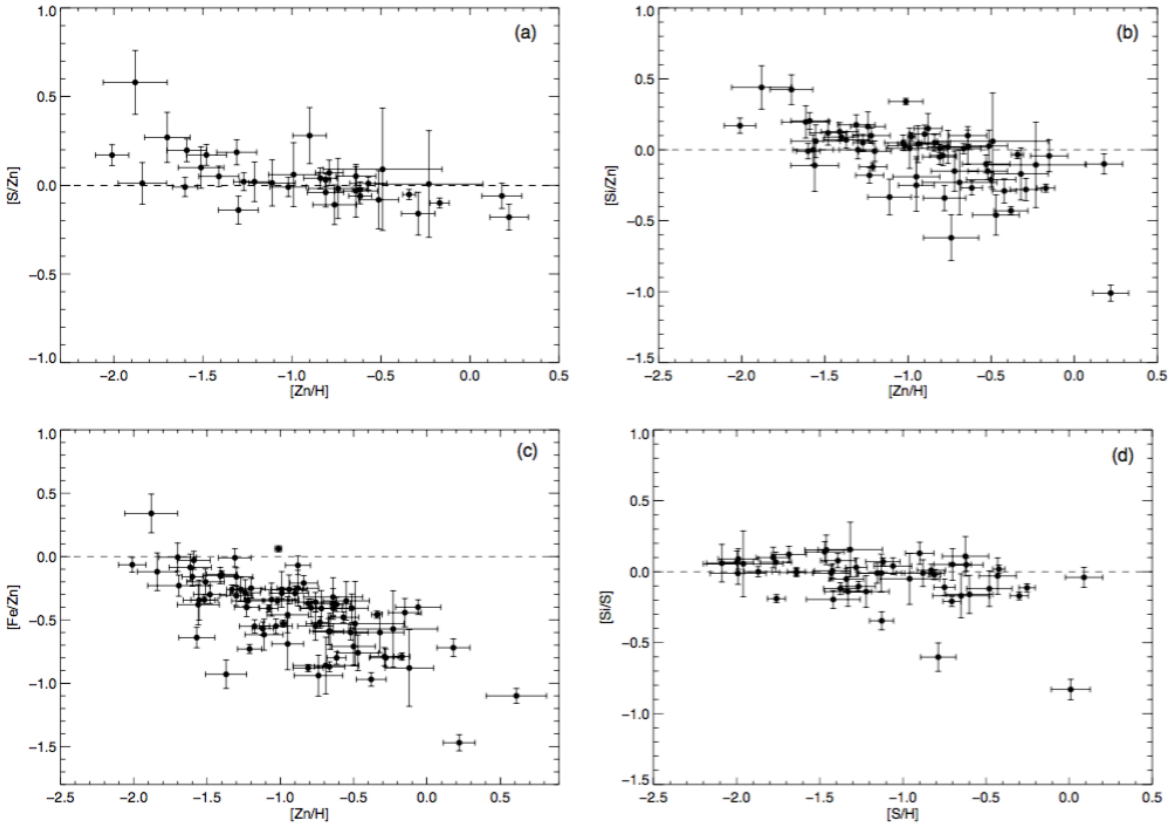

FIGURE 1.20: Different metals abundances comparison: (a) the relative abundances [S/Si] versus Zn abundance. (b) [S/Zn] versus Zn abundance. (c) relative abundance [Fe/Zn] against Zn abundance. The most clear correlation is in (c), which indicates the dust depletion. (d) relative abundance [Si/S] against [S/H]. Panel (d) suggests that Si is not more significantly depleted than S, aside from a few special cases. Adapted from Rafelski et al. (2012).

between observed and intrinsic colors: E(B-V) = $(B\text{-}V)_{\text{observed}}$ - $(B\text{-}V)_{\text{intrinsic}}$ = A(B) - A(V). B and V are the Blue and Visual bands in the UBV photometric system. The color differences and attenuation are related by the parameter R_V:

$$R_V = \frac{A_V}{E(B-V)}$$

R_V for our galaxy is found to be 3.1 (Fitzpatrick 1999); it varies slightly from one line of sight to the other.

When the dust effect applied on galaxies for which the geometry of sources like stars, dust distributions in the galaxies to be considered, this effect we call it attenuation. While with the background source like quasar and GRB, along the line-of-sight, the integrated dust effect on the absorption and scattering of the emission is called extinction. For

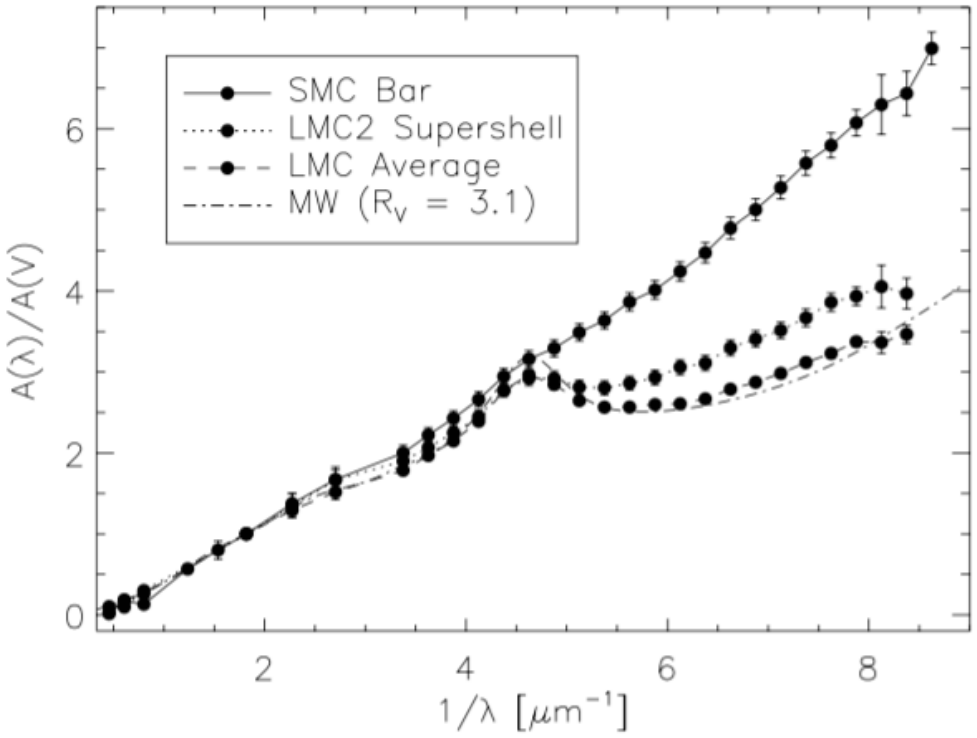

FIGURE 1.21: Adapted from Gordon et al. (2003). Different lines represent different average extinction curves: SMC, LMC supershell, LMC average and MW respectively.

quasar spectrum, we mainly talk about the dust extinction effect, the function is:

$$I_\nu = I_\nu^0 e^{-\tau}$$

where I_ν is the radiation intensity, τ is the optical depth. The observed quasar spectra are already dust-attenuate, and the differences between intrinsic QSO spectra are small. Therefore a spectrum composite is needed for the study of dust extinction. Sets of previous works create this composite spectrum with different data (Cristiani & Vio 1990; Boyle 1990; Francis et al. 1991; Zheng et al. 1997; Vanden Berk et al. 2001; Glikman et al. 2006; Lusso et al. 2015; Selsing et al. 2016). Fig.1.23 presents different composite spectra. Vanden Berk et al. (2001) use over 2000 spectra from SDSS to obtain their composite quasar spectrum. The redshift range is between 0.044 and 4.789. This has been widely used to constrain dust extinction in quasar spectra. The only constraint for this composite is that the host galaxy contamination contribute significantly to the steepening. Therefore Selsing et al. (2016) tries to select UV-brighter QSO from VLT X-Shooter to eliminate this constraint. Fig.1.23 is a comparison of different quasar composite. It is clear that the composite in Vanden Berk et al. (2001) is contaminated by dust of the host galaxy especially at $\lambda > 5000$Å.

After assuming an intrinsic quasar spectrum, then different extinction curves are applied

onto the 'true' composite spectrum to constrain the dust content and attenuation. This is done by matching the corrected SED with the observed quasar spectrum (see Fig.1.22 for an example). Different attenuation curves are derived in different galaxies: Large-Magellanic-Cloud (LMC), Small-Magellanic-Cloud (SMC), Milky-Way (MW) curves and star-burst galaxies (Calzetti et al. 2000). The attenuation curve is generally described by seven free parameters initiated in Fitzpatrick & Massa (1990):

$$k(\lambda - V) = \begin{cases} c_1 + c_2 x + c_3 D(x, x_0, \gamma), x \leq c_5 \\ c_1 + c_2 x + c_3 D(x, x_0, \gamma) + c_4 (x - c_5)^2, x > c_5 \end{cases}$$

where x is the reciprocal of wavelength, x $\equiv \lambda^{-1}$. c_1 and c_2 are the parameters corresponding to the UV linear component, c_3, x_0 and γ describe the 2175Å bump, and

$$D(x, x_0, \gamma) = \frac{x^2}{(x - x_0)^2 + x^2 \gamma^2}$$

The details about this bump is discussed below.

1.4.4.1 Dust-to-gas ratio and dust-to-metal ratio

From the observed QSO spectrum, we can only obtain the gas-phase metallicity. However, part of metals are locked into the dust. Therefore the observed metallicity and the dust depletion can provide information on the dust-to-gas ratio and dust-to-metal ratios (Vladilo 1998). It has been found that the dust-to-gas ratio in DLAs is far smaller than that in our Galaxy (Pettini et al. 1994, 1997a). The dust-to-gas ratio is defined in (Pei et al. 1991) as:

$$\kappa = 10^{21} \ (\tau_B / N_H) \ \mathrm{cm}^{-2}$$

where τ_B is the extinction optical depth in the B band in the rest frame of an absorber. In different papers the definition changes by adopting different dust properties. Vladilo et al. (2006) define the dust-to-gas ratio by A_V and N_H

$$\kappa = A_V / N_H$$

Fig.1.24 gives the dust-to-gas ratio versus the metallicity. They found significant deviations of the DLA dust-to-gas ratio from the MW ratio $A_v/N_H \sim 5.3 \times 10^{-22}$ mag cm^2 atoms^{-1} (Bohlin et al. 1978). It is apparent that this ratio increases with metallicity. Whether the dust-to-gas ratio evolves with time is unclear yet. The Galactic dust-to-gas

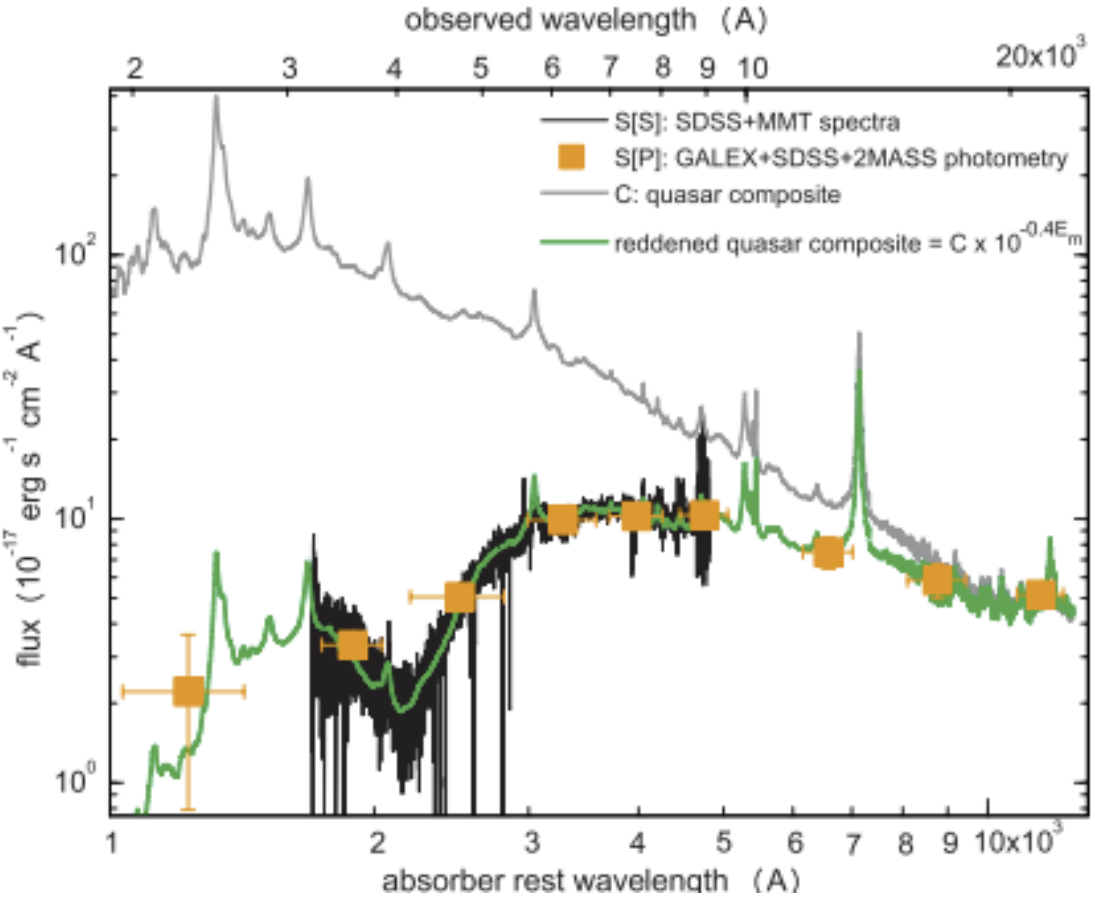

FIGURE 1.22: Example of the reddened quasar spectra composite. The grey curve is the quasar composite from Vanden Berk et al. (2001); the green line is the fit after applying the extinction curve. Adapted from Zhou et al. (2010).

ratio is $1.7\times\ 10^{-22}$ mag cm^2 atoms^{-1}. Chen et al. (2013) combined 10 gravitational-lensed galaxies with 12 GRBs and 4 QSOs and found the value is $1.17\ \times\ 10^{-22}$ mag cm^2 atoms^{-1}, which is slightly lower than the Galactic value. Pei et al. (1991) also reported the dust-to-gas ratio in their DLA systems which at $2 <\ z\ < 3$ are 5% - 20% of that in the Milky Way. From previous studies we can conclude that the dust-to-metal ratio does not change with redshift in DLAs (Edmunds & Eales 1998; Franco & Cox 1986; Zafar et al. 2013), though Chen et al. (2013) reported a slight evolution of the dust-to-metal ratio. The dust-to-metal ratio is defined as the dust properties such as A_V to the total metal content in the gas. De Cia et al. (2013) claim that the dust-to-metal ratio in GRBs and QSO-DLAs increases with metallicity. In their work, 20 GRBs and 72 QSO DLAs are selected in the redshift range $1.2 <\ z\ < 4.0$ (see Fig. 1.25). This relation is also confirmed by Wiseman et al. (2017) with a sample of 17 GRB-DLAs. Therefore based on previous empirical surveys we can assume that the main factor to affect the dust in DLA systems is metallicity.

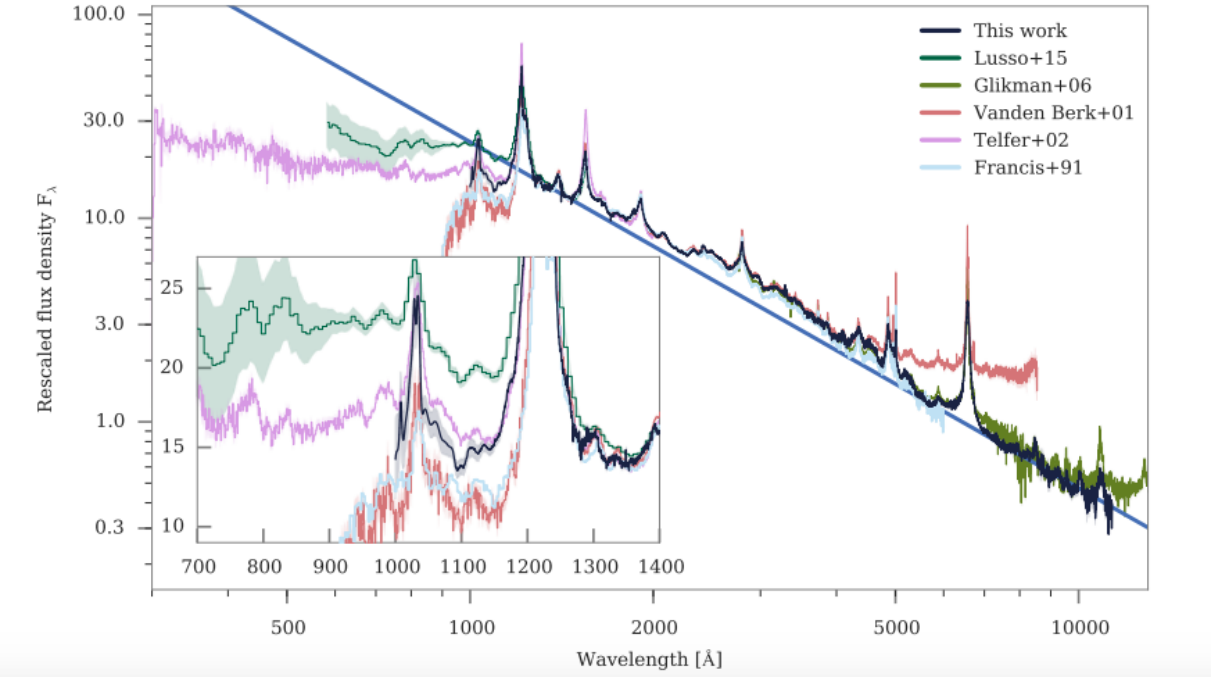

FIGURE 1.23: Comparison of different quasar composites. The blue line is from Selsing et al. (2016), which is one of the widely used composite. Adapted from Selsing et al. (2016).

1.4.4.2 The 2175Å Bump

2175 bump is the dust absorption feature at the rest-wavelength 2175Å (Stecher 1965). This feature is uniquely observed in the MW and strong LMC extinction curves but not in the SMC and star-burst galaxies attenuation curves (Gordon et al. 2003). The physical processes behind the formation of this feature is unknown yet (Draine & Malhotra 1993). Several detections have been done in DLAs. But whether there is a necessary association between this feature and DLAs is unknown (Wucknitz et al. 2003; Prochaska et al. 2009). However, Jiang et al. (2011) systematically studies 39 MgII-associated 2175 absorbers from SDSS-DR3, in their sample, the rather weak 2175 bump appears in the LMC supershell. Up to till now, it is found that this feature is possibly associated with heavy reddeining and/or highly [Fe/Zn] depletions. Ma et al. (2017) observed 13 absorbers with 2175 bump and compared their dust depletion pattern with that of normal DLAs. They found that the [Fe/Zn] in their sample is lower than the value in normal DLAs ($\sim$ -1.2). They also found that the kinematics in their sample is similar to a MW-halo pattern. Simulations has also been conducted to derive the formation of 2175 Bump. Several simulations suggest that the bump can correlate with the dust grain types. Pei (1992) firstly suggests that the different ratio of graphite to silicate grain in Megellanic Clouds can be adopted to reproduce the observed extinction curves with the bump. Bekki

et al. (2015) initiated a simplified model to reproduce the 2175 Bump scarcity in the SMC. They introduce the idea that the generation or absence of the bump is correlated with different types of grains and different star formation histories. They define two types of dust grains, those formed with Carbon are called C-grains, the others are called Si-grains. In SMC, while metallicity is low and strong starburst is undergoing, dust grains are large. Small grains are formed but they are blown away by the radiation-driven dust wind over a time period of 0.2 Gyr. Therefore in their model in the early time of SMC formation, the 2175 bump may be present. For MW and LMC, the gravitational potential is large enough to retain C-grains therefore the generation of the bump is possible.

1.4.5 Association with Galaxies

The association between DLAs and their host galaxies has long been studied. The direct detection of Lyα emission and star light from high-z DLA-galaxy counterparts (z>1.6) are rare (Wolfe et al. 2005). This is due to the DLAs selected by cross-section, which trace the faint end of the galaxy luminosity function (Krogager et al. 2012). Also, the strong emission contamination from the background quasars affects the direct detection for DLA galaxies. Blind detection of the galaxies giving rise to DLAs results in very low success rate (Fumagalli et al. 2015). Though a few detections have been made during recent years (Fynbo et al. 2010, 2011; Noterdaeme et al. 2012c; Péroux et al. 2011; Krogager et al. 2012; Bouché et al. 2012; Krogager et al. 2017).

In the past, it was assumed that the DLA related galaxies can be dominated by one main kind of galaxy type. Recent studies indicate that the host galaxies of DLAs cover all kinds of morphologies. Vladilo et al. (1997) predict that DLAs at intermediate redshift are associated with dwarf galaxies or low surface brightness galaxies. A few detections cast some doubt on this (Chen & Lanzetta 2003; Rao et al. 2003; Nestor et al. 2002). Morphologies of 6 DLA-related galaxies detected by Nestor et al. (2002) cover dwarf, late spiral and low surface brightness galaxies ($0.09 < z < 0.54$), with luminosity between 0.03 L^* - 1.3 L^* and impact parameter between 4–34 kpc. Chen & Lanzetta (2003) detect 11 DLA galaxies at $z < 1$. The morphologies of these galaxies and the impact parameters also vary. However, for these works, the statistics is small therefore clear conclusion can not be reached.

Direct detection of DLA-galaxy counterparts emission are rare. Several indirect methods have been used to derive this association: the strong MgII systems connection with the galaxy; the scaling relations between DLA properties and related galaxy properties and

the DLA galaxies with star forming galaxies connection directly. Furthermore, simulations are conducted for the derivation of this association (Fumagalli et al. 2011; Bird et al. 2014, 2015). Bird et al. (2014, 2015) compared the parameters from their simulations with the observations in Noterdaeme et al. (2012a) and Rafelski et al. (2012). They found that DLAs probe a wide range of halo-mass and have typical virial velocities of 50-100 km s^{-1}.

•MgII systems-galaxy counterparts

Strong MgII absorption lines are associated with large amount of neutral gas (Rao & Turnshek 2000; Rao et al. 2006). From low to higher redshift (z∼3), many emission from MgII-related galaxies have been detected (Rauch et al. 2008; Rauch & Haehnelt 2011; Schulze et al. 2012). The key questions are: from where do the MgII absorbers arise and how do their kinematic structures correlate with the star forming region and the whole galaxy kinematic structure. It is found that MgII systems can arise in infalling gas in the halo or in the the rotation disk.

Kacprzak & Churchill (2011) devote efforts to the relation between neutral hydrogen mass in halo (excludes the neutral hydrogen in DLA) with the star formation in galaxies. They found that infall/accretion H I is traced by small W(MgII) (W≤ 0.3 Å). While the outflow/winds are traced by strong MgII absorption ($W > 1$ Å). Kacprzak et al. (2010) selected 10 MgII-associated galaxies and found among all of the 10 galaxies, the strongest MgII components are consistent with the galaxy rotation curve. Bouché et al. (2013) study the relation between the cold flow from the intergalactic gas relation and W(MgII). Bouché et al. (2016) combine the systems from Bouché et al. (2013) with strong MgII absorption lines (W >1Å) and the new VLT/MUSE data to look for the MgII-related star forming host galaxies. They successfully detected a quasar-galaxy pair at $z = 0.9096$ with the dust-corrected SFR = 4.7 ± 2.0 $M_\odot$ yr^{-1}, with a wind mass outflow rate equals to 0.5-5 M⊙ yr^{-1}.

• Scaling relations

Apart from MgII studies, observational scaling relations between the fundamental properties of host galaxies such as luminosity, stellar mass, star formation rate with the metallicity in DLAs are studied. These relations include: **luminosity-metallicity** relation (Møller et al. 2004); **velocity-metallicity** relation (Ledoux et al. 2006); **stellar mass-metallicity** relation(Bouché 2008; Christensen et al. 2014; Møller et al. 2013; Neeleman et al. 2013); the **spin temperature-metallicity** relation (Kanekar et al. 2009, 2014); the **stellar mass-metallicity** relation (Maiolino et al. 2008; Møller et al. 2013); the **impact parameter-metallicity** relation (Krogager et al. 2017).

Among these relations, the velocity-metallicity relation is the most direct observational relation for DLA system itself. The relation is initiated by Ledoux et al. (2006). With the underlying simple linear scaling relation of the galaxy luminosity with the mass of the dark-matter halo, they found a simple scaling relations between the weak absorption lines widths with the DLA metallicity, this relation is expressed as below:

$$[\mathrm{X/H}] = 1.35(\pm 0.11)\log \mathrm{W}_1 - 3.69(\pm 0.18)$$

where W_1 is the velocity width of the low-ionization metal lines. They find that the slope of the DLA velocity-metallicity relation is consistent with that of the luminosity-metallicity relation derived for local galaxies. Also from the velocity width of the absorption line width, we can use it as an proxy for the gravitational mass of the host galaxies. That means DLA systems with lower metallicities associate with the galaxies having the lower masses. This is also can explain why the DLA systems with Lyα emission detection has high metallicity.

Møller et al. (2004) found that the DLA metallicity correlate galaxy luminosity. They suggest that if we select higher metallicity DLAs, there is higher probability to detect Lyα emission from the host galaxies. They observed a Lyα emission in a DLA trough centered at z=2.0395. The Lyα emission flux is 5.4×10^{-17} ergs $\mathrm{s}^{-1}\mathrm{cm}^{-2}$, which is similar as the results of GRB DLA-galaxies at similar reshift Fynbo et al. (2002). By combining the four Lyα emitters out of seventeen DLAs in Warren et al. (2001), they suggest a positive Lyα emission luminosity - DLA metallicity (L_α - Z) relation. Møller et al. (2013) further quantify if there is an evolution of the DLA gravitational mass metallicity relation and the connection between the galaxy mass metallicity relation and the star formation activities. This work study 110 DLAs within $0.11 < z < 5.06$ and found the zero-point of this relation change with redshift significantly. They compared the galaxies mass-metallicity relation as a function of stellar mass in Maiolino et al. (2008), and find a remarkable agreement of the evolution of the zero point of the DLA velocity-metallicity correlation with the galaxy stellar mass-metallicity evolution when $z \leq 2.6$. In the end, they draw a direct link between a flux selected galaxy sample and their DLA sample using the evolution of the mass-metallicity relation,

This relation is described as:

$$\log[\mathrm{M}_*/\mathrm{M}_\odot] = 1.76[\mathrm{M/H}] + \mathrm{C}_{[\mathrm{M/H}]} + 0.35\mathrm{z} + 5.04$$

where [M/H] is metallicity, $C_{[M/H]}$ is the parameter which keeps the consistency between absorption and emission metallicity. The relation is supported by the studies of Christensen et al. (2014). Christensen et al. (2014) measure 12 galaxy-DLA pairs at redshift

range [0.1,3.2] and found the slope is in good agreement with the previous assumption.

Besides of these fundamental correlations, Kanekar et al. (2014) reported an anti-correlation

$$T_s = (-0.83 \pm 0.16) \times [\mathrm{Z/H}] + (1.94 \pm 0.20)$$

where T_s is the spin temperature comes from the comparison between the H I column density measured from the Lyα absorption and the integrated H I 21 cm optical depth. The spin temperature contains information on the distribution of neutral gas between the different temperature phases of the ISM in the absorber, specifically on the fractions of warm and cold gas. It has been found that the spin temperature appeared systematically higher in high-z DLAs. This anti-correlation suggests that systems with high metallicity have higher cold gas fraction, thus low spin temperature. Also, Kanekar et al. (2014) reported a 4σ difference of T_s for DLA at $z < 2.4$ than $z > 2.4$. This is consistent with the sharp difference of M_* - Z relation in Møller et al. (2013). Therefore it is plausible to claim that at high-z, DLAs have lower metallicity and stellar mass, and are also with warmer phase neutral gas.

1.4.6 SFR in DLAs

In order to study the star formation over time, the star formation rate (SFR) is the most important parameter to be measured. It is in the unit of $M_\odot$ yr^{-1}. In general, the SFR can be measured from the ratio of the young stars($<$ 1Gyr) to the old stars (3-15 Gyr) luminosities (Kennicutt 1998b). In the galaxy spectrum, the young and old stars are with different colors. By calculating the flux of stars at different colors, the mean SFR over 10^8 - 10^9 years can be obtained. Different techniques are used to measure SFR: UV emission, FIR emission and nebular recombination lines such as Hα, Hβ, Pα, Pβ. The UV SFR is measured directly by the UV continuum luminosity over the rest frame wavelength range 1250-2500 Å . With increasing redshift, this range is shifted into optical wavelength, which is easy to detect for most of spectroscopic instruments up to $z \sim 5$. Dust in the ISM can absorb the galaxy bolometric luminosity and re-emit it in the infrared (IR) wavelength range 10-300 μm. Thus the SFR can be measured from the FIR emission. Since the dust cross section peaks in the UV, so the re-emitted FIR emission is a good tracer of the young population stars SFR. The emission dominates around 40-120 μm. Kennicutt (1998a) measured the UV SFR $SFR_{UV} = 1.4 \times 10^{-28}$ Lν (ergs s^{-1} Hz^{-1}). The SFR from the FIR given in Kennicutt (1998a) is $SFR_{IR} = 4.5 \times 10^{-44}$ L$_{IR}$. Apart from UV and FIR measurements, nebular recombination lines redwards the Lyman limit especially Hα are also used widely to measure the SFR. The relation measured in Kennicutt et al.

(1994); Madau et al. (1998) is:

$$\mathrm{SFR}(\mathrm{M_\odot yr^{-1}}) = 7.9 \times 10^{42} \mathrm{L(H}\alpha)(\mathrm{ergs\ s^{-1}})$$

Fig.1.27 presents the extinction corrected relation between different SFR estimators with the FIR SFR from Rosa-González et al. (2002). In the plot, we can see that the standard SFR measurements provide good agreement between SFR(Hα), SFR(OII) and SFR(UV) with SFR(FIR).

Once luminosity of Lyα emission has been measured, one can convert it into SFR via Kennicutt relation (Kennicutt 1998a). Kennicutt (1998a) measure the SFR from H I, Hα and CO distributions of 61 spiral galaxies and far-infrared CO observations from 36 infrared-selected starburst galaxies. The results they obtained is :

$$\Sigma_{SFR} = (2.5 \pm 0.7) \times 10^{-4} \left(\frac{\Sigma_{gas}}{1 M.pc^{-2}} \right)^{1.4 \pm 0.15} M.yr^{-1} kpc^{-2}$$

Studies devote efforts on whether the DLAs galaxies and the typical star-forming galaxies are from the same galaxy population (Fynbo et al. 1999; Bunker et al. 1999; Warren et al. 2001; Møller et al. 2002; Weatherley et al. 2005; Rauch et al. 2008). As pointed out in Berg et al. (2016), there is an overlap between star forming galaxies selected by different methods, including color-selected and magnitude-selected galaxies. Lyman-break Galaxies (LBG) is one kind of strong star forming galaxies (Giavalisco 2002). These galaxies are selected via colors (Steidel et al. 1996). In the UGR filter system, they exhibit flat G-R color and extremely red U-G color. For high redshift galaxies, since the Lyman break shifts into optical wavelengths, the feature is easy to select them (Ouchi et al. 2004; Bouwens et al. 2010; Stewart et al. 2013). Lyman alpha emitters (LAE) are one type of galaxy with strong Lyα emission selected through narrowband imaging (Cowie & Hu 1998). The emission is considered to be produced by star formation. LAEs have been largely searched for systematically at high redshift especially $5 < z < 7$ (Ouchi et al. 2008, 2010, 2018). Previous studies indicate there is a large possible overlapping between LBG and LAEs (Fynbo et al. 2008). We now need to study whether there are overlaps between DLA galaxies with theses two types of galaxies. Møller et al. (2002) claim that DLA host galaxies are LBGS. Some DLA emission properties (half-light radius, radial profile, optical to near-infrared color, morphology, Lyα emission EW and velocity structure) have been compared with LBGs with similar absolute magnitude. Fynbo et al. (2008) construct a model assuming that DLAs and star forming galaxies are from the same parent population of galaxies at $z \sim 3$. This model assumes an empirical relation

between DLA metallicity and luminosity of the host galaxy:

$$Z = Z_* \left(\frac{L}{L*}\right)^{\beta}$$

where, Z_* is the metallicity for the L_* of the LBG metallicity from Pettini et al. (2001), β is the slope. Then a Holmgerg relation is used to describe the connection between the H I cross section and the luminosity R_{H_I} / R_* = (L / L_*)^t. with

$$R_* = \sqrt{\frac{dn}{dz}\frac{2H_0\sqrt{(1+z)^2(\Omega_m z+1)-\Omega_\Lambda z(z+2)}}{\pi c(1+z)^2 I}}$$

where $I = \int_L^\infty min\Phi_*(4L/L_*)^{\alpha+2t}exp(-L/L*)dL$, the Φ_* is the luminosity function. Krogager et al. (2017) detected 7 Lyα emission in 11 metal-rich DLA systems, which supports the simple model in Fynbo et al. (2008).

Another method iniated by Wolfe et al. (2003b,a) is to use the [C II] $\lambda 158\mu m$ cooling rate to measure the SFR per unit area ($\dot{\Phi}^*$) in DLAs. When the photon spontaneously decays from C+ (C II*λ 1335.7 Å) $^2P3/2$ to $^2P1/2$, it produces [C II] 158 μm emission. This process is the main cooling process of neutral gas. With the assumption that gas in DLA is in thermal balance, the heating rate equals to cooling rate. If the heating provided by the FUV background radiation is much lower than the cooling rate derived from C II, then there is another source of radiation to balance the cooling rate which is thought to be the radiation from hot stars. The cooling rate is measured using the C II fine structure absorption (C II*λ 1335.7). The spontaneous emission of C II$158\mu m$ per H atom is defined as below (Wolfe et al. 2005)

$$\mathrm{l_c} = \frac{\mathrm{N(CII*)h}\nu_{\mathrm{ul}}\mathrm{A_{ul}}}{\mathrm{N(H\ i)}}\mathrm{ergs^{-1}H^{-1}}$$

where hν_{ul} is the [C II] 158 μm emission energy and A_{ul} is the Einstein coefficient. A two-phase model of DLAs is also introduced in Wolfe et al. (2003b): the cold neutral medium (CNM) with T $\sim$ 100 K and n $\sim$ 10 cm^{-3} is surrounded by the warm neutral medium (WNM) with T $\sim$ 3000 K and n $\sim$ 0.02 cm^{-3}. The cooling rate in WNM is a factor of 10 higher than it is in CNM. This model has been developed in Wolfe et al. (2008) and Neeleman et al. (2013). Wolfe et al. (2004) measured the SFR per unit area for 22 DLAs at $1.6 < z < 4.5$ with this technique. They obtained $\langle\Phi_*\rangle$ for CNM 11.3 $\times$ $10^{-3} M_\odot$ year^{-1} kpc^{-2} and for WNM 0.21 $M_\odot$ year^{-1} kpc^{-2}.

• Simulations

Simulations have been performed to investigate the connection between DLAs and SFR in the associated galaxies (Wolfe et al. 2003b,a; Nagamine et al. 2004; Fynbo et al. 2008; Berry et al. 2016; Krogager et al. 2017). Nagamine et al. (2004) study the distribution of the star formation rate (SFR) and metallicity of DLAs in the redshift range $z = 0$–4.5 by SPH simulations of the ΛCDM model. The simulation includes the standard cooling and heating effects and a phenomenological model for feedback by galactic winds. The latter one can be used to constrain the effect of galactic outflows on the distribution of the SFR and metallicity of DLAs. They presented in their model the projected SFR density as a function of N(H I) follows the Kennicutt law well at all redshifts. However, they find that the median metallicity in their simulated DLAs is close to that of LBGs but is higher than that for typical DLAs by nearly an order of magnitude. This could be due to the lack of consideration of the SN feedback or the multiphase structure of the gas in their simulations. Berry et al. (2016) introduced a semi-analytic model to find that the DLA-galaxies and star formation galaxies (SFGs) are similar in stellar mass, SFR and dust extinction at z=2. This model is based on Popping et al. (2014); Somerville et al. (2015) which includes the recipe of separated tracking of atomic, molecular and ionised gas and H2 based star formation. This model successfully reproduce the properties of DLA at similar redshift. The model indicates that DLA host galaxies and SFGs follow the same relations between stellar mass and DLA cross-section, cold gas fraction, SFR and metallicity, and dust extinction as observed in the overall galaxy population. But DLAs preferentially select galaxies with more cold gas, which causes them to have higher cold gas fractions, higher SFRs, lower metallicities, and less dust extinction at a given stellar mass than the overall galaxy population. The results are shown in Fig. 1.28. Mannucci et al. (2010) present a fundamental relation between stellar mass, SFR and gas-phase metallicity (FMR relation), which is a tight surface in the 3D space (see Fig. 1.29) observed from local until $z \sim 2.5$. In this relation, the metallicity increases with stellar mass and decreases with SFR. They found that there is no evolution between FMR when $z < 2.6$. At $z \sim 3.3$, an evolution about 0.6 dex is reported. The galaxies sample is extracted from SDSS for z=0 and the literature at $z = 0.5$-2.5 (Savage & Sembach 1991; Shapley et al. 2005; Liu et al. 2008; Epinat et al. 2009; Law et al. 2009; Lehnert et al. 2009) and at $z = 3$-4 (Maiolino et al. 2008; Mannucci et al. 2009). The derived FMR relation is presented in Fig.1.29. The existence of the FMR can be explained by the interplay of infall of pristine gas and outflow of enriched material. At high-z, the dependence of metallicity with SFR results from the former effect and the metallicity dependence on stellar mass and dominates at low redshift. If we need to derive this relations in DLA systems, we need firstly figure out the differences and/or connections between the metallicity measured from emission and absorption profiles. The metallicity measured in Mannucci et al. (2010) is from emission-line ratios. Due to there is no consensus on the

association between metallicity measured from absorption and emission. FMR with the metallicity in DLA is not clear yet.

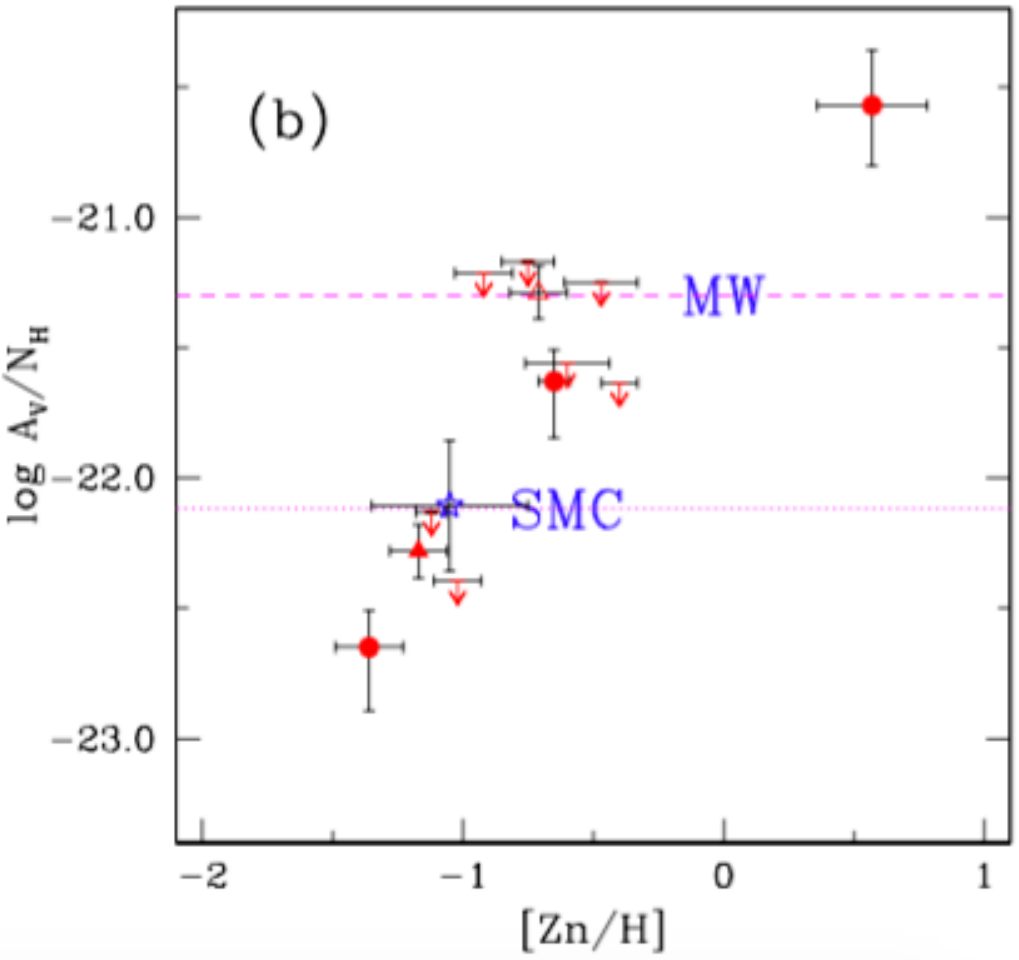

FIGURE 1.24: Dust-to-gas ratio versus metallicity. The extinction is calculated in the rest frame of the absorber. Circles and arrows pointing down: A_v measurements and upper limits from Vladilo et al. (2006); Triangles: QSO/DLAs from Ellison et al. (2005); empty triangle: B0438436. Square: extinction for J0121+0027 from Wang et al. (2004). Open star: SMC line of sight towards Sk 155 Welty & Hobbs (2001); Fitzpatrick (1985). Dashed line: mean MW dust-to-gas ratio for $R_V = 3.1$ (Bohlin et al. 1978). Dotted line: mean SMC dust-to-gas ratio Gordon et al. (2003). Adapted from Vladilo et al. (2006).

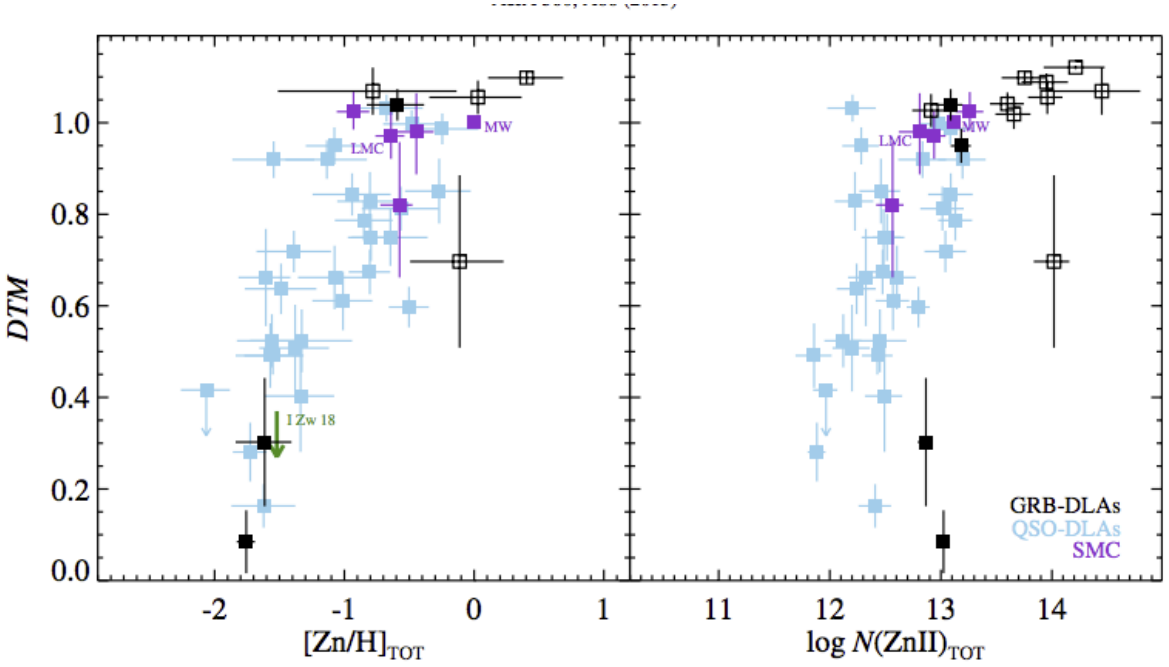

FIGURE 1.25: Dust-to-metal ratio in DLAs versus metalliciy indicated by Zn (left panel) and the column densities of ZnII (right panel). The blue squares are QSO-DLAs; black squares are the GRB-DLAs. It is clear that the dust-to-metal ratio in DLA increase with metallicity. Adapted from De Cia et al. (2013).

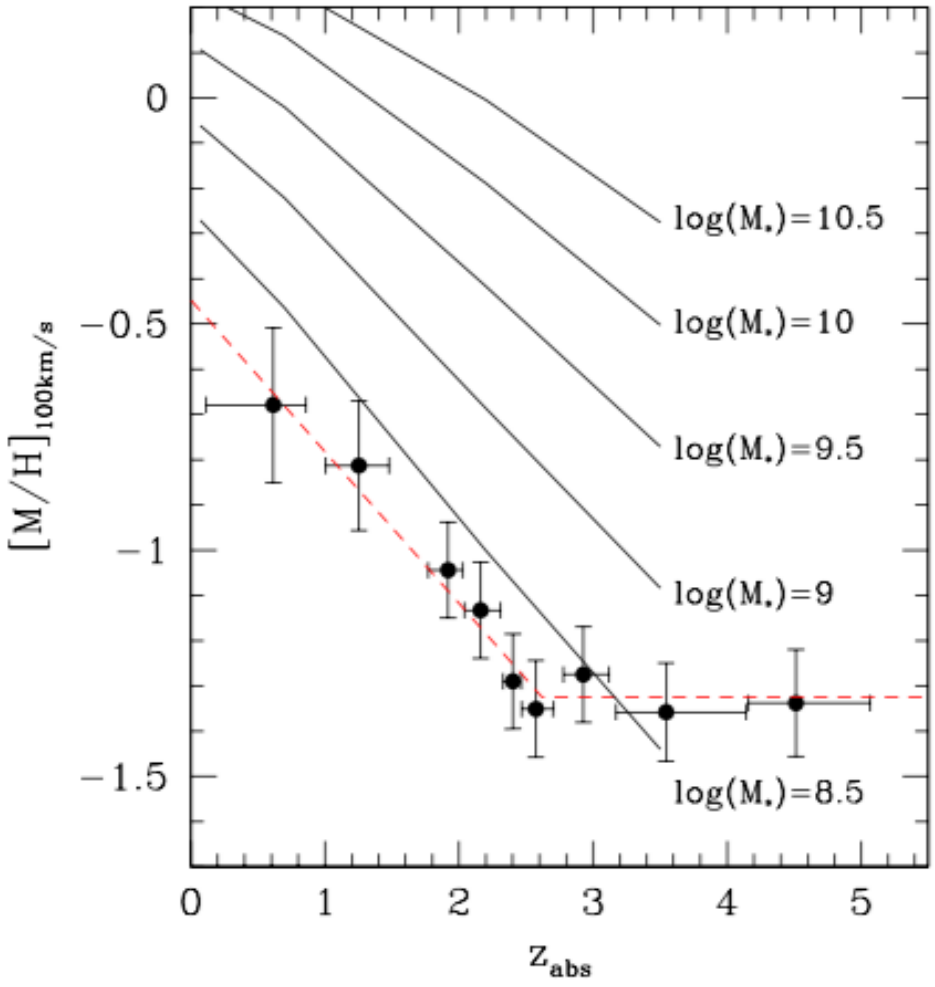

FIGURE 1.26: Stellar mass - metallicity relation. The black dots are the DLA systems from Møller et al. (2013). Different galaxy mass is from (Maiolino et al. 2008). The red dashed line Adapted from Møller et al. (2013). Adapted from Møller et al. (2013).

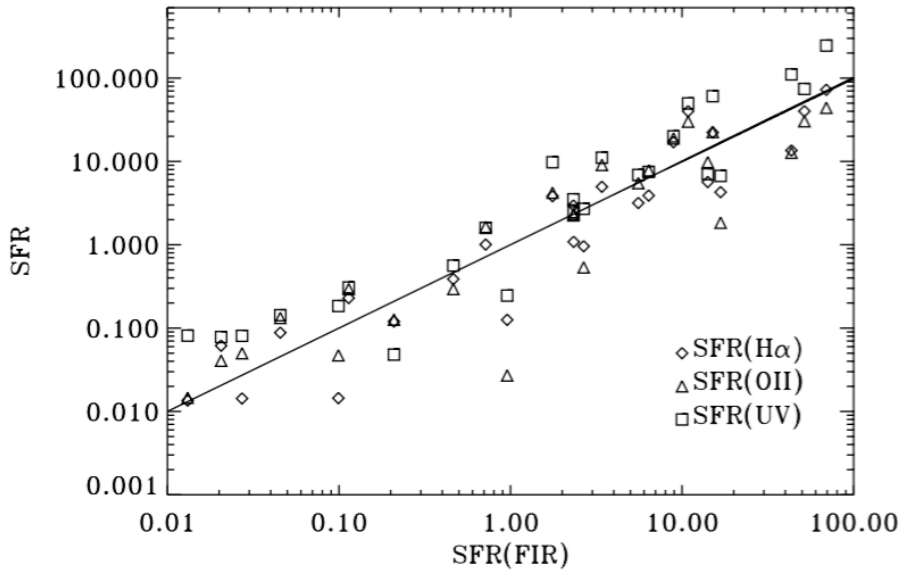

FIGURE 1.27: Adapted from Rosa-González et al. (2002). Corrected SFR estimators versus SFR(FIR). The dust extinction correction is applied to the data. The solid line represents equal values.

.

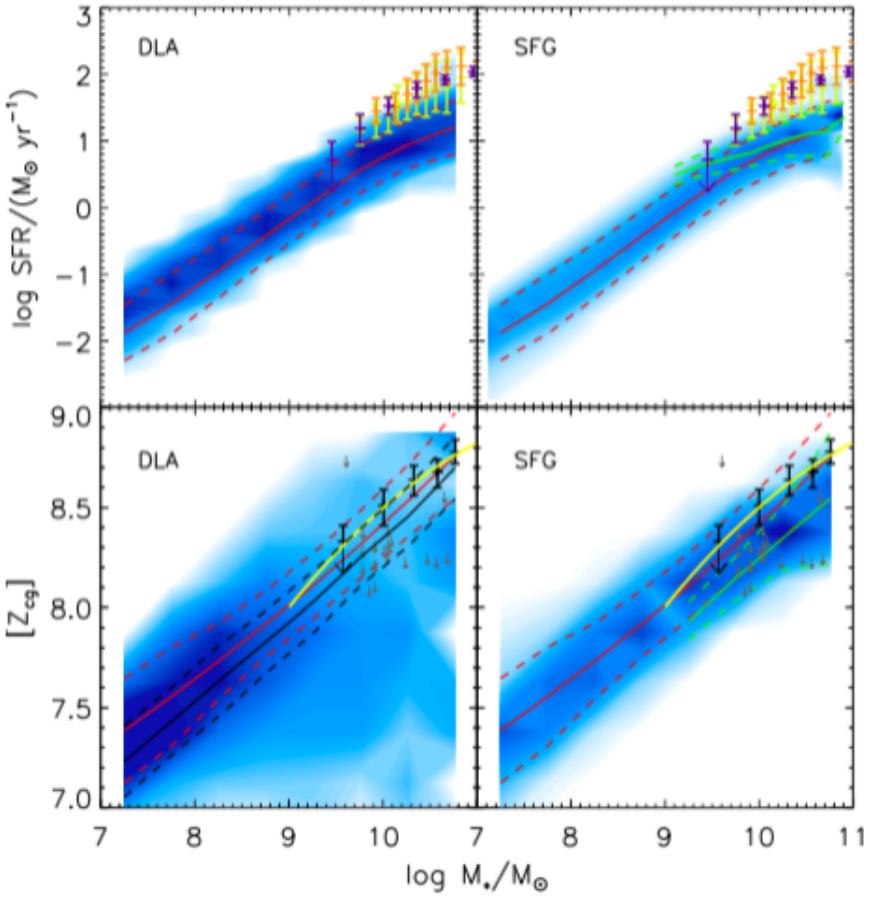

FIGURE 1.28: Adapted from Berg et al. (2016). Upper panels are the SFR against stellar mass in both DLA and SFG. Lower panels are the average metallicity against the stellar mass. The squares with error bars are the galaxies from literature.

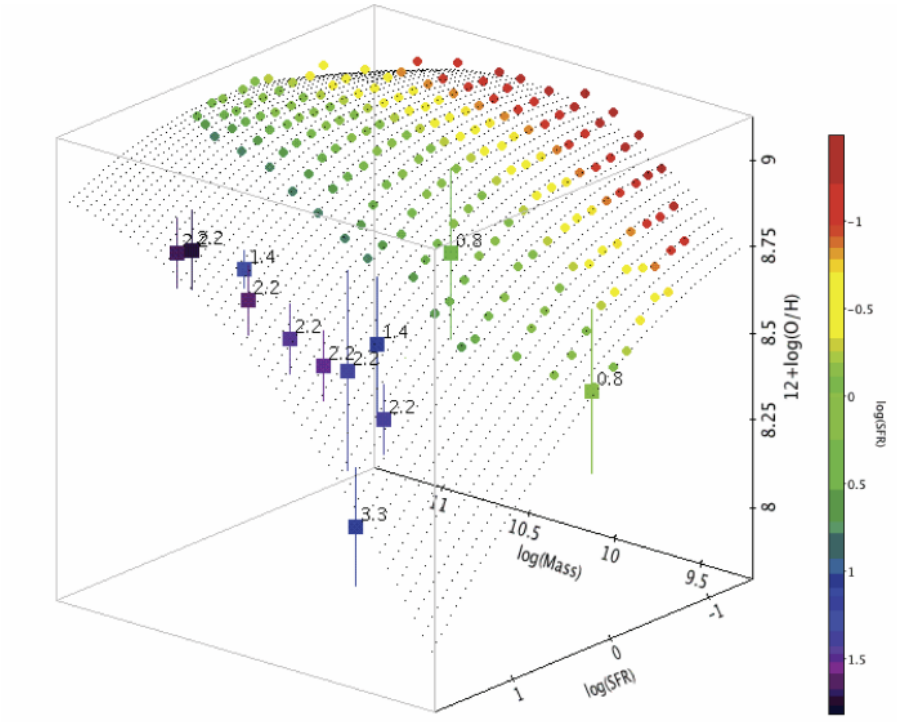

FIGURE 1.29: The stellar mass, SFR and gas-phase metallicity measured from emission lines. The colorful dots are the galaxies selected from SDSS in the bin of M_* and SFR, different colors indicate different SFR. Circles without error bars are the median values of metallicity of local SDSS galaxies in bin of M and SFR, colour-coded with SFR as shown in the colour bar on the right-hand side. The black dots show a second-order fit to these SDSS data, extrapolated towards higher SFR. Square dots with error bars are the median values of high-redshift galaxies. Labels show the corresponding redshifts. Adapted from Mannucci et al. (2010).

Chapter 2

Project I: C I observation in NIR

Contents

This chapter is based on the published paper "Near Infrared spectroscopic observations of high redshift C I absorbers" (Zou et al. 2017).

2.1 Introduction

2.1.1 Star formation in cold gas

Understanding the mechanisms of star formation at high redshifts is central to our knowledge of how galaxies formed and subsequently evolved chemically. Stars form in molecular clouds (e.g. Snow & McCall 2006) that are located in the interstellar medium (ISM) of galaxies whose properties are regulated in turn by radiative and mechanical feedbacks from stars.

Deriving the physical properties of the gas in the ISM, in particular in the diffuse molecular phase of galaxies, is crucial for our understanding of how stars formed in the early Universe. It is not easy to detect the cold neutral gas in absorption and attempts to do so have been pursued for many years. In particular, attention has been brought to molecular hydrogen as it has numerous detectable absorption lines in the UV (Ledoux et al. 2003; Cui et al. 2005; Noterdaeme et al. 2008). It has been shown that H_2 is detected with overall molecular fractions > 0.1 % in about 10% of the DLAs (Noterdaeme et al. 2008) or possibly less (Jorgenson et al. 2014). When detected, the associated gas is usually cold with T_e∼150 K and dense with n_H∼100 cm^{-3} (Srianand et al. 2005; Balashev et al. 2011). The latter systems are directly probing the diffuse interstellar medium (ISM) of high redshift galaxies and are places where it is possible to study the relation between the physical properties of the ISM and star-formation activity (Noterdaeme et al. 2012c). These are also places where one can probe the H I-to-H_2 transition in the diffuse interstellar medium of high-redshift galaxies (Noterdaeme et al. 2015; Ma et al. 2015; Balashev et al. 2017).

2.1.2 C I – new tracer

It is not that easy to preselect systems where molecular hydrogen can be found. As the gas in DLA systems are mainly neutral but necessarily cold, thus we need a new tracer to trace the cold gas directly. One way is to concentrate on the presence of neutral carbon. Indeed, carbon can be ionized by photons of energy (11.26 eV) smaller than the H I ionization limit (13.6 eV), therefore CII is the dominant species in the ISM. Hence the detection of neutral carbon is nor normal and should indicate the presence of neutral, cold and well-shielded gas, thus the presence of H_2. The ionization source can come from collisional excitation and de-excitation, UV pumping and CMB radiation(Jorgenson et al. 2010). Ground state of C I has three fine structures C I, C I*, and C I** ($^3P_0$, $^3P_1$, $^3P_2$)

which normally blends with each other. Systematic studies on C I at high redshift have not been done in the previous work. Though it has been detected together with H_2 in some individual cases (see Ge & Bechtold 1997, 1999; Srianand et al. 2005; Noterdaeme et al. 2007). By combining the contents of C I fine structures, ionization state of C and the rotation level of H_2, one can constrain the density of hydrogen, the gas temperature and pressure, also the density of electrons, and put constraints on the UV background.

Srianand et al. (2005) detected C I and its fine structures from a complete 33 H_2 DLA sample. Together with the column densities of molecular hydrogen at different rotation levels and the column densities of C I, C I*, C I** and CII*, they discovered these systematic temperature T = 100-300 K and the hydrogen density n_H = 10-200 cm^{-3}. Jorgenson et al. (2010) initiated the C I survey at high redshift. The sample consists of 11 C I systems, seven are DLAs observed by the Keck I/HIRES and VLT-UVES. They foud that the detected C I systems are generally with high densities. Different than previous work, they use a method to simultaneously constraint both the volume density and the temperature of the gas, rather than to assume a temperature in advance. They developed the technique introduced in Jenkins & Shaya (1979)which used the C I fine structure to study the ISM pressure in MW. With the assumption of ionization equilibrium, the gas temperature and density are obtained by the C I absorbers.

Therefore We have thus embarked in a survey of systems selected only on the basis of the presence of strong C I absorption in quasar spectra from the Sloan Digital Sky Survey (SDSS). With the aim to trace the cold gas at high redshifts directly and thus trace the star formation nearby. The selection of systems, the main characteristics of the sample, the detection rate and the H I content have been described in Ledoux et al. (2015) and the detailed analysis of the metallicities will be discussed in Ledoux et al. (in prep). Out of 66 strong C I systems detected in the SDSS DR7, 17 have been observed with the ESO spectrograph X-shooter which offers the unique opportunity to study the associated metal lines redshifted in the infrared region of the spectrum and in particular the Ca II, Na I and Ti II lines that are frequently used in the local universe to study the interstellar medium. The large spectral range of X-shooter is also ideal to derive the dust attenuation of the quasar spectrum induced by the presence of the DLA along the line of sight.

2.2 Sample and observations

2.2.1 SDSS C I survey

Ledoux et al. (2015) systematically searched the SDSS-DR7 (Abazajian et al. 2009) quasar

spectra (Schneider et al. 2010) for C I absorption systems and found 66 out of 416969 QSOs spectra at $z > 1.5$ with W_r(C Iλ1560) > 0.4 Å. The doublet CI λ1560,1656 is used as the template to select the systems. An IDL procedure is used to find absorption lines, details are similar as the methods used in Noterdaeme et al. (2010b). Firstly the spectra are normalized, then they are smoothed and convolved. The smoothed spectra are then cross-correlated with the C I template. With a positive correlation within 2σ and 2.5 σ, the systems are then pre-selected as candidates. After that, all the fake detections are double checked and removed by hand. The sample is complete for W_r(C Iλ1560) > 0.40 Å. As introduced in Ledoux et al. (2015), the limit EW is calculated by the

$$W_{r,lim}(\lambda)1560 \simeq n \times \frac{1560}{R} \times S/N^{-1}$$

with n=2. For SDSS, the average resolution is about 2000, therefore the equivalent width limit comes out as 0.4 Å.

Ledoux et al. (2015) found the number of C I system per unit redshift increases rapidly at z <2. It is thought to be solely due to the star formation activity peak at z $\sim$ 2 (see Fig 2.1). Another noticeable feature of this sample is its reddening. The result is presented in Fig2.2. The upper panels are the different color excesses (g-r), (r-i), (r-z) of the control quasar sample(black points) and the C I sample (red circles). It is apparent that the C I sample is redder than the control quasar sample. This point is strengthened by the lower panels, which are the different color excess frequency distributions. To obtain the reddening E(B-V), the composite from Vanden Berk et al. (2001) is added by the extinction curve LMC, SMC and MW. The results show that the reddening in C I sample is about 0.05 mag higher than that in the control sample.

The interesting point is that we found that our C I sytems do not entirely overlap with the normal DLA systems (Noterdaeme et al. 2010a) (see Fig. 2.3). The logarithmic HI column densities can go down to 19.0. How does C I still be detected in these systems worth more attention. Also based on the Kolmogorov-Smirnov test between the C I sample and normal DLA sample from Noterdaeme et al. (2009) with log N(HI) > 20.3, there in little possibility that these two samples come from the same parent population.

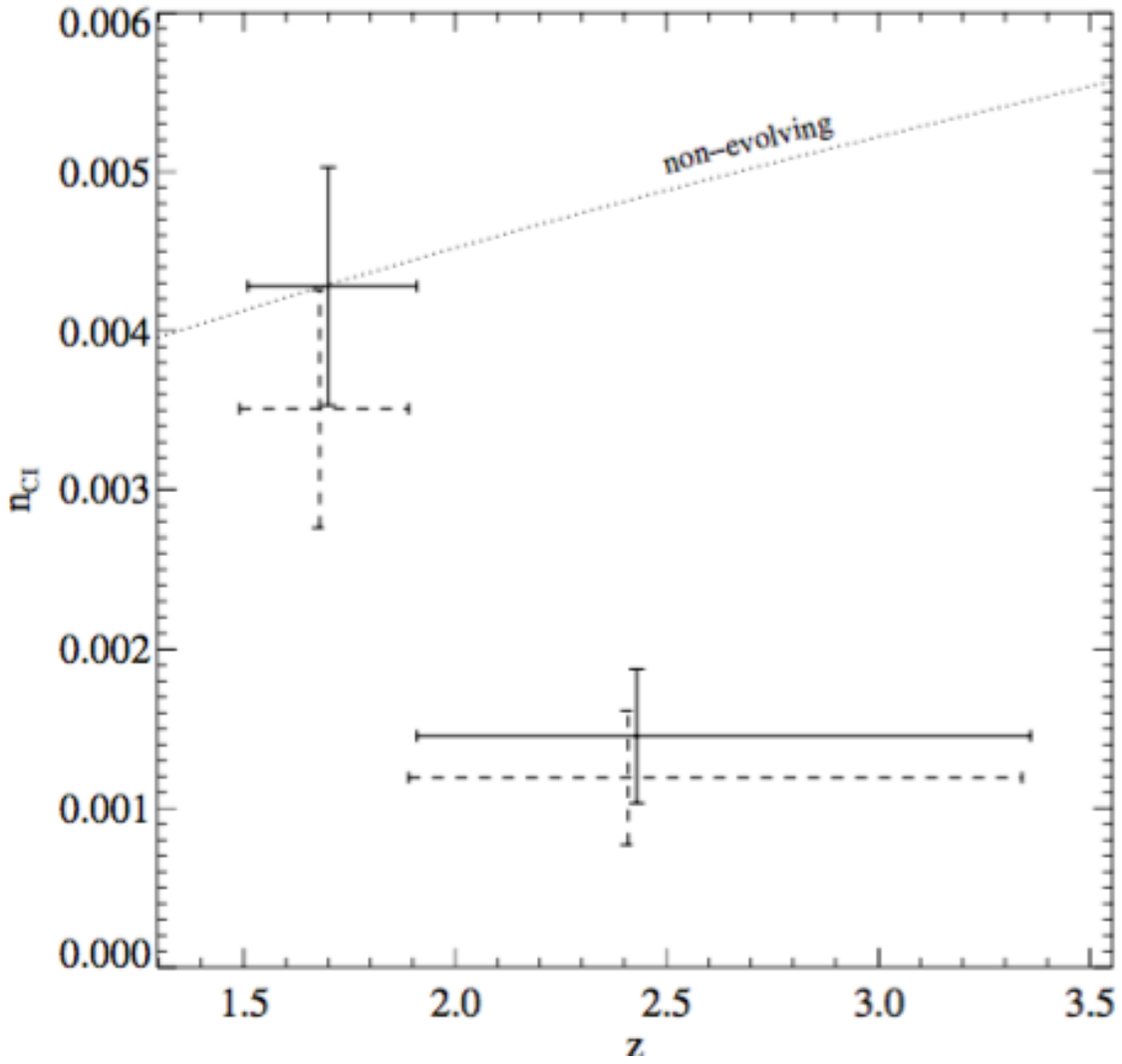

FIGURE 2.1: The statistical evolution of C I absorbers numbers in their work. The solid crosses are observed measurements corrected for incompleteness, the dashed crosses are the uncorrected measurements. The dahshed line is the the non-evolving population.

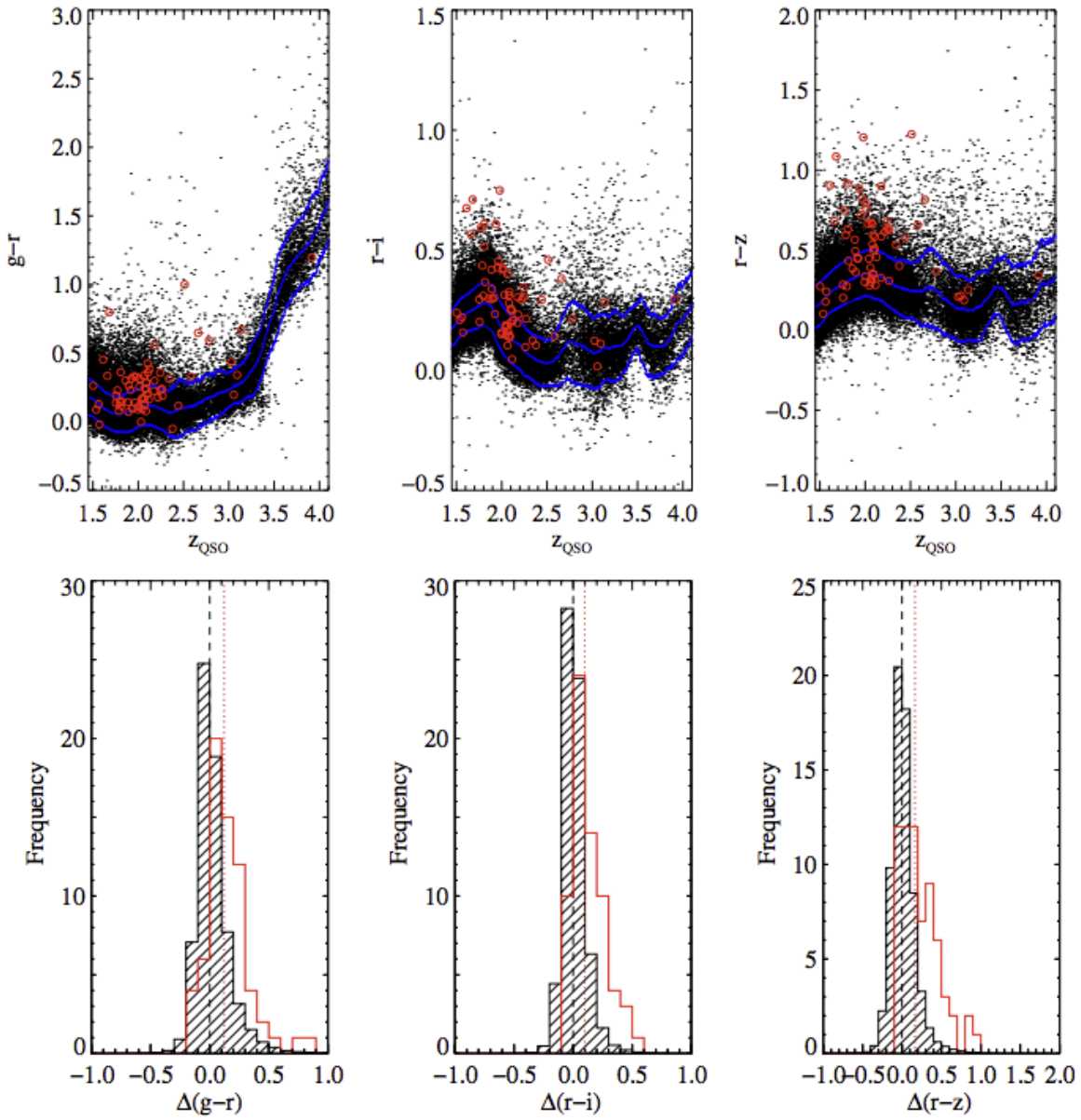

FIGURE 2.2: Adapted from Ledoux et al. (2015). Upper panels: colours of the 41 696 SDSS QSOs whose spectra were searched for C I absorption versus QSO emission redshift. (g r), (r i) and (r z) colours are displayed in the left-, middle-, and right-hand panels, respectively. The thick blue line shows the median QSO colour as a function of redshift. Thin blue lines show one standard deviation away from that median. The red circles indicate the 66 lines of sight passing through C I-detected gas. Lower panels: distribution of colour excesses (defined as, e.g.: (g r) (g r)$zQSO$ for Δ(g r)) for the 66 QSOs whose spectra were found to exhibit C i absorption (thick red histogram) compared to the whole QSO sample (thin-hashed histogram, scaled down by a factor of 632 to have the same area). In each panel (from left to right: Δ(g r), Δ(r i) and Δ(r z)), vertical dotted red lines indicate the median colour excesses of the sample of QSOs with detected C I absorption. The median values for the whole QSO sample are shown by vertical dashed lines.

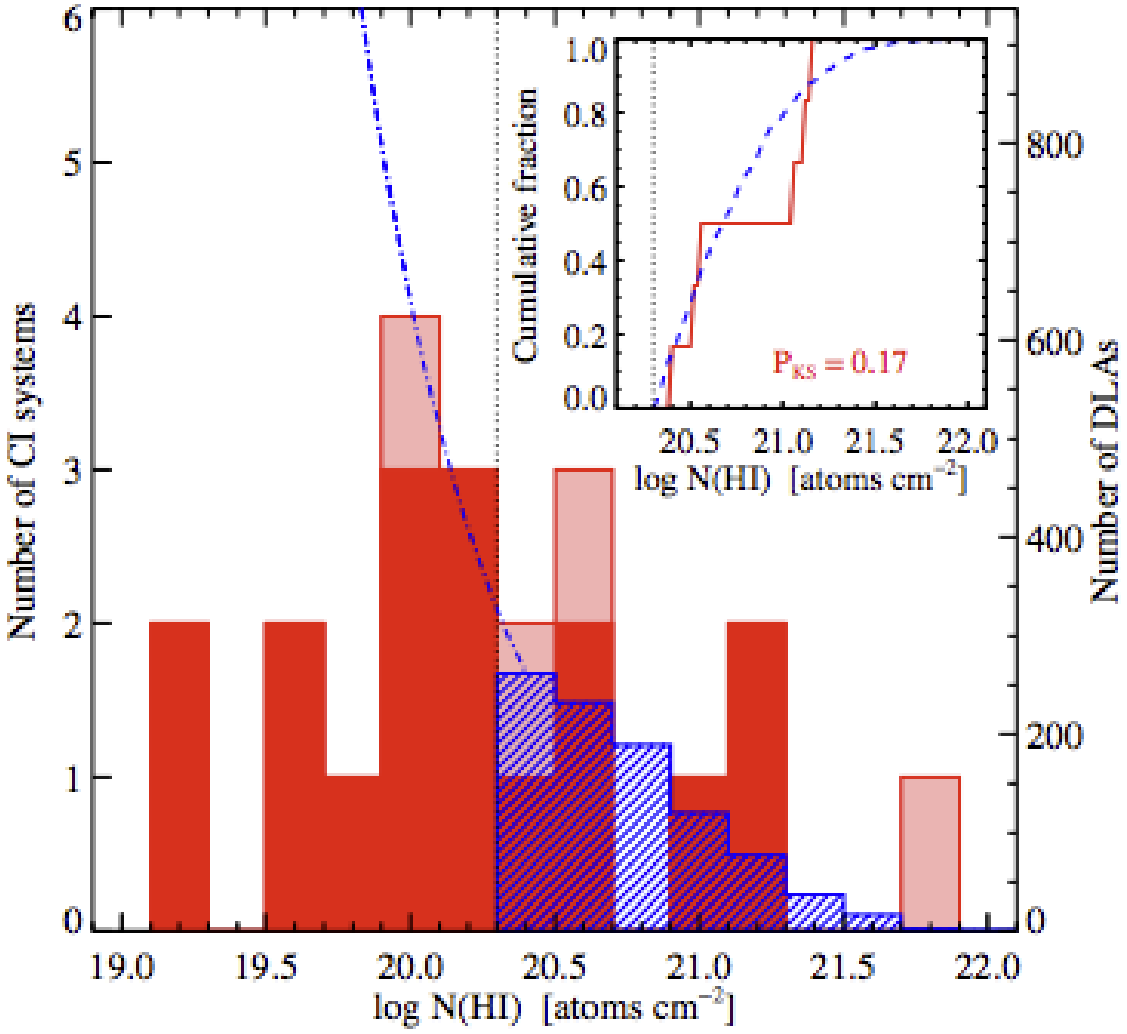

FIGURE 2.3: The red histograms are the neutral hydrogen column density distribution of the C I sample, the salmon ones are the approximate systems. The blue dashed curve is the N(H_I distribution of a normal DLA sample from Noterdaeme et al. (2009). Adapted from (Ledoux et al. 2015).

Spectrograph resolution, for the NIR arm with the new slits wheel

arm	slit width [2]	R= (λ/ Δλ)	sampling	arm	slit width	R=(λ/ Δλ)	sampling	arm	slit width	R= (λ/ Δλ)	sampling
	(")		(pix/FWHM)		(")		(pix/FWHM)		(")		(pix/FWHM)
UVB	0.5	9700	2.9	VIS	0.4	18400	2.8	NIR	0.4	11600	8.4
	0.8	6700	4.2		0.7	11400	4.5		0.6	8100	12.0
									0.6JH [4]	8100	12.0
	1.0	5400	5.2		0.9	8900	5.8		0.9	5600	17.4
									0.9JH [4]	5600	17.4
	1.3	4100	6.9		1.2	6500	7.9		1.2	4300	22.6
	1.6	3200	8.9		1.5	5000	10.3				
UVB	IFU [3]	8600	3.3	VIS	IFU [3]	13500	3.8	NIR	IFU [3]	8300	11.7

FIGURE 2.4: The instrumentation information of VLT X-Shooter.

2.2.2 Xshooter sub-sample

Follow-up observations have been performed with the ESO-UVES spectrograph for 27 systems and the ESO/X-shooter spectrograph for 17 systems (see Ledoux et al. in prep). In this chapter we will present the results in the 17 X-shooter sub-sample.

For quasar absorption studies, high resolution instrument like HIRES (High Resolution Echelle Spectrometer) on W.M.Keck and VLT-UVES have already provided large set of data to solve the questions in N(HI) distribution and the chemical abundances in ISM at high redshift. However, if we need to approach the fainter quasar beyond HIRES or UVES detection limit (V$\sim$ 19), a high efficiency, wide spectral range down to the atmospheric cutoff is needed. This is one of the science motivation for the generation of X-Shooter.

The instrument X-shooter (Vernet et al. 2011) covers the full wavelength range from 300 nm to 2.5 μm at intermediate spectral resolution using three spectroscopic arms (UV-blue (UVB), visible (VIS) and near-IR (NIR)). The main instrument parameters are listed in Fig.2.4. Generally the final spectra are close to the nominal resolving power of R = 4350, 7450 and 5300 in the UVB, VIS and NIR arms, for slit widths of 1.0, 0.9 and 0.9 arcsec, respectively.

We observed the quasars in slit mode for slightly more than 1 h each. To optimise the sky subtraction in the NIR, telescope nodding was performed following an ABBA scheme with a nod throw of 5 arcsec and a jitter box of 1 arcsec. The two-dimensional (2D) and

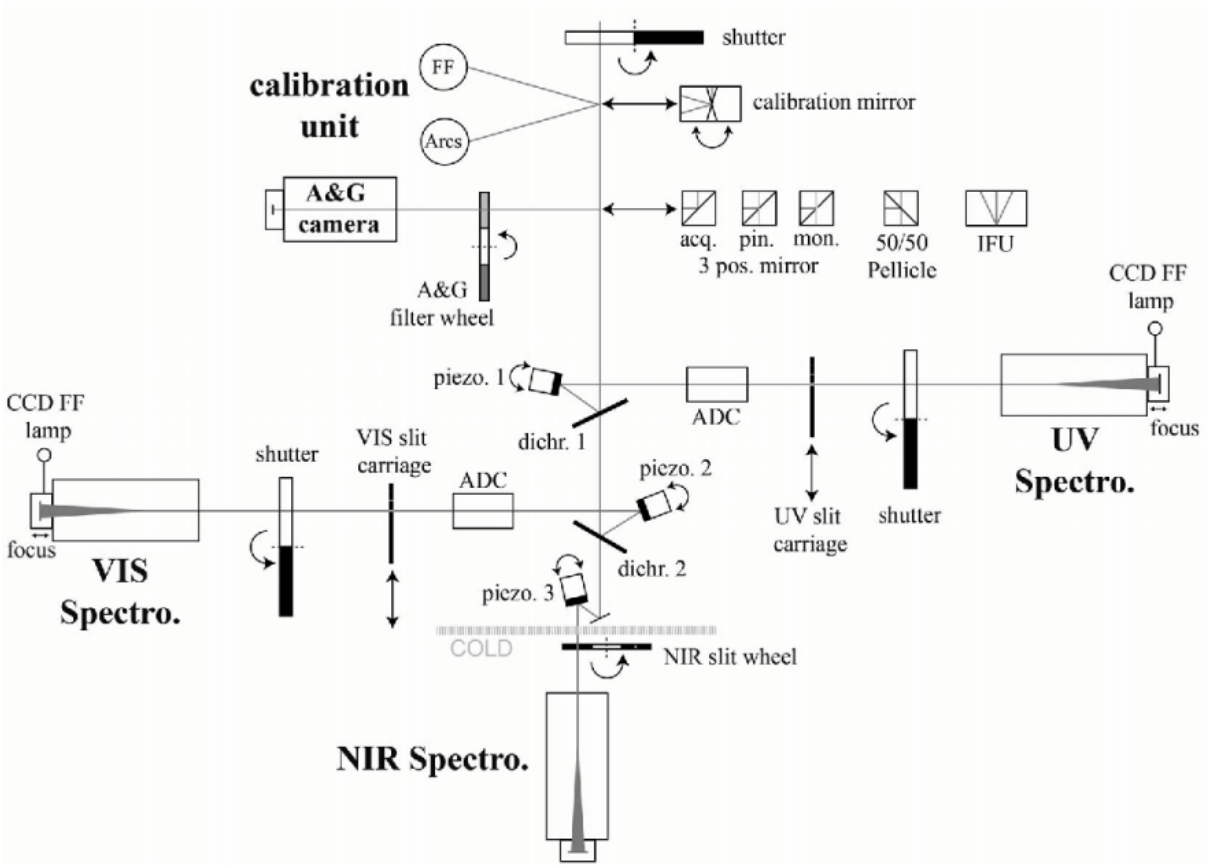

FIGURE 2.5: The instrumentation in formation of VLT X-Shooter

one-dimensional (1D) spectra were extracted using the X-shooter pipeline in its version 2.5.2 (Modigliani et al. 2010).

For some objects however, the seeing was better than the widths of the slits and resolutions were higher. We estimated the actual resolution following the method described in Fynbo et al. (2011). Flux calibration has been performed using observations of standard stars provided by ESO. We note that observations have been performed when the ADC was still in use.

There is no clear distinction between the X-shooter sub-sample and the overall sample of C I absorbers. A comparison between subsamples will be performed in Ledoux et al. (in prep). Names of the objects and characteristics of the C I absorption systems derived from X-shooter data are given in Tables 2.2 and 2.3. Spectra and absorption profiles are shown in the Appendices.

2.3 Measurements

2.3.1 Equivalent widths

For isolated transitions we measure the equivalent width directly from the spectrum, integrating the observed normalized flux over the absorption profile.

In the case of C I, the C I, C I* and C I** transitions are blended together so that we used VPFIT (Carswell & Webb 2014) to desentangle the absorptions. Results of the fits are shown in Appendix 7.3. Equivalent widths of the *overall* C I $\lambda\lambda$1560,1656 absorption with errors measured at the 1σ level are given in columns 2 and 3 of Table 2.3. These values are derived by integrating the observed normalized flux in the spectrum except for QSO J0917+0154, for which C Iλ1560 is strongly blended with other metal lines, thus we used the value obtained from the fit. We follow Vollmann & Eversberg (2006) to estimate the errors.

When Na I and/or Ca II absorption lines are detected, we fit the absorption feature with a Gaussian function and derive the equivalent widths from the fit. The results are shown in Appendix 7.3. When no line is detected, we derive and upper limit on the equivalent width as $EW_{\rm lim} = 3.2{\times}FWHM/SNR$ in 3σ where SNR is the signal-to-noise ratio at the expected position of the line, and $FWHM$ corresponds to twice the width of an unresolved spectral feature. The absorption redshift is determined by the position of the strongest C I component and is used as the zero of the velocity scale for the figures in Appendix 7.3.

2.3.2 Metallicities and extinction

The spectral resolution of X-shooter is not high enough to obtain trustful Doppler parameters and column densities except when either the absorption is optically thin (e.g. Zn II) or several transitions of the same species are observed. This is the case for Fe II and Si II for which we derive column densities from Voigt profile fitting of all observed transitions together (see Table 2.2). We used VPFIT (Carswell & Webb 2014) to model the absorption profiles. The redshift and Doppler parameter of the components were imposed to be the same in all profiles. When estimating best-fit parameters, VPFIT takes as input the normalised spectrum and the resolution provided by the user. This means that continuum placement uncertainties is not reflected in the error estimates. We therefore estimated the errors in column densities by varying slightly the continuum for lines that are not fully saturated. When one of the lines was optically thin, we derived the error

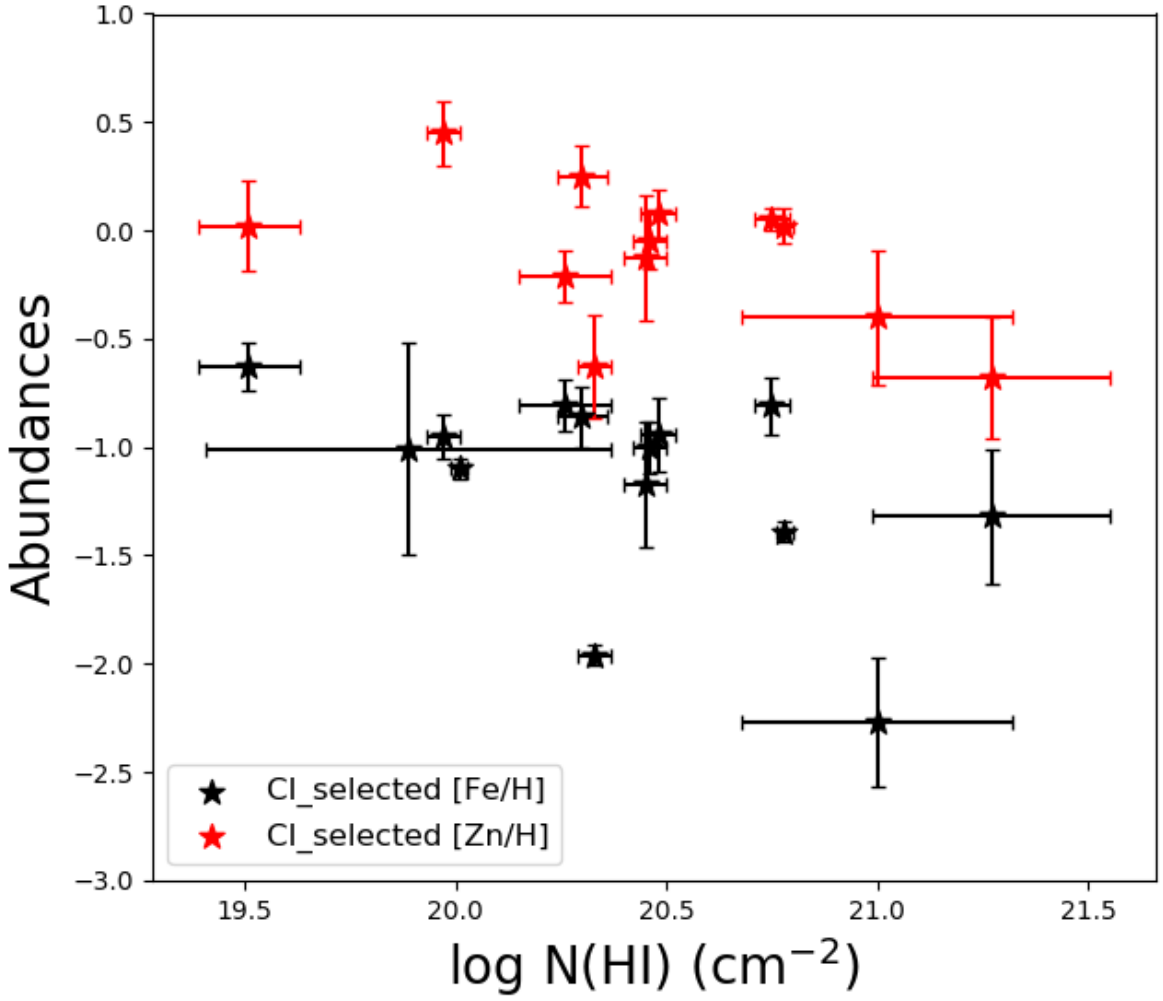

FIGURE 2.6: Metal abundances versus N(H I) column density in our sample, red stars are for [Zn/H] and black stars are for [Fe/H]. We use the gas-phase metal abundances and H I column densities from Table 2.2.

in the column density from the error in the equivalent width (see Section 3.1). For other species we measured only the equivalent width without trying to derive a column density.

Gas-phase metal abundances derived from Fe II, Si II and Zn II absorptions are listed in Table 2.2. We added the molecular contribution to the total hydrogen column density whenever H_2 is detected (see Noterdaeme et al. 2018). This contribution is non negligible in the cases of J1237+0647 and J0917+0154. We plot in Fig 2.6 the metal abundances versus H I column density (red and black stars for, respectively, Zn and Fe). It is apparent that the C I systems have large metallicities (around solar) and in any case larger than what is measured in typical DLAs at similar redshifts (e.g. Rafelski et al. 2014). Depletion of iron onto dust measured as [Zn/Fe] is significant. What is stricking also is that not only H I column densities are not very large (several systems do not qualify as standard

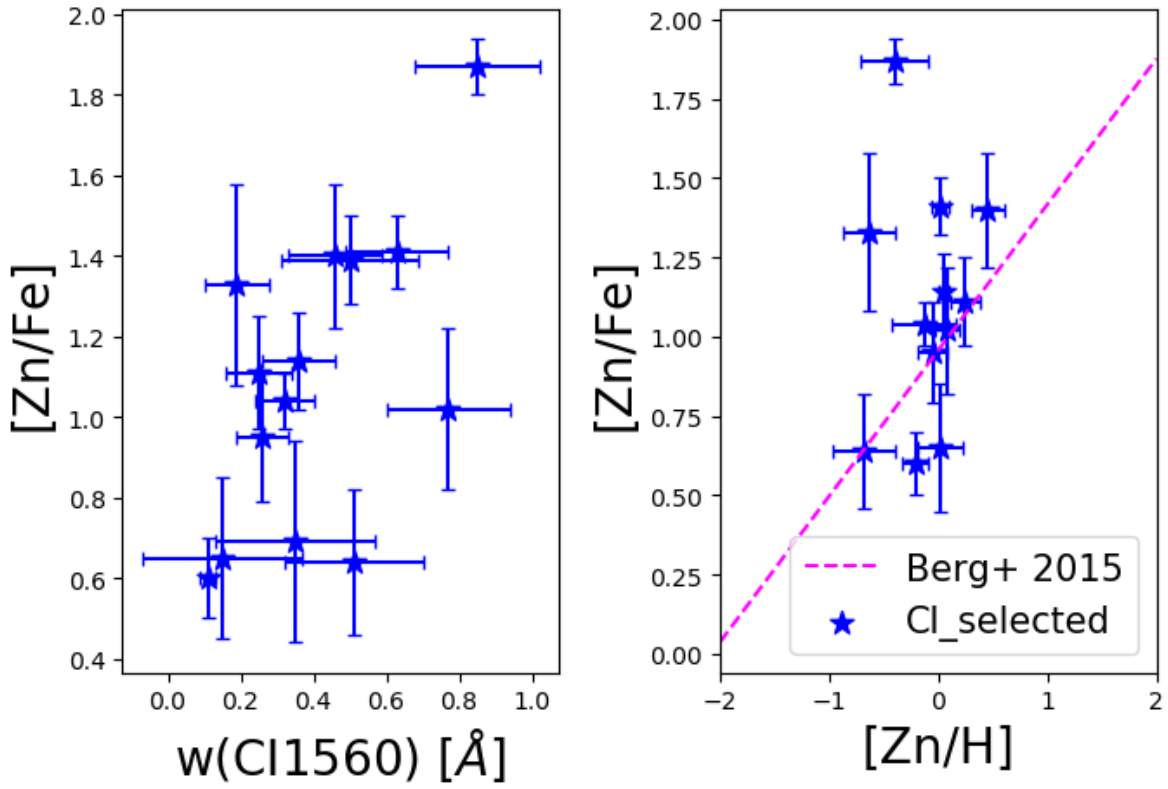

FIGURE 2.7: *Left panel*: Depletion factor [Zn/Fe] versus W(C Iλ1560). *Right panel*: Depletion factor [Zn/Fe] versus metallicity, [Zn/H]. The purple dashed line corresponds to the relation in Berg et al. (2015).

DLAs as they show log N(H I) < 20.3), but also there is a tendancy for metallicity to decrease as column density increases. This may well be a consequence of the usual dust bias which implies that systems with both high H I column densities and metallicities drop out of the sample, because the quasar flux is attenuated below the flux limit of the quasar survey (Boissé 1995). It could be as well that the quasars colours are affected by the presence of dust, shifting the quasar out of colour selection of the quasar survey.

The dust depletion indicator [Zn/Fe] is plotted versus W(C Iλ1560) and metallicity (as [Zn/H]) in the two panels of Fig. 2.7. It is apparent in the left panel that dust depletion is significant. There is however no strong correlation between the amount of dust depletion and the amount of neutral carbon. The purple dashed line in the right panel is the mean relation observed for typical DLAs (Berg et al. 2015). The relation seems to hold even for the high metallicities measured in our sample although a large scatter is observed in the measured depletion factors. Although these considerations are useful for the following discussions, it is clear that these properties should be studied in the complete sample of C I systems, not only in the sub-sample of quasars observed with X-shooter. This will be done in a companion paper (Ledoux et al. in prep).

Given the metallicities and dust depletions measured in our sample, the quasar spectra are significantly attenuated by the presence of dust in the absorption systems. We estimate this attenuation, measured as $A_{\rm V}$ and $E(B-V)$, by fitting a quasar spectral template to the data assuming a set of fixed extinction curves (SMC, LMC and LMC2) parametrized by Gordon et al. (2003). The dust reddening is assumed to be caused solely by the foreground C I absorber. We use the quasar template derived by Selsing et al. (2016) and fit only the data in bona fide continuum regions, i.e., regions which are not strongly affected by absorption or broad emission lines. This template has been obtained by combining seven spectra of bright quasars taken with X-shooter. Signal-to-noise ratio varies from 50 in the UV to 200 in the optical and 100 in the near infrared. Before fitting, the template is smoothed with a Gaussian kernel ($\sigma = 7$ pixels) to prevent the noise in the template to falsely fit noise peaks in the real data. In order to take into account the uncertainty in the template, we subsequently convolve the errors on the observed data with the uncertainty estimate for the template. In the near-infrared, we perform a 5-σ clipping in order to discard outlying pixels introduced by the removal of skylines during data reduction.

We furthermore allow for variations in the iron pseudo-continuum in the rest-frame UV by including the template derived by Vestergaard & Wilkes (2001). We separate the contributions from FeII and FeIII into different templates and allow each to vary independently.

During the observations of the target J1302+2111, the atmospheric dispersion correction (ADC) malfunctioned leading to strong chromatic slit losses for the UVB and VIS arms (the NIR arm does not have an ADC unit and hence is not affected). Similar artefacts from malfunctioning ADCs of X-shooter have been reported by López et al. (2016). By comparing the X-shooter spectrum to the available SDSS spectrum, we conclude that the UVB arm is not strongly affected by chromatic slit loss, however, the VIS arm is heavily affected. We therefore do not use the VIS arm for the extinction analysis.

We then fit the template to the data using four free parameters: the attenuation $A_{\rm V}$, the two scaling parameters for the FeII and FeIII contributions and an arbitrary flux scale which corresponds to the flux in the IR as the attenuation is usually negligible at these wavelengths. We fit the template to the data for each of the three extinction curves considered, SMC, LMC and LMC2, and we assign the best-fit as the solution with the lowest χ^2. We note that for the target J2340–0052, the lowest χ^2 is obtained with an LMC2 extinction law, however, upon visual inspection it is clear that the fit is not good as the best-fit iron contribution over-estimates the actual fluctuations in the data. Thus, when removing the iron contribution the spectrum is fit better with the SMC extinction

curve. The best-fit reddening and the associated best-fit extinction curve are given in Table 2.4. In cases where the reddening is too small to distinguish between various extinction curves, we list the best-fit extinction curve as 'N/A' in Table 2.4 and give the R_V value for the SMC curve for simplicity. We note that for such small values of A_V, the value of R_V does not change the resulting $E(B-V)$ significantly. The main uncertainty for the dust fitting comes from intrinsic variations to the template. We have modelled this by assuming a distribution of the relative intrinsic spectral slope ($\Delta\beta$) as modelled by a Gaussian function with a width of 0.2 dex (Selsing et al. 2016). This yields an estimated 0.07 mag uncertainty on the best-fit A_V which by far dominates the total uncertainty as the statistical uncertainty from the fit is of the order 0.01 mag.

For the cases where an SMC extinction curve is preferred by the fit, the resulting A_V should be regarded as an upper limit, since for this extinction curve it is very difficult to disentangle dust in the quasar and dust in the absorber (see discussion in Krogager et al. 2015). In Figure 2.8, we show the best-fit model for one target (the other spectra are shown in Appendix 7.1).

2.3.3 Decomposition of C I

By assuming the C I and its fine structure with the same dopper parameters, we obtained the column densities of C I, C I* and C I** via VPFIT. The results are listed in Table 2.1. With the column densities ratio of C I fine structures, one can estimate the particle densities of the systems. We use a simple model here to estimate the volume particle densities, the model is described in Silva & Viegas (2001). With the assumption of statistical equilibrium, all the processes that populate level i should be balanced by the processes de-populate level i. The bound-bound processed include: spontaneous decay, radiation transition and collision transition. For level i and j. we have

$$\sum_j n_j \Big(A_{ji} + B_{ji} u_{ji} + \sum_k n^k q^k_{ji} \Big) = n_i \sum_j \Big(A_{ij} + B_{ij} u_{ij} + \sum_k n^k q^k_{ij} \Big)$$

where A_{ij} is the transition probability of spontaneous decay from level i to level j, B_{ij} are the Einstein coefficients, which correlates to the radiation field, n^k is the particle volume density, the k depends on the medium is neutral or ionized. Since n*/n = N*/N. We manually fit our N(C I*)/N(C I) ratio with the curve in Fig.4 in Silva & Viegas (2002). This curve is the relation between the $^3P_0$/ $^3P_1$ ratio of neutral carbon and the volume densities n_H. With the $z = 2$ curve, we found that most of the systems in this subsample with the densities range 10-100 cm^{-3} at T$\sim$ 100K. This meet our expectation that C I absorbers are in the cold gas in the ISM.

We also plot the N(C I*)/N(C I) against N(C I) in Fig. 2.9 right panel. The ratio of N(C I*)/N(C I) does not change largely with the increasing N(C I). The black triangles are the data in H_2-selected DLAs and the green dots are from ISM. We found our C I column densities are consistent with the results in ISM. For the NC I*/N(C I) values, they are generally consistent with the values in Srianand et al. (2005) , which means much higher than the values in Galaxy. This can be explained by that our systems has higher metallicitie (close to solar) than normal DLAs, thus it present similar N(C I) with stars. Meanwhile, as claimed in Srianand et al. (2005), with a given temperature, NC I*/N(C I) is more determined by N(Hi). However, in our sample, not all the systems are DLA, we can assume that temperature is the main parameter to influence the NC I*/N(C I).

Nevertheless, what should be bear in mind is that the resolution of X-shooter is not good enough for clearly resolving the C I fine structures, so the results obtained should be treat conservatively. Meanwhile, from high resolution data from UVES, many C I absorbers in the whole sample are saturated. Thus the decomposition of the C I are even more difficult. Thus we list the values measured by an apparent line optical-depth (AOD) method described in Savage & Sembach (1991). This is a method to derive the absorption line files column densities by a function the peak absorption (i.e. the line amplitude). Details are described in Ledoux in prep. We compared the VPFIT results and AOD values in Table2.1, except for one case J1047+2057 for which we think the C I lines are strongly saturated, other values are in a good agreement.

2.4 Results

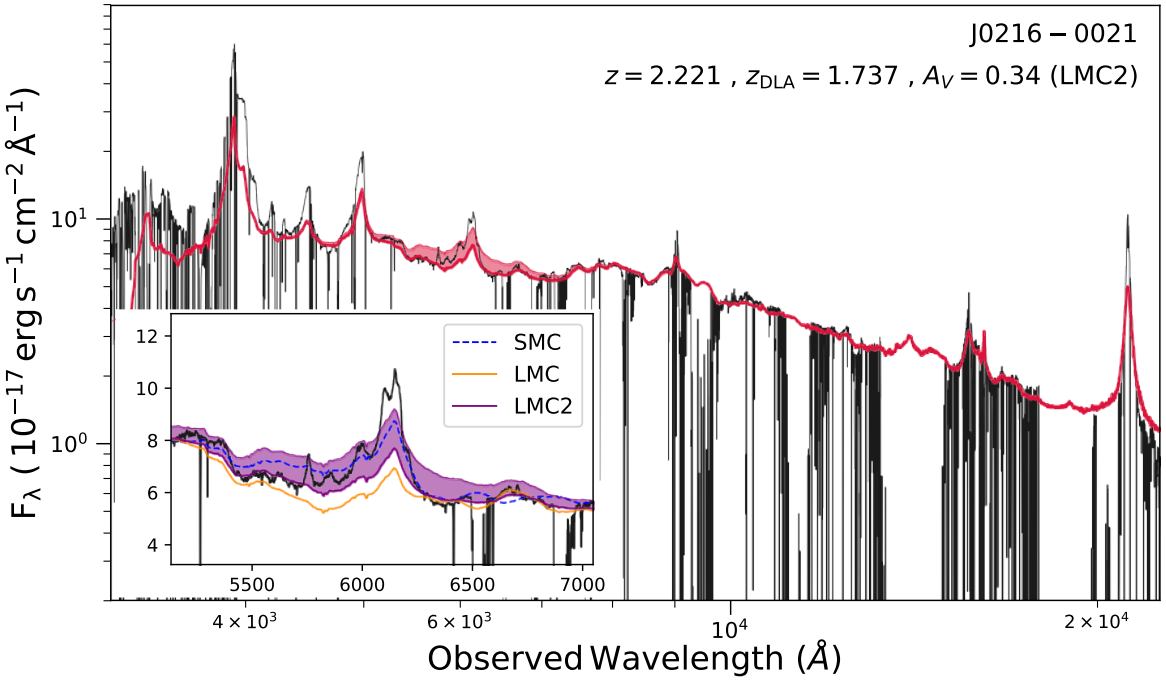

FIGURE 2.8: X-shooter spectrum of J0216-0021. The red curve corresponds to the quasar template of Selsing et al. (2016) reddened by different extinction curves (see insert).

TABLE 2.1: Column densities of C I and its fine structures.

QSO	log N(C I)	log N(C I*)	log N(C I**)	$\log\frac{N(C_I*)}{N(C_I)}$	$\log\frac{N(C_I**)}{N(C_I*)}$	N_{tot}	N^a_{tot}	n_H cm^{-3}
J0216-0021	14.26±0.20	14.08±0.06	13.61±0.06	-0.18	-0.47	14.53	14.25	80
J0815+2640	14.67±0.06	14.10±0.02	13.32±0.07	-0.57	-0.78	14.79	>14.73	13
J0854+0317	14.07±0.03	13.46±0.18	13.06±0.28	-0.61	-0.40	14.20	14.23	9
J0917+0154	15.77±0.29	13.87±0.02	13.62±0.09	-1.9	-0.25	14.25	14.32	-
J1047+2057	17.14±0.03	16.73±0.04	11.26±0.44	-0.41	-5.47	17.28	>14.90	-
J1122+1437	13.85±0.10	13.60±0.04	13.01±0.11	-0.25	-0.59	14.08	13.83	56
J1133-0057	14.34±0.07	14.80±0.10	14.64±0.08	0.46	-0.16	15.10	15.12	-
J1237+0647	14.63±0.12	14.32±0.11	13.96±0.44	-0.31	-0.36	14.86	15.01	46
J1248+2848	14.24±0.67	13.95±0.44	13.51±1.25	-0.29	-0.44	14.47	14.25	55
J1302+2111	14.10± 0.05	13.94±0.03	13.26±0.13	-0.16	-0.68	14.36	14.40	81
J1314+0543	14.52±0.28	14.15±0.13	13.67±0.09	-0.37	-0.48	14.72	14.30	42
J1341+1852	13.87±0.06	13.69±0.78	14.16±1.06	-0.18	0.47	14.43	14.40	81
J1346+0644	14.46±0.09	14.17±0.04	13.65±0.12	-0.29	-0.52	14.68	14.51	55
J2229+1414	13.65±0.29	13.39±0.09	12.72±0.32	-0.26	-0.67	13.87	13.96	61
J2336-1058	14.06±0.10	13.69±0.03	13.13±0.08	-0.37	-0.56	14.25	14.07	39
J2340-0053	14.32±0.40	13.64±0.10	13.6±0.20	-0.68	-0.03	14.47	14.09	7
J2350-0052	14.44±0.38	14.11±0.08	13.86±0.11	-0.33	-0.25	14.67	14.36	46

[a]Value from Ledoux in prep, which are measured via AOD method.

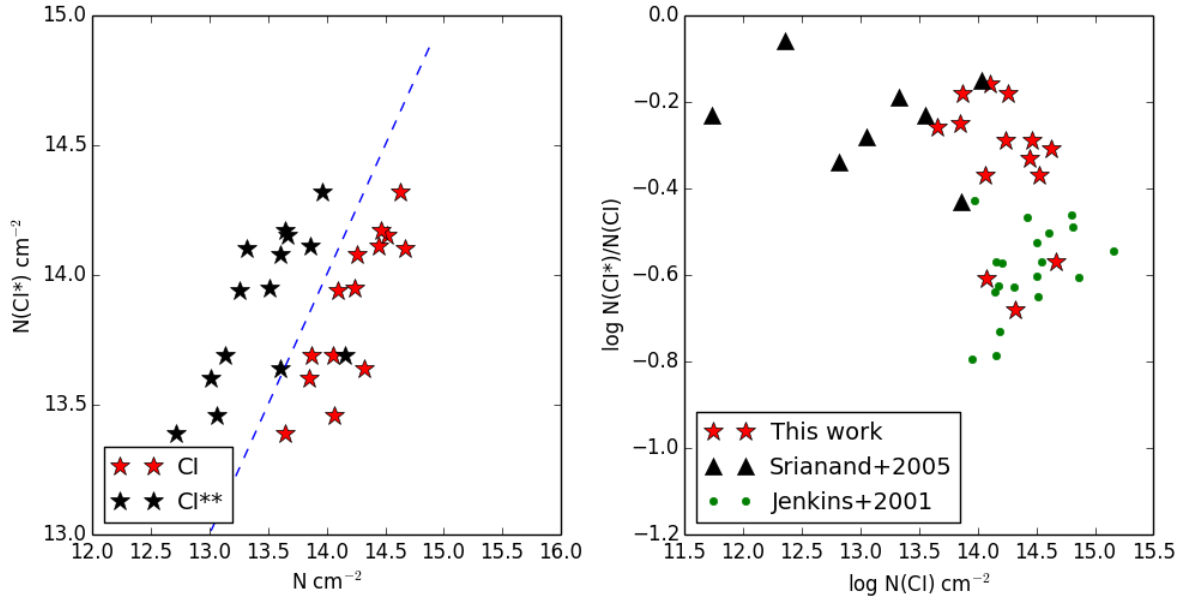

FIGURE 2.9: Column densities ratio of C I*/C I as a function of N(C I). Stars are from this work, black triangles are from Srianand et al. (2005), the green dots are the data from Jenkins & Tripp (2001).

TABLE 2.2: Column density measurements using Voigt profile fitting

QSO	z_{abs}	log N(H I)	log N(Fe II)	log N(Zn II)	log N(Si II)	[Fe/Zn]	[Fe/H][c]	[Si/H][c]	[Zn/H][c]
J0216-0021	1.7359	20.01±0.04	14.41±0.05	-	15.21±0.09	-	-1.10±0.07	-0.31± 0.10	-
J0815+2640	1.6798	20.78±0.04	14.89±0.05	13.36±0.08	15.52±0.07	-1.41±0.09	-1.39±0.07	-0.77± 0.07	0.02±0.08
J0854+0317	1.5663	20.46±0.06	14.96±0.11	12.97±0.12	15.58±0.11	-0.95±0.16	-1.00±0.12	-0.39± 0.12	-0.05±0.13
J0917+0154	2.1059	20.75±0.04	15.44±0.11	13.64±0.05	16.17±0.06	-1.14±0.12	-0.97±0.12	-0.25± 0.08	0.17±0.07
J1047+2057	1.7740	20.48±0.04	15.04±0.17	13.12±0.11	15.68±0.08	-1.02±0.20	-0.94±0.18	-0.31± 0.09	0.08±0.12
J1122+1437	1.5538	20.33±0.04	13.87±0.05	12.26±0.24	14.72±0.09	-1.33±0.25	-1.96±0.08	-1.12± 0.10	-0.63±0.25
J1133-0057	1.7045	21.00±0.32[a]	14.23±0.03	13.16±0.06	15.71±0.06	-1.87±0.07	-2.27±0.32	-0.80± 0.33	-0.40±0.33
	1.7063								
J1237+0647	2.6896	19.89±0.48	14.53±0.06	-	15.26±0.22	-	-1.01±0.49	-0.29± 0.53	-
J1248+2848	1.5124	-	15.07±0.17	12.82±0.19	15.75±0.06	-0.69±0.25	-	-	-
J1302+2111	1.6556	21.27±0.28	15.45±0.16	13.15±0.09	16.01±0.05	-0.64±0.18	-1.32±0.32	-0.77± 0.29	-0.68±0.30
J1314+0543	1.5829	19.97±0.04	14.52±0.10	12.98±0.15	15.36±0.11	-1.40 ±0.18	-0.95±0.11	-0.12± 0.12	0.45±0.16
J1341+1852	1.5442	18.18±0.07	12.98±0.05	-	13.92±0.11	-	[b]	[b]	-
J1346+0644	1.5120	-	14.70±0.07	13.15±0.08	15.51±0.08	-1.39±0.11	-	-	-
J2229+1414	1.5854	19.51±0.12	14.38±0.05	12.09±0.19	15.29±0.12	-0.65±0.20	-0.63±0.14	0.27± 0.17	0.02±0.23
J2336-1058	1.8287	20.30±0.06	14.98±0.06	13.15±0.13	15.54±0.07	-1.11±0.14	-0.86±0.09	-0.31± 0.09	0.25±0.15
J2340-0053	2.0546	20.26±0.11	14.96±0.06	12.62±0.08	15.14±0.08	-0.60±0.10	-0.81±0.13	-0.64± 0.14	-0.21±0.14
J2350-0052	2.4265	20.45±0.05	14.79±0.03	12.89±0.06	15.36±0.05	-1.04±0.07	-1.17±0.07	-0.61± 0.08	-0.13±0.08

[a]Value from the fit by Fathivavsari et al. (2017)

[b]Ionization correction should be taken into account

[c]We added the molecular contribution to the total hydrogen column density whenever H_2 is detected (see Noterdaeme et al. 2018).

TABLE 2.3: Equivalent widths (Å) of absorption features

QSO	C Iλ1560	C Iλ1656	Na Iλ5891	Na Iλ5897	Ca IIλ3934	Ca IIλ3969	Mg IIλ2798	Mg IIλ2803	Mg Iλ2852
J0216-0021	0.32±0.14	0.84±0.11	0.34±0.05	0.09±0.03	0.23 ±0.09	<0.22	2.62±0.04	2.21±0.05	0.78±0.04
J0815+2640	0.63±0.14	0.99±0.13	0.82±0.21	0.45±0.14	0.47 ±0.16	<0.31	2.89±0.06	2.69±0.05	-
J0854+0317	0.26±0.07	0.46±0.08	<0.23	<0.23	0.66 ±0.28	<0.12	2.89±0.04	2.73±0.03	0.79±0.06
J0917+0154	0.36±0.10	0.61±0.32	-	-	<0.53	<0.53	3.81±0.09	3.73±0.08	1.59±0.11
J1047+2057	0.77±0.17	1.17±0.13	0.86±0.15	0.75±0.14	0.59 ±0.14	0.50 ±0.15	3.50±0.06	3.68±0.04	1.33±0.05
J1122+1437	0.19±0.09	0.26±0.08	0.56±0.10	0.53±0.09	0.21 ±0.24	<0.28	0.83±0.03	0.65±0.03	0.21±0.03
J1133-0057	0.85±0.17	1.42±0.17	1.00	0.88	0.17 ±0.07	0.07 ±0.10	2.91±0.07	2.80±0.09	1.20±0.06
	-	-	0.88	0.67	-	-	-	-	-
J1237+0647	0.39±0.22	0.60±0.17	0.51±0.21	0.34±0.23	-	<0.16	4.28±0.16	3.84±0.21	0.99±0.24
J1248+2848	0.35±0.13	0.55±0.17	-	-	0.87 ± 0.10	0.75 ±0.20	4.03±0.07	3.68±0.07	1.21±0.10
J1302+2111	0.51±0.19	0.59±0.17	0.80±0.21	<0.40	1.06 ± 0.30	0.48 ±0.20	2.87±0.07	2.73±0.06	1.30±0.09
J1314+0543	0.46±0.13	0.65±0.15	0.92±0.13	1.00±0.12	<0.35	<0.35	2.04±0.08	1.79±0.09	0.43±0.08
J1341+1852	0.13±0.06	0.14±0.06	-	-	<0.14	<0.14	0.32±0.01	0.25±0.02	0.03±0.01
J1346+0644	0.50±0.19	0.80±0.18	-	-	<0.31	<0.31	2.98±0.07	2.69±0.07	0.84±0.11
J2229+1414	0.15±0.22	0.21±0.24	0.51±0.14	0.37±0.12	<0.50	<0.50	2.70±0.13	2.32±0.11	0.51±0.11
J2336-1058	0.25±0.09	0.35±0.06	0.24±0.11	0.17±0.07	-	-	3.08±0.05	2.68±0.04	1.23±0.07
J2340-0053	0.11±0.02	0.17±0.03	-	-	0.25 ± 0.02	0.10 ±0.10	1.66±0.01	1.53±0.01	0.47±0.01
J2350-0052	0.32±0.08	0.51±0.03	-	-	-	-	3.06±0.05	2.66±0.05	0.80±0.08

TABLE 2.4: Dust extinction in the sample, second column is the extinction law used when fitting the dust attenuation. The mean SNRs in each of the X-shooter arms are given in the last three columns.

QSO	Ext law	$E(B-V)$	A(V)	Rv	UVB SNR	VIS SNR	NIR SNR
J0216-0021	LMC2	0.123	0.34	2.76	49	66	55
J0815+2640	LMC	0.138	0.47	3.41	35	39	18
J0854+0317	SMC	0.099	0.27	2.74	52	66	50
J0917+0154	SMC	0.135	0.37	2.74	22	25	8
J1047+2057	LMC2	0.174	0.47	2.76	60	69	27
J1122+1437	N/A	0.000	0.00	2.74	35	76	35
J1133-0057	SMC	0.226	0.62	2.74	45	63	50
J1237+0647	LMC2	0.152	0.42	2.76	40	55	21
J1248+2848	N/A	0.000	0.00	2.74	28	33	28
J1302+2111	SMC	0.051	0.14	2.74	30	33	16
J1314+0543	SMC	0.036	0.10	2.74	42	45	20
J1341+1852	SMC	0.033	0.09	2.74	75	80	22
J1346+0644	N/A	0.018	0.05	2.74	29	32	30
J2229+1414	N/A	0.000	0.00	2.74	25	28	11
J2336-1058	N/A	0.007	0.02	2.74	62	65	40
J2340-0053	SMC	0.066	0.18	2.74	150	180	115
J2350-0052	LMC	0.038	0.13	3.41	50	70	35

2.4.1 MgII

The W(Mg IIλ2796) observed in our C I systems are large, 13 out of 17 (82%) of these systems have W(Mg IIλ2796) $>$ 2.5 Å when such strong systems are rare in Mg II surveys even at high redshifts (see Rao et al. 2005). As can be seen in Fig. 2.10, this is systematically larger than what is observed in systems selected on the basis of the presence of Ca II in SDSS spectra (Wild & Hewett 2005; red histogram in Fig. 2.10). The sample of Wild & Hewett (2005) includes 31 Ca II absorbing systems in the redshift range $0.84 < z < 1.3$. This number of strong systems can be compared with what is observed in high-redshift DLAs. Berg et al. (2016) study the 36 blindly selected DLAs with $2<z<4$ detected in the XQ-100 legacy survey (López et al. 2016). Only three of their DLAs have W(MgIIλ2696) $>$ 2.5 Å and much lower metallicities.

We have measured the velocity spread of the Mg II absorption, Δv. Since, the SNR in the infrared is not optimal, we measure Δv as the velocity separation between the two extreme pixels where $\tau < 0.1$. This is similar to the standard Δv_{90} definition and more robust for our data. The idea is to include all satellite absorption and to have a good representation of the kinematical extent of the absorption. In Fig. 2.11, it can be seen that the W(Mg IIλ2796) equivalent width is strongly correlated with $\Delta\, v$. The correlation we see is quite similar to what is seen for typical DLAs (Ellison 2006). The difference resides again in the presence in our sample of a high fraction of large (>300 km s^{-1}) Δv

values. The median value of Δv in our sample is $\sim$400 km s^{-1} ; three absorbers have Δv>500 km s^{-1}. Few such extreme systems are known in the literature at high redshift (Ledoux et al. 2006) are found to be associated with molecular hydrogen (Petitjean et al. 2002; Ledoux et al. 2002). Only three DLAs out of 36 have kinematical extention larger than 200 km s^{-1} in the sample of Berg et al. (2016), when seven of our systems have Δv>400 km s^{-1}. It is therefore surprising that our C I-selected systems show such disturbed kinematics. The dashed line in Fig. 2.11 is the relation one expects if the lines are completely saturated over the whole absorption profile. It is therefore clear that above 300 km s^{-1}, the velocity spread of the absorption is dominated by satellite components.

These large kinematical spreads could be due to strong winds or the consequences of interactions between several galaxies. Interestingly, we find three systems in the spectra of J1047+2057, J1133-0057 and J2350-0052 where the Mg II absorption shows two distinct saturated sub-systems separated by more than 200 km s^{-1} in the C I and Mg II absorption profiles. In J1133-0057, we detect also two distinct Na I components. Therefore probably both processes can be invoked to explain the large velocity spreads of Mg II absorptions in our sample.

2.4.2 Ca II and Na I

The presence of Ca II absorption is of particular interest for studying the properties of the interstellar medium of high-z galaxies. It is important to bear in mind that Ca is usually highly depleted onto dust and that the ionization energy of Ca II being 11.87 eV, Ca II may not be the dominant ionization stage of Ca even in H I dominated gas. Even though the presence of strong Ca II absorption is therefore not a characteristic of cold gas, its presence or absence can yield interesting information on the amount of dust and on the radiation density below the Lyman limit. In turn, Na I is ionized above 5.14 eV and is therefore associated with cold and neutral gas. In the local universe a tight correlation is seen between N(Na I) and N(H I) (Ferlet et al. 1985; Wakker & Mathis 2000). It will be interesting to verify if such correlation holds at high redshift as well. In addition the ratio of the Na I and Ca II column densities is a useful probe of the physical state of the gas (Routly & Spitzer 1952; Welty et al. 1996).

In our Galaxy, when observed at high spectral resolution, the Na I complexes break into subcomponents with median Doppler parameter of $\sim$0.73 km s^{-1} and median separation between adjacent components of $\sim$2 km s^{-1}. The typical temperature of the gas is 80 K (Welty et al. 1994). The velocity distribution of the corresponding Ca II absorption is

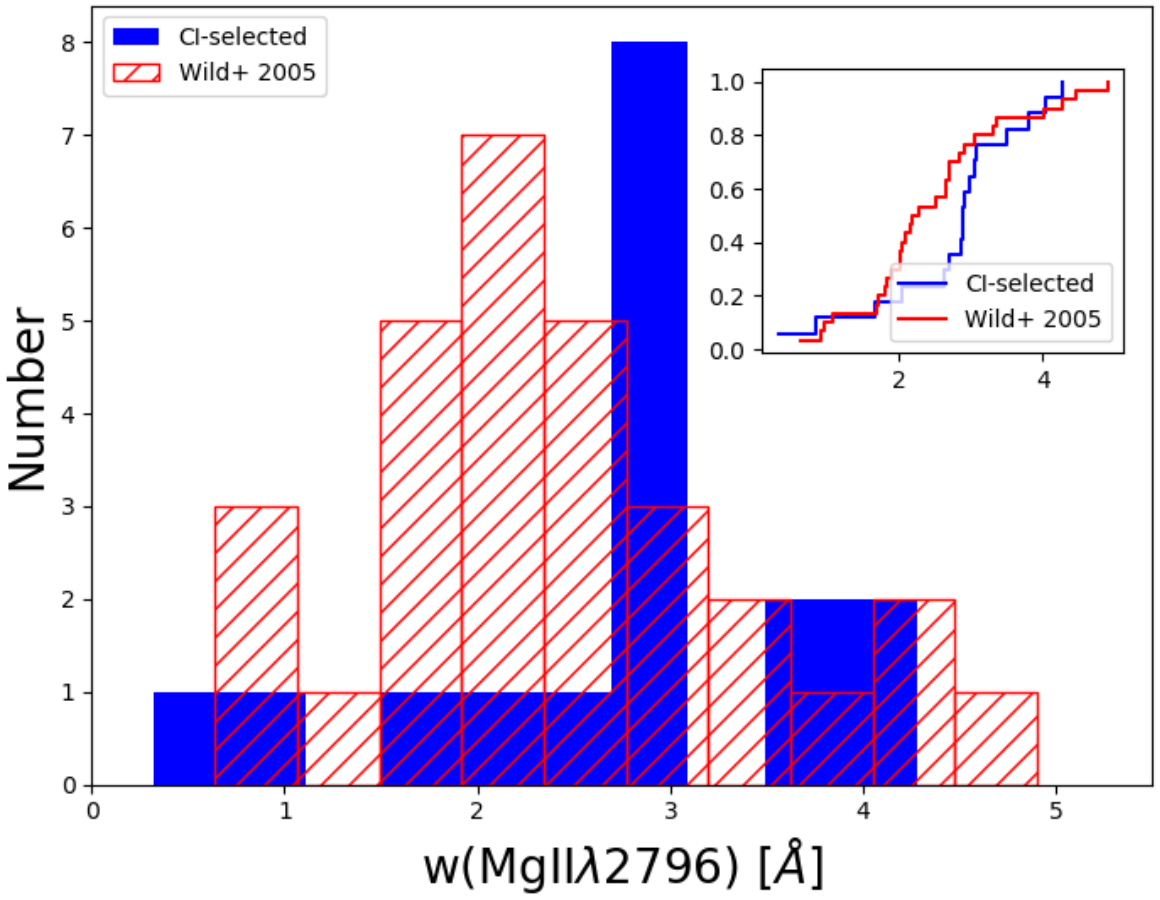

FIGURE 2.10: W(Mg IIλ2796) distributions. The blue histogram is for our sample of C I absorbers. The red hashed histogram is for the Ca II sample of Wild & Hewett (2005) at $0.84 < z < 1.3$. The lines in the insert are the cumulative distributions of the two samples.

broader, due to outlying components at higher temperature ($T > 6000$ K) seen only in Ca II. Even individual Ca II components are broader than the corresponding Na I or K I components implying that the Ca II absorption arises predominantly in warmer and more diffuse gas occupying a larger volume (Hobbs 1974, 1975; Welty et al. 1996; Welty & Hobbs 2001). Ca II absorption can arise both from cold, relatively dense gas, where Ca is typically heavily depleted onto grains and Ca II is its dominant ionization state, and also in warmer, lower density gas, where Ca is less depleted but Ca II is a trace ionization state.

Ca II (Na I) absorbers at intermediate and high radial velocities are present in 40–55% (20–35%) of the sightlines through the halo of our Galaxy (Bekhti et al. 2008; Ben Bekhti et al. 2012). The Ca II/Na I ratio is found to be smaller in halo gas compared to what is observed in the disk of the Galaxy (Keenan et al. 1983; Ferlet et al. 1985; Vladilo et al. 1993; Sembach et al. 1993a; Ben Bekhti et al. 2012).

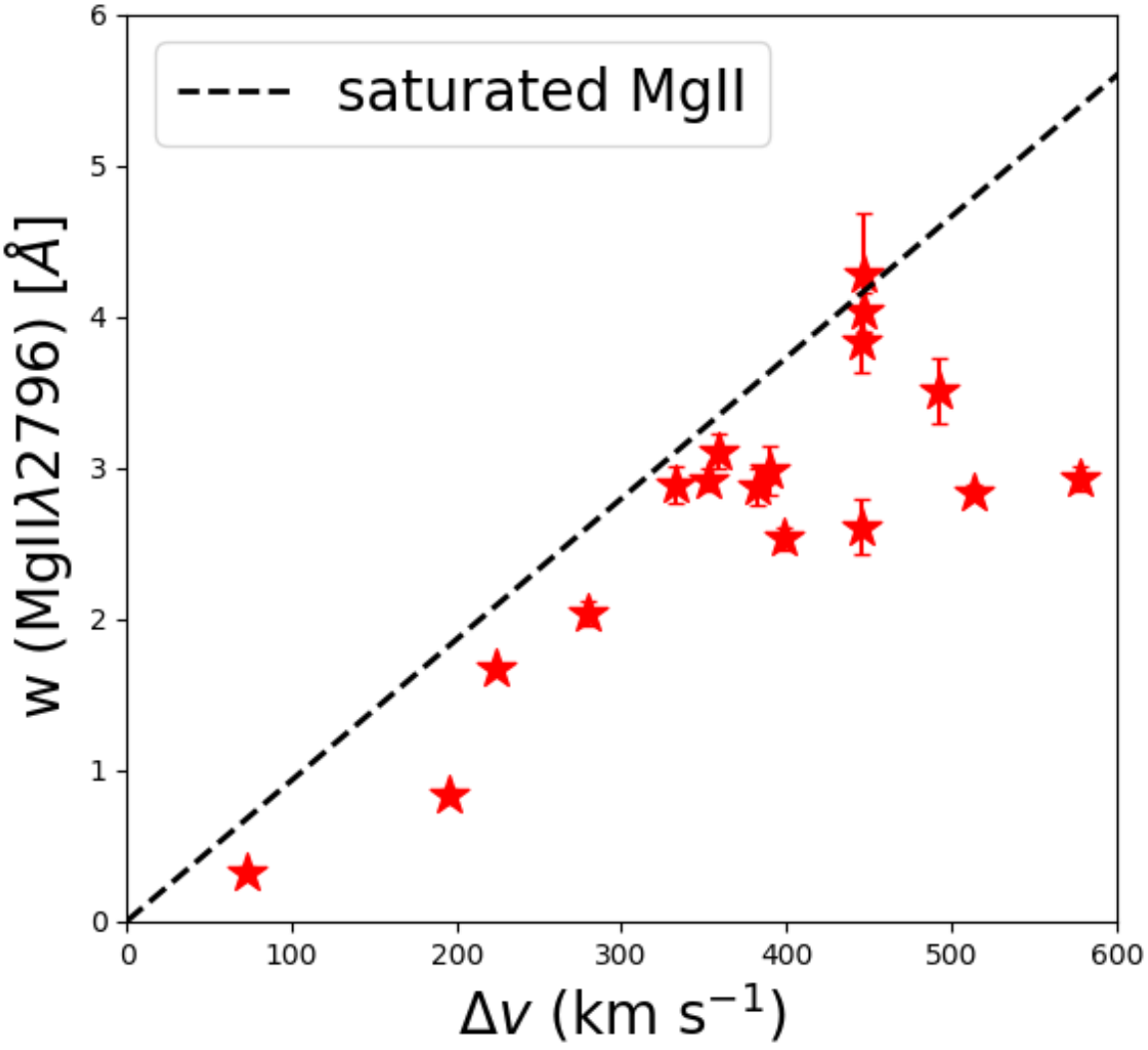

FIGURE 2.11: W(Mg IIλ2796) versus the width of the absorption profile (see text for definition). The black dashed line is the relation expected when the Mg II line is totally saturated.

Previous studies of Ca II and Na I absorption outside the Galaxy were carried out at low redshift so that the absorption lines are redshifted in the optical window ((see Blades et al. 1988) Bowen et al. (1991). In Fig. 2.12 we plotted the redshift distribution of Na I and Ca II absorbers in the previous and ours. It is obvious that our survey contribute to higher redshfit range. The impact parameters of the Ca II–associated galaxies have also been studied previously (Kunth & Bergeron 1984; Womble et al. 1990; Petitjean et al. 2000; Hall et al. 2002; Wang et al. 2005; Cherinka & Schulte-Ladbeck 2011; Zych et al. 2007; Rahmani et al. 2016)

Wild & Hewett (2005) were the first to search SDSS spectra systematically for Ca II absorbers and to show that they induce a reddening of the quasar spectrum with an

average E(B-V) = 0.06 (Wild et al. 2006) and that they are more evolved than the overall population of DLAs. Sardane et al. (2014, 2015) used SDSS-DR9 data and showed that the equivalent width distribution reveals two populations of Ca II systems with W_r(Mg IIλ2796)/W_r(Ca IIλ3934) less and greater than 1.8, respectively. These authors show as well that the systems with W_r(Ca IIλ3934) smaller and larger than ∼0.7 Å have properties, respectively, consistent with those of halo gas and intermediate between halo-type and disk-type gas (see Zych et al. 2009). Guber & Richter (2016) study the dust depletion of Ca II and Ti II in 34 systems at $z < 0.4$ and conclude that these lines trace predominantly neutral gas in the disks and inner halo regions of galaxies (see also Cox et al. 2007). Finally, Na I and Ca II have been detected in a DLA at $z \sim 1$ towards QSO APM 08279+5255 (Petitjean et al. 2000). In this system, it is clear that Na I absorption is confined to narrow components whereas Ca II has a shallow and broad profile very much consist with what have been found in the Galaxy and its halo.

• Ca II

Due to the absorber redshifts, the Na I and Ca II lines in our sample are redshifted to the near-infrared wavelength range. The data quality in the NIR arm is not good enough to derive robust column densities. Thus we decided to use the equivalent width only to discuss the observations of Na I and Ca II. The results are listed in Table 2.3. We detect Ca II in 9 systems out of 14 where we could obtain an equivalent width limit. The other spectra are spoiled by atmospheric features.

Wild & Hewett (2005) and Sardane et al. (2014) searched for Ca II systems in the SDSS data and therefore at $z_{abs} < 1.3$. Nestor et al. (2008) searched for Ca II in 16 known DLAs with $0.6 < z_{abs} < 1.3$ and detected Ca II in 12 of them. They warn however that their sample is biased towards strong Mg II systems. The Mg II mean equivalent width in their sample is 1.9 Å compared to 1.35 Å in an unbiased sample. The sample by Rahmani et al. (2016) consists of 9 DLAs at $z \sim 0.6$. In five of the seven observed fields they could detect associated galaxies for which they estimate a metallicity of 0.2 to 0.9 solar when the gas has a metallicity in the range 0.05 to 0.6 solar.

Sardane et al. (2014) find 435 Ca II doublets in the SDSS DR7 and DR9 databases, with $z < 1.34$. In Fig. 2.13 we plot their equivalent width distribution (scaled for convenience and shown in black histogram) together with ours (blue histogram). There is no obvious difference between the two distributions. The discrepancy in the first bin is probably due to the higher detection limit of the SDSS study. Assuming the SDSS detection limit is ∼ 0.35 Å, we applied a Kolmogorov–Smirnov test above this limit. A p value of 0.96 indicates that the two samples are drawn from a similar population.

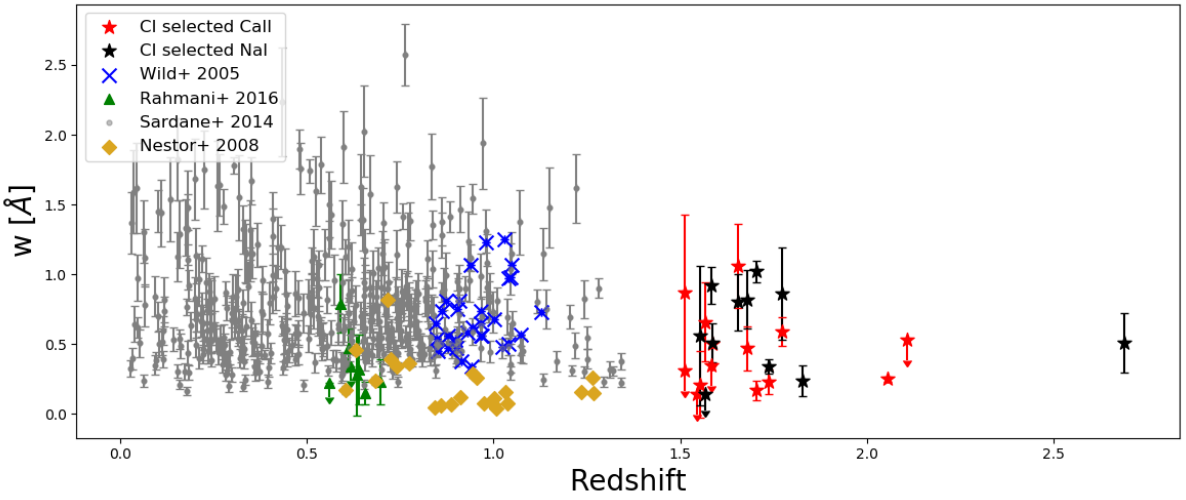

FIGURE 2.12: W versus z for Ca II absorbers detected in different studies: red stars are for the C I-selected sample (this work, arrows indicate upper limits), blue crosses are for the 31 Ca II absorbers detected in the SDSS by Wild & Hewett (2005), green triangles are for DLAs at $z_{\rm abs} \sim 0.6$ observed by Rahmani et al. (2016). Orange diamond are the 16 DLA and 8 sub-DLA sample in Nestor et al. (2008), the gray points are the Ca II absorbers in Sardane et al. (2014). We also overplot our Na I measurements as black stars.

• Na I

We detect Na I in 10 systems out of 11 systems for which spectral range has a good signal-to-noise. In other spectra, the wavelength range where the Na I absorption is expected to be redshifted is spoiled by atmospheric features. Results are listed in column 4 of Table 2.3. We compare in Fig. 2.14 the Na I rest equivalent width distribution in our sample to the distribution in the sample of 30 $z < 0.7$ Ca II systems detected in SDSS spectra by Sardane et al. (2015). It is apparent that the sample by Sardane et al. contains more systems with large Na I equivalent widths. We caution however that a few of these systems have inconsistent doublet ratios. We therefore checked the absorption in the SDSS spectra and noticed that some of the strong lines are affected by noise. A few strong Na I systems seem to be real however. It seems that in the sample of C I-selected systems the strong Na I systems are missing. This is somewhat surprising as we would expect some correlation between Na I and C I absorptions (see Fig. 2.18). This possibly can be explained by the fact that strong Na I systems drop out of our sample because of additional extinction as the corresponding extinction does affect the spectrum more strongly at higher redshift. Alternatively there could be some evolution with redshift, strong Na I systems being absent at high redshift. This could be related to the possibility that strong winds are more frequent at lower redshift.

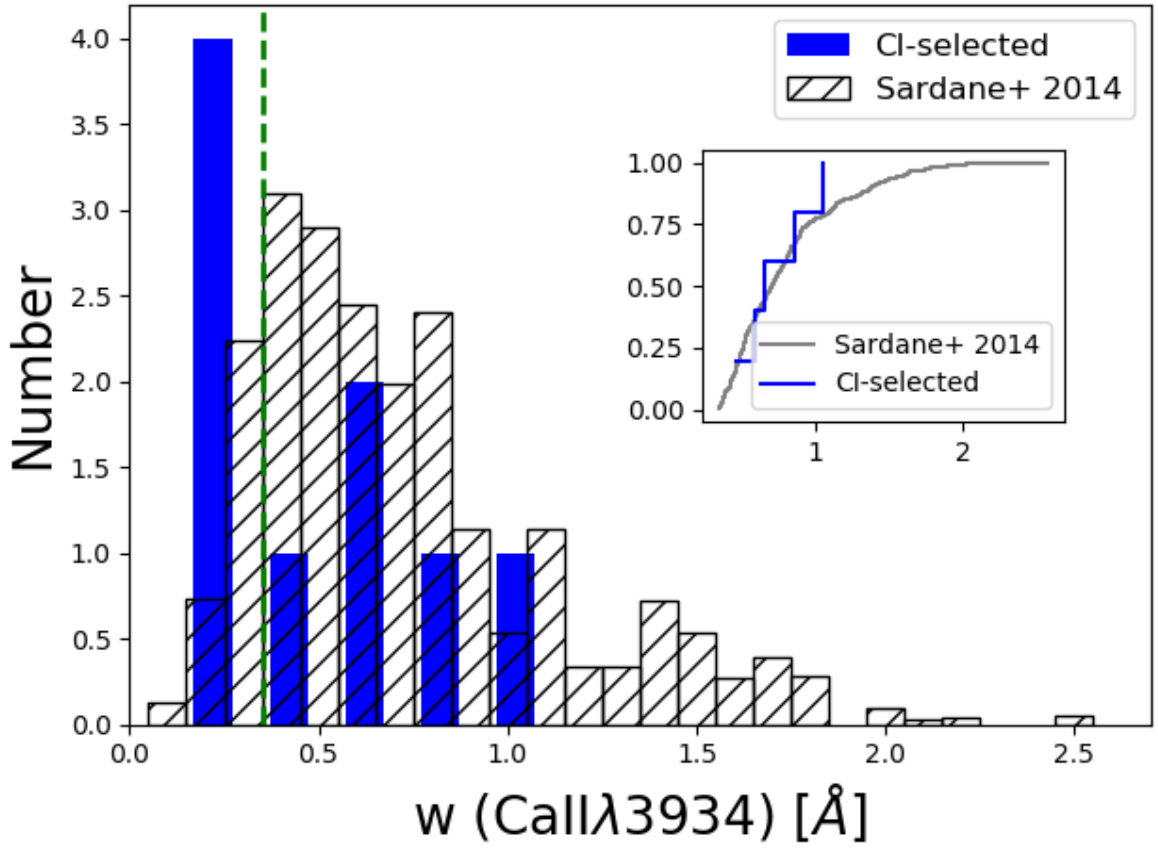

FIGURE 2.13: Blue histogram is the rest equivalent width distribution of the Ca II K lines detected in our sample; grey-hashed histogram is the scaled equivalent width distribution of Ca II K lines detected in the SDSS by Sardane et al. (2014). The two cumulative distributions are shown in the insert, considering the detection limit of SDSS we applied the Kolmogorov–Smirnov test when W(Ca IIλ3934) > 0.35 Å.

2.5 Discussion

2.5.1 Dust dimming

Vladilo et al. (2006) studied the extinction induced by DLAs on the quasar flux. They find that the extinction A_V is increasing with the column density of iron locked into dust calculated as follows:

$$\begin{aligned} N(\mathrm{Fe})_{\mathrm{dust}} &= N(\mathrm{Fe}) - N(\mathrm{Fe})_{\mathrm{gas}} \\ &= N(\mathrm{Zn})_{\mathrm{gas}} \times (10^{[Fe/Zn]_{\odot}} - 10^{[Fe/Zn]_{gas}}). \end{aligned}$$

In Fig. 2.15 we plot the attenuation A_V versus the column density of iron into dust measured in the C I systems. Points by Vladilo et al. (2006) are indicated as blue triangles. Apart from a few points with low A_V, the trend is found to be the same for the

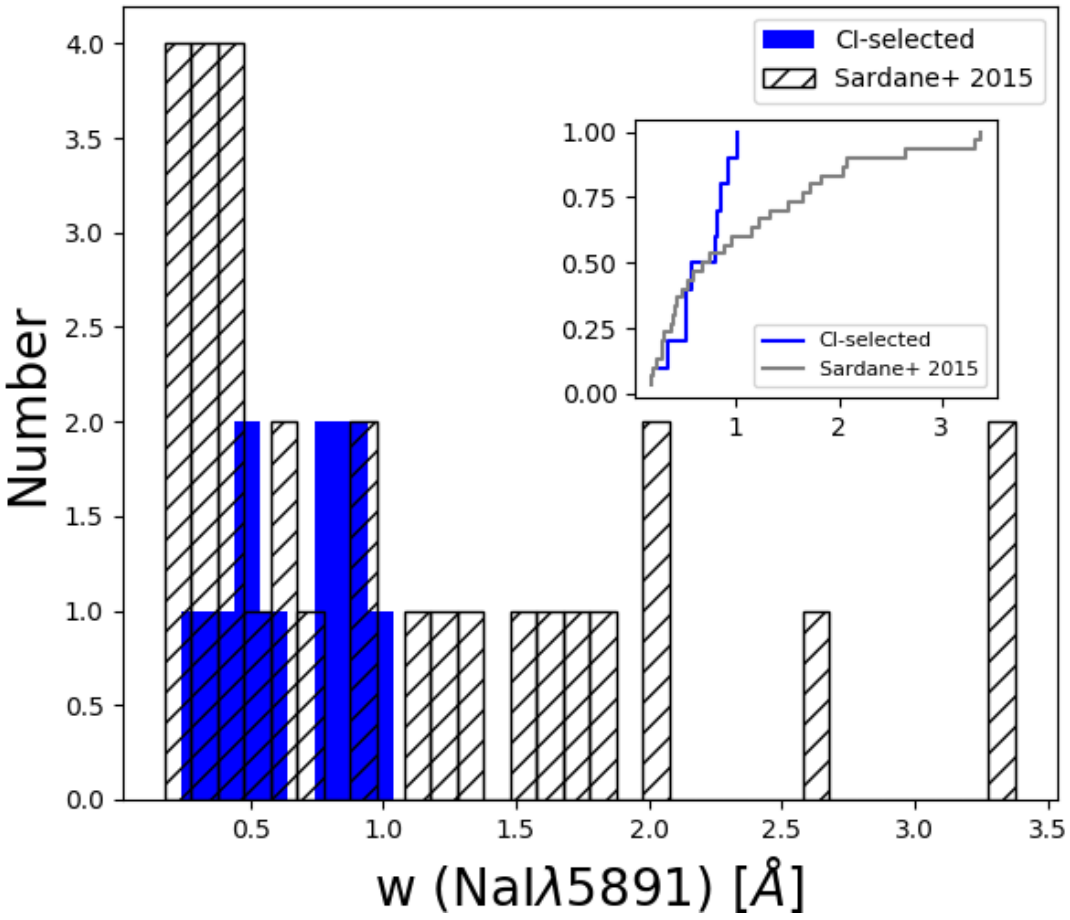

FIGURE 2.14: Blue histogram is the rest equivalent width distribution of the Na I lines detected in our sample; grey-hashed histogram is the equivalent width distribution of Na I lines detected in the SDSS by Sardane et al. (2015). The two cumulative distributions are shown in the insert.

different samples. We note that these low values are quite uncertain. We note also that most of our systems have $\log N_{\rm dust}({\rm Fe}) \sim 16$. It has been shown that for a column density larger than this, the molecular hydrogen content of DLAs is high (Ledoux et al. 2003; Noterdaeme et al. 2008). We calculated the dust-to-gas ratio $\kappa_{\rm X}$ based on the metallicity [X/H] and iron to metal ratio [Fe/X], according to the definition in Ledoux et al. (2003),

$$\kappa_{\rm X} = 10^{[{\rm X/H}]}(1 - 10^{[{\rm Fe/X}]}).$$

It is clear that this ratio is directly proportional to the metallicity. We therefore plot this number minus the metallicity as a function of zinc metallicity in the right panel of Fig. 2.15. It can be seen this number is larger at higher metallicities (see also Wiseman et al. 2017). It is intriguing as well to see that the scatter is much less as soon as

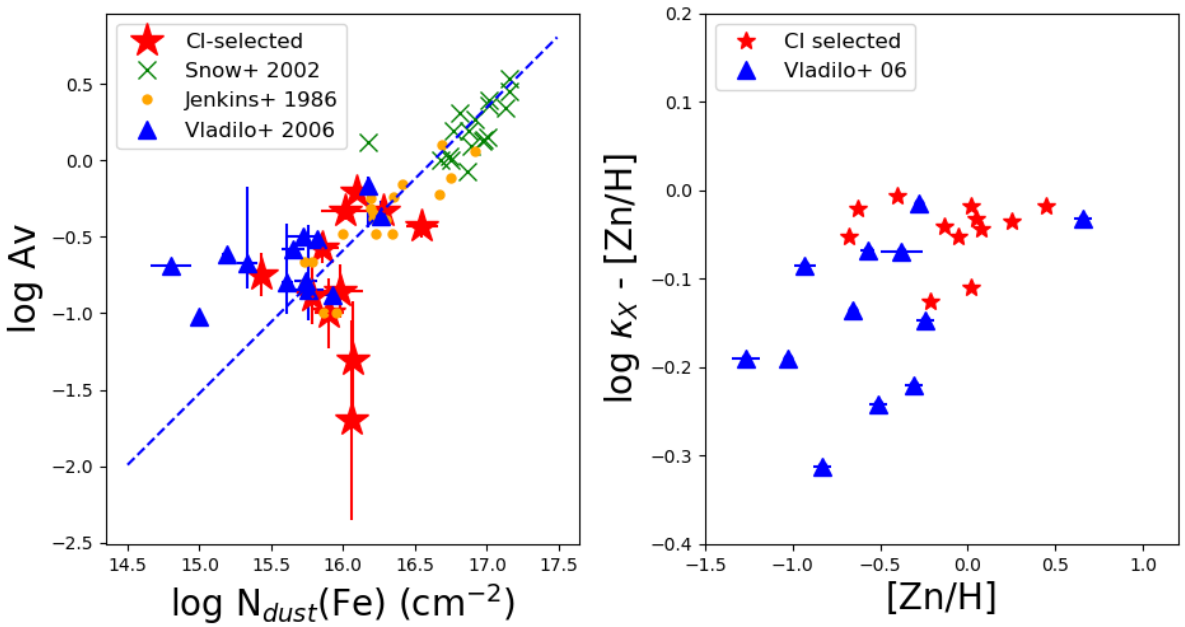

FIGURE 2.15: *Left panel*: Attenuation A_V versus the Fe II column density into dust. Red stars are for the C I-selected sample, blue triangles correspond to the data from Vladilo et al. (2006), green crosses and orange points are for samples of local interstellar clouds from Snow et al. (2002) and Jenkins et al. (1986), respectively. Blue dashed line is a linear regression of the MW data with fixed unit slope (see Vladilo et al. 2006). *Right panel*: The dust-to-gas ratio minus metallicity is plotted against metallicity.

metallicity gets closer to the solar value. This may be a consequence of these systems being somehow chemically mature. Ledoux et al. (2003) indicate that the detection probability of H_2 in DLAs increases as soon as $\log\kappa > -1.5$. It is clear that all our systems fulfill this condition. Actually Noterdaeme et al. (2018) show indeed that H_2 is present in all systems where the H_2 molecular transitions are covered by our spectra.

Wild & Hewett (2005) indicated that quasars with strong Ca II systems along their line of sight tend to have larger color excess. In the left panels of Fig. 2.16 we plot the W(Ca IIλ3934) and W(Na Iλ5891) as a function of $E(B-V)$. The mean value of Wild & Hewett (2005) is $E(B-V) \sim 0.06$ for W(Ca IIλ3934)$\sim$0.55 Å. It can be seen in the figure that our systems have slightly smaller equivalent widths, albeit errors are large, for the same color excess.

Correlation between dust reddening and the presence of Ca II and/or Na I absorption lines in our Galaxy has been investigated by Poznanski et al. (2012) and more recently Murga et al. (2015). The Na I doublet absorption strength in particular is generally expected to correlate with the amount of dust along the line of sight. Richmond et al. (1994) have shown, using 57 high-resolution stellar spectra taken by Sembach et al. (1993b), that the

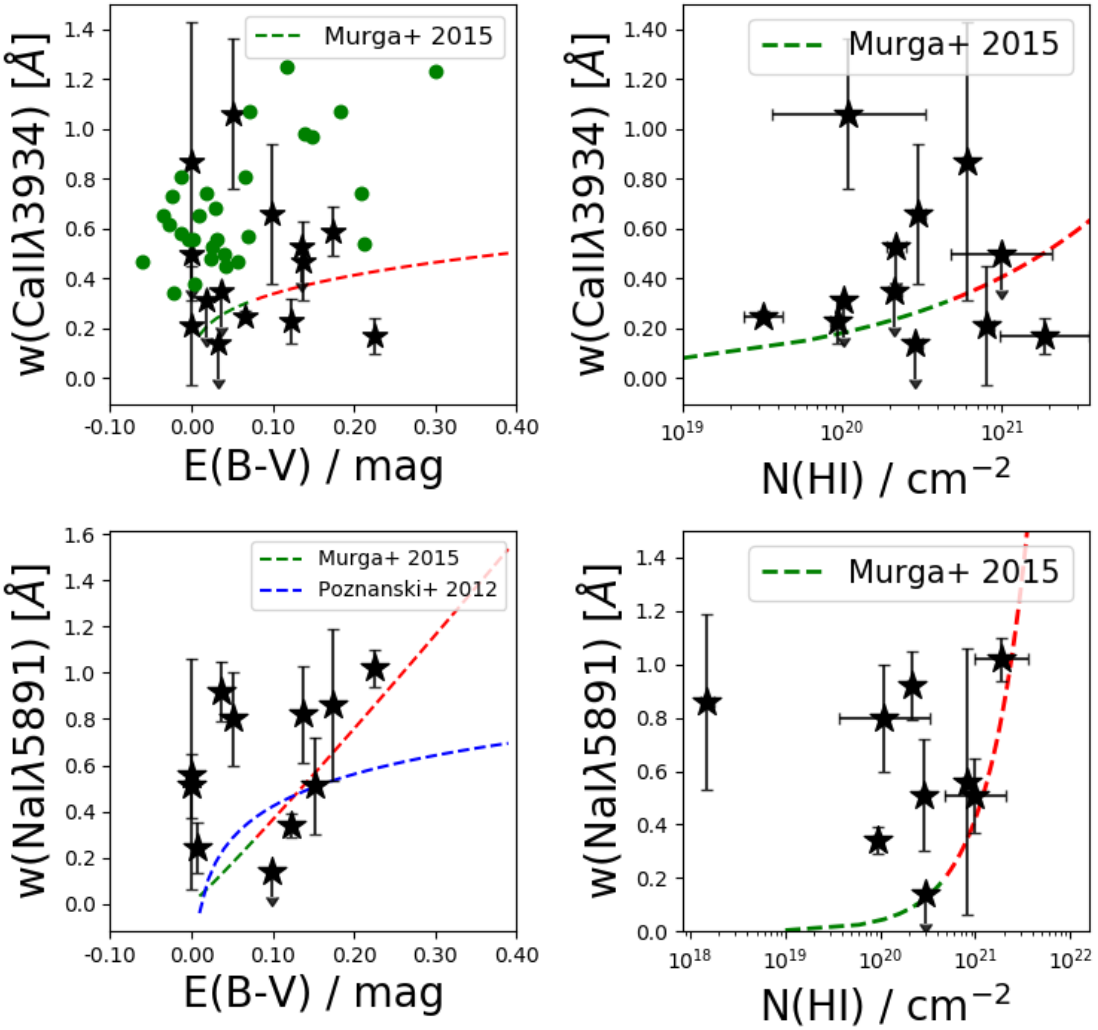

FIGURE 2.16: *Left panels*: W(Ca IIλ3934) in the upper panel and W(Na Iλ5891) in the lower panel as a function of the color excess $E(B-V)$. The green dots are the data from Wild & Hewett (2005). In all panels the green dashed lines correspond to the observations of Murga et al. (2015) in the interstellar and circumgalactic media of the Milky Way. The red dashed lines are extrapolations of these relations. The blue line in the W(Na I) versus $E(B-V)$ plot is an empirical relation given by Poznanski et al. (2012): $\log(E(B-V)) = 2.16\times W - 1.91$. *Right panels*: Same as left panels with log N(H I) on the x-axis.

equivalent width of individual Na I components correlate with the colour excess measured for these stars, albeit with a noticeable scatter. At lower resolution, the correlation survives although the scatter is even larger due to blending of individual components. Poznanski et al. (2012) combined two samples of Na I lines observed at high and low resolutions from, respectively, HIRES and ESI spectrographs on the Keck telescope and SDSS and derived an empirical relation between $E(B-V)$ and W(Na I). This relation is overplotted in the left-bottom panel of Fig. 2.16. It can be seen that our points are not inconsistent with this relation although W(Na Iλ5891) in C I systems seem to be larger than what is expected.

Murga et al. (2015) used SDSS spectra to obtain mean Na I and Ca II absorptions on the sky and correlate them with N(H I) and extinction maps. Both Ca II and Na I absorption strengths correlate strongly with N(H I) and $E(B-V)$, increasing linearly towards higher values until saturation effect becomes important at N(H I)$\sim 5\times10^{20}$ cm^{-2} and $E(B-V)\sim 0.08$ mag. Their relations are overplotted in Fig. 2.16 as the green and red dashed lines.

The dust-to-metal ratio defined as $E(B-V)/N$(Zn II) is plotted versus the Zn II column density in Fig. 2.17. Values measured in the MW, LMC and SMC are indicated as horizontal dashed lines. Green points indicate values measured by Wild et al. (2006) in Ca II systems and sub-samples of strong and weak systems. It is noticeable that most of the C I systems have dust-to-metal ratios of the order of what is seen in the MW, LMC and SMC at the exception of four systems, J1133-0057, J2340-0053, J0854+0317 and J1047+2057 which show much larger (by a factor of two to three) values than in the MW. Wild et al. (2006) have already noticed that the values of the dust-to-metal ratios determined for the Ca II absorbers were in the range R_{DM} =(4–8)$\times$ 10^{-15} mag cm^2, that is often higher than the values derived for the Milky Way. This were particularly true for their strong-system sample including all systems with W(Ca IIλ3934) $>$ 0.7 Å. Out of the four C I systems with large values, none qualifies for this denomination. The equivalent widths are observed to be in the range 0.17-0.6 Å. We already noticed that the C I system towards J1133-0057 is very peculiar as it is at the redshift of the quasar and arises from a very small cloud (Fathivavsari et al. 2017). Errors are quite large for the system towards J2340-0053 since $E(B-V)$ and N(Zn II) are small. For the two other systems, there is no apparent explanation. It may be conjectured that dust composition is quite different in these systems and high resolution data may help investigate this issue.

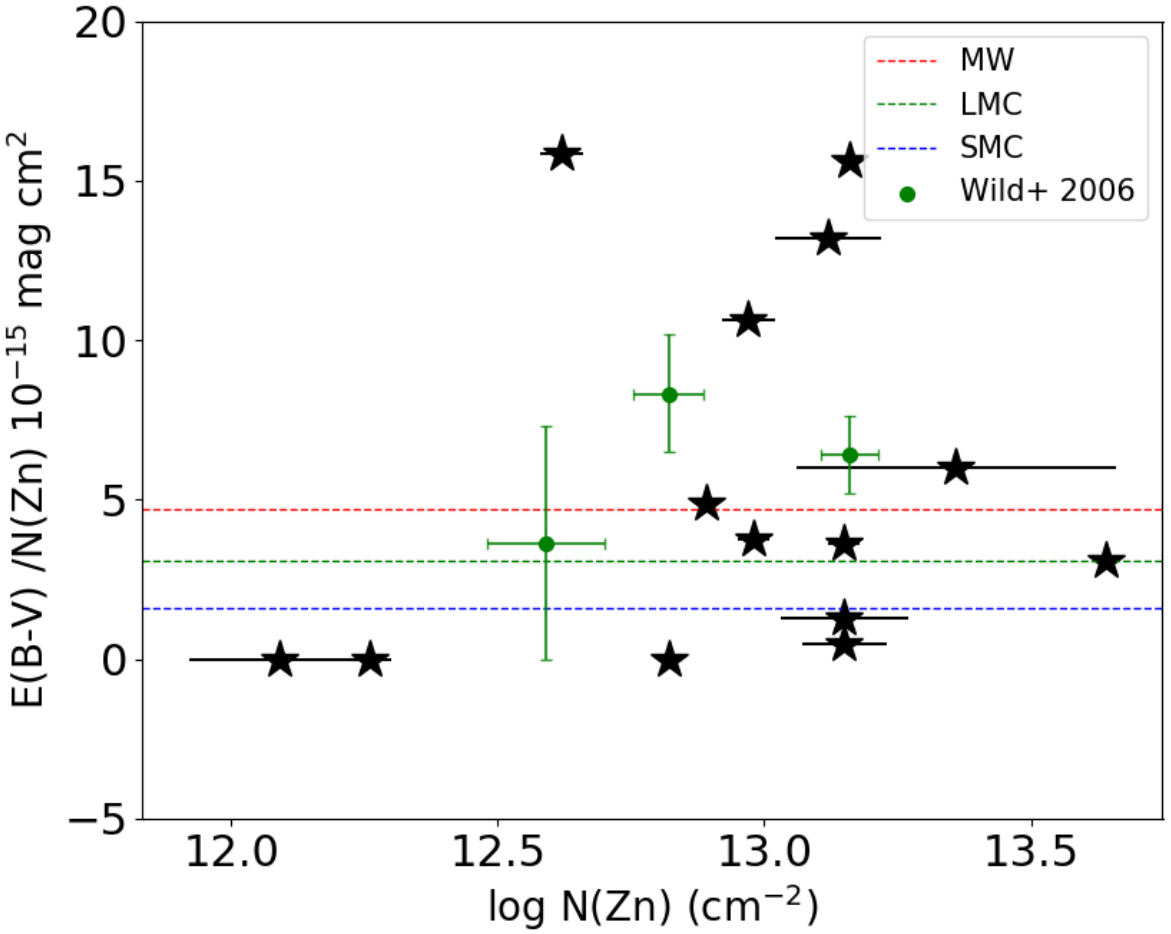

FIGURE 2.17: Dust-to-metal ratio against column density of Zn II. Dashed lines indicate values measured in the MW, LMC and SMC. Green points correspond to values derived in, respectively, all Ca II systems and sub-samples of high-W value and low-W Ca II systems by Wild et al. (2006).

2.5.2 Nature of the systems

We plot in Fig. 2.18 the W(Ca IIλ3934) (black stars) and W(Na Iλ5891) (red stars) as a function of the W(C Iλ1560). There is a positive correlation for Na I with a linear correlation coefficient of 0.80. This is expected as Na I is seen in cold gas as traced by C I. We note that the correlation can be interpreted as a consequence of an increasing number of components as the equivalent widths increase. If there is a correlation for Ca II, it is positive, but there is no strong evidence for it the linear correlation coefficient being only 0.36. This may indicate that depletion of Ca is varying strongly from one system to the other.

The correlation between equivalent widths is seen also between Mg II and Mg I (Fig. 2.19; see also Wild et al. 2006). This is also probably related to the increase of the kinematical

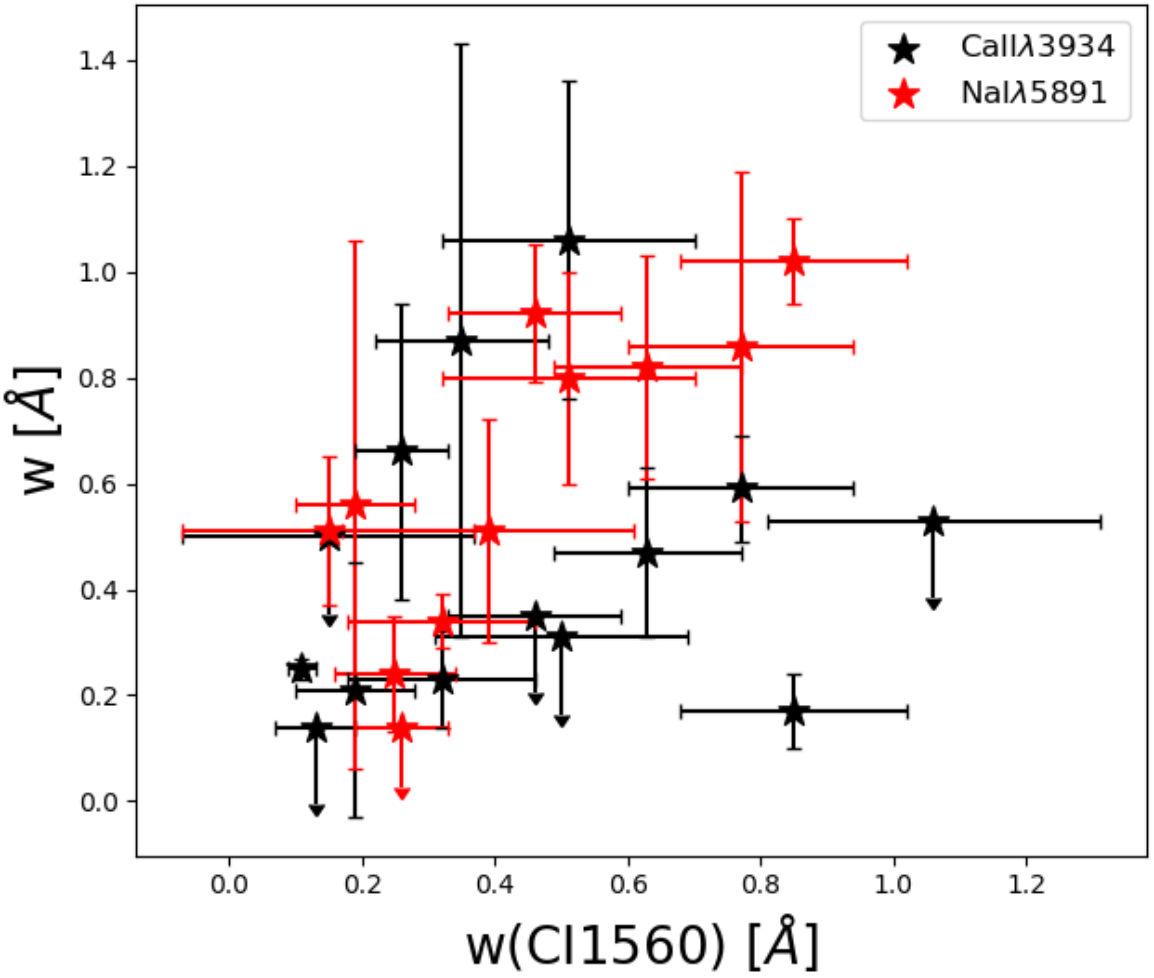

FIGURE 2.18: W(Ca IIλ3934) (black stars) and W(Na Iλ5891) (red stars) as a function of the W(C Iλ1560).

extension of the absorptions with increasing rest equivalent width (see Fig. 2.11).

From the right panels of Fig. 2.16, we have seen that there is no simple relation between W(Ca IIλ3934) and N(H I). This has been already emphasized by Nestor et al. (2008) at lower redshift. The latter authors conclude that systems with $W > 0.25$ Å should be DLAs. This conclusion is verified in our sample.

2.5.2.1 Association with galaxies

Two characteristics of our C I systems are clearly specific namely: the velocity spread of the Mg II absorption is unusually large (9 out of 17 of our systems have $\Delta v > 400$ km s^{-1}; see Fig. 5) and 10 out of 11 of our systems where we could investigate the presence of Na I absorptions have a detection. In Fig. 2.20 we plot the W(Mg IIλ2796) versus the Ca II (red

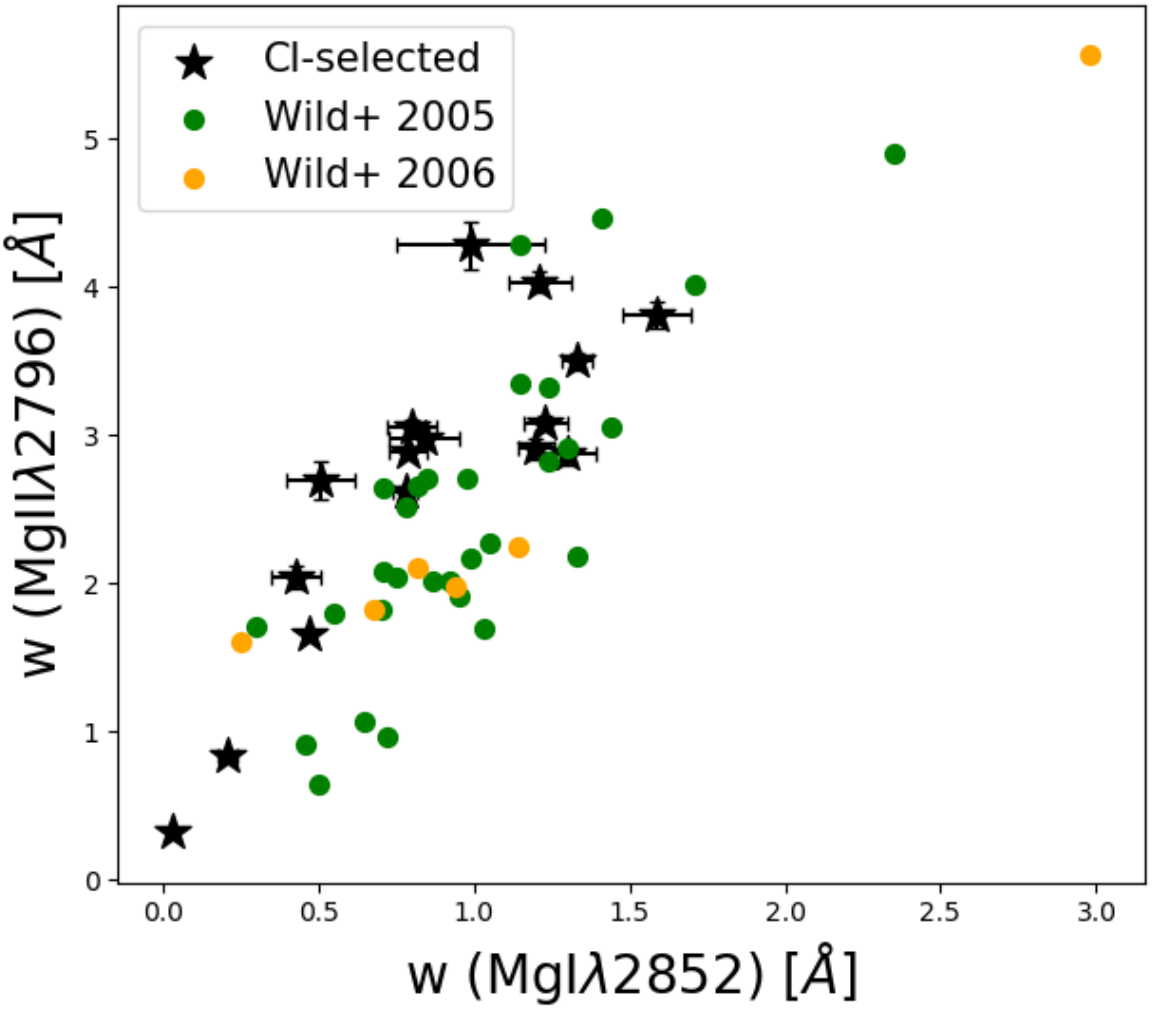

FIGURE 2.19: W(Mg IIλ2796) versus W(Mg Iλ2852) equivalent width. The green dots are the data from Wild & Hewett (2005), the orange dots are from Wild et al. (2006).

stars) and Na I (blue stars) equivalent widths. Data by Wild & Hewett (2005) at lower redshift are overplotted as green points. Orange triangles are for Richter et al. (2011). It is apparent that W(Mg IIλ2796) measured in our systems are amongst the largest. A trend can be seen in the sense of larger W(Mg IIλ2796) for larger W(Ca IIλ3934) although the scatter is very large. This may be an indication that large W(Mg IIλ2896) can be found in a wide variety of situations and in particular at any distance from the associated galaxy. We should note that in the sample of star-forming galaxies in the redshift range 0.4−1.4 observed by Martin et al. (2012), about 12% have W(Mg IIλ2796) > 2.5 Å and there is an apparent correlation between the stellar mass and the W(Mg IIλ2796).

It is well known that DLAs are not always detected in the disk of galaxies and that the DLA phase is extended towards the halo and even the intergalactic filaments (e.g.

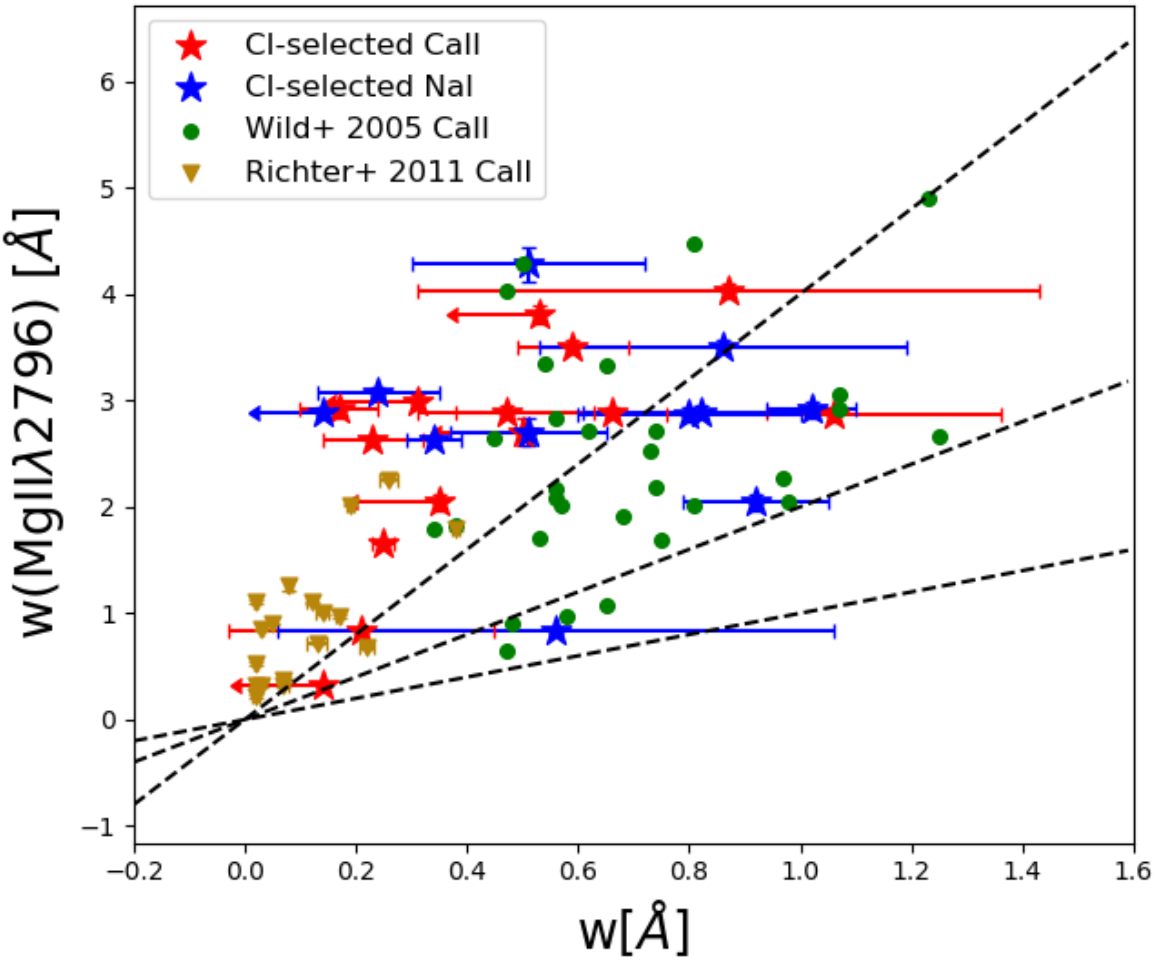

FIGURE 2.20: W(Mg IIλ2796) as a function of Ca IIλ3934 (red stars) and Na Iλ5891 (blue stars) equivalent widths. Green points are from Wild & Hewett (2005) for systems with $0.6 < z_{\rm abs} < 1.3$. The orange triangles are the sample from Richter et al. (2011). The three dashed lines are for W(MgII) / W(CaII) = 1,2 and 4 respectively.

Pontzen et al. 2008; Bouché et al. 2013). This may well be the case as well for the C I systems in our sample.

Several studies have been dedicated to the link between Ca II systems and associated galaxies at low redshift (Bowen et al. 1991; Hewett & Wild 2007; Richter et al. 2011; Zych et al. 2007). Galaxies are detected with impact parameters from 5 kpc (Petitjean et al. 1996) to more than 30 kpc (Rahmani et al. 2016). In turn, cold gas detected by the presence of molecular hydrogen or very high H I DLA systems seems to be located in disks of galaxies (see Noterdaeme et al. 2014). The C I systems studied here are associated with cold gas and Ca II absorptions but are not always DLAs. It is probable that they arise in different environment. It would therefore be of particular interest to search for the associated galaxies.

Zych et al. (2007) were able to associate luminous, metal-rich, star-forming spiral galaxies with five strong Ca II absorbers at $z < 0.5$ from the SDSS. The W(Ca IIλ3934) are between 0.47 and 0.79 Å. For respectively J0019-1053 at $z_{\rm abs} = 0.347$; J0912+5939 at $z_{\rm abs} = 0.212$; J1118-0021 at $z_{\rm abs} = 0.132$; J1219-0043 at $z_{\rm abs} = 0.448$ and J2246+1310 at $z_{\rm abs} = 0.395$ they detect the associated galaxy at 17, <5, 23, 7, and 6 kpc. In four out of five cases the galaxies are luminous ($L \sim L^*$), metal-rich ($Z \sim Z_\odot$), massive (velocity dispersion $\sigma \sim 100$ km s^{-1}) spirals. We searched, when possible, the SDSS spectra for the the Mg II absorptions and measured, W(Mg IIλ2796) = 1.5 and 2.26 Å for J1219-0043 and J2246+1310 respectively. Petitjean et al. (1996) detect a $z = 0.101$ spiral galaxy ($L \sim 0.45L^*$) with an impact parameter of 5 kpc at the same redshift as an absorption system with W(Mg IIλ2796) = 1.64 Å and W(Ca IIλ3934) = 0.34 Å. Rahmani et al. (2016) searched for galaxies associated with DLAs at $z < 0.6$. Six of them have W(Ca IIλ3934) $\sim$ 0.3 Å. Four galaxies are detected at impact parameters of 15, 20, 12 and 10 kpc. Two are not detected. In two other DLAs with no Ca II absorption associated, the galaxy is detected at 30 and 10 kpc. We note that in 21 DLAs with associated galaxies they find 110< v_{90} < 350 km s^{-1}.

In Fig 2.21 we plot the Ca II equivalent width versus the impact parameter of the associated galaxies as reported in the literature. We overplot the range of W from our sample. It is apparent that Ca II systems can be observed at large distances from the associated galaxy. This large spread of the neutral gas around galaxies is already known. Rahmani et al. (2016) shows that the impact parameters of DLA galaxies at $z < 1$ is larger than what would be expected around our galaxy according to the H I surface density for the disc of the Milky Way (Kalberla & Kerp 2009). It is interesting to note that there is no obvious trend in this plot at least up to ∼25 kpc and the scatter in W is large for any given impact parameter. This may be again an indication that there is no preferred location of the systems relative to the associated galaxy.

2.5.2.2 C I systems and outflows

We have seen that the C I systems in our sample show very large Mg II velocity extends. Very large Mg II absorbers are relatively rare although the large statistics of the SDSS implies that a large number of systems with W(Mg IIλ2796) > 3 Å is known (Nestor et al. 2005; Prochter et al. 2006; Quider et al. 2010). By stacking thousands of relatively shallow SDSS images of the fields around strong Mg II absorption systems, Zibetti et al. (2007) demonstrated that the strongest systems are associated with bluer galaxies closer to the sightline to the background quasar compared to weaker systems. This suggests a relation between star forming galaxies and strong Mg II systems, the velocity extent of the

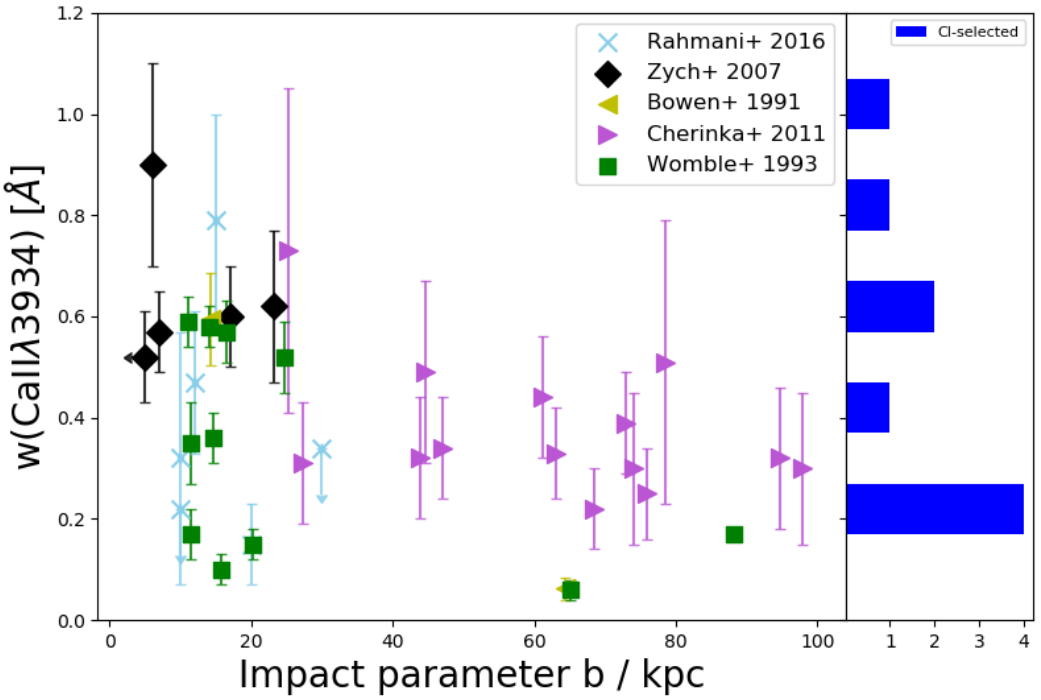

FIGURE 2.21: The W(Ca IIλ3934) versus the impact parameter of associated galaxies. Light-blue crosses are from Rahmani et al. (2016), black diamonds are from Zych et al. (2007), yellow triangles are from77 Bowen et al. (1991), orchid triangles are from Cherinka & Schulte-Ladbeck (2011), green squares are from Womble (1993), blue histogram on the right are the W(Ca II) which are observed in this work.

latter possibly arising in a super wind. This is strengthened by the correlation between W(Mg II) and the mean [OII] luminosity in the associated galaxy detected by Ménard & Chelouche (2009) and Noterdaeme et al. (2010b). Joshi et al. (2017) also found that the [OII] luminosity of the galaxy associated with Mg II systems increases with W(Mg II).

On the other hand, Nestor et al. (2011) studied two fields of ultra-strong Mg II systems (J0747+305, $z_{\rm abs} = 0.7646$, W(Mg IIλ2796) = 3.6 Å and J1417+011, $z_{\rm abs} = 0.669$, W(Mg IIλ2796) = 5.6 Å). They detect two galaxies in each field at the same redshift as the absorption at 36 and 61 kpc for J0747+305 and 29 and 58 kpc for J1417+011 from the line of sight to the quasar. This means that either the associated galaxy is at a very small impact parameter and is not seen in the ground-based images or the system can arise at large distances from the host galaxy as suggested in the previous Section.

Bouché et al. (2007) surveyed 21 fields around $z_{\rm abs} \sim 1$, W(Mg IIλ2796) > 2 Å systems and detected strong Hα emission in 14 of the fields. The corresponding star-formation rate is in the range 1–20 $M_\odot$ yr^{-1}. The impact parameter is <10 kpc for only two of the galaxies and between 11 and 54 kpc for the 12 others.

In our sample, 13 out of 17 systems have W(Mg IIλ2796) $>$ 2 Å (see Fig. 5). Out of these systems, 8 are departing from the relation corresponding to a saturated line. This shows that the kinematics is strongly perturbed for most of these systems. It would be surprising they arise in quiet disks and they must be located close to regions of star formation activity and/or are part of objects in interaction. However, Bouché et al. (2012) searched the fields of 20 strong (W(Mg IIλ2796) $>$ 2 Å) $z \sim 2$ Mg II systems for star-formation activity and detect only four of them. This may indicate that not all strong Mg II systems are related to strong star-formation activity. Since our systems contain cold gas, it would be most interesting to search for the counterparts of star-formation activity around the systems in our sample. As noticed before, we find three systems in the spectra of J1047+2057, J1133-0057 and J2350-0052 where the Mg II absorptions show two distinct saturated sub-systems separated by more than 200 km s^{-1} in the C I and Mg II absorption profiles. In J1133-0057, we detect also two distinct Na I components. This is a small but significant fraction of the sample where it is reasonable to believe that the systems arise in interacting objects. We should note that in the case of J2350-0052, Krogager et al. (2017) detect Ly-α emission at an impact parameter of $\sim$ 6 kpc.

In any case, all this suggests that a large fraction of the cold gas at high redshift arises in disturbed environments probably in places with strong star-formation activity.

2.6 Conclusion

In this thesis we have studied a sample of 17, $z_{\rm abs} > 1.5$, absorption systems selected only on the basis of the presence of C I absorption in the SDSS spectrum of background quasars (Ledoux et al. 2015) and observed with the ESO spectrograph X-shooter. The W(C Iλ1656) are in the range 0.17 to 1.42 Å. Thanks to the large wavelength coverage of the X-shooter instrument, we can study, for the first time at these high redshifts, the Ca II$\lambda\lambda$3934,3969 and Na I$\lambda\lambda$5891,5897 absorption together with Mg II and Mg I absorptions.

We show that most of these systems have high metallicities and dust content compared to standard DLAs at these redshifts. We detect 9 Ca II absorptions with W(Ca IIλ3934) $>$ 0.23 Å out of 13 systems where we could have observed the line. The observed equivalent widths are similar to what is observed in other lower redshift surveys. We detect 10 Na I absorptions out of 11 systems where we could observe this species. No trend is seen between either W(Ca II) or W(Na I) and metallicity. While most of the systems have dust-to-metal ratios of the order of what is seen in the Milky Way, Large and Small Magellanic Clouds, four of the systems have values two or three times larger than what

is observed in the Milky Way. Although the errors affecting our estimates are still large, this may be an indication that these C I systems are at an advanced stage of chemical evolution. There is however no indication that the systems with large dust-to-metal ratios are a peculiar subset of the overall sample.

The systematic presence of Na I in these C I systems indicates that they probably probe the cold gas in the ISM of high redshift galaxies. The characteristics of the systems are such that most of the systems should show molecular hydrogen. This will be confirmed in an associated paper (Noterdaeme et al. 2018).

Most of the systems (12 out of 17) have W(Mg IIλ2796) > 2.5 Å. The Mg II absorptions are spread over more than $\sim$400 km s^{-1} for half of the systems; three absorbers have an extension larger than 500 km s^{-1}. This is reminiscent of the detection of molecular hydrogen (log $N(H_2) = 17.4$ and 16.5) in Q0551−366 and Q0013-004 where the Mg II absorptions are spread over $\Delta v \sim 700$ and 1000 km s^{-1}, respectively, for a metallicity relative to solar [Zn/H] $= -0.13$ and -0.02 and W(C I) ~ 0.25 and 0.33 Å (Ledoux et al. 2002; Petitjean et al. 2002). These large velocities can be the consequence of either interaction or star-formation activity in the associated galaxy or cold flow disks (Stewart et al. 2013). Ledoux et al. (2006) have interpreted the observed correlation between Δv and metallicity in DLAs as a tracer of an underlying mass-metallicity relation. This is based on the assumption that Δv is a tracer of the virial velocity and thus the halo mass. Others have interpreted large velocities as the consequences of strong winds powered by star formation (e.g. Bouché et al. 2016). We note that both interpretations would imply that if the kinematics is strongly perturbed for most of these systems, the latter probably do not arise in quiet disks and are located close to regions of intense star formation activity and/or are part of objects in interaction. However, Bouché et al. (2012) searched the fields of 20 strong (W(Mg IIλ2796) > 2 Å) $z \sim 2$ Mg II systems for star-formation activity and detect only four of them. This may indicate that not all strong Mg II systems are related to strong star-formation activity. Since our systems contain cold gas, it would be most interesting to search for their optical counterparts and associated star-formation activity in emission.

Chapter 3

Individual systems

Contents

3.1 Lyman-Limit-System J1341+1852

In this section we study a special system J1341+1852 from this C I sample. It is peculiar because the neutral hydrogen column density log N(H I) $\sim$ 18 is much smaller than N(H I) in other systems in our sample. We not only detect Fe II, Al II, Si II absorption lines but also higher ion species CII, C IV Al III, Si III and Si IV. Hydrogen in this system is partly ionized. At the same time, we still observe C I, which is rare in Lyman limit systems. We built a simple model of the ionization state and constrain the incident UV flux applied onto this system.

3.1.1 Introduction

Many previous studies on LLSs show that the metallicities of LLSs are quite uncertain. The values can range from -3 to super-solar. Fumagalli et al. (2013) applied a simple ionisation modelling on a composite spectrum of 38 LLSs at $z \sim 2.8$. The derived metallicity is -1.5. Prochaska et al. (2015) demonstrated that there a wide spread in metal-enrichment within LLSs, likely spanning four orders of magnitude. LLSs in their sample are generally enriched by heavy elements and about 10% LLSs exhibit even upto solar or super-solar enrichment. This indicates that non-negligible fraction of the LLS gas has been passed through the furnaces of stellar interior. This gas is thought to be expelled from galaxies supernovae explosion. LLSs in the CGM is promising to link diffused gas in IGM with the stellar activity and the gas in the ISM. Lehner et al. (2013) studied 28 LLSs with at $z < 1$ and found the metallicity distribution is a bimodel. They divided the gas in LLSs into two branches: the metal-rich branch of the population likely traces winds, recycled outflows, and tidally stripped gas; the metal-poor branch has properties that are consistent with cold accretion streams thought to be a major source of fresh gas for star forming galaxies. The outflow metallicity is around -0.3 and the cold flows metallicity is around -1.6. Cooper et al. (2015) presented 17 LLSs from SDSS at $3.3 < z < 4.2$. They found that high-redshift LLSs span a range of metallicity between $-3.0 < \log Z/Z_{\odot} < -1.5$.

Unlike the highly ionised diffuse gas in the IGM, LLSs are optically thick and the neutral hydrogen in the cloud is partly recombined. Part of the ions are ionized by the UV flux. The source of UV flux comes from I: the background radiation II: the emission from nearby star formation. The most important and difficult part when modelling LLS is to determine or at least constrain the ionization parameter U, the definition is below (Ferland et al. 2013).

$$U \equiv \frac{\Phi(H)}{n(H)c}$$

where n_H is the volume density of hydrogen and $\Phi(H)$ is the surface flux of ionizing photons. LLSs are hopefully provide important information for the metal transfer between galaxies and IGM.

3.1.2 Cloudy

Cloudy is a program designed for the simulation of photoionized regions such as the IGM or the BLR of quasars. It is based on the assumption that the region is in radiative and

collisional equilibrium. The first version was released by Ferland et al. (1998), and then implemented in Ferland et al. (2013) and Ferland et al. (2017). This program aims at modelling clouds from fully ionized to molecular. By varying the input parameters such as metal species, UV background flux and ionization parameter, one can model the physical state of the gas: metal abundances, neutral hydrogen column density, gas density and temperature. We briefly introduce the most-used input parameters in this work below:

• Radiation-bound geometries

The geometry of the cloud in CLOUDY is always 1D spherical but can be made effectively plane parallel by making the inner radius much larger than the thickness of the cloud. The default is for the gas to have constant density and to fully fill its volume. CLOUDY normally assumes an open geometry, or one in which the gas has a very small covering factor. By changing the covering factor one can change the geometry to a closed geometry.

•Incident radiation field

The spectral energy distribution (SED) of the incident radiation field should be specified between the energies of 1.001×10^{-8}Ryd and 7.354×10^{6} Ryd. The options for the incident radiation field continuum include: black body, AGN and the local galactic ISM radiation. When the cloud is illuminated by an AGN, the command *AGN* or *table AGN* specify the shape and intensity of the incident radiation continuum. Normally it comes with an optional parameter ionization parameter which indicates the ionization state of the cloud. The *table ISM* is the command for the radiation in the local ISM. The optional parameter ismfactor is to control the intensity of the radiation. The default option is the ISM field from Black (1987) (hereafter BLACK) except that the radiation field between 1 and 4 Ryd is interpolated from the observed or inferred values.

The command HM05 enters the Haardt & Madau (2005 private communication) radiation field at any redshift $0 \leq z \leq$8.9 (same as the UV background in Haardt & Madau 2012). There are two forms of the radiation field - the default includes both quasars and galaxies, the second is just quasars included. The *tableCMB* command generates a blackbody radiation field in strict thermodynamic equilibrium. This table specifies both the shape and intensity of the radiation field. There is an optional multiplicative scale factor to change the intensity. The temperature of the blackbody is given by

$$T_{CMB} = T_0(1+z)\mathrm{K}$$

where $T_0 = 2.725 \pm 0.002$ K (Wilkinson 1987; Mather et al. 1999). The cosmic rays background can also be added in the CLOUDY model. Physics about cosmic rays background is described in Ferland & Mushotzky (1984). The galactic background cosmic rays is added by the command *cosmic rays background*.

• **Hydrogen density**

The hydrogen density n(H) is the total hydrogen density given by:

$$n(H) = n(H^0) + n(H^+) + 2n(H_2) + \sum_{other} n(H_{other})[cm^{-3}]$$

where the $n(H_{other})$ is the H in all other hydrogen-bearing molecules.

• **Metals and grains**

The metal abundances of the cloud are defined by command with a varying factor number. The dust effect can also be added by adding grains. The command *grains* can specify the types of grains. For instance, grains ISM will create grains with both graphit and silicate, for which the extinction has a ratio R(V)= A(V)/E(B-V) = 3.1. Grain extinction is given by the cross section per H nucleon: $\sigma_s = \kappa$/n(H), where κ is the opacity due to grains. In some cases, dust depletion is also non-negligible. For example, in the ISM the observed depletion is a function of the gas density. When the metal abundances and grains type are defined, command *depletion* introduces the dust depletion. By defining the type of grains and the amount of dust, we can quantify the depletion.

3.1.3 Preliminary Results

3.1.3.1 Metallicity

We fit this system with VPFIT using different Doppler parameters. The X-SHOOTER resolution is not enough to confirm the saturation of the lines or the column densities of species. Therefore we give a range of the column densities of different ions. Then we vary different input parameters in CLOUDY: ionization parameter, metallicity and hydrogen volume density to reproduce the observations.

• Different b values

We fix the b values at 2.50, 4.50, 5.50, 8.50 and 10.50 km s^{-1} and obtained a range of column densities. The results are listed in Table 3.1 and Table 3.2. We start the fit with O I and C I lines, then tied O I line with other metal lines (Fe II, Si II, Si III, Al II and Al III) with the same b values. H I is added in the end with the same b value but

TABLE 3.1: Column density meansurements of J1341+1852.

z (C I) =1.5441					
Species	N cm^{-2} (b=2.50 km s^{-1})	N cm^{-2} (b=4.50 km s^{-1})	N cm^{-2} (b=5.50 km s^{-1})	N cm^{-2} (b=8.50 km s^{-1})	N cm^{-2} (b=10.50 km s^{-1})
C I	14.40±0.31	13.80± 0.08	13.67±0.06	13.53±0.06	13.44±0.10
C I*	12.90±0.20	13.25±0.08	13.26±0.07	13.25±0.08	13.24±0.07
C I**	11.96±0.52	12.52±0.26	12.54±0.25	12.51±0.29	12.71±0.19
C II	17.92±0.05	17.94±0.04	17.90±0.05	17.56±0.19	16.40±0.24
C II*	14.24±0.26	13.92±0.14	13.85±0.12	13.74±0.10	13.71±0.07
Fe II	13.16±0.08	12.98±0.04	12.94±0.04	12.88±0.05	12.86±0.05
Mg II	16.23±0.02	15.85±0.08	15.52±0.18	14.04 ±0.21	13.58±0.05
Al II	13.59±0.28	12.60±0.10	12.45±0.07	12.34±0.07	12.30±0.05
Si II	15.46±0.22	14.09±0.15	13.87±0.10	13.67±0.08	13.62±0.05
Al III	12.25±0.14	12.17±0.10	12.16±0.10	12.15±0.10	12.15±0.09
Si III	15.65±0.40	15.62±0.41	15.42±0.55	14.65±0.79	13.91±0.75
O I	16.96±0.25	16.55±0.43	15.10±0.39	14.49±0.16	14.36±0.10
H I	18.18±0.07	18.18± 0.07	18.18 ±0.09	18.18 ±0.09	18.17 ±0.05

different component position (redshift). Note that, as seen in Fig. 3.6, Si IVλ 1548,1560 are strongly blended with other absorption lines, we derived an upper limit fit for Si IV.

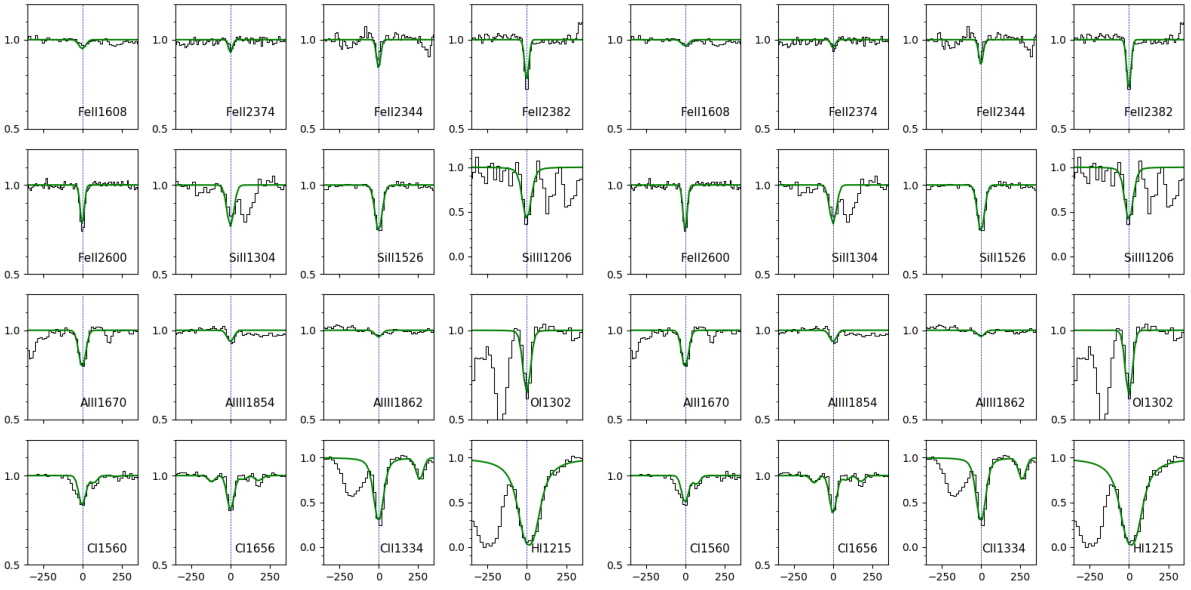

FIGURE 3.1: J1341+1853 VPFIT fit with b = 2.5 km s^{-1}

FIGURE 3.2: J1341+1853 VPFIT fit with b = 4.5 km s^{-1}

3.1.3.2 Modelling of ionization state

We conduct the modelling with CLOUDY to reproduce the observation results. The most difficult part is to reproduce C I together with other higher ionised atoms. There

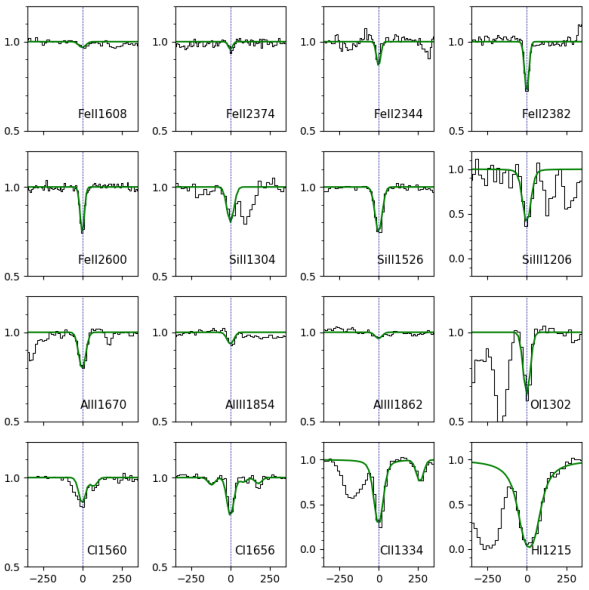

FIGURE 3.3: J1341+1853 VPFIT fit with b = 5.5 km s^{-1}

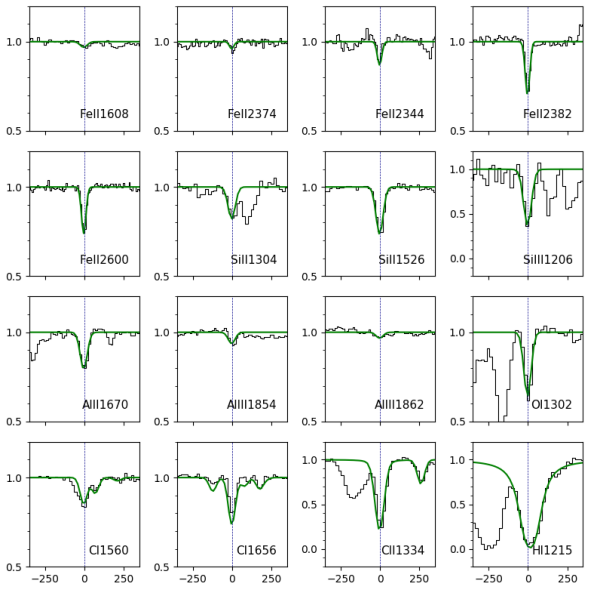

FIGURE 3.4: J1341+1853 VPFIT fit with b = 8.5 km s^{-1}

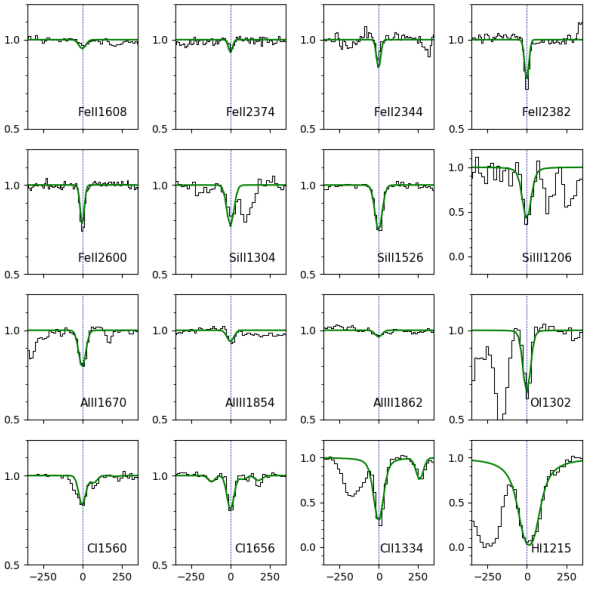

FIGURE 3.5: J1341+1853 VPFIT fit with b = 10.0 km s^{-1}

are two possibilities: 1. This system has high metallicity which can be close to solar or supersolar. 2. Low UV background radiation. In these simple models below, we focus on three parameters: metallicity, ionization parameter and the hydrogen volume densities.

• **Stop Criteria**

As we set the loops in varying input parameters, there should be a criteria to stop the

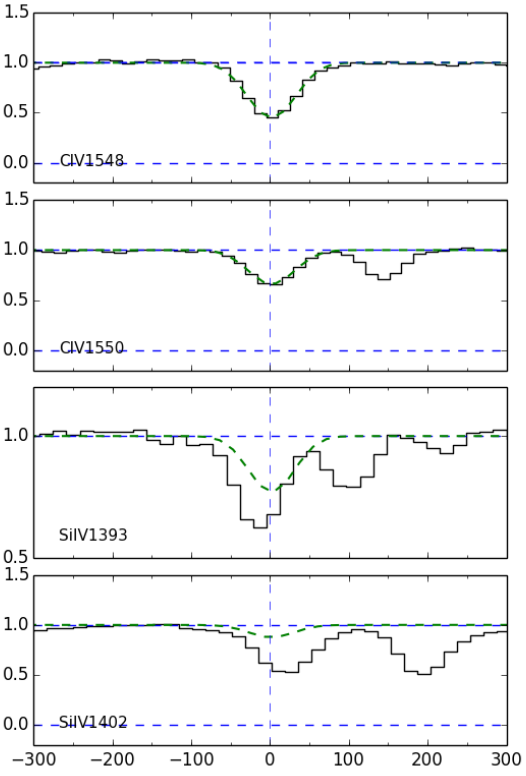

FIGURE 3.6: Fits of C IV and Si IV, the Si IV doublets are in the forest and blended.

TABLE 3.2: Column density ranges of J1341+1852

Species	min	max
C I	13.70 cm^{-2}	14.42 cm^{-2}
CII	16.40 cm^{-2}	17.94 cm^{-2}
Si II	13.62 cm^{-2}	15.46 cm^{-2}
Al II	12.30 cm^{-2}	13.59 cm^{-2}
Fe II	12.67 cm^{-2}	13.16 cm^{-2}
Si III	13.91 cm^{-2}	15.65 cm^{-2}
Al III	12.10 cm^{-2}	12.38 cm^{-2}
OI	14.36 cm^{-2}	16.96 cm^{-2}
CII/C I	2.70	4.06
Al III/Al II	- 1.34	-0.16
Si III/Si II	0.19	1.53

TABLE 3.3: CLOUDY model input file parameters for J1341+1852.

Parameters	Y/N	conditions
Cosmic rays background	Y	
CMB	Y	$z = 1.5442$
Table HM05	Y	$z = 1.5442$
Table ISM	Y	factor vary

loops. The stop column density of neutral hydrogen $\sim$ 18.18, which is the observation value.

• Background source

We start the modelling with the assumption that all the metals reside in the same phase. Firstly we adopted background radiation only (HM05+CMB at $z = 1.5442$ and cosmic rays background). For HM05, we adopted the default option which contains both galaxies+quasars. As seen in Fig. 3.7, we start with the solar metallicity and vary nH. It is obvious that only the background radiation with solar metallicity can not reproduce all ions content. With n_H = -1.5, most ions can be reproduced. We then tried different metallicities (log $Z/Z_\odot$) in the range of [-2,1], (see Fig.3.8). It indicates that with only the background source, it seems that Fe II, Si II, Si III, Al II and Al III can be reproduced with log $Z/Z_\odot$ $\sim$-1 and O and part of Si II, Si III can be constrained with about solar metallicity. But for carbon, higher metallicity is required. Note that with these conditions, all the ratios in the right panel can be reproduced.

• Extra radiation field

Besides the cosmic background radiation, we then introduce galactic interstellar medium incident radiation field with different intensities. As seen in Fig 3.9 and Fig.3.10, we present the different ions column densities and the relative ratios as functions of metallicity. Models adopt different ISM radiation field intensity. The volume density of neutral hydrogen is assumed to be log n_H = -1.5.

We found with log $Z/Z_\odot = 1$ and nH = -1.5, CI can be reproduced together with CII and OI and Si III. With the same hydrogen density and metallicity in the range of [-1.5,-1.0], we can reproduce higher ionization ions Fe II, Si II, Si III, Al II and Al III at logarithmic ISM factor between [-1,-0.75].

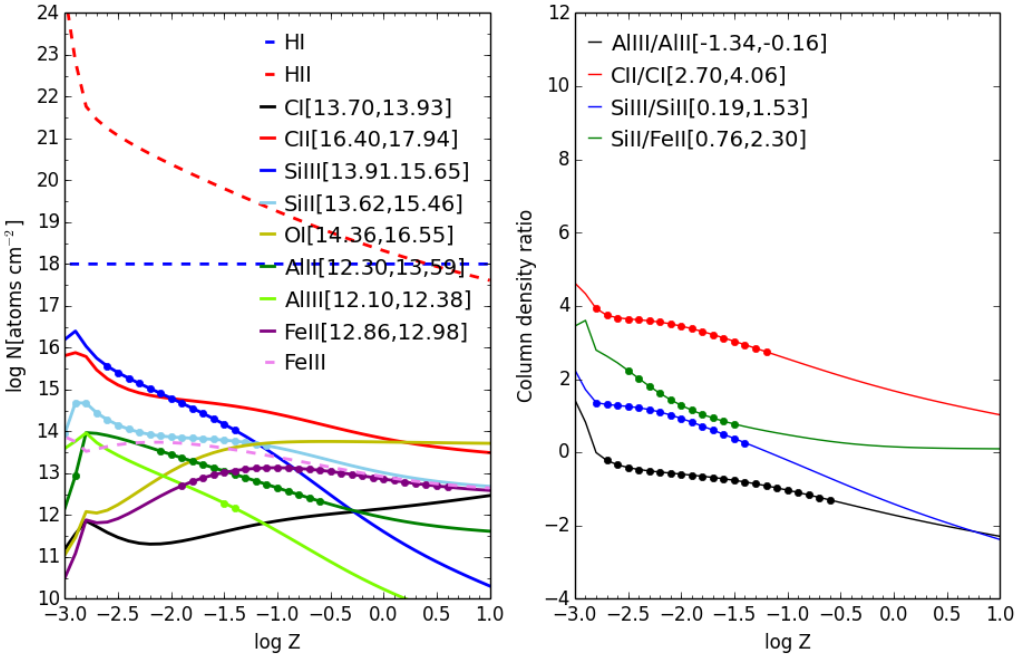

FIGURE 3.7: J1341+1852 CLOUDY model with cosmic background and UV-Xray background from HM05 at different nH. *Left*. The red dashed line is H I, blue dashed line is HII. The red solid line is CII, the black solid line is C I, the blue line is Si III and the sky blue line is Si II, the green line is Al II and the light green line is Al III, the purple line is Fe II and the pink dashed line is Fe III. *Right*: The red line is the ratio of log N(CII)/log N(C I), the green line is the ratio of log N(Si II)/log N(Fe II), the blue line is the ratio of log N(Si III)/log N(Si II), the black line is the ratio of log N(Al III)/log N(Al II). The numbers and bold points are the observational range.

3.1.4 Discussion

From the modelling, we can tell that the carbon and oxygen abundances can be roughly constrained with other ions with the same radiation intensity but not the same metallicity. If this is true, the possible explanation could be 1) The intrinsic metal composition of our systems is different than the solar composition. 2) The dust effect has not yet been taken into account.

In standard stellar evolution models, massive stars (M $> 10^6$ $M_\odot$) which then exploded as Type II SNe yield the predominantly α elements (C, O, Ne, Mg, Si, S, Ar, Ca). The less massive stars ($0.5 \leq M/M_\odot < 6$, called asymptotic giant branch (AGB) stars) produce C,O. Type-I supernovae will largely generate Fe. The lifetimes differences between massive stars, AGB stars and Type-I SN can be the reason of [α/Fe] enhancements in star-forming elliptical galaxies (Sharma et al. 2018). This lifetimes differences are also the possible cause for the generation of one kind of carbon-enhances metal-poor stars (CEMP). For

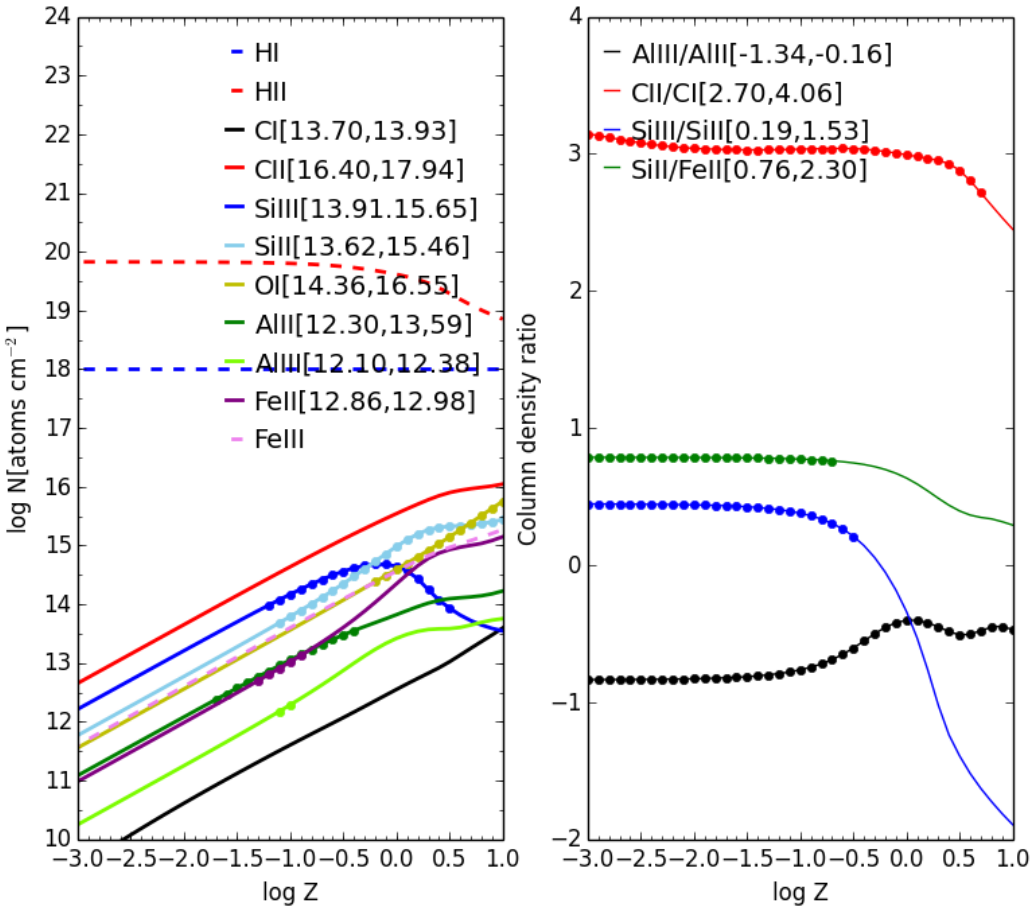

FIGURE 3.8: J1341+1853 CLOUDY model with cosmic background and UV-Xray background from HM05 at different metallicity. Labels are the same as Fig. 3.7.

CEMP, [C/Fe] can reach 1 (Beers & Christlieb 2005). In Sharma et al. (2018), they conduct simulation which include the physics of enrichment by asymptotic giant branch (AGB) stars, winds from massive stars, AGB stars and Type Ia and Type II supernovae (SNe) (see in Fig. 3.11).

If we start from our preliminary modelling in Fig.3.9. The "upper limit" abundance of O is 1 and "lower limit" is solar. If we take metallicity -1.3 for Fe and 1 for C and O. Then our modelled [C/Fe] $\sim$ 2.3, [O/Fe] $\sim$ 2.3, [C/O] $\sim$ 0 and [Fe/H] $\sim$-1.3. If we take [O/H] $\sim$ 0, then we have [C/O] $\sim$ 1.0, [C/Fe] $\sim$ 2.3 and [O/Fe] $\sim$ 1.3. These two limit points drops in the area where CEMP appear in Fig. 3.11. However, normally the metal-poor stars are with Fe abundance [Fe/H] $\leq$ -2. However, the depletion effect has not been taken into account in this model. These will introduce uncertainties to Fe abundances, thus at this stage the assumption of the appearance of CEMP has to be confirmed.

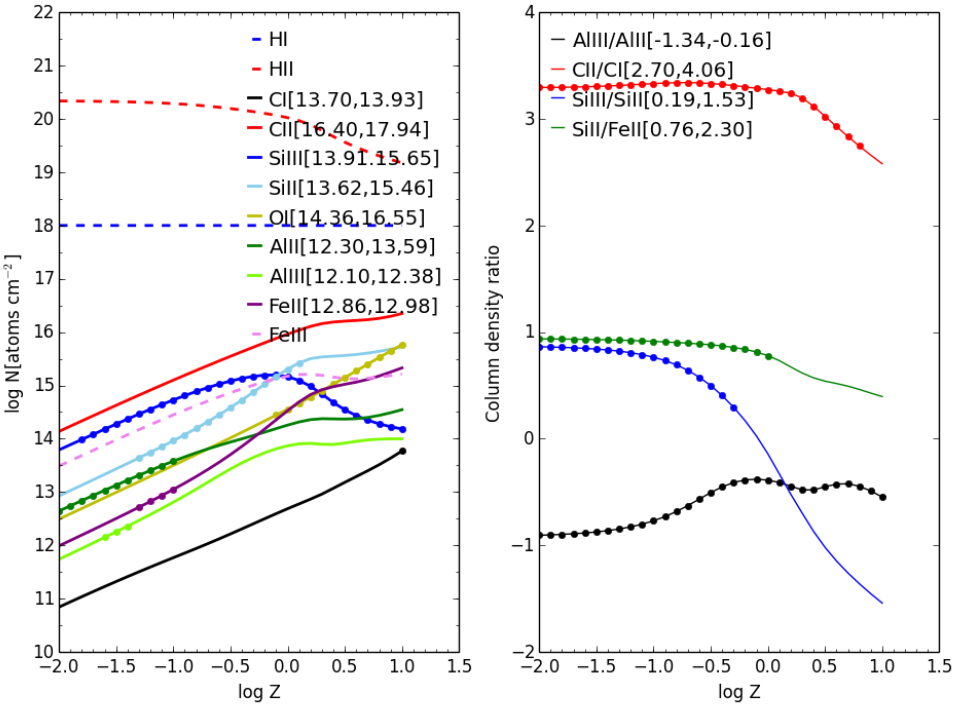

FIGURE 3.9: J1341+1853 CLOUDY model with ISM factor = -1, log n_H =-1.5. Labels are the same as Fig. 3.7.

Indeed, we are limited by the moderate resolution of this spectrum, the absolute ions column densities can not be determined accurately. Also from the moderate resolution spectrum, there is only one component. Thus the kinematic structure of the absorption system is not clear. With higher resolution data, we will see much more details in the kinematic structure which will help us to model the ions distribution. For now, we can not reach a firm conclusion about the physics of this system. We will ask for high resolution data with UVES.

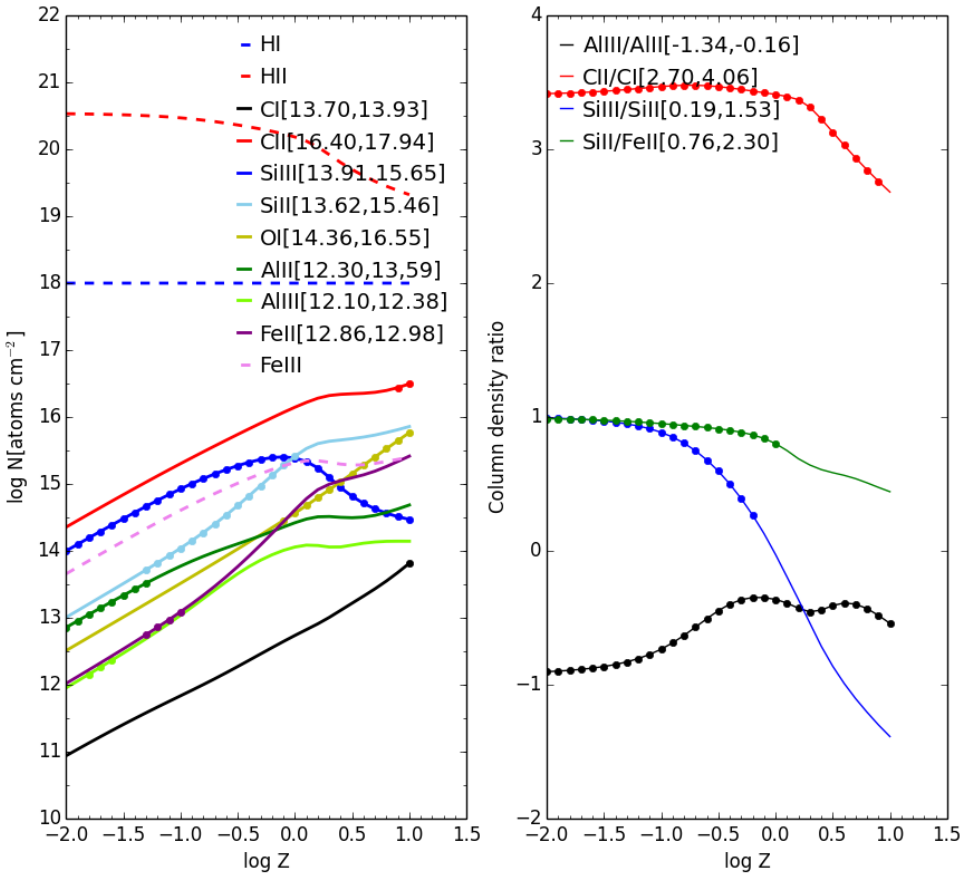

FIGURE 3.10: J1341+1853 CLOUDY model with ISM factor = -0.75, log n_H =-1.5. Labels are the same as Fig. 3.7.

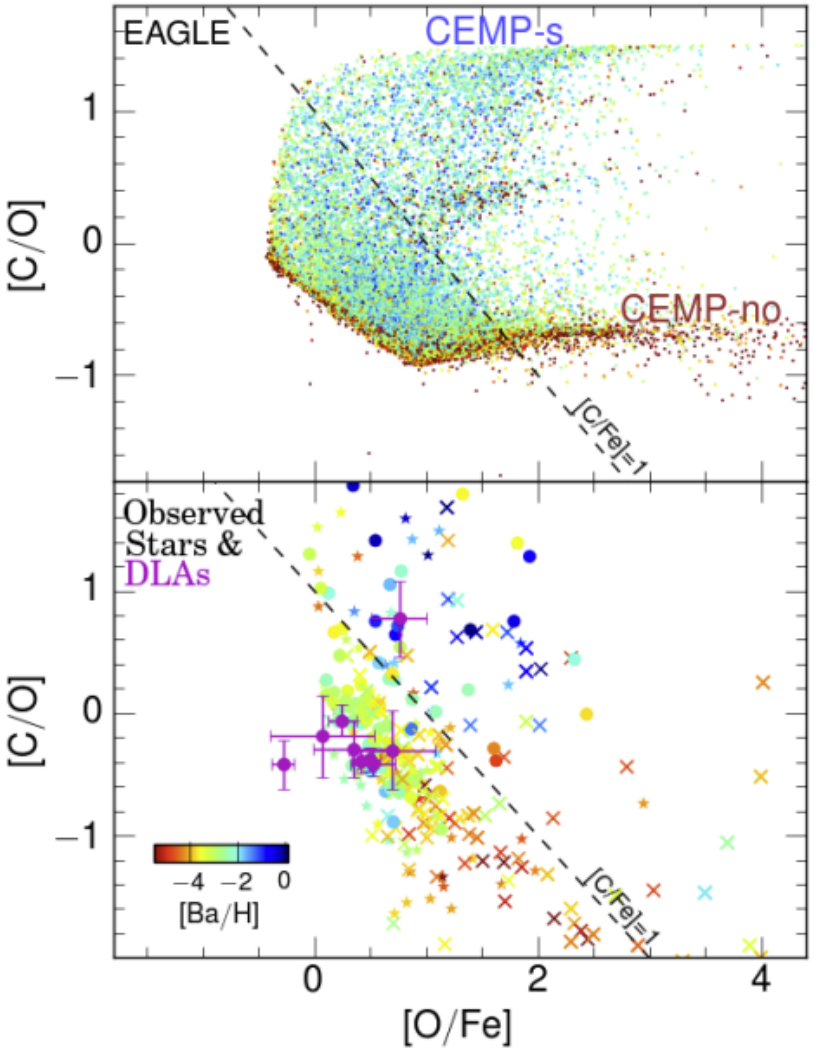

FIGURE 3.11: Adapted from Sharma et al. (2018). [C/O] as a function of [O/Fe]. Top panel: distribution of EAGLE stars that formed before $z = 6$ with cyan–green–red colour map representing the variation in [Ba/H]. Bottom panel: distribution of metal-poor MW stars with [Fe/H] <-2, taken from the SAGA data base (Suda et al. 2008). Observed stars, coloured according to their [Ba/H], are shown as circles; crosses for limits. In this panel, we also include red giants (surface gravity log10(g/(cm s^{-2})) < 3.2); they are plotted using star symbols. The [C/O] of RGB stars is a lower limit as surface carbon may be depleted due to nuclear burning. Purple symbols with error bars are DLAs data from Cooke et al. (2017)

3.2 "Ghostly" DLA – J1133-0057

This system is also a peculiar and very interesting system. In the spectrum, there is no Lyα trough observed, but clear C I absorptions. This is because the cloud is at the redshfit of the quasar and does not cover the quasar BLR completely, which makes the physics behind this system quite different than in other systems of our sample. This system has been singled out as a "ghostly" DLA and is described in details in Fathivavsari et al. (2017).

For intervening absorption systems, the absorber and the quasar are distant from each other, and the broad emission line region (BLR) of the AGN is fully covered by the absorber along the line-of-sight. But when the absorber is small, it may not fully cover the BLR. The damped Lyα trough is filled by the leak emission from the AGN BLR. This kind of quasar absorption cloud is rarely observed or has not been systematically studied previously. This cloud is towards quasar J1133-0057.

A ghostly damped Lyα system revealed by metal absorption lines ⋆

H. Fathivavsari,[1,2]† P. Petitjean[1], S. Zou[1], P. Noterdaeme[1], C. Ledoux[3], T. Krühler[4] and R. Srianand[5]

[1] *Institut d'Astrophysique de Paris, Université Paris 6-CNRS, UMR7095, 98bis Boulevard Arago, 75014 Paris, France*
[2] *School of Astronomy, Institute for Research in Fundamental Sciences (IPM), P. O. Box 19395-5531, Tehran, Iran*
[3] *European Southern Observatory, Alonso de Córdova 3107, Casilla 19001, Vitacura, Santiago 19, Chile*
[4] *Max-Planck-Institut für extraterrestrische Physik, Giessenbachstraße, D-85748 Garching, Germany*
[5] *Inter-University Centre for Astronomy and Astrophysics, Post Bag 4, Ganeshkhind, 411 007, Pune, India*

Accepted 000. Received 000; in original form 000

ABSTRACT

We report the discovery of the first 'ghostly' damped Lyα absorption system (DLA), which is identified by the presence of absorption from strong low-ion species at $z_{\rm abs} = 1.70465$ along the line of sight to the quasar SDSSJ113341.29−005740.0 with $z_{\rm em} = 1.70441$. No Lyα absorption trough is seen associated with these absorptions because the DLA trough is filled with the leaked emission from the broad emission line region of the quasar. By modeling the quasar spectrum and analyzing the metal lines, we derive $\log N({\rm H\,I})({\rm cm}^{-2}) \sim 21.0 \pm 0.3$. The DLA cloud is small (≤ 0.32 pc) thus not covering entirely the broad line region and is located at ≥ 39 pc from the central active galactic nucleus (AGN). Although the DLA is slightly redshifted relative to the quasar, its metallicity ([S/H]$=-0.41\pm0.30$) is intermediate between what is expected from infalling and outflowing gas. It could be possible that the DLA is part of some infalling material accreting onto the quasar host galaxy through filaments, and that its metallicity is raised by mixing with the enriched outflowing gas emanating from the central AGN. Current DLA surveys miss these 'ghostly' DLAs, and it would be important to quantify the statistics of this population by searching the SDSS database using metal absorption templates.

Key words: quasars: absorption lines – quasars: emission lines –quasars: individual: SDSS J113341.29−005740.0

1 INTRODUCTION

Quasars are powered by the infall of gas into the gravitational potential well of super-massive black holes, residing at the center of distant galaxies. The infall of gas occurs, preferentially, through the so-called *cold flows* along the filaments of the cosmic web (van de Voort et al. 2012) that are predicted by simulations (Martin et al. 2016). These cold flows of low metallicity gas can also feed and trigger star formation activities in the host galaxies, hence, enriching their interstellar medium (Sánchez Almeida et al. 2015). Strong AGN-driven outflows, on the other hand, are required to regulate and quench star formation activities, and also prevent overgrowth of the galaxy (and the central black hole) by ejecting the available material back into the intergalactic medium (IGM) and/or circum-galactic medium (CGM; Silk & Rees 1998; Cano-Díaz et al. 2012; Carniani et al. 2016).

Luminous quasars are capable of launching powerful and energetic outflows of gas up to very large distances. The pristine infalling gas can therefore merge with the enriched outflowing material anywhere from the innermost region of the AGN to the outermost region of the halo of the host galaxy. When the infalling and outflowing gas collide, they get mixed, shocked and compressed to a high density, probably for a short period, before getting evaporated by the incident energetic outflows (Namekata, Umemura & Hasegawa 2014). If a line of sight to the central AGN passes through this shocked material, one would expect to detect a strong H I absorption in the spectrum with $N({\rm H\,I}) > 10^{17}$ cm^{-2} at the redshift of the quasar (van de Voort et al. 2012; Finley et al. 2013; Fathivavsari et al. 2015, 2016).

Since the gas is compressed to a very small size, it may

⋆ Based on data obtained with XSHOOTER on the ESO-VLT; Prgm. 084.A-0699(A).

† E-mail: h.fathie@gmail.com

not fully cover the broad emission line region (BELR) of the quasar. Therefore, for any given neutral hydrogen column density, there could be a combination of the cloud projected angular size and its relative velocity from the AGN for which the partial coverage is such that the leaked emission from the Lyα BELR could almost fully fill the strong (or damped) Lyα absorption trough. If this happens, one would not detect the corresponding Lyα absorption in the quasar spectrum. So far, no such combination of DLA size and relative velocity (from the AGN) has ever been found along quasars' sightlines. For the first time, in this letter, we report the discovery of such a ghostly DLA cloud along the line of sight to the quasar SDSS J113341.29−005740.0 (here after J1133−0057). The presence of this DLA is revealed through the detection of absorption lines from neutral (e.g. C I or Na I) and low-ion species associated with it. This absorber is part of the Ledoux et al. (2015) sample. These authors systematically looked for C I absorption in the Sloan Digital Sky Survey (SDSS) quasar spectra in a search for cold gas at high redshift. We show that the cloud is compressed to a very small size, and is located very close to the central AGN. We argue that proximity to the quasar's central engine, and small physical dimension are the common characteristics of ghostly DLAs.

Ghostly DLAs are important objects as (by definition) they always show signature of negligible covering factor of at least the Lyα BELR, and probably probe the innermost regions of the AGNs. Current surveys of DLAs miss this class of objects as their employed techniques to find DLAs rely at least partly on the fact that the residual flux at the bottom of the DLA reaches zero intensity (Prochaska & Herbert-Fort 2004; Noterdaeme et al. 2009), which is not the case in this new class of DLAs. Therefore, we might actually be witnessing the tip of an iceberg as new techniques based on metal absorption line templates would probably find more of these ghostly DLAs in the SDSS spectroscopic database.

2 OBSERVATION

The spectrum of the quasar SDSS J1133−0057 was taken on 2011 January 7, using the XSHOOTER spectrograph (Vernet et al. 2011) mounted on the Very Large Telescope in the course of a program to search for cold gas using neutral carbon (see Ledoux et al. 2015 for more details). The spectrum covers the wavelength range from 3000 Å to 2.5 μm with the nominal resolving power of R = 4350, 7450, and 5300 in the UVB, VIS, and NIR arms, respectively, corresponding to slit widths of 1.0, 0.9 and 0.9 arcsec. We used the ESO pipeline v2.5.2 to reduce the raw spectrum. The $11''$-long slit of the spectrograph provided us with enough spatial pixels free of quasar emission, to perform optimal sky subtraction. Arc lamp spectra were used for wavelength calibration, and the spectrum of a standard star observed during the same night was used to flux calibrate the spectrum.

3 A GHOSTLY DLA

We detect a metal absorption line system in the spectrum of the quasar J1133−0057, with an absorption redshift coincident with the emission redshift of the quasar. The presence of species like C I, Cl I, Mg I, and especially Na I suggests that the absorber has a high neutral hydrogen column density and is probably a DLA (Petitjean et al. 2000). However, as shown in Fig. 1, no apparent DLA absorption line is detected in the spectrum at the redshift of the low ion species, i.e. $z_{\rm abs} = 1.70465$. If one assumes that the Lyα BELR of the quasar is only partially covered by the DLA, then the leaked Lyα emission from the BELR could fill the DLA absorption trough and prevent direct detection. We show below that this is indeed the case, and we demonstrate that the shallow absorption dip seen around 3300 Å in the spectrum is actually a ghostly signature of an otherwise strong DLA absorption (see section 3.2). This shallow absorption feature allows us to constrain the H I column density of this elusive DLA.

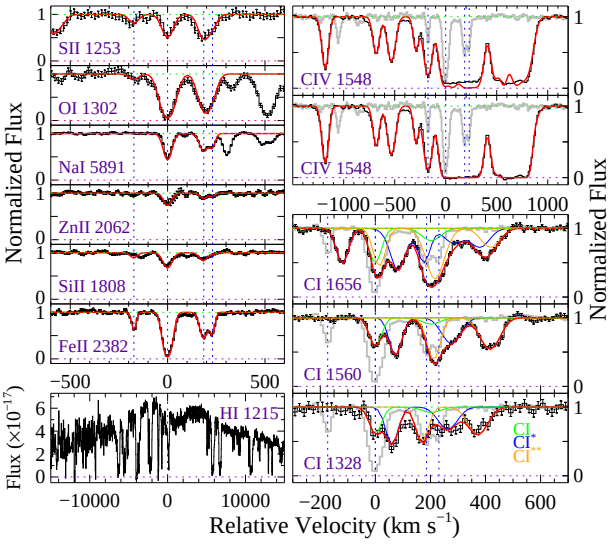

Figure 1. Velocity plots and VPFIT solutions for the absorption lines of the low and high ion species detected in the ghostly DLA. The origin of the velocity scale is at $z_{\rm abs} = 1.70465$. The grey curve in the C I and C IV panels is the Fe II λ2382 absorption profile. Note that no strong Lyα absorption is seen at the redshift of the low ionization lines in the Lyα velocity panel. The upper (resp. lower) C IV panel shows the result before (resp. after) taking the partial coverage effect into account.

3.1 Quasar emission lines

We detect [O II]λ3728, Lyα, Hα, Hβ, and Hγ emission lines associated with the quasar, as shown in Fig. 2. A Gaussian function fitted to the [O II] emission line doublet gives $z_{\rm em} = 1.70441 \pm 0.00011$, which is adopted as the systemic redshift of the quasar. We simultaneously fit a 2-component Gaussian function on the hydrogen Balmer emission lines, and obtain $z_{\rm N} = 1.70668 \pm 0.00002$, FWHM$_{\rm N} = 2344$ km s^{-1} and $z_{\rm B} = 1.70272 \pm 0.00005$, FWHM$_{\rm B} = 6048$ km s^{-1} as the redshift and FWHM of the narrow and broad components of the fit, respectively (see Fig.2).

3.2 Reconstructing the DLA absorption profile

As mentioned earlier, the DLA absorption trough is almost completely filled with the leaked emission from the BELR

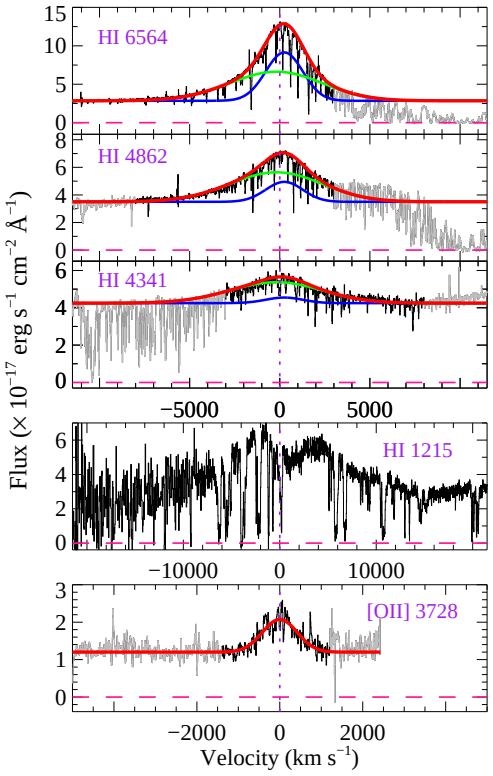

Figure 2. Velocity plots and Gaussian function fits (where applicable) to the Hα, Hβ, Hγ, Lyα and [O II] emission lines. The H-Balmer lines are fitted simultaneously with two Gaussian components shown by the green and blue curves in their corresponding panels. Note again that no DLA absorption profile is seen in the H I λ1215 panel. The origin of the velocity plot is at $z_{[\rm O\,II]} = 1.70441$. Regions shown in grey are excluded from the fit.

of the quasar. In this section, we model the Lyα and N V emission lines from the BELR, and predict the amount of neutral hydrogen that is needed to reproduce the shape of the observed spectrum in the Lyα spectral region. In our models, we assume that the Lyα and N V emission lines are each composed of a narrow and a broad component, similar to what is seen for H-Balmer lines (see section 3.1). During calculations, the redshift of the DLA is fixed to the value obtained for the main component of the low-ion species ($z_{\rm abs} = 1.70465$). Below, we briefly explain how the reconstruction is performed.

First, we define the quasar's reddened continuum as a power law function with $\alpha = +1.5$. The power law index, α, is obtained by fitting the quasar continuum observed at 3700, 4300, and 4660 Å. The broad component of Lyα (dashed green curve in Fig. 3) and N V (dashed pink curve) BEL are then added to this continuum to produce the spectrum seen by the DLA cloud. The resulting spectrum after passing through the DLA is shown as a blue curve in Fig. 3. Here, we assume that the covering factor of the broad component of these emission lines is 1.0. The final simulated spectrum, which is shown as a red curve in Fig. 3, is obtained by adding to the blue curve the narrow components of the Lyα and N V BEL profiles, which are assumed to have covering factor of 0.0.

We first tried to reconstruct the observed spectrum with the maximum number of fixed parameters. The result is shown in the left panel of Fig. 3, and the parameters of the fit are listed in the third column of Table 1. In this model, the redshifts and the widths of the emission lines were fixed to those of the H-Balmer lines. The H I column density and the amplitude of the emission lines are the only free parameters in this model. The final fit, which is shown as a red curve in the left panel of Fig. 3, has a reduced chi-square of $\chi^2_{\rm red} = 16.25$ and does not match the observed spectrum very well especially near the blue wing of the Lyα emission line. We, therefore, tried to construct a second model in which we also relax the redshift and the width of the BLR Lyα emission line components. The result of this new model, which now fits the observed spectrum more satisfactorily with $\chi^2_{\rm red} = 0.47$, is shown in the right panel of Fig. 3, and the parameters of the fit are listed in the fourth column of Table 1. This model converges with $\log N({\rm H\,I}) = 21.0$. We also checked that H I column densities smaller than 20.70 and larger than 21.30 results in fits with large $\chi^2_{\rm red}$. Therefore, in this work, we adopt $\log N({\rm H\,I}) = 21.0 \pm 0.3$. We emphasize that the H I column density is not very sensitive to the choice of the free parameters, thanks to the presence of the shallow dip seen around 3300 Å, which strongly constrains the H I column density to be $\sim 10^{21}$cm^{-2}.

Table 1. Parameters of the two models constructed to explain the observed spectrum in the Lyα emission line spectral region. Log N(H I): H I column density of the DLA. $z_{\rm DLA}$: redshift of the strongest component of the low-ion species. $F_{\rm Ly\alpha}$: peak flux of the broad component of the Lyα emission line profile in 10^{-17} erg s^{-1} cm^{-2} Å^{-1}. $Q_{\rm Ly\alpha}$: ratio of the peak flux of the narrow component to that of the broad component of the Lyα emission line profile. $F_{\rm NV}$: peak flux of the broad component of the N V emission line profile, with the same unit as $F_{\rm Ly\alpha}$. $Q_{\rm NV}$: ratio of the peak flux of the narrow component to that of the broad component of the N V emission line profile. $z^{\rm B}_{\rm Ly\alpha}$ and $z^{\rm N}_{\rm Ly\alpha}$: redshifts of the broad and narrow components of the Lyα emission. $z^{\rm B}_{\rm NV}$ and $z^{\rm N}_{\rm NV}$: redshifts of the broad and narrow components of the N V emission. FWHM$^{\rm B}_{\rm Ly\alpha}$ and FWHM$^{\rm N}_{\rm Ly\alpha}$: velocity widths of the broad and narrow components of the Lyα emission. FWHM$^{\rm B}_{\rm NV}$ and FWHM$^{\rm N}_{\rm NV}$: velocity widths of the broad and narrow components of the N V emission. All velocity widths are given in km s^{-1}.

		Model(1)	Model(2)
1	$\log N({\rm H\,I})$	21.1 ±0.30	21.0 ±0.30
2	$z_{\rm DLA}$	1.70465	1.70465
3	$F_{\rm Ly\alpha}$	11.75	5.46
4	$Q_{\rm Ly\alpha}$	0.51	1.07
5	$F_{\rm NV}$	0.99	0.63
6	$Q_{\rm NV}$	1.06	0.00
7	$z^{\rm B}_{\rm Ly\alpha}$	1.70272	1.70159
8	$z^{\rm N}_{\rm Ly\alpha}$	1.70668	1.70241
9	$z^{\rm B}_{\rm NV}$	1.70272	1.70272
10	$z^{\rm N}_{\rm NV}$	1.70668	1.70668
11	FWHM$^{\rm B}_{\rm Ly\alpha}$	6048	10550
12	FWHM$^{\rm N}_{\rm Ly\alpha}$	2344	3180
13	FWHM$^{\rm B}_{\rm NV}$	6048	6048
14	FWHM$^{\rm N}_{\rm NV}$	2344	2344

3.3 Elemental abundances and depletion

In this DLA, we detect metal absorption lines from O I, O I**, Si II, Si II*, C I, C I*, C I**, C II, C II*, S II, Fe II, Zn II, Al II,

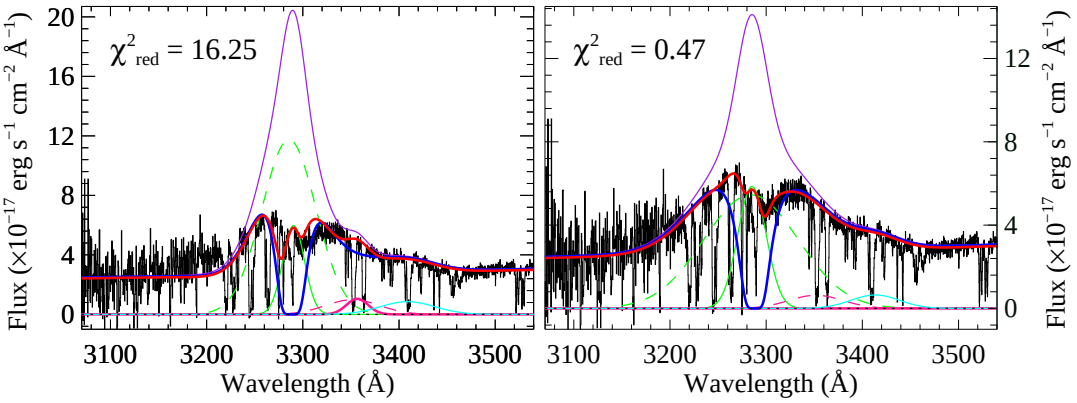

Figure 3. Reconstruction of the observed spectrum around the Lyα emission line spectral region. *Left panel*: spectrum corresponding to model(1) in Table 1. The dashed (resp.solid) green and pink curves are the broad (resp. narrow) components of the BLR Lyα and N v emission lines, respectively. The cyan curve shows the Si II emission line of the quasar, and the purple curve is the combination of the quasar continuum and all green, pink and cyan curves. The blue curve shows the combination of the quasar continuum, the dashed green and pink curves, and a DLA absorption profile with $\log N(\mathrm{H\,I}) = 21.1$. Combining the blue line with the solid green, pink and cyan curves gives the final fit, which is overplotted on the observed spectrum as a red curve. *Right panel*: the lines are the same as in the left panel. In contrast with the model shown in the left panel, in this model, the redshifts and the widths of the broad and narrow components of the Lyα BELR are free parameters (i.e. model(2) of Table 1). The H I column density in this model is $\log N(\mathrm{H\,I}) = 21.0$.

Al III, Mg I, Mg II, Ca II, Na I, Cl I, C IV, Si IV, and N V. The velocity plots and VPFIT (Carswell & Webb 2014) solutions for some important transitions are shown in Fig. 1 and the derived total column densities are listed in Table 2. We used the same technique as in Fathivavsari et al. (2013) to fit the absorption lines. We simultaneously fit five Fe II transitions to derive the redshifts and the Doppler b-parameters of individual components. The fits to the other low-ion transitions were conducted by fixing the redshifts and the b-values to those obtained for Fe II. The metallicity of the DLA is $[\mathrm{S/H}] = -0.41 \pm 0.30$ and $[\mathrm{Zn/H}] = -0.36 \pm 0.30$. The abundance of iron relative to sulphur and Zinc (i.e. $[\mathrm{Fe/S}] = -1.93 \pm 0.10$, $[\mathrm{Fe/Zn}] = -1.98 \pm 0.10$) suggests that the heavy elements are highly depleted onto dust grains. Indeed, the quasar continuum is strongly reddened. Solar photospheric abundances used here were taken from Asplund et al. (2009).

3.4 Partial coverage

The flat-bottomed structure of the C IV absorption profiles suggests that they are saturated. However, as shown in Fig. 1, the residual flux at the bottom of the profiles does not reach zero intensity, implying that the C IV absorber may not be fully covering the C IV BELR of the quasar. In the upper C IV panel in Fig. 1, we show that it is not possible to fit the observed spectrum without correcting for partial coverage. Indeed, after correcting for the residual flux, we could successfully fit the observed spectrum (see the lower C IV panel in Fig. 1). The subtracted residual flux amounts to about 7.5 per cent of the continuum and BLR emission. This implies that $\sim$ 19 per cent of the C IV BELR is not covered by the C IV phase of the cloud.

In our spectrum, we also detect absorption from C I multiplets associated with the DLA in three different spectral regions, with one multiplet (i.e. C I λ1560) located on the red wing of the quasar C IV emission line. As shown in Fig. 1, we could successfully conduct a 2-component fit on the C I multiplet transitions without invoking partial coverage. This may imply that the C I-bearing gas fully covers the BELR of the quasar at the corresponding velocity. However, we checked that even if we remove residual flux of up to 10 per cent from the bottom of the C I λ1560 absorption lines, we could still consistently fit the C I multiplet transitions, without increasing the $\chi^2_{\rm red}$ of the fit by more than 5 per cent. Therefore, the observed C I multiplet absorption lines are *not* inconsistent with the presence of partial coverage. Higher spectral resolution would allow a deeper investigation of this issue.

Table 2. Column densities (in cm^{-2}) of some important species in logarithmic units. The uncertainty on the column densities from the fits are about 0.1 dex.

S II	Fe II	Zn II	Si II	O I	Na I	C I	C I*	C I**
15.71	14.16	13.20	15.63	$\geq$16.48	12.94	14.30	14.76	14.74

4 CONSTRAINING THE DLA LOCATION AND SIZE FROM FINE STRUCTURE LINES

Partial coverage of the Lyα BELR along this line of sight implies that the cloud transverse size should be smaller than the projected size of the BELR whose typical size is of the order of $\sim$1 pc (Kaspi et al. 2005). Below, we constrain the DLA size using the physical state of the gas derived from the observation of the C I fine structure transitions.

The observed column density ratios of the C I multiplet populations detected in the DLA are $N(\mathrm{C\,I^*})/N(\mathrm{C\,I}) \sim 2.88$ and $N(\mathrm{C\,I^{**}})/N(\mathrm{C\,I}) \sim 2.75$. The high values of these ratios imply that the fine structure states are thermalized in the cloud. As shown in figure 11 of Jorgenson et al. (2010), the level populations at low densities (i.e. $n_{\rm HI} < 1000$ cm^{-3}) depend on the strength of the incident radiation field, J_ν. We extend their calculations to higher values of J_ν and find that to match the observations, a radiation field with an intensity

of $J_\nu = 1.4 \times 10^{-16}$ erg s^{-1} cm^{-2} Hz^{-1} sr^{-1} is needed. On the other hand, if the density of the gas is high enough (e.g. $n_{\rm HI} > 1000$ cm^{-3}), then collisional excitation alone will be sufficient to thermalize the system. In this case, the presence of the incident radiation field will have no further effect on the population of the fine structure states.

If J_ν were known, this would in principle allow us to constrain the density, $n_{\rm HI}$. Here, we follow the technique introduced by Wolfe et al. (2003 ; see also Srianand et al. 2005), using the C II* optical depth, to estimate an upper limit to the intensity of the radiation field, J_ν, to which the DLA gas is exposed. Since C II and C II* absorption lines are saturated in the spectrum, we assume [C/H] = [S/H] and obtain $\log N({\rm C\,II}) = 17.02$. We further assume $N({\rm C\,II^*})/N({\rm C\,II}) \leq 2.0$ (see upper panel of figure 4 in Silva & Viegas 2002) and get $\log N({\rm C\,II^*}) \leq 17.32$. The radiation field intensity, J_ν, is determined by assuming a steady state condition and equating the heating rate, Γ, with the cooling rate, l_c. The heating rate is given by

$$\Gamma = 10^{-5}\,\kappa\,\epsilon\,J_\nu \qquad {\rm erg\ s^{-1}\ H^{-1}} \tag{1}$$

where κ is the dust-to-gas ratio, ϵ, the grains heating efficiency, and J_ν, the intensity of the radiation field in erg s^{-1} cm^{-2} Hz^{-1} sr^{-1}. The dust-to-gas ratio is calculated using equation 7 of Wolfe et al. (2003). With minimal depletion model, we get $\kappa_1 = 0.30$ while maximal depletion model results in $\kappa_2 = 0.48$. In this work, we adopt the mean value of $\kappa = 0.39$. Depending on the temperature of the cloud, the grains heating efficiency, ϵ, varies between 0.05 and 0.09 (Bakes & Tielens 1994; Wolfire et al. 1995, see their figure 1). Adopting $\epsilon = 0.07$ as in Wolfe et al. (2008) , and using equation 1, we obtain the heating rate as $\Gamma = 2.73 \times 10^{-7}\,J_\nu$. The cooling rate, on the other hand, is $l_c = 2.89{\times}10^{-20} N({\rm C\,II^*})/N({\rm H\,I}) \sim 7.59 \times 10^{-24}$ erg s^{-1} H^{-1}. By equating the cooling rate with the heating rate, we get $J_\nu \leq 2.78 \times 10^{-17}$ erg s^{-1} cm^{-2} Hz^{-1} sr^{-1} as an upper limit to the intensity of the radiation field that is impinging upon the DLA cloud. This value of J_ν is $\sim$5 times lower than what is needed to thermalize the C I fine structure levels (see above), implying that these fine structure states are thermalized predominantly through collisional excitation.

With the above limit on J_ν, the observed $N({\rm C\,I^*})/N({\rm C\,I})$ and $N({\rm C\,I^{**}})/N({\rm C\,I})$ ratios can be reproduced *only* when $n_{\rm HI} > 1000$ cm^{-3}. This results in a characteristic size of the cloud of $l = N({\rm H\,I})/n_{\rm HI} \lesssim 0.32$ pc. One can also use the quasar luminosity, L_ν ($=2.28 \times 10^{27}$ erg s^{-1} Hz^{-1}), to derive from the upper value on J_ν a lower limit of $d \geq 66$ pc for the DLA-quasar separation.

Grains in the DLA clouds are mainly heated by photons with energy $h\nu = 6{-}13.6$ eV (Wolfe et al. 2003). As these photons can reach deeper into the cloud, they are absorbed by dust. When this extinction by dust grains is taken into account, the lower limit to the DLA-quasar separation decreases to $d \geq 39$ pc.

5 SUMMARY AND CONCLUSIONS

We reported the discovery of the first ghostly DLA found along the line of sight to the quasar SDSS J1133−0057. No Lyα absorption line is seen in the quasar spectrum at the redshift of the detected low-ion species such as C I, Na I, Ca II, etc because the leaked emission from the Lyα BELR fills the DLA absorption trough. The DLA cloud is small ($\leq$0.32 pc), and is located at $d \geq 39$ pc from the central AGN thus not covering entirely the broad line region.

Interestingly, this ghostly DLA has characteristics similar to those of the 'eclipsing' DLA found along the line of sight to the quasar J0823+0529 (Fathivavsari et al. 2015). Both DLAs have very small sizes and are located close to the central AGN. However, in contrast to the newly found ghostly DLA, the eclipsing DLA towards J0823+0529 shows strong DLA absorption profile in the quasar spectrum. This implies that the eclipsing DLA, with a transverse size of $2.3 \leq l({\rm H\,I}) \leq 9.1$ pc, blocks most of the radiation emitted by the quasar BELR. Because of the sub-parsec size of the ghostly DLA, most emission from the quasar Lyα BELR is freely passing by the DLA and consequently filling the DLA absorption trough, resulting in the observed spectral profile shown in Fig. 3. It could be possible that the two (ghostly and eclipsing) DLAs are from the same population and are just two stages of the same flow. Eclipsing DLAs could turn into ghostly DLAs as strong outflowing material from the central AGN strikes and compresses them into clouds of smaller size and higher density. Statistical study of a large sample of ghostly and eclipsing DLAs would in principle allow us to confirm whether there is any connection between the two absorbers, and what importance they have over the whole DLA population.

REFERENCES

Asplund, M., Grevesse, N. et al., 2009, ARA&A, 47, 481
Bakes, E. L. O., Tielens, A. G. G. M., 1994, ApJ, 427, 822
Cano-Díaz, M., Maiolino, R. et al., 2012, A&A, 537,8
Carniani, S. et al., 2016, A&A, 591, 28
Carswell R.F., Webb J. K., 2014, VPFIT, Astrophysics Source Code Library ascl:1408.015
Fathivavsari, H., Petitjean, P. et al., 2013, MNRAS, 435, 1727
Fathivavsari, H., Petitjean, P. et al., 2015, MNRAS, 454, 876
Fathivavsari, H., Petitjean, P. et al., 2016, MNRAS, 461, 1816
Finley, H. et al., 2013, A&A, 558, 111
Jorgenson, R. A. et al., 2010, ApJ, 722, 460
Kaspi, S. et al., 2005, ApJ, 629, 61
Ledoux, C., Noterdaeme, P. et al., 2015, A&A, 580, 8
Martin, D. C. et al., 2016, ApJ, 824, 5
Namekata, D., Umemura, M., Hasegawa, K., 2014, MNRAS, 443, 2018
Noterdaeme, P., Petitjean, P. et al., 2009, A&A, 505, 1087
Petitjean, P., Aracil, B. et al., 2000, A&A, 359, 457
Prochaska, J. X., Herbert-Fort, S., 2004, PASP, 116, 622
Sánchez Almeida, J., Elmegreen, B. G. et al., 2015, ApJ, 810, 15
Silk, J., Rees, M. J., 1998, A&A, 331, 1
Silva, A. I., Viegas, S. M., 2002, MNRAS, 329, 135
Srianand, R., Petitjean, P. et al., 2005, MNRAS, 362, 549
van de Voort, F., Schaye, J. et al, 2012, MNRAS, 421, 2809
Vernet, J. et al., 2011, A&A, 536, 105
Wolfe, A. M., Prochaska, J. X., Gawiser, E., 2003, ApJ, 593, 215
Wolfe, A. M. et al., 2008, ApJ, 681, 881
Wolfire, M. G. et al., 1995, ApJ, 443, 152

This paper has been typeset from a TEX/LATEX file prepared by the author.

Chapter 4

Project II: Molecular gas

In this chapter we will introduce the work has been done on the molecular gas in this sample. The molecular gas fraction in the ISM is found to be less than 10% in the DLAs (Srianand et al. 2005). Direct detection of H_2 at high redshift is not easy (see however Balashev et al. 2014 and Balashev & Noterdaeme 2018). Since our sample is a blind C I sample without any pre-assumption on the molecular gas, thus we will derive the association between C I absorption and H_2 absorption. Also, in section 2.1.2, we already discussed about the high dust-to-gas ratio in our sample which indicates high probability of molecular gas existence. In the following paper Noterdaeme et al. (2018), H_2 has been detected in all the systems within our detection limit. The detail is seen below.

Astronomy & Astrophysics manuscript no. CImol
January 29, 2018

Spotting high-z molecular absorbers using neutral carbon

Results from a complete spectroscopic survey with the VLT ⋆

P. Noterdaeme[1,⋆⋆], C. Ledoux[2], S. Zou[1], P. Petitjean[1], R. Srianand[3], S. Balashev[4], and S. López[5]

[1] Institut d'Astrophysique de Paris, CNRS-UPMC, UMR7095, 98bis boulevard Arago, F-75014 Paris, France
[2] European Southern Observatory, Alonso de Córdova 3107, Vitacura, Casilla 19001, Santiago 19, Chile
[3] Inter-University Centre for Astronomy and Astrophysics, Post Bag 4, Ganeshkhind, 411 007, Pune, India
[4] Ioffe Institute, Polyteknicheskaya 26, 194021 Saint-Petersburg, Russia
[5] Departamento de Astronomía, Universidad de Chile, Casilla 36-D, Santiago, Chile

Received/Accepted

ABSTRACT

While molecular quasar absorption systems provide unique probes of the physical and chemical properties of the gas as well as original constraints on fundamental physics and cosmology, their detection remains challenging. Here we present the results from a complete survey for molecular gas in thirty-nine absorption systems selected solely upon the detection of neutral carbon lines in SDSS spectra, without any prior knowledge of the atomic or molecular gas content. H_2 is found in all twelve systems (including seven new detections) where the corresponding lines are covered by the instrument setups and measured to have $\log N(H_2) \gtrsim 18$, indicating a self-shielded regime. We also report seven CO detections (7/39) down to $\log N(CO) \sim 13.5$, including a new one, and put stringent constraints on N(CO) for the remaining 32 systems. N(CO) and N(C I) are found to be strongly correlated with $N(CO)/N(C\,I) \sim 1/10$. This suggests that the C I-selected absorber population is probing gas deeper than the H I-H_2 transition in which a substantial fraction of the total hydrogen in the cloud is in the form of H_2. We conclude that targeting C I-bearing absorbers is a very efficient way to find high-metallicity molecular absorbers. However, probing the molecular content in lower metallicity regimes as well as high column density neutral gas remains to be undertaken to unravel the processes of gas conversion in normal high-z galaxies.

Key words. ISM: molecules - quasars: absorption lines

1. Introduction

The detection and analysis of molecular absorption lines along the lines of sight to background light sources has proven to be an extremely useful tool to investigate the physical and chemical state of the interstellar medium (ISM) thanks to the sensitive formation, destruction and excitation processes of molecules. Such technique applies from the Solar neighbourhood towards nearby stars (e.g. Savage et al. 1977; Boissé et al. 2013) to the gas in and around high redshift galaxies revealed by Damped Lyman-α systems (DLAs) (e.g. Levshakov et al. 1989; Ge et al. 1997; Petitjean et al. 2000; Cui et al. 2005; Srianand et al. 2005; Noterdaeme et al. 2008; Jorgenson et al. 2010; Carswell et al. 2011; Balashev et al. 2017). In addition, the detection of molecular species at high-redshift provides original and sensitive probes of fundamental physics and cosmology. Tiny shifts in the relative wavelengths of H_2 Lyman and Werner lines can be used to constrain the possible space-time variation of the proton-to-electron mass ratio down to a few parts-per-million over a timescale of Gyrs (see Ubachs et al. 2016, and references therein). The excitation of CO rotational levels provides in turn one of the best thermometers for measuring the temperature of the cosmic microwave background (CMB) radiation at high redshift (Srianand et al. 2008; Noterdaeme et al. 2011). Last but not least, the molecular phase of the ISM makes the link between the gas accreted onto galaxy and its gravitational collapse that gives birth to stars. However, the small number of known molecular absorbers contrasts with the huge number of DLAs detected so far (e.g. Prochaska et al. 2005; Noterdaeme et al. 2012): only about 25 confirmed high-redshift H_2-bearing DLAs have been reported to date (see Balashev et al. 2017 and references therein), highlighting the small covering factor of the molecular gas and the need of efficient selection techniques.

In the local ISM, early works using Copernicus showed that H_2 and neutral carbon (C I) were frequently observed in the same absorption systems (e.g. Liszt 1981). Despite the high abundance of carbon, it is usually found in ionised forms in high-redshift DLAs and the neutral carbon is see only in a small fraction of DLAs that also show H_2 absorption (e.g. Ge et al. 2001; Srianand et al. 2005). This is likely due to the first ionisation potential of carbon (11.26 eV) being close to the energy of Lyman-Werner photons that

⋆ Based on observations and archival data from the European Southern Observatory (ESO) prog. IDs 060.A-9024, 072.A-0346, 278.A-5062, 080.A-0482, 080.A-0795, 081.A-0242, 081.A-0334, 082.A-0544, 082.A-0569, 083.A-0454, 084.A-0699, 086.A-0074 and 086.A-0643. using the Ultraviolet and Visual Echelle Spectrograph (UVES) and X-shooter at the Very Large Telescope (VLT), on Cerro Paranal, Chile.

⋆⋆ email: noterdaeme@iap.fr

lead to H_2 dissociation (through Solomon process, see e.g. Stecher & Williams 1967). C I also conveniently produces absorption lines out of the Lyman-α forest that can be identified even at low spectral resolution. We have therefore performed the first blind survey for neutral carbon lines in quasar spectra from the Sloan Digital Sky Survey (Ledoux et al. 2015), without any prior knowledge of the associated atomic and molecular content. The 66 C I candidates constitute our parent sample. We report here on the complete follow up of this sample with the Ultraviolet and Visual Echelle Spectrograph (UVES) at a resolving power $R \sim 50\,000$ and the X-Shooter spectrograph ($R \sim 5000$) at the Very Large Telescope.

2. Observations and Results

We obtained spectra for almost all systems that are observable from Paranal Observatory, i.e. a sample of thirty nine confirmed C I absorbers. Details about the observing procedures, data reduction, and metal line measurements are presented in Ledoux et al. (in prep). A near-infrared study of the Na I and Ca II lines as well as the dust extinction properties are presented in Zou et al. (submitted). Here, we focus on the detection of H_2 and CO. Wavelengths and oscillator strengths for H_2 and CO lines are from the compilations of Malec et al. (2010) and Daprà et al. (2016), respectively.

2.1. Molecular hydrogen

We detect H_2 absorption lines whenever covered by our spectra (twelve systems). Five of these are already reported in the literature (Noterdaeme et al. 2007; Srianand et al. 2008; Jorgenson et al. 2010; Noterdaeme et al. 2010; Klimenko et al. 2016), from which we have taken the H_2 column densities, and seven are new detections. We estimated the total H_2 column densities for the new detections through Voigt-profile fitting, focusing on the low rotational levels that contain most of the H_2. We note that while the velocity profile of singly ionised metals is wide with a large number of components, we detect H_2 only at velocities where C I is also detected. Below we comment on each system, in order of increasing right ascension of the background quasar.

J091721+015448, $z_{\rm abs} = 2.107$

This system was observed with X-shooter at a spectral resolution of $\sim$60 km s^{-1}. We obtain an accurate measurement of the total H_2 column density thanks to the damping wings that are seen for the low rotational levels in the four bands covered by our spectrum (see Fig. 1) and obtain $\log N(H_2) = 20.11 \pm 0.06$.

J111756+143716, $z_{\rm abs} = 2.001$

This system is characterised by two narrow H_2 components seen in the UVES spectrum (Fig. 2) in different rotational levels. These components also correspond to those seen in the neutral carbon lines. While our best-fit value is found to be around $\log N(H_2) \sim 18$, we note that the data quality is poor and that only one band is covered, making it impossible to assess the presence of blends. In addition, at such

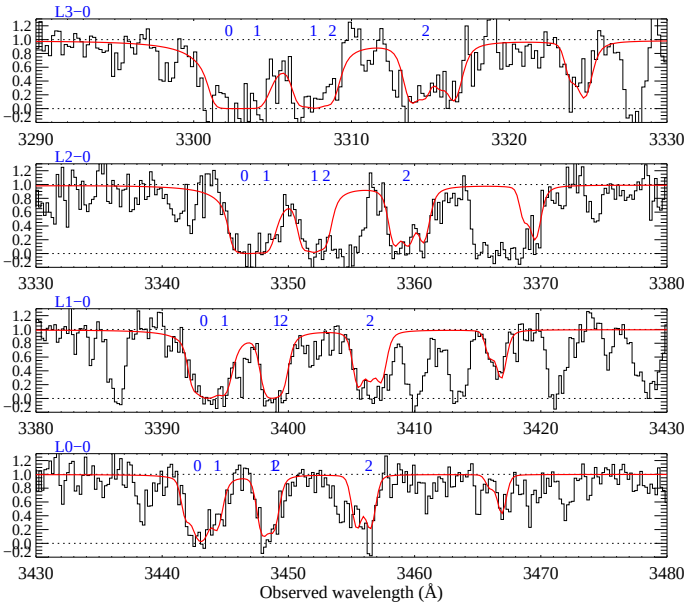

Fig. 1. Selected regions of the X-Shooter spectrum of J0917+0154 featuring H_2 lines. The rotational levels J=0 to J=2 are indicated in blue above their corresponding absorption line and the label above each panel indicates the band they belong to. Higher rotational levels are fitted but not labelled to avoid overcrowding the figure.

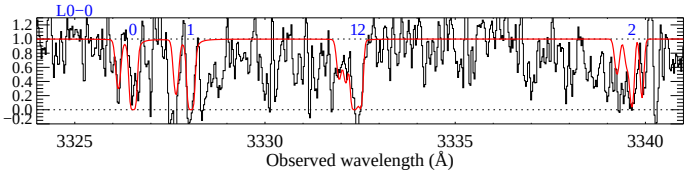

Fig. 2. Same as Fig. 1 for the UVES spectrum of J1117+1437.

column density, the absorption is in the logarithmic part of the curve of growth. We are therefore unable to associate an uncertainty to this measurement that we display with a large arbitrary (albeit quite conservative) 1 dex error bar in Fig. 9.

J131129+222552, $z_{\rm abs} = 3.092$

Thanks to the high absorption redshift, no less than twenty Lyman and Werner H_2 bands are covered by our UVES spectrum, shown on Fig. 3. Four components can be distinguished in the high rotational levels but lines from the $J = 0$ and $J = 1$ rotational levels are strongly damped and therefore modelled using a single component. The damping wings together with the large number of detected transitions and the high achieved S/N allows a very accurate measurement of the *total* H_2 column density which we found to be $\log N(H_2) = 19.69 \pm 0.01$.

J164610+232922, $z_{\rm abs} = 1.998$

While the S/N of our UVES spectrum in the region of H_2 lines (see Fig. 4) is quite low[1], two narrow H_2 components are clearly seen in rotational levels J = 0-3 and our spec-

[1] Although SDSS J164610+232922 is a relatively bright quasar ($g = 18.5$), only a single 4000 s exposure could be obtained at a high airmass (1.7).

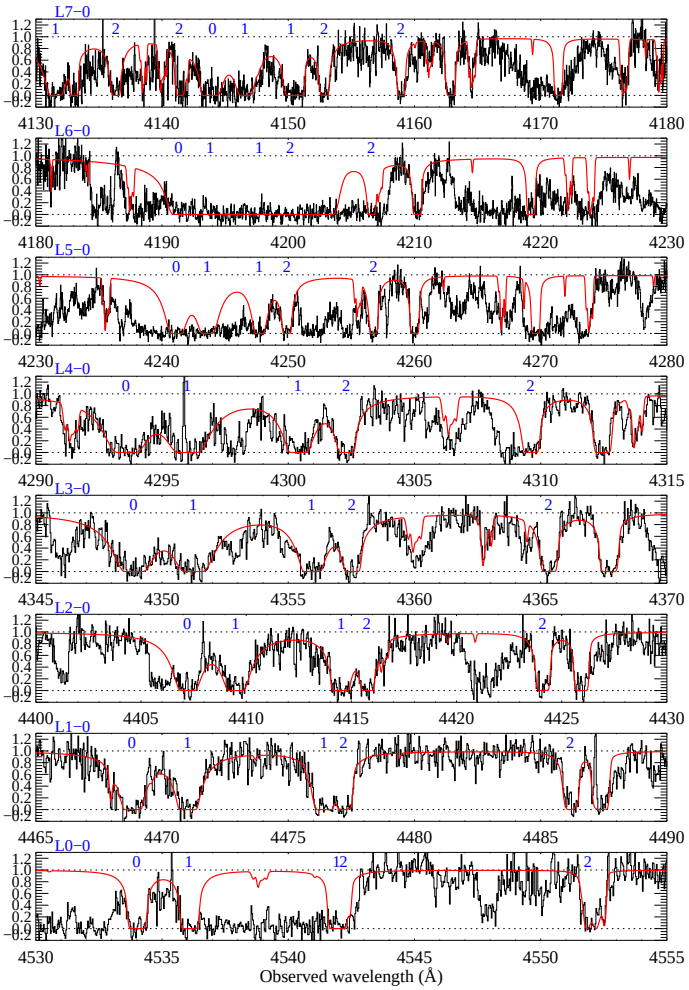

Fig. 3. Same as Fig. 1 for the UVES spectrum of J1311+2225. Note that different bands start to overlap which each other at the shortest wavelength. As for other systems, the label indicated on the top left of each panel corresponds to the band to which the identified rotational levels belong.

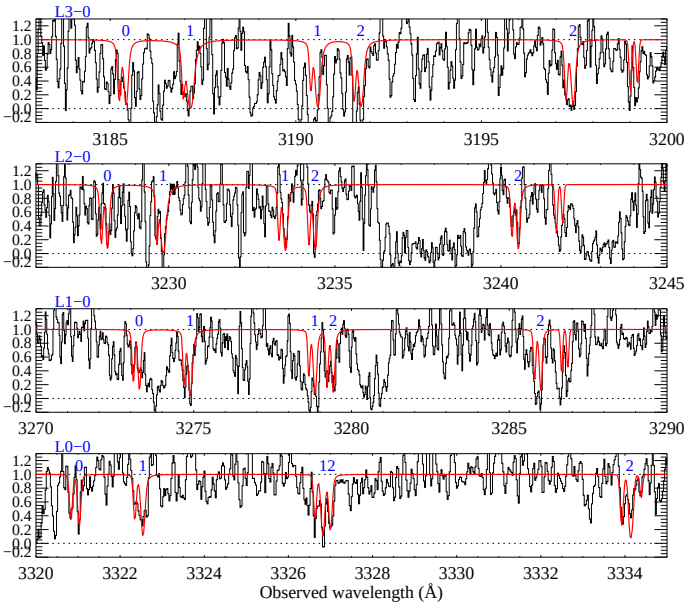

Fig. 4. Same as Fig. 1 for the UVES spectrum of J1646+2329.

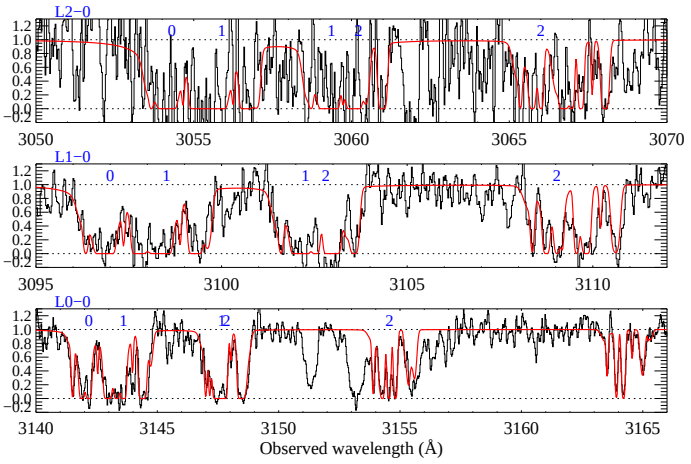

Fig. 5. Same as Fig. 1 for the UVES spectrum of J2257−1001.

trum covers four Lyman bands, that span more than an order of magnitude in oscillator strengths. We find a total column density $N(H_2) \approx 10^{18}$ cm^{-2} with a ∼30% uncertainty.

J225719−100104, $z_{abs} = 1.836$

This system is more complex with no less than eight H_2 components, strongly blended with each other. Unfortunately, only three Lyman H_2 bands are covered by the UVES data (Fig. 5), the bluest of which in a region with low S/N ratio. To remove strong degeneracy between parameters, we had to fix the excitation temperature T_{01} to 100 K. While this is a strong assumption, we note that varying T_{01} within a factor of two has little effect on the total column H_2 density (changes ∼0.1 dex). Still, we caution that this error may be underestimated and covering bluer transitions is required to confirm our column density measurement ($\log N(H_2) = 19.5 \pm 0.1$).

J233156-090802, $z_{abs} = 2.142$

In spite of the low S/N achieved this system, shown on Fig. 6, the data is clearly consistent with strongly damped H_2 lines at the same redshift as that of CO lines (see next section). We fitted the $J = 0, 1, 2$ lines, from which we obtain realistic excitation temperatures, $T_{01} \sim 140$ K and $T_{02} \sim 180$ K. The total H_2 column density is found to be $\log N(H_2) = 20.57 \pm 0.05$.

J233633-105841, $z_{abs} = 1.829$

The H_2 profile in this system is well modelled by two components, that are partially blended at the X-Shooter spectral resolution. The bluest component dominates however the total column density, and the measurement is facilitated by the presence of damping wings and the high S/N achieved. We note that the L0-0 band is partially blended with unrelated absorption lines, which we modelled when fitting H_2 (see Fig. 7). We obtain $\log N(H_2) = 19.0 \pm 0.12$.

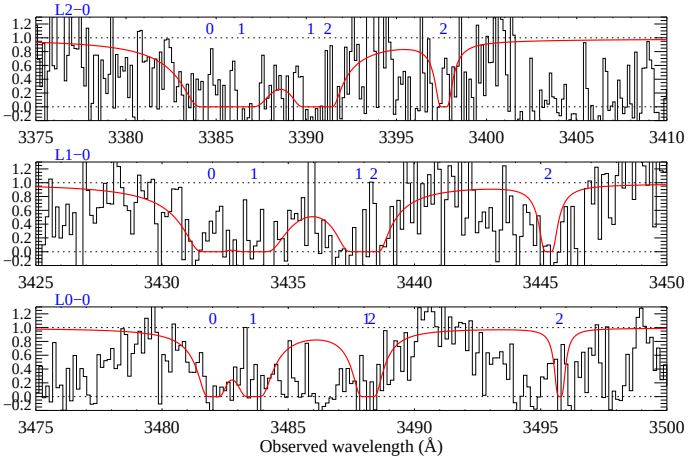

Fig. 6. Same as Fig. 1 for the UVES spectrum of J2331−0908. The data has been rebinned by 7 pixels for visual purpose only.

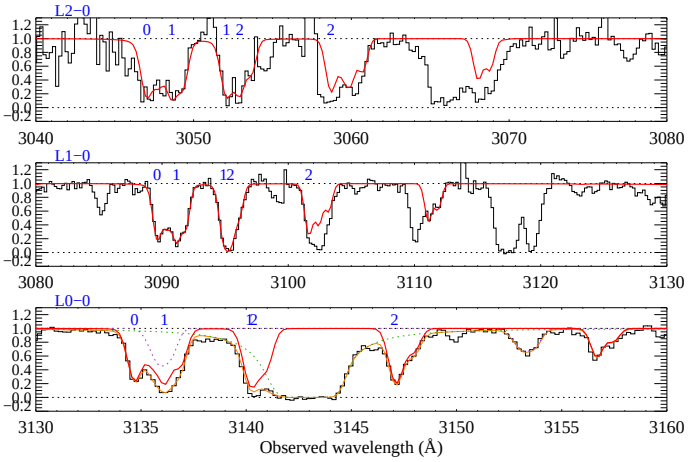

Fig. 7. Same as Fig. 1 for the X-Shooter spectrum of J2336-1058. The green and purple dotted lines in the bottom panel show the contribution from unrelated Lyα (from a sub-DLA at $z_{\rm abs} = 1.585$) and O VI ($z_{\rm abs} = 2.039$) absorption, respectively. The contribution from H_2 alone is shown in red and the total absorption-line profile is depicted in orange.

2.2. Carbon monoxide

CO is detected in seven systems in our sample, six of them already reported by our group and one being a new detection presented here for the first time. This brings the number of known high-z CO-bearing quasar absorbers to nine[2]. We measured upper limits on N(CO) for all systems assuming the Doppler parameter to be 1 km s^{-1}, similar to what has been measured in all high-z CO absorbers to date. We also assume the CMB radiation to be the main excitation source in diffuse gas at high-z (as observed by Srianand et al. 2008; Noterdaeme et al. 2011).

We calculated the local (i.e. for each band individually) and global χ^2 values for a range of total column densities. CO is detected when the χ^2 curves are consistent with each other and present a clear inflexion point, defining the best-fit value. For non-detections, $\chi^2(N(\rm CO))$ is generally monotonic with a minimum consistent with that

[2] The detections towards J1211+0833 (Ma et al. 2015) and J0000+0015 (Noterdaeme et al. 2017) are not formally part of the *statistical* sample although selected upon their C I content.

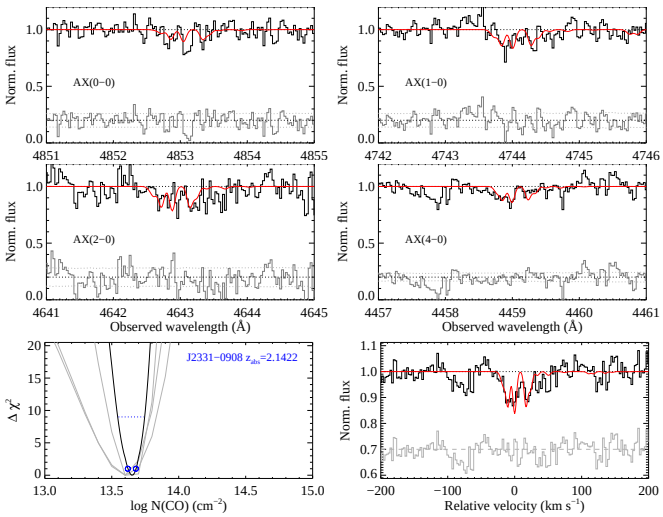

Fig. 8. CO AX bands at $z_{\rm abs} = 2.1422$ towards J 2331−0908 (top four panels, AX(3-0) is not covered by the instrument setup). The bottom-right panel shows a co-addition of the CO bands, using $(f/\sigma)^2$-weighting, where f is the oscillator strength and σ the uncertainty on the normalised flux, for easy visualisation of the detection. The bottom-left panel shows the $\Delta\chi^2 = \chi^2 - \chi^2_{\rm min}$ curves (grey for individual band, black for total).

of N(CO)=0 within uncertainty. Our 3 σ upper limit corresponds to the column density where the χ^2 is 9 above this minimum. With this method, not only we recover all the known CO absorbers but we also identify the new CO system, at $z = 2.143$ towards SDSS J2331−0908 (Fig. 8), observed by Nestor and collaborators (Prog. ID 080.A-0795). This is only the fourth high-z system with direct and simultaneous measurements of N(CO) and $N(H_2)$.

Before discussing our findings, it is worth mentioning that, in the local ISM, the excitation temperature of CO is found to be a few degrees above the CMB temperature (e.g. Burgh et al. 2007), owing to additional excitation processes such as collisions, far-infrared dust emission and possibly cosmic rays. Relaxing our assumptions we find that the derived CO column density limits (as well as the CO column density for the new detection at $z_{\rm abs} = 2.143$ towards SDSS J2331−0908) are not changed significantly as the total band equivalent width is almost conserved. For example, allowing an excitation temperature 5 K above the CMB temperature only increases the derived values by less than 0.04 dex.

3. Discussion

Table 1 summarises the H_2 and CO detections and column density measurements. Figure 9 presents the H_2 and CO column densities as well as the *overall* molecular fraction $\langle f_{\rm H2}\rangle = 2N(H_2)/(2N(H_2) + N(\rm H\,I))$ as a function of N(C I) for our complete sample. Known systems from the literature are also added for comparison but not considered for statistical analysis.

We find that H_2 is detected with $N(H_2) \gtrsim 10^{18}$ cm^{-2} in all systems with $\log N(\rm C\,I) > 13.5$. In this regime, H_2 is likely to be self-shielded and the molecular fraction substantial in the H_2-bearing gas. We also observe a possible trend for increasing $N(H_2)$ with increasing N(C I) (Spearman rank correlation coefficient $r = 0.4$, 1.2 σ significance)

Table 1. CO and H_2 content of strong C I absorbers

Quasar	z_{abs}	log N (cm^{-2})			Ref
		C I	CO	H_2	
J0216−0021	1.737	14.25±0.02	<12.97	–	1
J0300−0721	1.536	>14.77	≤13.79	–	1
J0811+0838	1.906	13.68±0.13	<13.24	–	1
J0815+2640	1.681	>14.73	<13.68	–	1
J0820+1559	1.547	>14.71	<14.01	–	1
J0852+1935	1.788	15.01±0.12	<13.33	–	1
J0854+0317	1.567	14.23±0.01	<13.11	–	1
J0857+1855	1.730	14.57±0.13	13.54±0.05	–	2
J0917+0154	2.107	14.32±0.06	<14.07	$20.11^{+0.06}_{-0.06}$	1
J0927+1543	1.731	>14.61	<13.32	–	1
J1047+2057	1.775	>14.90	14.40±0.07	–	2
J1117+1437	2.001	14.40±0.03	<13.13	∼ 18	1
J1122+1437	1.554	13.83±0.03	<12.99	–	1
J1129−0237	1.623	>14.96	<13.31	–	1
J1133−0057	1.706	15.12±0.06	≤14.07	–	1
J1237+0647	2.691	15.01±0.02	14.17±0.09	$19.21^{+0.13}_{-0.12}$	3
J1248+2848	1.513	14.25±0.10	<13.25	–	1
J1302+2111	1.656	14.30±0.02	<13.48	–	1
J1306+2815	2.012	14.47±0.04	<13.26	–	1
J1311+2225	3.092	14.30±0.02	<13.43	$19.69^{+0.01}_{-0.01}$	1
J1314+0543	1.583	14.40±0.02	≤13.77	–	1
J1341+1852	1.544	13.51±0.03	<13.00	–	1
J1346+0644	1.512	14.51±0.02	<13.60	–	1
J1439+1117	2.418	14.81±0.02	13.89±0.02	$19.38^{+0.10}_{-0.10}$	4
J1459+0129	1.623	14.32±0.09	<13.57	–	1
J1522+0830	1.627	>14.47	<13.50	–	1
J1603+1701	1.890	13.80±0.10	<12.88	–	1
J1604+2203	1.641	>15.14	14.59±0.11	–	5
J1615+2648	2.118	14.49±0.06	<13.16	–	1
J1623+1355	1.751	14.41±0.07	<13.30	–	1
J1646+2329	1.998	14.32±0.06	<13.40	$18.02^{+0.11}_{-0.11}$	1
J1705+3543	2.038	>15.01	14.14±0.03	–	2
J2123−0050	2.060	14.11±0.02	<13.07	$17.94^{+0.01}_{-0.01}$	1,6
J2229+1414	1.586	13.96±0.05	<13.55	–	1
J2257−1001	1.836	14.65±0.01	<13.09	19.5 ± 0.1	1
J2331−0908	2.143	>14.70	13.65±0.03	$20.57^{+0.05}_{-0.05}$	1
J2336−1058	1.829	14.07±0.02	<12.93	$19.00^{+0.12}_{-0.12}$	1
J2340−0053	2.054	13.99±0.02	<12.58	$18.47^{+0.04}_{-0.04}$	1,7
J2350−0052	2.426	14.36±0.01	<12.94	$18.52^{+0.29}_{-0.49}$	1,8

References. The references listed in last column are for molecular measurements. When two references are listed, they correspond to CO then H_2, in this order. (1) This work; (2) Noterdaeme et al. (2011); (3) Noterdaeme et al. (2010); (4) Srianand et al. (2008); (5) Noterdaeme et al. (2009); (6) Klimenko et al. (2016); (7) Jorgenson et al. (2010); (8) Noterdaeme et al. (2007). Unless already available from the literature, C I column densities were obtained through the apparent optical depth method.

in our statistical sample, albeit with a large dispersion. We note that systems that were *not* C I-selected (from literature) seem not to follow this trend. Four of them indeed have $N(H_2) > 5 \times 10^{19}\,cm^{-2}$ in spite of relatively low C I column density ($\log N(C\,I) \lesssim 14$). This difference is likely due to the different chemical enrichments: C I-selected systems probe mostly high-metallicity gas (Zou et al. sub., Ledoux et al. in prep.) while the four mentioned literature systems all have low metallicities.

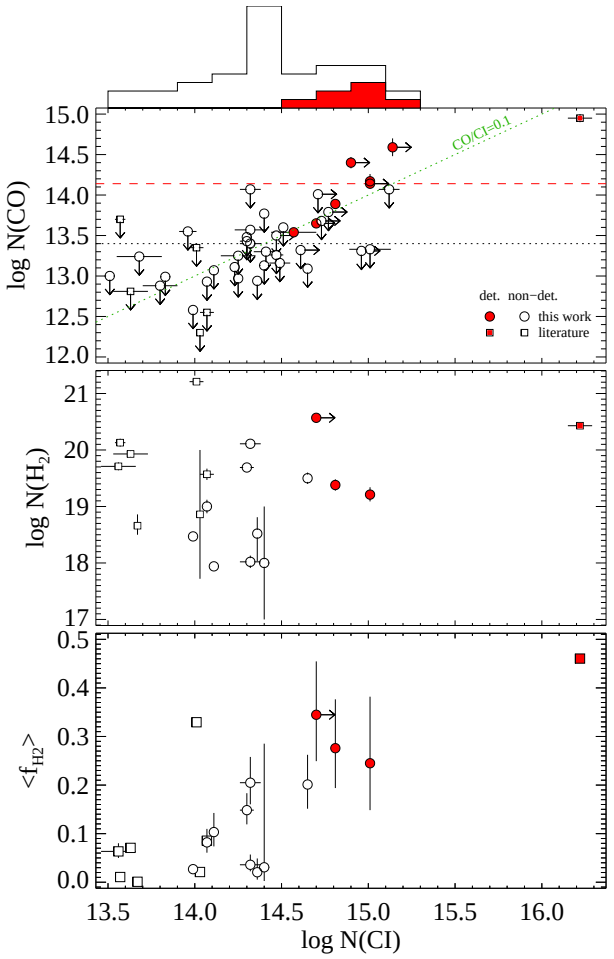

Fig. 9. Column densities of CO (top), H_2 (middle) and overall molecular fractions (bottom) vs N(C I). CO detections are represented by red colours. The N(C I)-distributions and median log N(CO) values (horizontal lines) are shown for the statistical sample only (circles). Squares correspond to high-z H_2 DLA systems from the literature (Balashev et al. 2010, 2011, 2017; Carswell et al. 2011; Guimarães et al. 2012; Noterdaeme et al. 2015, 2017; Petitjean et al. 2002).

Since the column density at which H I is converted into H_2 strongly depends on the chemical properties of the gas, in particular the abundance of dust grains (e.g. Bialy & Sternberg 2016), we can expect less H I in the molecular cloud envelope for high-metallicity systems compared to low-metallicity ones. In addition, contrary to DLAs, C I systems were selected without any a priori knowledge of the H I content (Ledoux et al. 2015) and should have less contribution from unrelated atomic gas that does not belong to the envelope of the H_2 cloud. This is seen in the bottom panel of Fig. 9, where the correlation between $\langle f \rangle$ and N(C I) is seen with $r = 0.6$ at $2.1\,\sigma$: the average overall H_2 molecular fraction is about 15% in our sample (and about 30% when CO is detected) but < 3% at $\log N(C\,I) < 14$.

The correlation between N(CO) and N(C I) for CO detections is strong with $r = 0.88$ ($2.6\,\sigma$). From the column density distributions, we can see that the probability to detect CO becomes much larger above $N(C\,I) \sim 5 \times 10^{14}\ cm^{-2}$(6/12) than below this value (1/27). In addition, there is no CO detection among the 18 systems with $\log N(C\,I) < 14.4$. Since the CO detection limits are signif-

icantly below ($\sim$ 1 dex) the typical N(CO) in the case of detection, this result is robust[3]. Considering also lower and upper limits on both N(CO) and N(C I), we still find the N(CO)-N(C I) correlation to have $\sim$92% probability.

This strong correlation is likely due to the strong dependence of CO abundance on the metallicity (through the abundance of carbon, the abundance of dust grains as molecule-formation catalyst and an effective shielding of UV photons). In Ledoux et al. (2015), we showed that strong C I systems produce more reddening than other classes of quasar absorbers. We further note that the dust-reddening is systematically higher in CO-bearing systems than other H_2 systems without CO. The relative behaviours of CO, H_2 and C I agree qualitatively with models of ISM clouds immersed into a UV radiation field: these clouds are expected to exhibit an onion-like structure where hydrogen converts from atomic to molecular form when going towards the centre of the cloud. Carbon is predominantly ionised in the external layers, then becomes neutral, while CO is dominant only in the inner dense molecular parts of the cloud (see. e.g. Bolatto et al. 2013). Unfortunately, it remains difficult to disentangle the atomic gas that belongs to a molecular cloud envelope and contributes to its shielding from unrelated H I, simply intercepted along the same line of sight. This means that the measured $\langle f \rangle$ is a lower limit to the actual H_2 molecular fraction in the C I-bearing cloud. Since CO and C I are only found in shielded gas, their observed abundance ratio should be less affected by the presence of unrelated gas. Indeed, we find CO/C I$\sim$ 0.1 for all detections (green dotted line in Fig. 9), a value which is also consistent with the non-detections at lower N(C I). This indicates a regime deeper than the layer where the H I-H_2 transition occurs.

The CO/H_2 ratio is found to be low ($\sim [3-9] \times 10^{-6}$) for three out of four cases where both these molecules are detected and can be more than an order of magnitude lower in other strong H_2 systems, including the new CO detection. Even in these cases, the high $N(H_2)$ likely indicates well-molecularized regions. Several factors such as the grain size distribution or the intensity of the cosmic ray field likely play important roles in determining whether CO will be present or not in H_2-dominated regions (e.g. Shaw et al. 2016; Noterdaeme et al. 2017; Bisbas et al. 2017). Multiple clouds can also easily explain large H_2 column densities without significant CO, in a similar way than multiple H I-H_2 transition layers explain higher N(H I) than predicted by single cloud models (Bialy et al. 2017).

We conclude that C I is a very good proxy to spot high-redshift molecular absorbers that can be used for a variety of studies including fundamental physics and cosmology. It is however crucial not only to constrain the physical parameters in individual systems (and hopefully for individual velocity components separately) but also to explore different metallicity regimes (Balashev et al. 2017) using different selections (e.g. Balashev et al. 2014) to understand better the molecular structure of ISM clouds at high redshifts.

Acknowledgements. We thank T. Krühler for help with the X-shooter data reduction. PN thanks the European Southern Observatory for hospitality and support during part of this work was done. PN, PPJ and RS acknowledge support from the Indo-French Centre for the Promotion of Advanced Research (Project 5504-B). We acknowledge support from the PNCG funded by CNRS/INSU-IN2P3-INP, CEA and CNES, France. This research is part of the projet *HIH2* funded by the *Agence Nationale de la Recherche*, under grant ANR-17-CE31-0011-01 (JCJC). SB thanks the Institut d'Astrophysique de Paris for hospitality and the Institut Lagrange de Paris for financial support. SL has been supported by FONDECYT grant 1140838 and by PFB-06 CATA.

[3] We note that N(CO)-limits also tend to be more stringent for systems with low N(C I). This is likely due to easier detection of small C I equivalent widths in SDSS towards bright quasars (or that such systems extinguish less the same), for which the follow-up data is also of better quality.

References

Balashev, S. A., Ivanchik, A. V., & Varshalovich, D. A. 2010, Astronomy Letters, 36, 761
Balashev, S. A., Klimenko, V. V., Ivanchik, A. V., et al. 2014, MNRAS, 440, 225
Balashev, S. A., Noterdaeme, P., Rahmani, H., et al. 2017, MNRAS, 470, 2890
Balashev, S. A., Petitjean, P., Ivanchik, A. V., et al. 2011, MNRAS, 418, 357
Bialy, S., Bihr, S., Beuther, H., Henning, T., & Sternberg, A. 2017, ApJ, 835, 126
Bialy, S. & Sternberg, A. 2016, ApJ, 822, 83
Bisbas, T. G., van Dishoeck, E. F., Papadopoulos, P. P., et al. 2017, ApJ, 839, 90
Boissé, P., Federman, S. R., Pineau des Forêts, G., & Ritchey, A. M. 2013, A&A, 559, A131
Bolatto, A. D., Wolfire, M., & Leroy, A. K. 2013, ARA&A, 51, 207
Burgh, E. B., France, K., & McCandliss, S. R. 2007, ApJ, 658, 446
Carswell, R. F., Jorgenson, R. A., Wolfe, A. M., & Murphy, M. T. 2011, MNRAS, 411, 2319
Cui, J., Bechtold, J., Ge, J., & Meyer, D. M. 2005, ApJ, 633, 649
Daprà, M., Niu, M. L., Salumbides, E. J., Murphy, M. T., & Ubachs, W. 2016, ApJ, 826, 192
Ge, J., Bechtold, J., & Black, J. H. 1997, ApJ, 474, 67
Ge, J., Bechtold, J., & Kulkarni, V. P. 2001, ApJ, 547, L1
Guimarães, R., Noterdaeme, P., Petitjean, P., et al. 2012, AJ, 143, 147
Jorgenson, R. A., Wolfe, A. M., & Prochaska, J. X. 2010, ApJ, 722, 460
Klimenko, V. V., Balashev, S. A., Ivanchik, A. V., & Varshalovich, D. A. 2016, Astronomy Letters, 42, 137
Ledoux, C., Noterdaeme, P., Petitjean, P., & Srianand, R. 2015, A&A, 580, A8
Levshakov, S. A., Foltz, C. B., Chaffee, F. H., & Black, J. H. 1989, AJ, 98, 2052
Liszt, H. S. 1981, ApJ, 246, L147
Ma, J., Caucal, P., Noterdaeme, P., et al. 2015, MNRAS, 454, 1751
Malec, A. L., Buning, R., Murphy, M. T., et al. 2010, MNRAS, 403, 1541
Noterdaeme, P., Krogager, J.-K., Balashev, S., et al. 2017, A&A, 597, A82
Noterdaeme, P., López, S., Dumont, V., et al. 2012, A&A, 542, L33
Noterdaeme, P., Petitjean, P., Ledoux, C., et al. 2010, A&A, 523, A80
Noterdaeme, P., Petitjean, P., Ledoux, C., & Srianand, R. 2009, A&A, 505, 1087
Noterdaeme, P., Petitjean, P., Ledoux, C., Srianand, R., & Ivanchik, A. 2008, A&A, 491, 397
Noterdaeme, P., Petitjean, P., Srianand, R., Ledoux, C., & Le Petit, F. 2007, A&A, 469, 425
Noterdaeme, P., Petitjean, P., Srianand, R., Ledoux, C., & López, S. 2011, A&A, 526, L7+
Noterdaeme, P., Srianand, R., Rahmani, H., et al. 2015, A&A, 577, A24
Petitjean, P., Srianand, R., & Ledoux, C. 2000, A&A, 364, L26
Petitjean, P., Srianand, R., & Ledoux, C. 2002, MNRAS, 332, 383
Prochaska, J. X., Tripp, T. M., & Howk, J. C. 2005, ApJ, 620, L39
Savage, B. D., Bohlin, R. C., Drake, J. F., & Budich, W. 1977, ApJ, 216, 291
Shaw, G., Rawlins, K., & Srianand, R. 2016, MNRAS, 459, 3234
Srianand, R., Noterdaeme, P., Ledoux, C., & Petitjean, P. 2008, A&A, 482, L39
Srianand, R., Petitjean, P., Ledoux, C., Ferland, G., & Shaw, G. 2005, MNRAS, 362, 549
Stecher, T. P. & Williams, D. A. 1967, ApJ, 149, L29
Ubachs, W., Bagdonaite, J., Salumbides, E. J., Murphy, M. T., & Kaper, L. 2016, Reviews of Modern Physics, 88, 021003

Chapter 5

Conclusion

In this chapter we summarise the main results of this thesis and highlight the new contributions to this field.

In this thesis, we present the first large complete sample of C I absorbers selected out of 41 696 low-resolution QSO spectra at high redshift. The motivation of this project is to trace the cold gas in the high-z galaxies efficiently via this new tracer – neutral carbon. Furthermore, we want to probe the star formation at high redshift. Since the stars form out of cold and molecular gas in the ISM, we need to search for the cold gas firstly. Therefore we chose this special tracer, C I, whose ionization energy is lower than the neutral hydrogen. This implies that it is located in the cold and shielded gas. We also aim to compare C I with normal DLAs to see the differences between these two systems.

I finished the analysis of a subsample of 17 systems having in particular the NaI and CaII absorptions in the NIR (Zou et al. 2017). These systems are re-observed by VLT X-shooter. I analysed one peculiar Lyman Limit System and built a simple model to explain the observations. I also contributed to the work in two articles Fathivavsari et al. (2017) and Noterdaeme et al. (2018). The main contribution of this whole C I project to the field is described as follows :

• I studied the physical properties of the C I bearing clouds at high redshift with $z > 1.5$. I derived the metallicity, dust extinction and depletion, equivalent width of absorption lines, as well as temperature and density estimation of the clouds. I found that the systems have high metallicity (close to solar), hence higher than found in the normal DLAs at similar redshifts.

• In the analysis of spectroscopic NIR data, I detected 10 of 11 Na I systems and 9 out of 13 Ca II systems where we could observe them. Due to the low SNR in the NIR, it

was challenging to detect and confirm the detections of Na I and Ca II. These detections are rarely found in the high-z galaxies. I found that equivalent width NaI is in strong correlation with the C I equivalent widths. I also found high dust-to-gas ratio in this subsample.

• I found that our systems are probably located in strongly disturbed area in the ISM of the absorbing galaxies. This is indicated by the very large equivalent width of Mg II in the subsample. Most of the systems (12 out of 17) have W(Mg IIλ2796) $>$ 2.5 Å. More than half of the Mg II absorption lines are spread over more than $\sim$ 400 km s^{-1}. Joshi et al. (2017) show the association between strong Mg II absorbers and the galaxy [OII] luminosity. Hence it is highly probable that there is emission around our systems.

• There are two peculiar systems found in this subsample. I built a simple model using CLOUDY to derive the ionization state of the peculiar Lyman Limit system J1341+1852 in our sample. Constrained by the instrument resolution, I can not reach a firm conclusion here. It is possible that this system is enriched by carbon-enhanced-metal-poor stars (CEMP) or we need to take the dust content into consideration. Fathivavsari et al. (2017) present a model for a peculiar system J1133-0057 having no Lyα trough in the observed spectra, because the absorber is very close to the quasar itself.

• We found that C I is a very promising tracer for the presence of molecular gas. Molecular gas is very difficult to detect directly, especially at high redshift. In **all** the systems within the detection limit we detected molecular hydrogen (Noterdaeme et al. 2018). Together with the high metallicity and high dust content results, we claim that our systems are metal-rich and are very likely to have star formation nearby.

Chapter 6

Perspective

In this chapter, I firstly describe the necessary steps to complete this work, then the possible future work.

• We will continue the C I decomposition by obtaining different column densities of C I, CI* and CI** for the whole sample. By combining the results with the molecular hydrogen measurements, we can strongly constrain the physical states of the whole sample.

• As our systems trace the cold gas efficiently in the ISM, it is very probable that there is star formation nearby. We will search for the emission lines in the spectra. If there is no star formation detected directly, at least we can obtain limits about the star formation therein. We will then apply for the observing time on the nearby galaxies in order to look for star formation.

• We will ask for high resolution data with UVES for this Lyman Limit System (J1341+1852) with the goal to test our assumption of CEMP.

For future work, I would like to combine the quasar absorption lines with the emission lines in galaxies to probe the cycle of galactic outflows, cold streams and stellar feedback. The most important question I would like to study that whether the galactic outflows are possibly driven from the star forming region or the cold gas region nearby. In order to address this goal, firstly I would like to initiate a systematic search for the Lyman Limit Systems with cold gas signatures to study their chemical enrichments and ionization states. This is inspired by the peculiar Lyman Limit System in our sample, because there is cold gas presented in this highly-ionised system. The simulation in Ford et al. (2014) show that the ionization level of absorbers is a primary factor in determining the physical conditions of absorbing gas, and also a determining factor for its dynamical state. For this project, I would like to use Multi Unit Spectroscopic Explorer (MUSE). MUSE is a

second generation instrument installed on the VLT, which has a panoramic integral-field spectrograph operating in the visible wavelength range, and combines a wide field of view with a fine spatial sampling and a large simultaneous spectral range. As its wavelength coverage is 4650Å−9300Å, it can trace the Lyα lines from redshift $2.83 < z < 6.65$. By combining the imaging and spectroscopic data of galaxies or the quasar-galaxy pair, it is very likely that one will be able to observe and confirm the existence of galactic outflows and even cold infall in the CGM.

Most of the recent theoretical work has focused on the cold inflows via filaments, which accrete directly onto the central regions of forming galaxies. But as pointed out in Steidel et al. (2010), previous simulations rarely consider that the interstellar gas may have been carried to large galactocentric radii by outflows. It may well be that the observational signatures of infall by cold accretion and outflows via supernova-driven winds are very subtle, and perhaps indistinguishable. Possibly the most telling differences would be kinematic differences between the absorption line signatures and the outflowing material. If there are only absorption or emission lines detected, it is normally unlikely to differentiate outflows and inflows. That is why it is important to combine the observations of the emission lines from the galaxies with the absorption lines in the ISM of the galaxies. The cold gas region can provide possible valuable information to test if the outflows may come from the ISM. Bouché et al. (2016) introduce a quasar-galaxy pair to show the kinematic evidence for cold gas inflow. The minimum gas accretion rate they estimated is comparable to the detected SFR. I would like to put efforts into studying the cold gas inflow to the ISM and the warm gas outflows cycle of the star forming region at high-z galaxies as well. This is observationally difficult and has not so far been studies with enough details.

I will work on the DARK ENERGY SPECTROSCOPIC INSTRUMENT (DESI) data in my post-doc (see Fig. 6.1). It is an instrument mounted on the 4-meter Mayall Telescope at Kitt Peak National Observatory. DESI will measure the position and receding velocity of about 40 million galaxies. One of its scientific missions is to looking at fainter and distant galaxies out to redshift 1.6, as well as quasars at high-z out to reshift 3.5. Studying absorption and emission lines located on the lines of sight of the quasars is a very promising way of analysing the inflow and outflow cycle of the galaxies.

Furthermore, the hydrodynamical simulations on the CGM tomography via Horizon-AGN are also interesting to compare with future observations. The Horizon-AGN simulation is a cosmological hydrodynamical simulation of 100 Mpc/h comoving volume with 1024^3 dark matter particles with the Planck cosmology. The simulation is performed with the adaptive mesh refinement code RAMSES (Teyssier 2002) including gas dynamics, gas

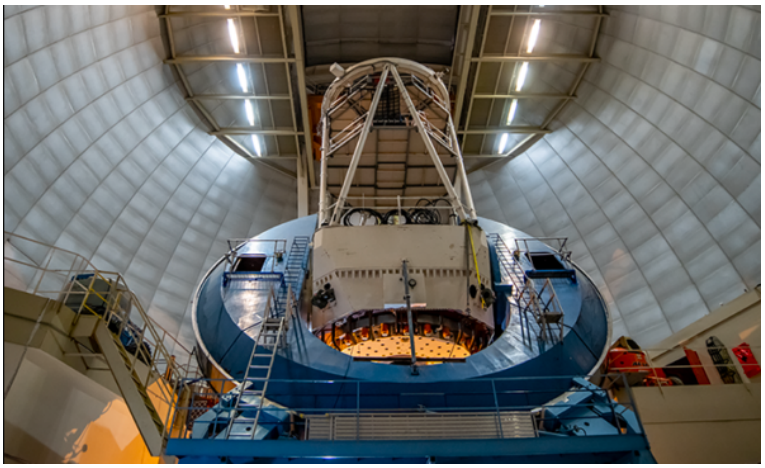

FIGURE 6.1: DESI instrument. Credit: DESI.

cooling and heating. In this simulation, the outflows from AGN are believed to play a crucial role in the formation of massive galaxies. In the new simulation NUT, the outflows driven by supernovae are turned off. The simulation comparison with our future MUSE observation will be interesting to further constrain the importance of stellar feedback in galaxy formation.

Chapter 7

Appendix

7.1 Extinction

X-shooter spectra of quasars in our sample. The red curve corresponds to the quasar template of Selsing et al. (2016) reddened by different extinction curves. See Table 3 for results.

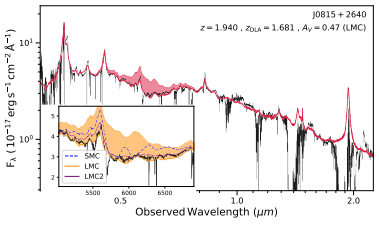

FIGURE 7.1

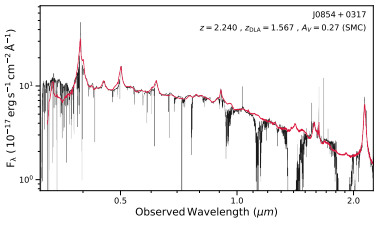

FIGURE 7.2

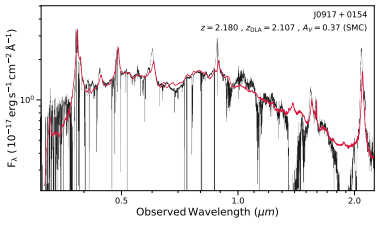

FIGURE 7.3

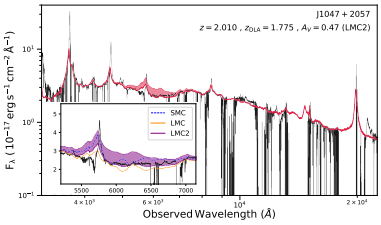

FIGURE 7.4

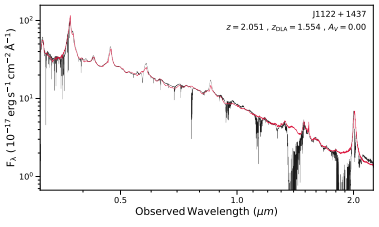

FIGURE 7.5

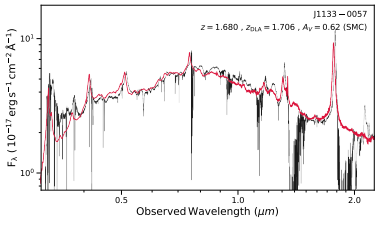

FIGURE 7.6

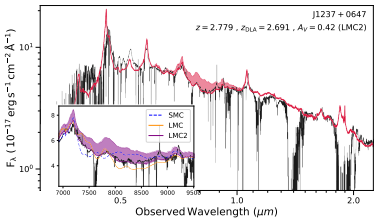

FIGURE 7.7

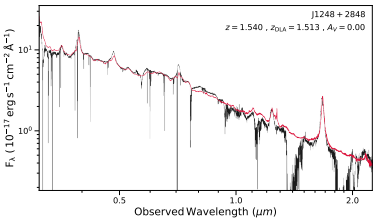

FIGURE 7.8

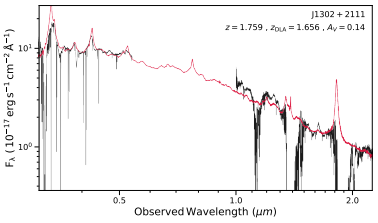

FIGURE 7.9

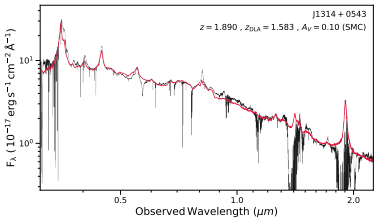

FIGURE 7.10

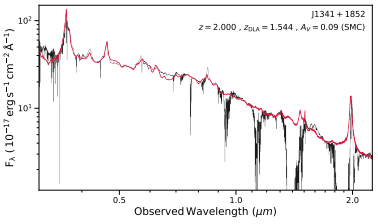

FIGURE 7.11

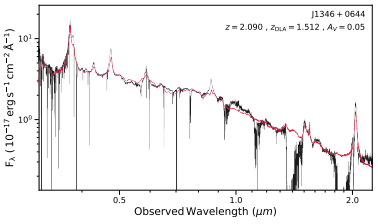

FIGURE 7.12

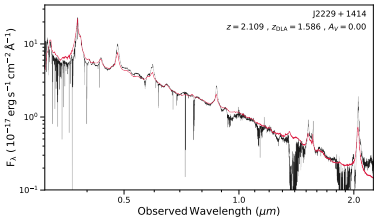

FIGURE 7.13

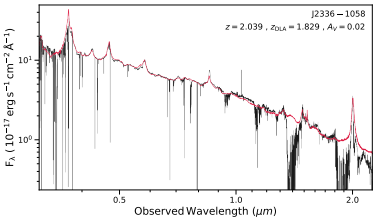

FIGURE 7.14

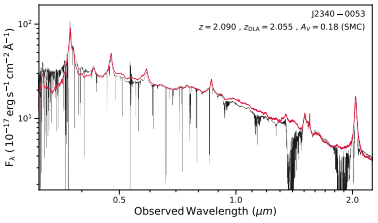

FIGURE 7.15

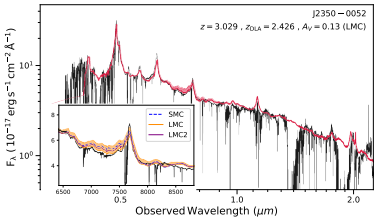

FIGURE 7.16

7.2 CI decomposition

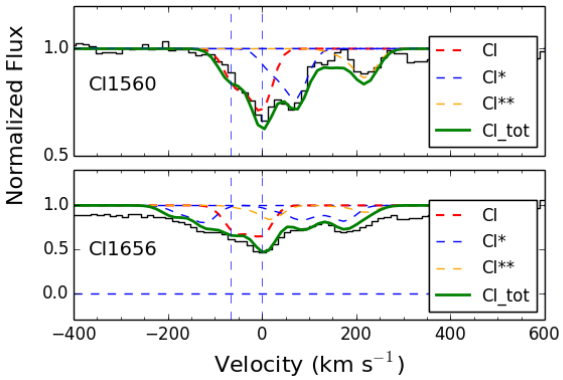

FIGURE 7.17: J0216-0021
C I decomposition.

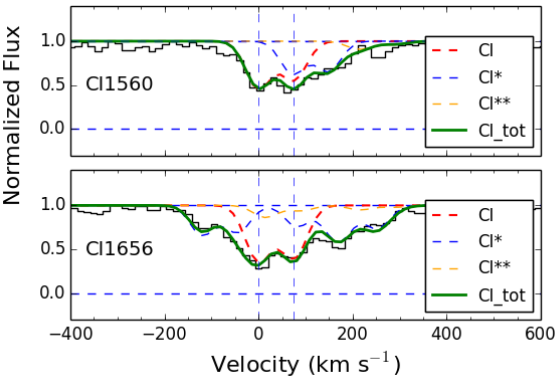

FIGURE 7.18: J0815+2640
C I decomposition.

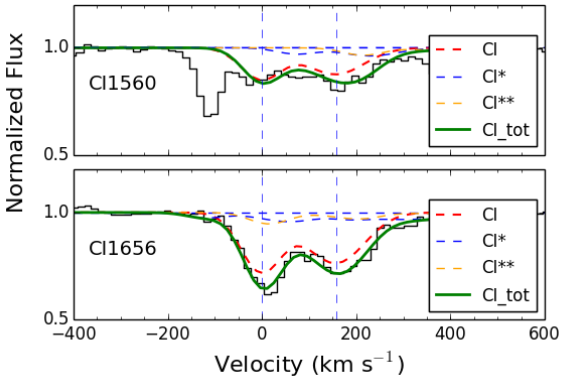

FIGURE 7.19: J0854+0317
C I decomposition.

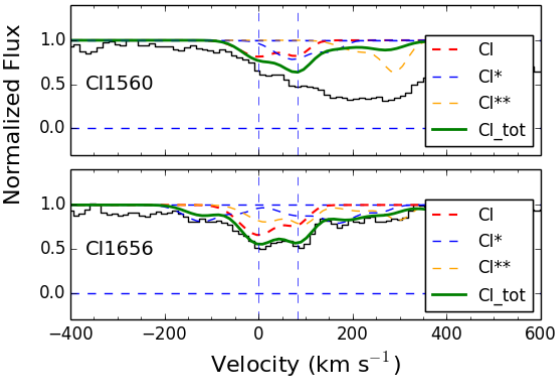

FIGURE 7.20: J0917+0154
C I decomposition.

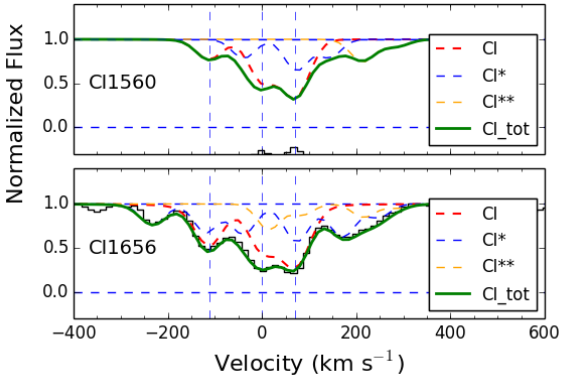

FIGURE 7.21: J1047+2057
C I decomposition.

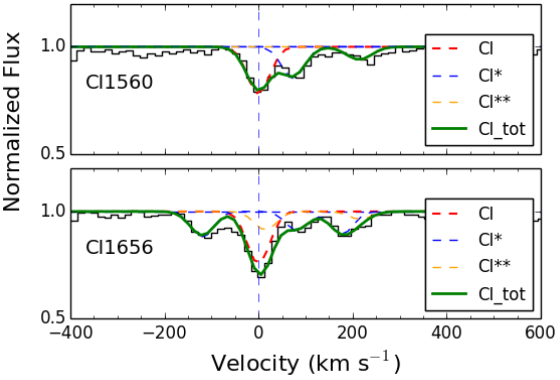

FIGURE 7.22: J1122+1437
C I decomposition.

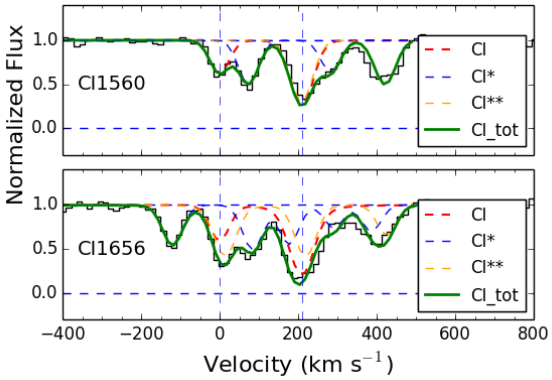

FIGURE 7.23: J1133-0057
C I decomposition.

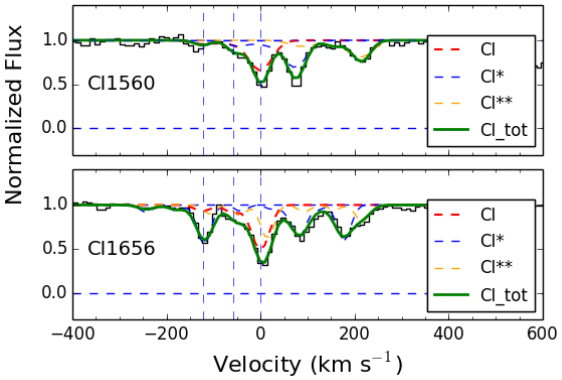

FIGURE 7.24: J1237+0647
C I decomposition.

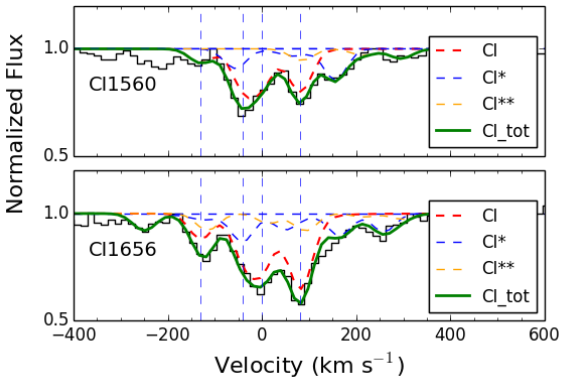

FIGURE 7.25: J1248+2848
C I decomposition.

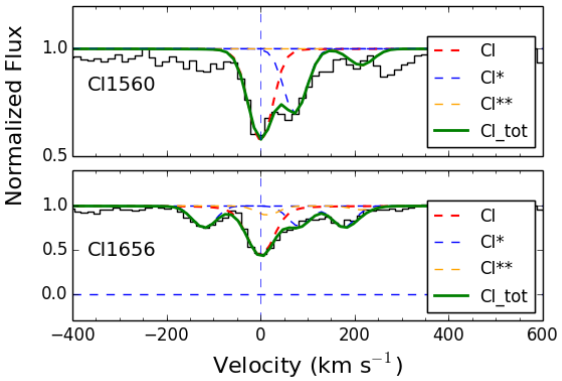

FIGURE 7.26: J1302+2111
C I decomposition.

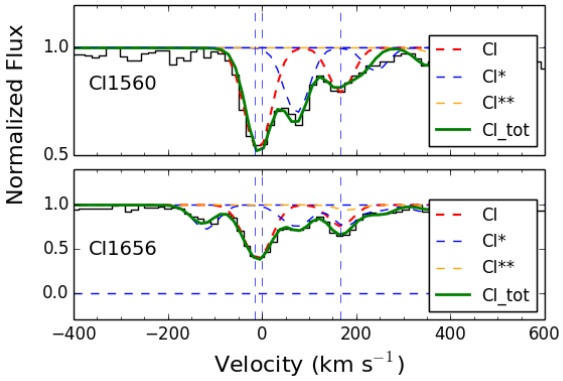

FIGURE 7.27: J1314+0543
C I decomposition.

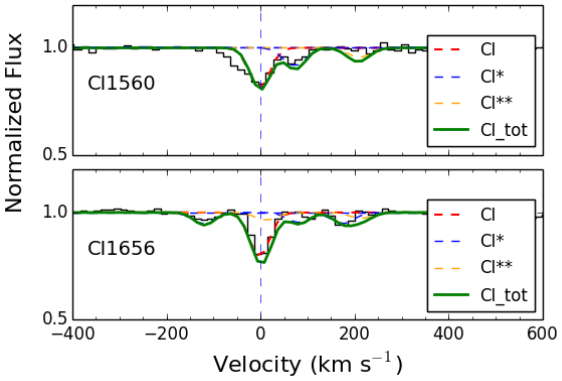

FIGURE 7.28: J1341+1852
C I decomposition.

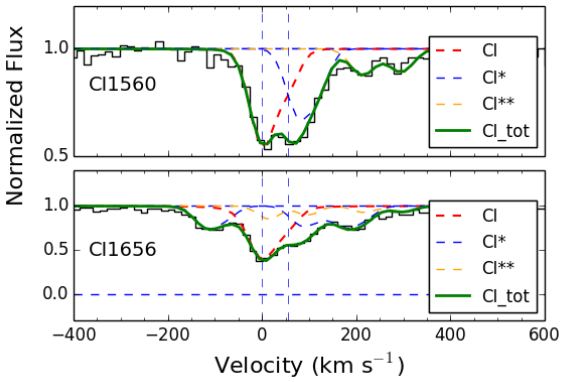

FIGURE 7.29: J1346+0644
C I decomposition.

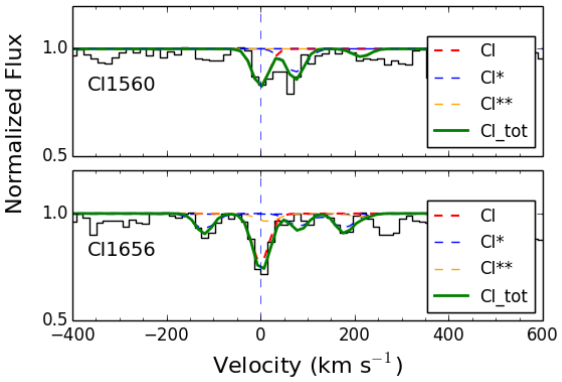

FIGURE 7.30: J2229+1414
C I decomposition.

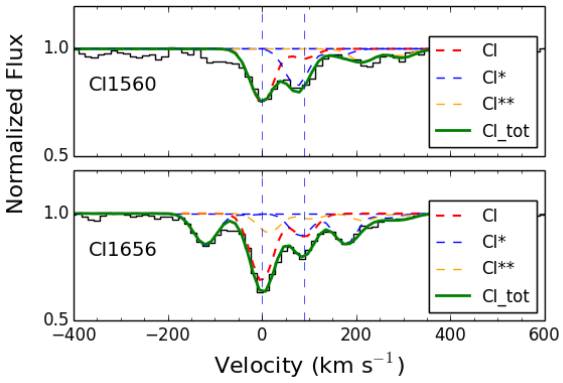

FIGURE 7.31: J2336-1058

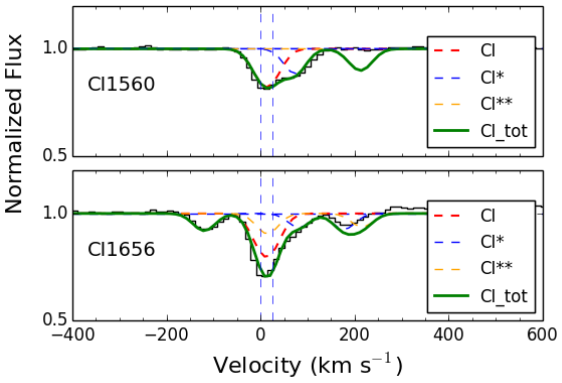

FIGURE 7.32: J2340-0053

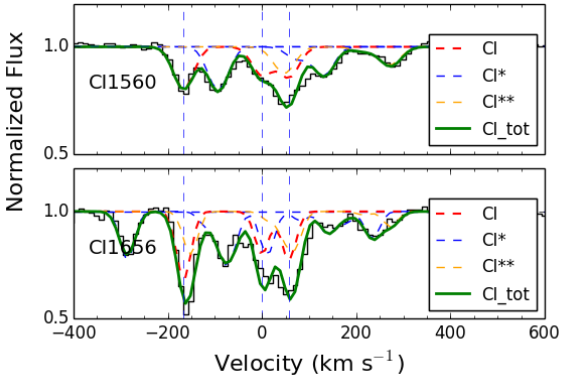

FIGURE 7.33: J2350-0052

7.3 Comments on individual systems

We use here the notations Ca II K and H for Ca IIλ3934Å and Ca IIλ3969Å, respectively, Na I D for the Na I$\lambda\lambda$5891,5897 doublet, and W for the rest equivalent width. The neutral carbon ground base fine structure levels are denoted as C I, C I*, and C I** for the $2s^2 2p^2 {}^3P_J{}^e$ levels where J = 0,1,2.

7.3.1 J0216-0021 – $z_{\rm abs}$ = 1.735888

In this system the Ca II K line is clearly detected but we indicate an upper limit for the H line since the data around the H line is noisy (see Fig. 7.34 right lower panel). The Na I D is detected clearly even though there are strong spikes close to the two absorption lines (see Fig. 7.34 right upper panel). We subtracted the equivalent width of the weak telluric contamination. The C Iλ1560 line is not used in the fit of the C I absorption as it is strongly blended. There are two components at z = 1.735283 and 1.735888, while the strongest component of Fe II, Si II, and Mg I is seen in-between these two components (see also J1248+2848). This could be an artefact due to the spectral resolution. To discuss the details of the structure of the absorbing cloud, higher resolution data are needed.

7.3.2 J0815+2640 – $z_{\rm abs}$=1.679778

The Ca II H and Na I D lines are clearly detected. We conservatively give an upper limit for the Ca II H line in Table 2.3. The Na I D line is somehow blended with telluric absorptions. We therefore have subtracted the sky contamination from the EW. The Mg Iλ2852 feature is strongly blended with absorption from the sky. Weak lines from the Ni II triplet are detected.

7.3.3 J0854+0317 – $z_{\rm abs}$ = 1.566320

The Ca II K line is detected in this system, when the Ca II H line is lost in the noise. The spectrum around the expected position of Na I D is relatively good but no absorption is seen down to 0.23 Å. There is a slight shift of ∼-25 km s^{-1} between the strongest component of Fe II and Si II and the strongest C Iλ1656 component. The C Iλ1560 line is blended with other lines at ∼ -125 km/s and 400 km/s. Weak lines of Zn II and Mn II are detected.

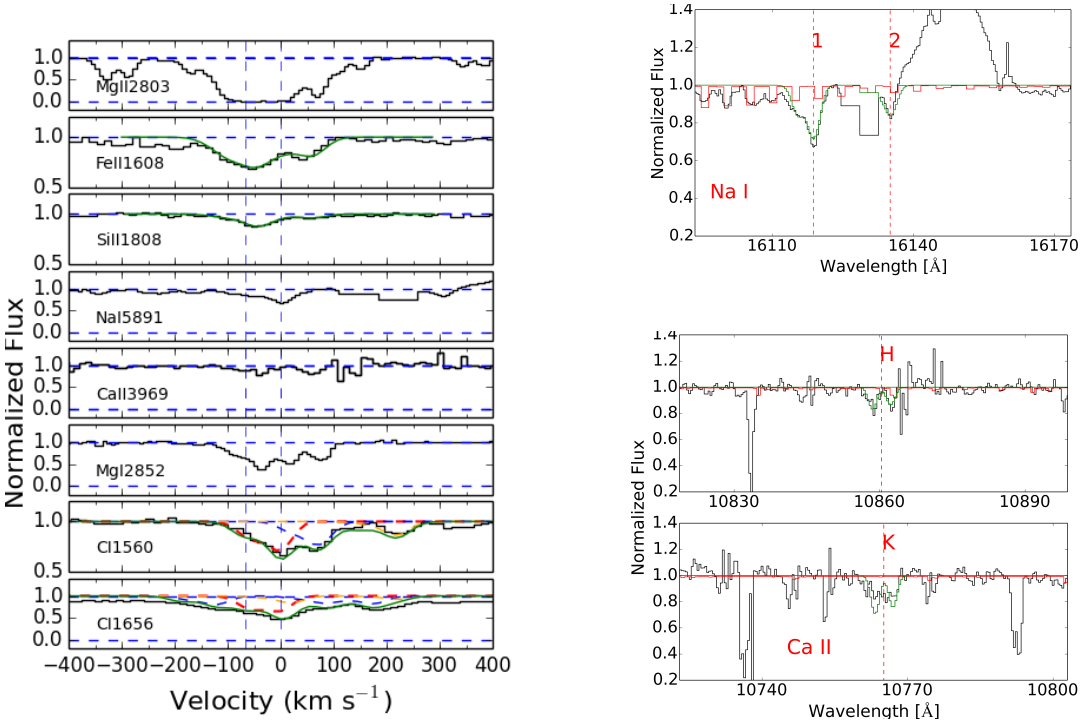

FIGURE 7.34: J0216-0021 (a) the velocity plot of a sub-set of the absorbing species. The vertical dashed lines indicate the positions of the C I components. Fits to the absorption profiles are over-plotted with the data. For C I transitions, the red dashed line corresponds to the true ground state, the blue dashed line is for the C I* absorption, and the orange dashed line is for the C I** absorption. The redshift is taken in Table 2.2 to give the zero velocity. Right panels (b): The upper panel is the spectrum at the expected position of Na I$\lambda\lambda$5891,5897, the 1 and 2 indicate the NaIλ5891 and NaIλ5897 lines respectively; the lower panel is the spectrum at the expected positions of the Ca II$\lambda\lambda$3934,3969 lines, the H and K notations indicate the CaIIλ3969 and CaIIλ3934 lines respectively. The red curve is the telluric spectrum template of X-shooter.

7.3.4 J0917+0154 – z_{abs} = 2.105934

Data are noisy at the expected positions of Ca II H&K. The Na I D is redshifted in the gap between the H and K bands. The Ni II and Zn II lines are also detected. There is no obvious CO line detection in the X-shooter spectrum. The C Iλ1560 line is strongly blended, therefore we did not include it in our fit.

7.3.5 J1047+2057 – $z_{\rm abs}$ = 1.773960

Both Ca II H&K and Na I D are detected and strong. The spectrum around Na I D is noisy however, thus the error on EW is relatively large. The redshift defined by the strongest C I component does not correspond to the exact centre of the Na I D lines.

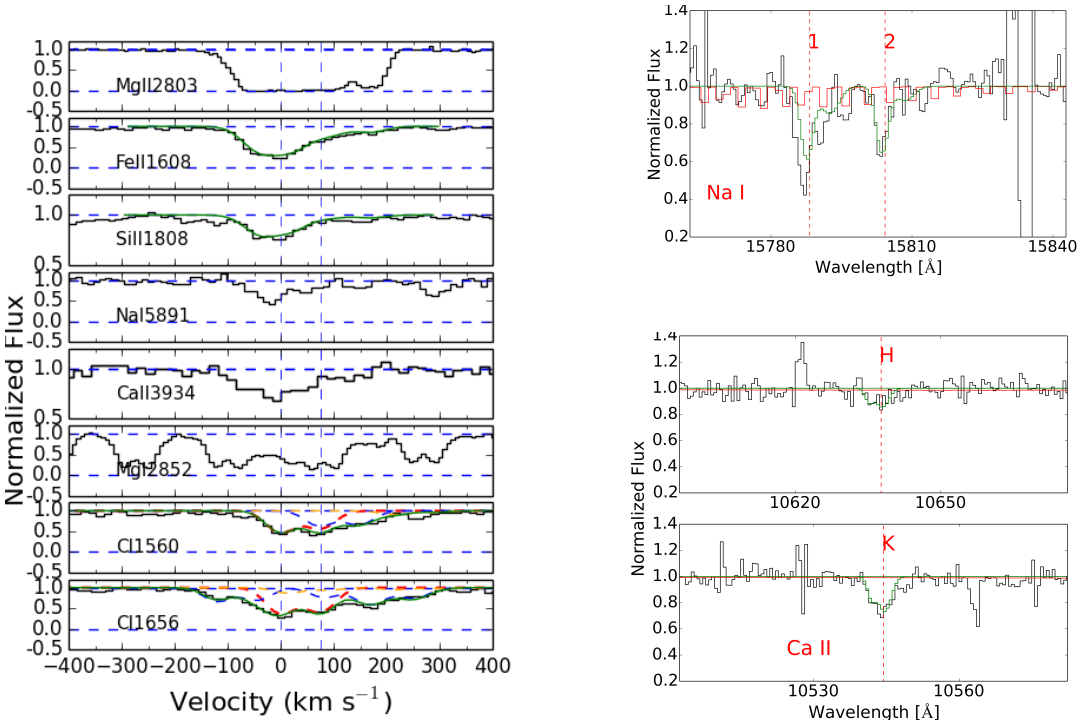

FIGURE 7.35: J0815+2640 − Same as Fig.7.34

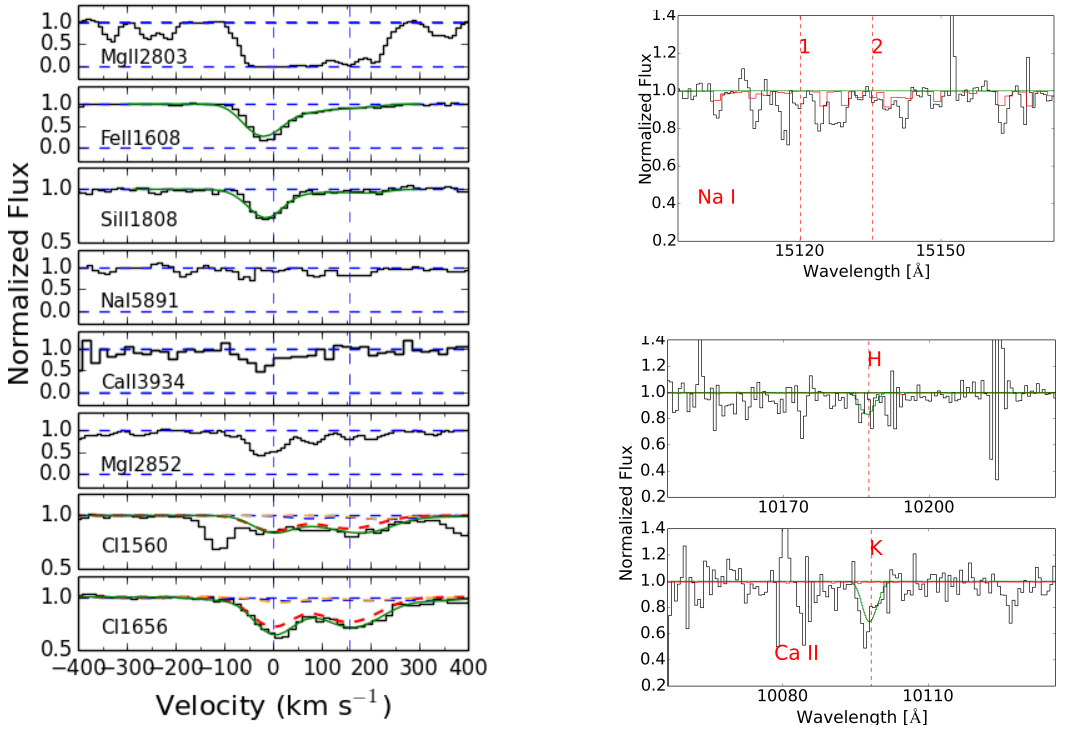

FIGURE 7.36: J0854+0317 − Same as 7.34.

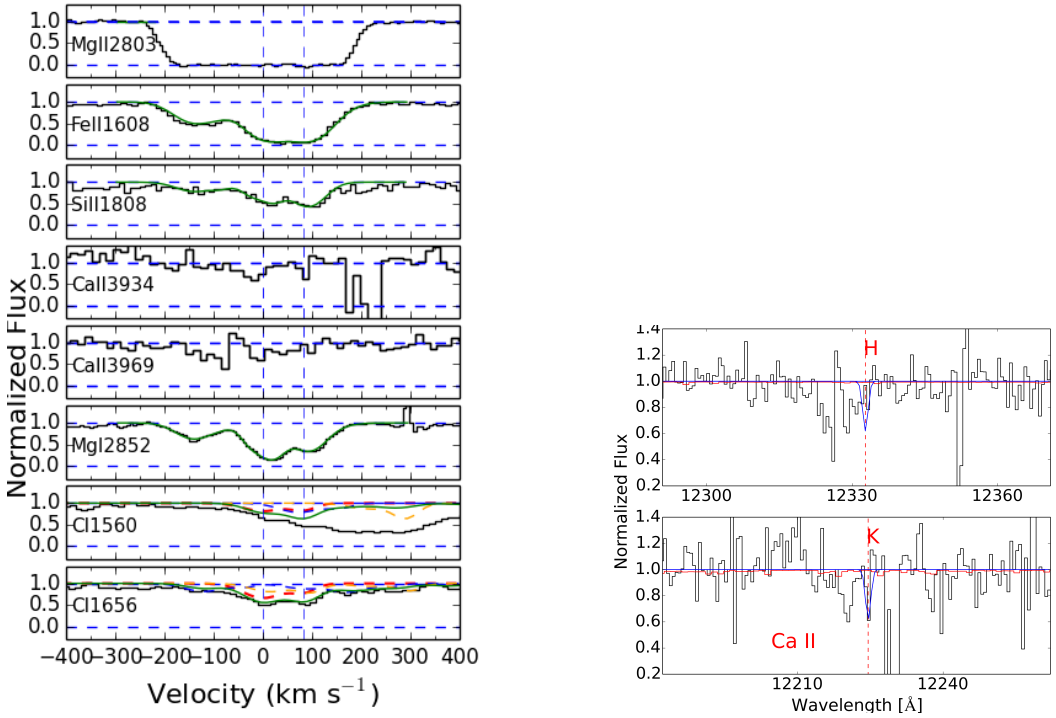

FIGURE 7.37: J0917+0154 − Same as 7.34.

The strongest component of Na I D is shifted by around 25 km/s compared to C I. This may be an artefact of the intermediate resolution of X-shooter as the C I fit is complex and needs at least three components. Higher resolution data are needed to study in more detail the structure of the absorbing cloud. The elements H_2 and CO are detected. Mg II for this system is uncommonly strong and spans around 800 km s^{-1} including components at -350 km s^{-1} and +400 km s^{-1}. Noterdaeme et al. (2010a) first detected CO in this system and used it to measure the cosmic microwave background (CMB) temperature at the corresponding redshift. They obtain a column density of log N(CO) = 14.74±0.07. From the X-shooter data we derive log N(CO) = 14.56±0.92, which is in agreement with the result by Noterdaeme et al. (2011). Daprà et al. (2016) used the CO absorption from this system to constrain the cosmological variation of the proto-to-electron mass ratio. NiII and ZnII are detected.

7.3.6 J1122+1437 − $z_{\rm abs}$ = 1.553779

In this spectrum Ca II and Na I are both detected. The Ca II K line is clearly detected but not Ca II H (see Table 2.3). For the Na I D doublet, both lines are detected. However, Na Iλ5891 is strongly blended with a telluric feature but there is an apparent excess that can be estimated and subtracted (Fig. 7.39 right upper panel). Metal lines and

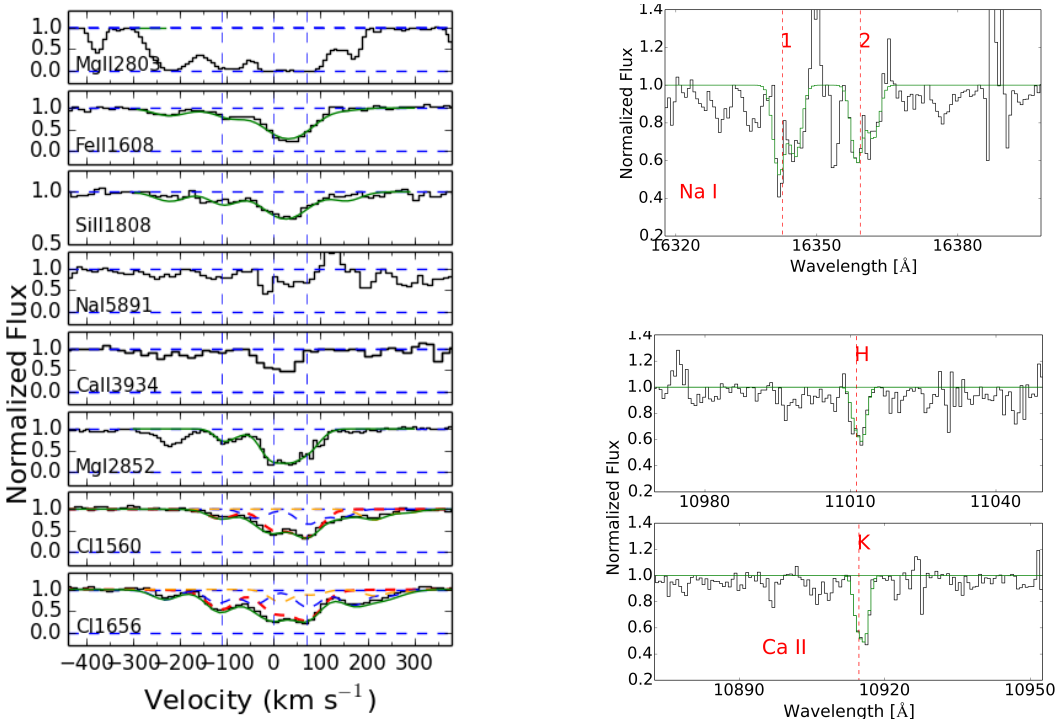

FIGURE 7.38: J1047+2057 − Same as 7.34.

C I absorptions are detected in one strong component plus several weaker components blueshifted by -170,-100, and -20 km s^{-1} relative to the main component.

7.3.7 J1133-0057 − z_{abs} = 1.704536

Both Ca II H&K and Na I D are clearly detected in this good spectrum. This system is a peculiar but interesting case for which the absorbing cloud is small and located at a short distance to the quasar. Indeed, the broad line region (BLR) is only partially covered by the cloud. This system has been analysed by Fathivavsari et al. (2017) who derived an H I column density of 21.00±0.30. There are two main components separated by ∼200 km/s. Although Ca II is detected only in the strongest system, Na I is detected in both. Ca must be highly depleted into dust, which is consistent with the corresponding large attenuation of the quasar (see Table 3).

7.3.8 J1237+0647 − $z_{\rm abs}$ = 2.689602

In this spectrum Na I D is clearly detected while Ca II H& K are strongly blended with telluric absorptions, so there is no EW upper limit for Ca II D. Detection of H_2 and CO

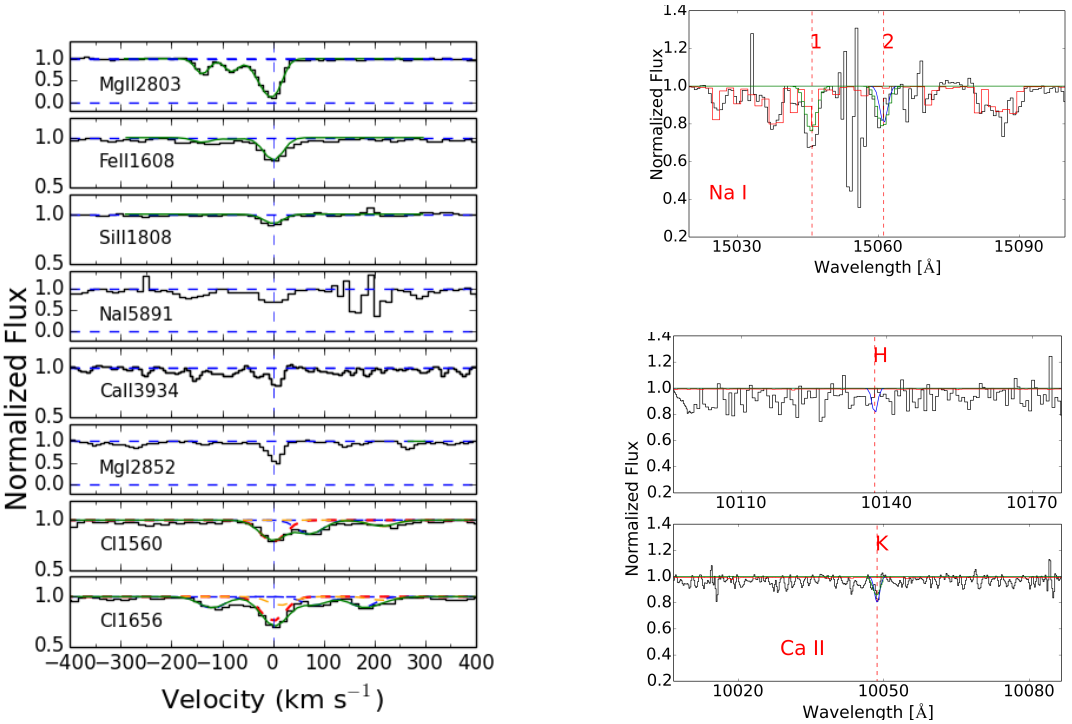

FIGURE 7.39: J1122+1437 – Same as 7.34.

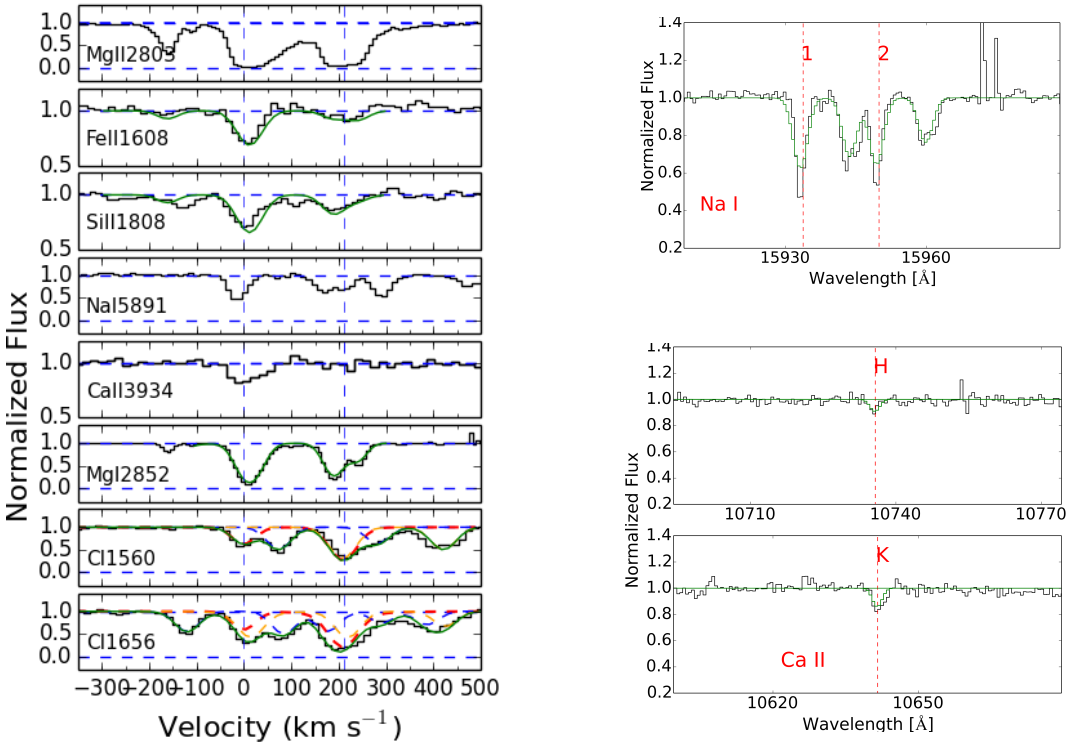

FIGURE 7.40: J1133-0057 – Same as 7.34.

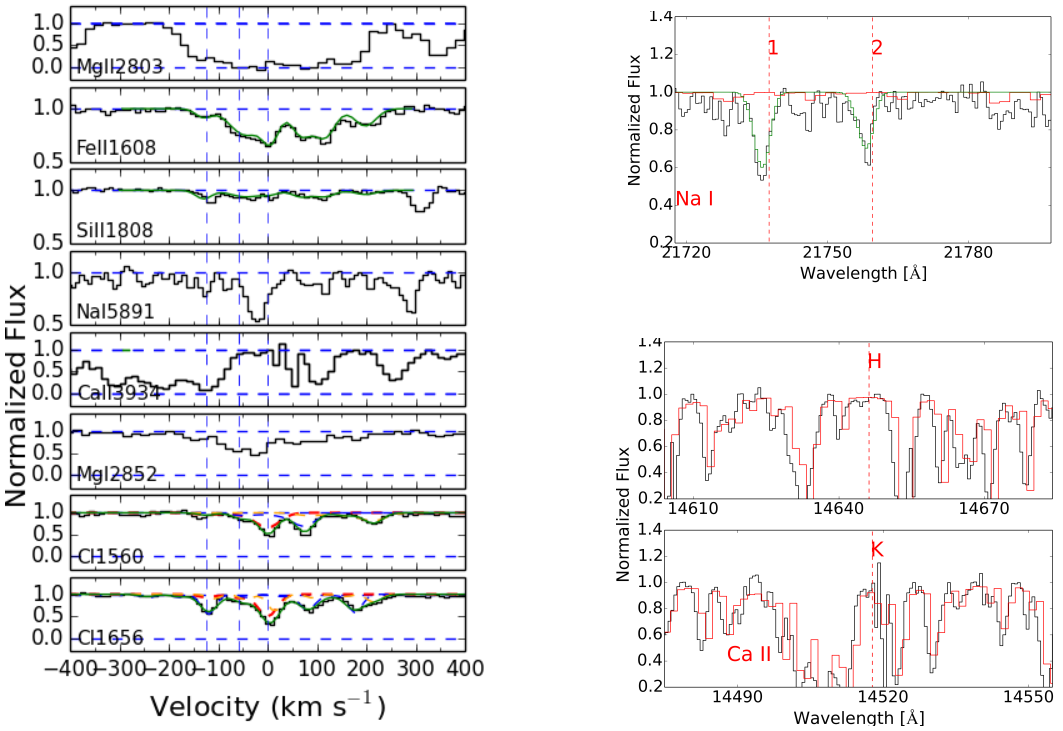

FIGURE 7.41: J1237+0647 : Same as 7.34.

in this system has been published by Noterdaeme et al. (2010a). The excitation of the CO rotational levels is used to measure $T_{\rm CMB}$. The spectrum used by Noterdaeme et al. (2010a) was obtained with UVES and the authors derive log N(HI) = 20.0±0.15, to be compared with our measurement 19.89±0.47. The system is also analysed by Daprà et al. (2016). Three components are used to fit the absorptions from C I and its fine structure lines. The components of Fe II and C I are in exactly the same place.

7.3.9 J1248+2848 – $z_{\rm abs}$ = 1.512373

Both Ca II K & H lines are detected for this system. The Ca II H line is, however, blended with a sky feature, thus the value given in Table 2.3 for the *EW* Ca II H line is somewhat tentative. As in the case of J1346+0644, Na I D lines are badly blended with strong telluric absorptions. This is why we do not give an *EW* upper limit for Na I D. The component at $v \sim$ -250 km s^{-1} is included into the fit and the measurement of W(Mg Iλ2852). The width of the metal line absorption profile is around 575 km s^{-1}.

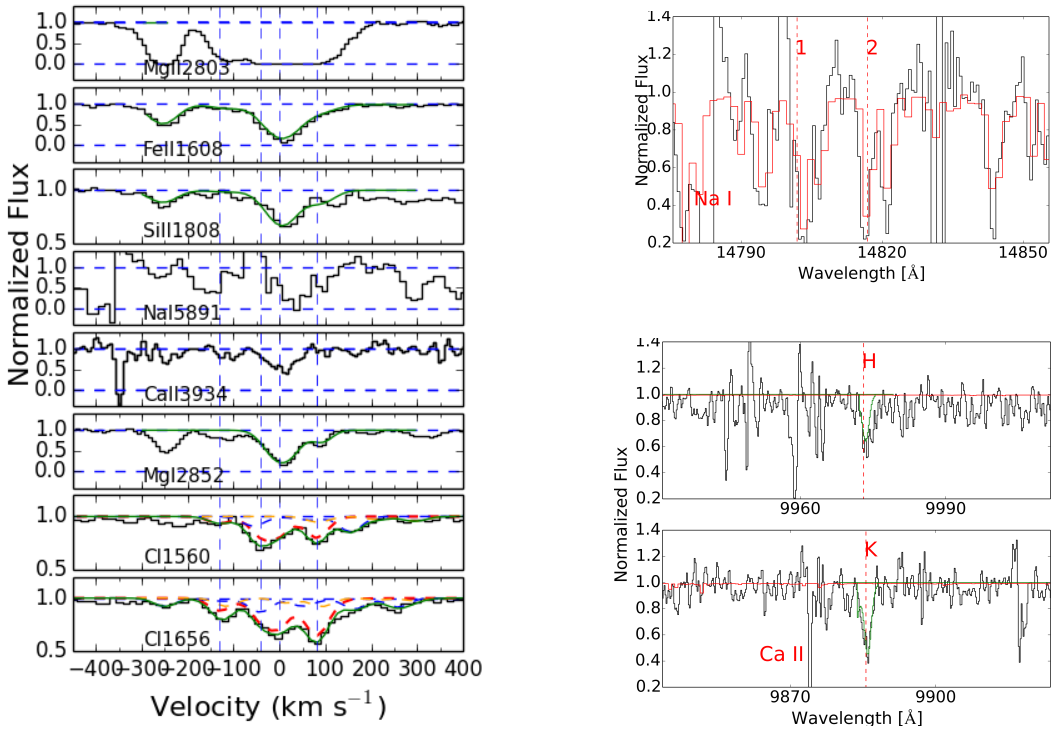

FIGURE 7.42: J1248+2848: Same as 7.34.

7.3.10 J1302+2111 – $z_{\rm abs} = 1.655602$

Both Na I and Ca II are detected for this system. The Na Iλ5891 line is clean, However, there is a spike close to Na Iλ5897 that prevents a direct measurement of the *EW* . We thus fit the doublet using VPFIT to derive the *EW* for Na Iλ5897. The Fe IIλ2586 and Fe IIλ2600 lines are strongly blended with sky absorptions, so we did not use them to fit the Fe II lines. C I is well fitted with one component.

7.3.11 J1314+0543 – $z_{\rm abs} = 1.5828$

There is a clear detection of Na I D in this system. The spectrum is affected by a spike near Na Iλ5897, thus we fit the Na Iλ5891 line and show the corresponding Na Iλ5897 line. The *EW* values in Table 2.3 are from the VPFIT fit. There is not apparent detection of Ca II and we give upper limits on *EW*. There are two strong components at $v = 0$, 160 km/s in the Fe II, Si II, C I, and Mg I absorption profiles. The spike in the spectrum could be due at least partly to Na Iλ5891 in the second component, the corresponding Na Iλ5897 being affected by a residual from sky subtraction. We detect Zn II, Mn II and Ni II , with depletion factor [Fe/Zn] = -0.95 ± 0.05.

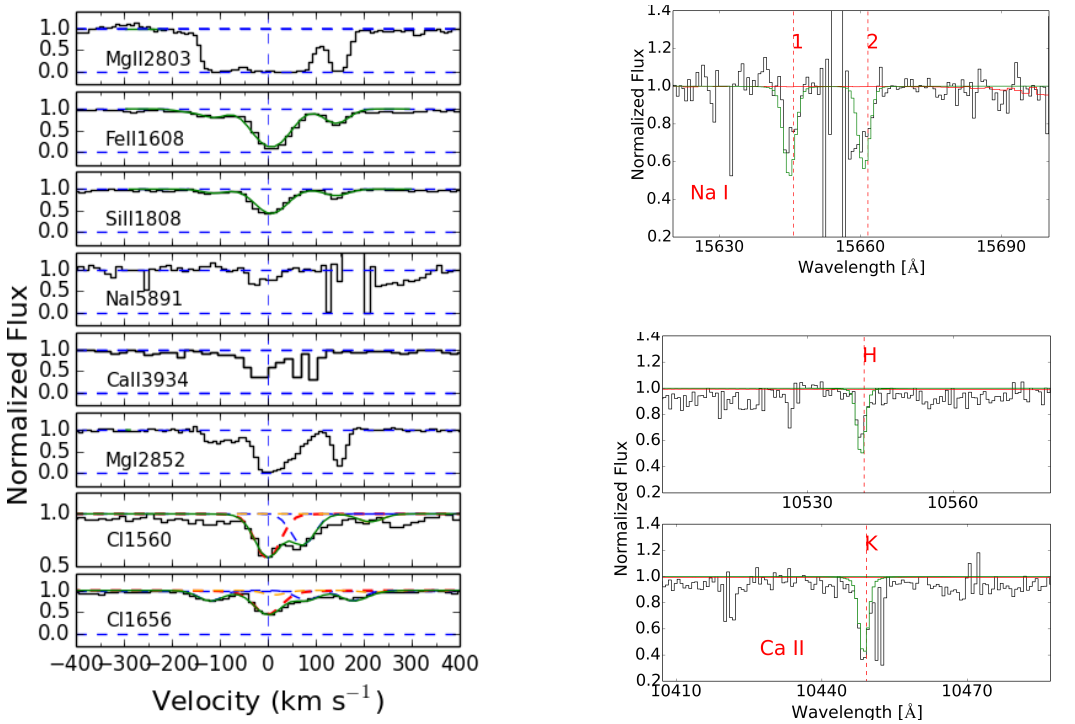

FIGURE 7.43: J1302+2111 : Same as 7.34.

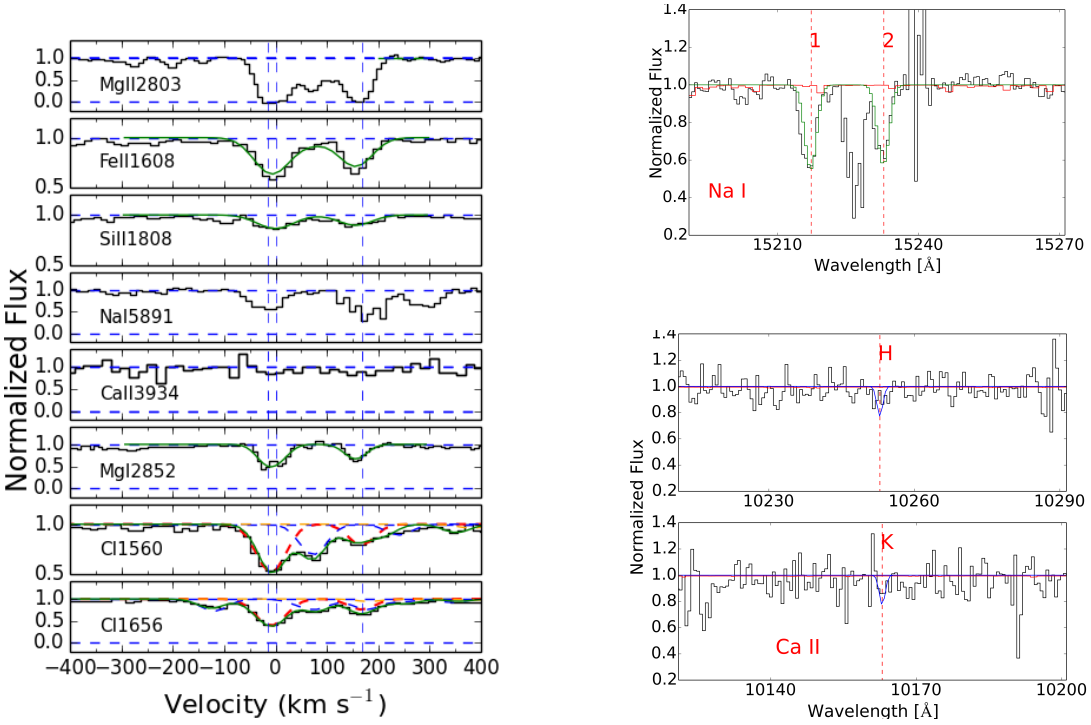

FIGURE 7.44: J1314+0543 : Same as 7.34.

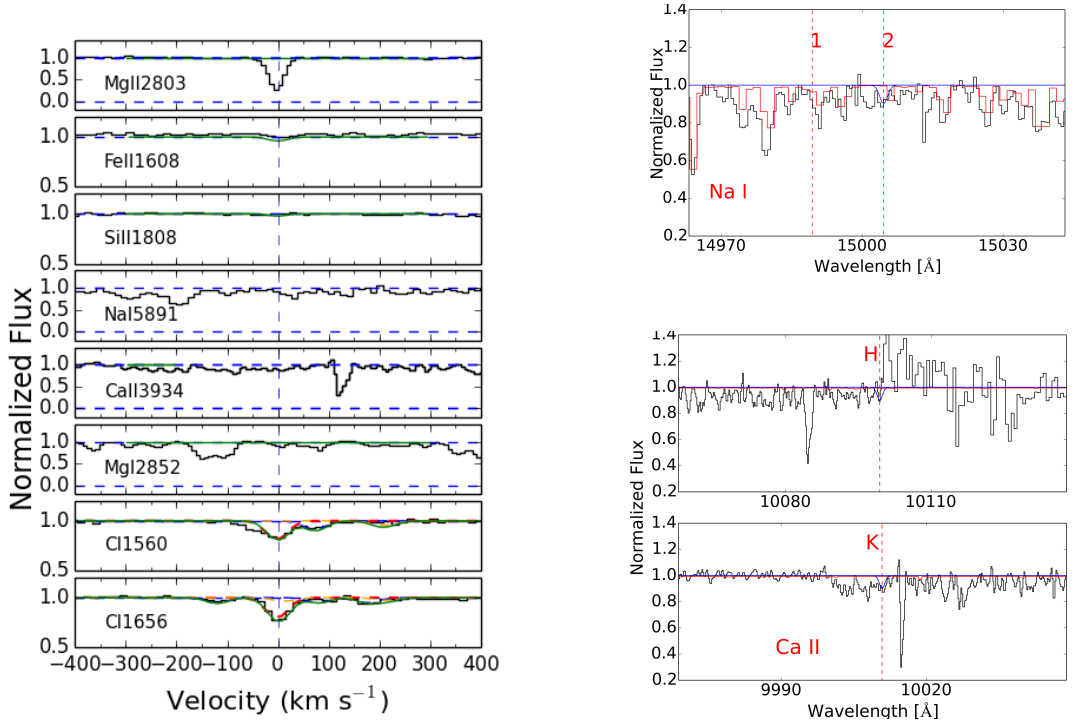

FIGURE 7.45: J1341+1852 : Same as 7.34.

7.3.12 J1341+1852 – $z_{\rm abs} = 1.5442$

This system is peculiar as it turns out to be a sub-DLA, with column density $\log N(\mathrm{HI}) = 18.18 \pm 0.05$. The C I and other metal line absorptions are weak, with C Iλ1560 equivalent width $\sim$0.13 Å (well below the mean $EW = 0.38$ Å in the sample), and W(Mg IIλ2798) = 0.33 Å (for a mean EW = 2.76 Å in the sample). The metallicity is high with [OI/HI] = +0.36, relative to solar. It might be interesting to derive the physical properties of this gas and in particular its ionization state. Indeed, it is surprising to detect C I in such a system. This is, however, out of the scope of the present paper. There are no obvious detections of either Ca II H&K or Na I D. We give EW upper limits for the lines.

7.3.13 J1346+0644 – $z_{\rm abs} = 1.511938$

The Na I D line is strongly blended with sky features so that it is difficult to measure even an upper limit. We did not detect Ca II i. The C I absorptions are fitted well with two components at $z = 1.511938$ and $z = 1.512393$ ($\Delta v \sim 50$ km s^{-1}). The Mg I absorption is extended over $\sim$200 km s^{-1}. The strongest components of Fe II and Si II are blueshifted by $\sim$100 kms^{-1} relative to the strongest components of C I and Mg I, which may indicate

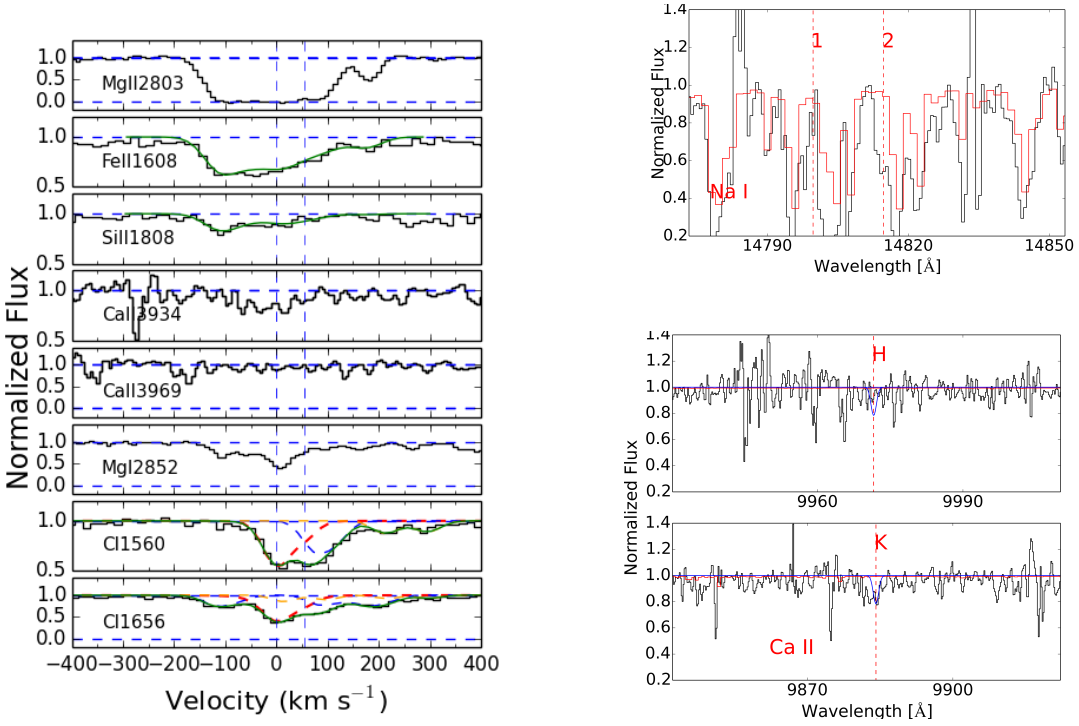

FIGURE 7.46: J1346+0644 : Same as 7.34.

there is one more component of C I at -100 kms^{-1}. Since there is basically no flux in the spectrum at wavelengths smaller than 3200 Å, we cannot derive the H I column density.

7.3.14 J2229+1414 – $z_{\rm abs}$ = 1.585372

For this system Na I D is clearly detected and strong. We derive upper limits for the Ca II lines (0.55 Å). The metal lines are relatively weak compared to other systems. The C I and Mg I main features are located on the blue edge of the Mg II profile, which is $\sim$200 km s^{-1} wide.

7.3.15 J2336-1058 – $z_{\rm abs}$=1.828723

For this system, the Ca II doublet is lost in strong sky absorption features. We detect Na I D. The Na Iλ5891 line is slightly blended with a sky absorption, which is subtracted to derive *EW*. The C I absorptions are not very strong but we can see two components. The Zn II line is detected and we derive a depletion factor [Fe/Zn] = -1.11 ± 0.10.

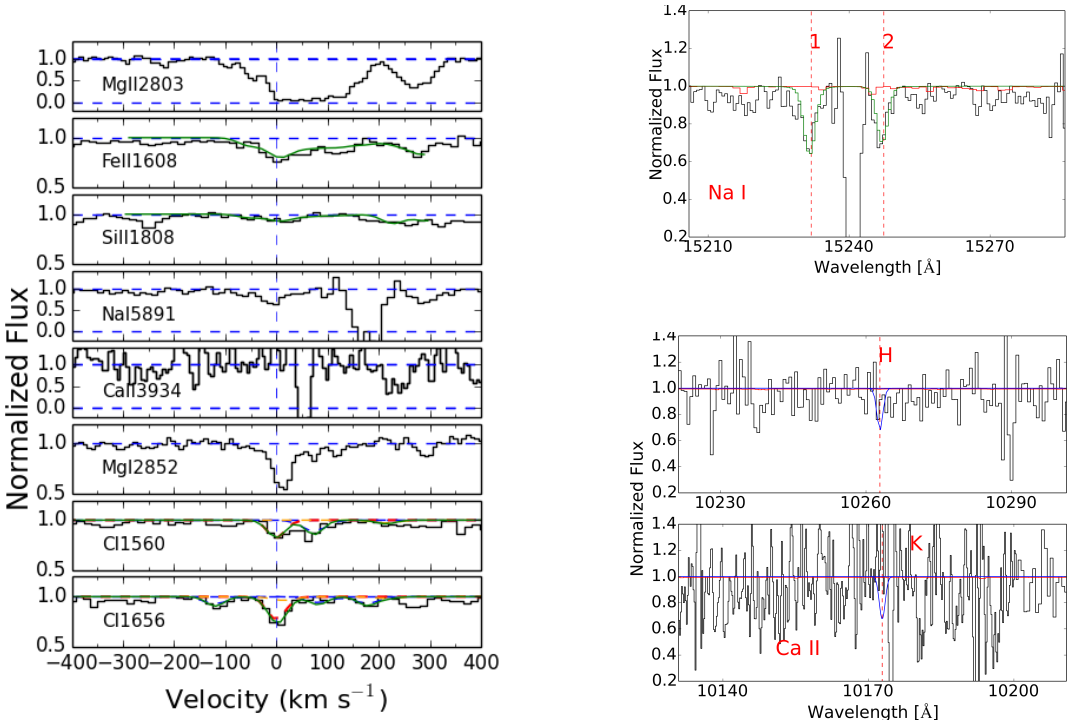

FIGURE 7.47: J2229+1414 : Same as 7.34.

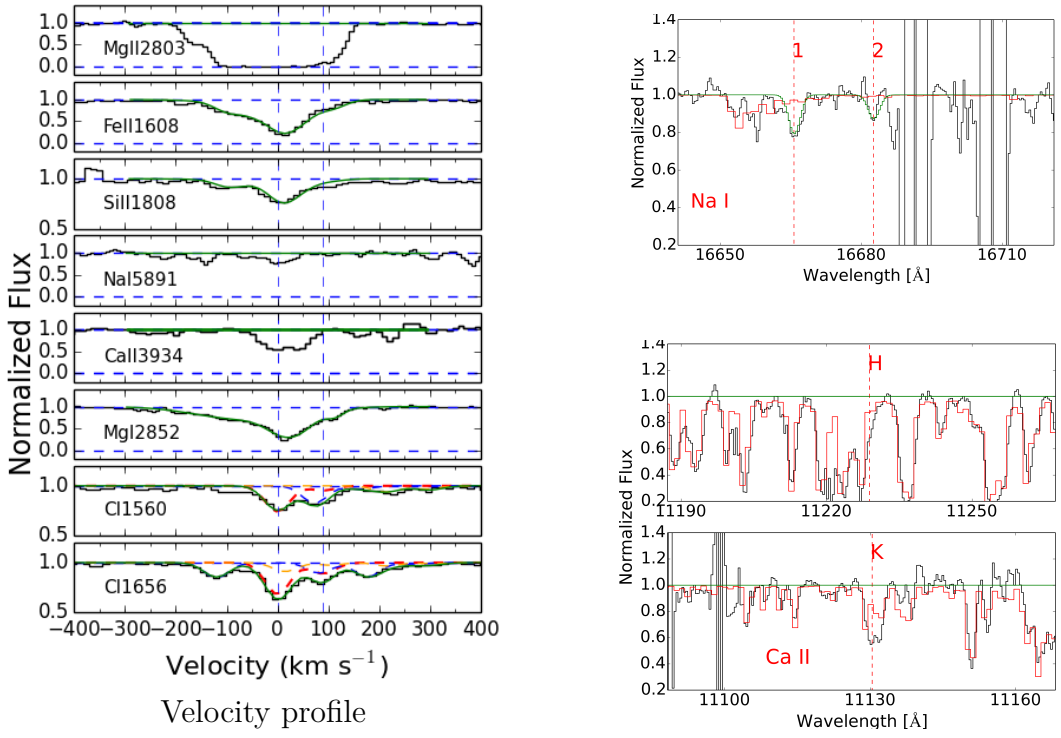

Velocity profile

FIGURE 7.48: J2336-1058 : Same as 7.34.

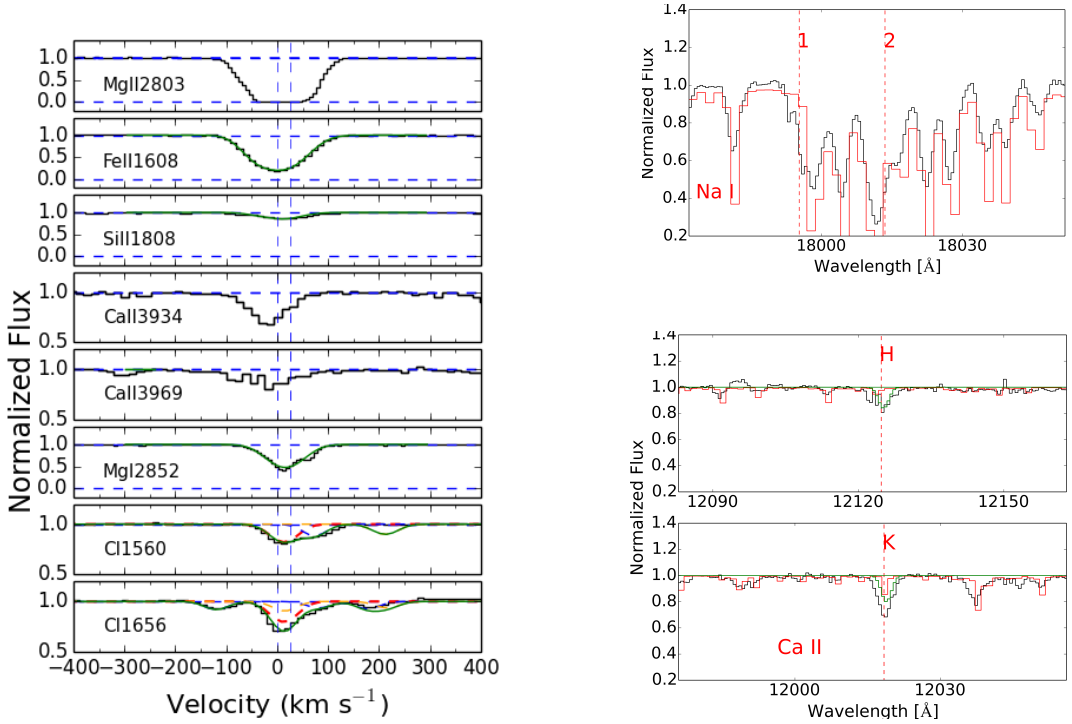

FIGURE 7.49: J2340-0053 : Same as 7.34.

7.3.16 J2340-0053 – $z_{\rm abs} = 2.054643$

For this system Na I D is lost in telluric absorptions. The C I structure is simple with two components. The Ca II doublet is detected although it is blended with weak sky features. We subtracted the latter. H2 is detected in this system. It is mentioned in Boissé et al. (2015), Balashev et al. (2015), who derived a column density of log $N(H_2) = 18.07 \pm 0.06$.

7.3.17 J2350-0052 – $z_{\rm abs} = 2.426475$

Unfortunately both Na I D and Ca II H&K are lost in telluric absorption features. The Fe IIλ1608 and Fe IIλ1611 lines seem to be blended with other lines. There is a $\sim$0.4 Å shift between the UVB and VIS arms that we corrected manually.

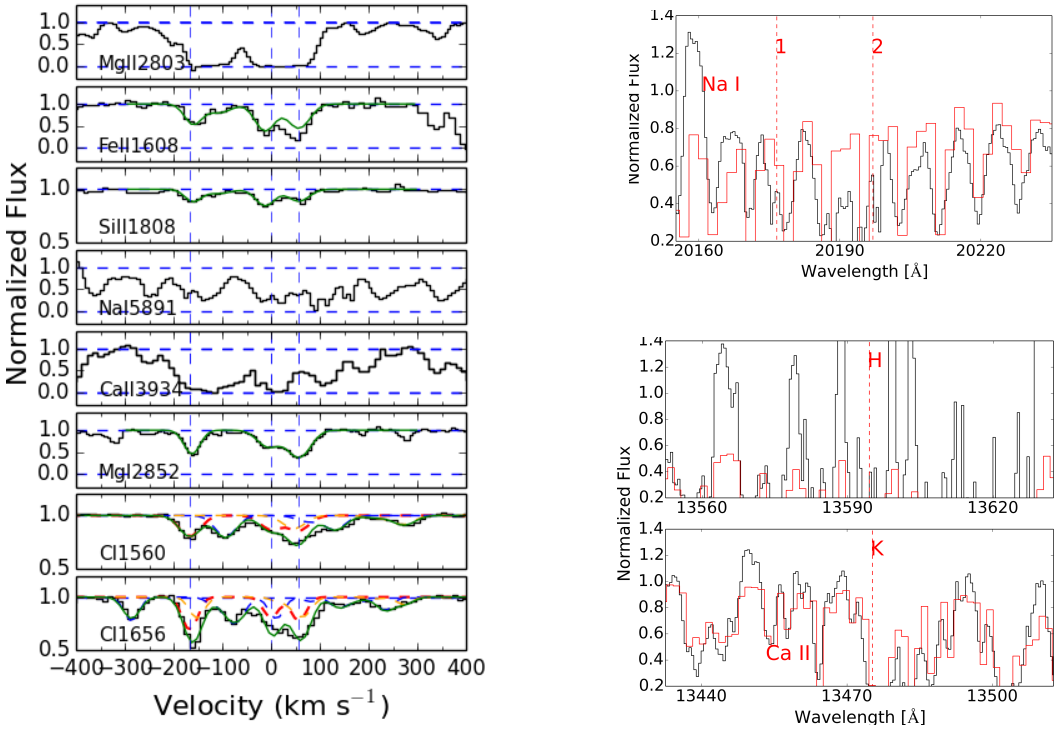

FIGURE 7.50: J2350-0052 : Same as 7.34

Bibliography

Abazajian, K. N., Adelman-McCarthy, J. K., Agüeros, M. A., et al. 2009, ApJS, 182, 543

Altay, G., Theuns, T., Schaye, J., Crighton, N. H. M., & Dalla Vecchia, C. 2011, ApJ, 737, L37

Aubourg, É., Bailey, S., Bautista, J. E., et al. 2015, Phys. Rev. D, 92, 123516

Bañados, E., Venemans, B. P., Mazzucchelli, C., et al. 2017, ArXiv e-prints [[arXiv]1712.01860]

Bahcall, J. N. & Peebles, P. J. E. 1969, ApJ, 156, L7

Balashev, S. A., Klimenko, V. V., Ivanchik, A. V., et al. 2014, MNRAS, 440, 225

Balashev, S. A. & Noterdaeme, P. 2018, MNRAS, 478, L7

Balashev, S. A., Noterdaeme, P., Klimenko, V. V., et al. 2015, A&A, 575, L8

Balashev, S. A., Noterdaeme, P., Rahmani, H., et al. 2017, MNRAS, 470, 2890

Balashev, S. A., Petitjean, P., Ivanchik, A. V., et al. 2011, MNRAS, 418, 357

Beaver, E. A., Burbidge, E. M., McIlwain, C. E., Epps, H. W., & Strittmatter, P. A. 1972, ApJ, 178, 95

Beers, T. C. & Christlieb, N. 2005, ARA&A, 43, 531

Bekhti, N. B., Murphy, M., Richter, P., & Westmeier, T. 2008, Astrophysics and Space Science Proceedings, 5, 273

Bekki, K., Hirashita, H., & Tsujimoto, T. 2015, ApJ, 810, 39

Ben Bekhti, N., Winkel, B., Richter, P., et al. 2012, A&A, 542, A110

Berg, T. A. M., Ellison, S. L., Prochaska, J. X., Venn, K. A., & Dessauges-Zavadsky, M. 2015, MNRAS, 452, 4326

Berg, T. A. M., Ellison, S. L., Sánchez-Ramírez, R., et al. 2016, MNRAS, 463, 3021

Bergeron, J., Aracil, B., Petitjean, P., & Pichon, C. 2002, A&A, 396, L11

Bergeron, J. & Stasińska, G. 1986, A&A, 169, 1

Berry, M., Somerville, R. S., Gawiser, E., et al. 2016, MNRAS, 458, 531

Bi, H. & Davidsen, A. F. 1997, ApJ, 479, 523

Bi, H., Ge, J., & Fang, L.-Z. 1995, ApJ, 452, 90

Bird, S., Haehnelt, M., Neeleman, M., et al. 2015, MNRAS, 447, 1834

Bird, S., Vogelsberger, M., Haehnelt, M., et al. 2014, MNRAS, 445, 2313

Black, J. H. 1987, in Astrophysics and Space Science Library, Vol. 134, Interstellar Processes, ed. D. J. Hollenbach & H. A. Thronson, Jr., 731–744

Blades, J. C., Turnshek, D. A., & Norman, C. A., eds. 1988, QSO Absorption Lines: Probing the Universe. Proceedings of the QSO Absorption Line Meeting held May 19-21, 1987, in Baltimore, MD USA.

Bohlin, R. C., Savage, B. D., & Drake, J. F. 1978, ApJ, 224, 132

Boissé, P. 1995, in QSO Absorption Lines, ed. G. Meylan, 35

Boissé, P., Bergeron, J., Prochaska, J. X., Péroux, C., & York, D. G. 2015, A&A, 581, A109

Bouché, N. 2008, MNRAS, 389, L18

Bouché, N., Finley, H., Schroetter, I., et al. 2016, ApJ, 820, 121

Bouché, N., Murphy, M. T., Kacprzak, G. G., et al. 2013, Science, 341, 50

Bouché, N., Murphy, M. T., Péroux, C., et al. 2012, MNRAS, 419, 2

Bouché, N., Murphy, M. T., Péroux, C., Csabai, I., & Wild, V. 2007, , 51, 131

Bouwens, R. J., Illingworth, G. D., Oesch, P. A., et al. 2010, ApJ, 709, L133

Bowen, D. V., Pettini, M., Penston, M. V., & Blades, C. 1991, MNRAS, 249, 145

Boyle, B. J. 1990, MNRAS, 243, 231

Brown, R. L. & Roberts, M. S. 1973, ApJ, 184, L7

Bunker, A. J., Warren, S. J., Clements, D. L., Williger, G. M., & Hewett, P. C. 1999, MNRAS, 309, 875

Busca, N. G., Delubac, T., Rich, J., et al. 2013, A&A, 552, A96

Carswell, R. F. 2003, QSO absorption lines, winds, and the high-redshift intergalactic medium

Carswell, R. F., Hilliard, R. L., Strittmatter, P. A., Taylor, D. J., & Weymann, R. J. 1975, ApJ, 196, 351

Carswell, R. F. & Webb, J. K. 2014, VPFIT: Voigt profile fitting program, Astrophysics Source Code Library

Cavaliere, A. & Vittorini, V. 2000, ApJ, 543, 599

Cen, R. & Chisari, N. E. 2011, ApJ, 731, 11

Cen, R., Miralda-Escudé, J., Ostriker, J. P., & Rauch, M. 1994, ApJ, 437, L9

Charlton, J. & Churchill, C. 2000, Quasistellar Objects: Intervening Absorption Lines, ed. P. Murdin, 2366

Charlton, J. C. & Churchill, C. W. 1996, ApJ, 465, 631

Chen, B., Dai, X., Kochanek, C. S., & Chartas, G. 2013, ArXiv e-prints [[arXiv]1306.0008]

Chen, H.-W. & Lanzetta, K. M. 2003, ApJ, 597, 706

Cherinka, B. & Schulte-Ladbeck, R. E. 2011, AJ, 142, 122

Christensen, L., Møller, P., Fynbo, J. P. U., & Zafar, T. 2014, MNRAS, 445, 225

Cooper, T. J., Simcoe, R. A., Cooksey, K. L., O'Meara, J. M., & Torrey, P. 2015, ApJ, 812, 58

Cowie, L. L. & Hu, E. M. 1998, AJ, 115, 1319

Cowie, L. L., Songaila, A., Kim, T.-S., & Hu, E. M. 1995, AJ, 109, 1522

Cox, N. L. J., Cordiner, M. A., Ehrenfreund, P., et al. 2007, A&A, 470, 941

Cristiani, S. & Vio, R. 1990, A&A, 227, 385

Cui, J., Bechtold, J., Ge, J., & Meyer, D. M. 2005, ApJ, 633, 649

Daprà, M., Niu, M. L., Salumbides, E. J., Murphy, M. T., & Ubachs, W. 2016, ApJ, 826, 192

De Cia, A., Ledoux, C., Mattsson, L., et al. 2016, A&A, 596, A97

De Cia, A., Ledoux, C., Savaglio, S., Schady, P., & Vreeswijk, P. M. 2013, A&A, 560, A88

Delubac, T., Bautista, J. E., Busca, N. G., et al. 2015, A&A, 574, A59

D'Odorico, V., Cristiani, S., Pomante, E., et al. 2016, MNRAS, 463, 2690

Draine, B. T. & Malhotra, S. 1993, ApJ, 414, 632

Edmunds, M. G. & Eales, S. A. 1998, MNRAS, 299, L29

Eisenstein, D. J., Weinberg, D. H., Agol, E., et al. 2011, AJ, 142, 72

Ellison, S. L. 2006, MNRAS, 368, 335

Ellison, S. L., Hall, P. B., & Lira, P. 2005, AJ, 130, 1345

Ellison, S. L., Lewis, G. F., Pettini, M., Chaffee, F. H., & Irwin, M. J. 1999, ApJ, 520, 456

Ellison, S. L., Songaila, A., Schaye, J., & Pettini, M. 2000, AJ, 120, 1175

Epinat, B., Contini, T., Le Fèvre, O., et al. 2009, A&A, 504, 789

Fan, X., Strauss, M. A., Becker, R. H., et al. 2006, AJ, 132, 117

Fan, X., Strauss, M. A., Schneider, D. P., et al. 2003, AJ, 125, 1649

Fathivavsari, H., Petitjean, P., Zou, S., et al. 2017, MNRAS, 466, L58

Ferland, G. J., Chatzikos, M., Guzmán, F., et al. 2017, , 53, 385

Ferland, G. J., Korista, K. T., Verner, D. A., et al. 1998, PASP, 110, 761

Ferland, G. J. & Mushotzky, R. F. 1984, ApJ, 286, 42

Ferland, G. J., Porter, R. L., van Hoof, P. A. M., et al. 2013, , 49, 137

Ferlet, R., Vidal-Madjar, A., & Gry, C. 1985, ApJ, 298, 838

Fitzpatrick, E. L. 1985, ApJ, 299, 219

Fitzpatrick, E. L. 1999, PASP, 111, 63

Fitzpatrick, E. L. & Massa, D. 1990, ApJS, 72, 163

Ford, A. B., Davé, R., Oppenheimer, B. D., et al. 2014, MNRAS, 444, 1260

Francis, P. J., Hewett, P. C., Foltz, C. B., et al. 1991, ApJ, 373, 465

Franco, J. & Cox, D. P. 1986, PASP, 98, 1076

Fumagalli, M., O'Meara, J. M., Prochaska, J. X., Rafelski, M., & Kanekar, N. 2015, MNRAS, 446, 3178

Fumagalli, M., O'Meara, J. M., Prochaska, J. X., & Worseck, G. 2013, ApJ, 775, 78

Fumagalli, M., Prochaska, J. X., Kasen, D., et al. 2011, MNRAS, 418, 1796

Fynbo, J. P. U., Laursen, P., Ledoux, C., et al. 2010, MNRAS, 408, 2128

Fynbo, J. P. U., Ledoux, C., Noterdaeme, P., et al. 2011, MNRAS, 413, 2481

Fynbo, J. P. U., Møller, P., Thomsen, B., et al. 2002, A&A, 388, 425

Fynbo, J. P. U., Prochaska, J. X., Sommer-Larsen, J., Dessauges-Zavadsky, M., & Møller, P. 2008, ApJ, 683, 321

Fynbo, J. U., Møller, P., & Warren, S. J. 1999, MNRAS, 305, 849

Ge, J. & Bechtold, J. 1997, ApJ, 477, L73

Ge, J. & Bechtold, J. 1999, in Astronomical Society of the Pacific Conference Series, Vol. 156, Highly Redshifted Radio Lines, ed. C. L. Carilli, S. J. E. Radford, K. M. Menten, & G. I. Langston, 121

Giavalisco, M. 2002, ARA&A, 40, 579

Glikman, E., Helfand, D. J., & White, R. L. 2006, ApJ, 640, 579

Gordon, K. D., Clayton, G. C., Misselt, K. A., Landolt, A. U., & Wolff, M. J. 2003, ApJ, 594, 279

Guber, C. R. & Richter, P. 2016, A&A, 591, A137

Gunn, J. E. & Peterson, B. A. 1965, ApJ, 142, 1633

Haardt, F. & Madau, P. 2012, ApJ, 746, 125

Haehnelt, M. G., Steinmetz, M., & Rauch, M. 1996, ApJ, 465, L95

Hall, P. B., Anderson, S. F., Strauss, M. A., et al. 2002, ApJS, 141, 267

Heisler, J. & Ostriker, J. P. 1988, ApJ, 325, 103

Hernquist, L., Katz, N., Weinberg, D. H., & Miralda-Escudé, J. 1996, ApJ, 457, L51

Hewett, P. C. & Wild, V. 2007, MNRAS, 379, 738

Hobbs, L. M. 1974, ApJ, 191, 381

Hobbs, L. M. 1975, ApJ, 202, 628

Hu, E. M., Kim, T.-S., Cowie, L. L., Songaila, A., & Rauch, M. 1995, AJ, 110, 1526

Hui, L., Gnedin, N. Y., & Zhang, Y. 1997, ApJ, 486, 599

Jenkins, E. B., Savage, B. D., & Spitzer, Jr., L. 1986, ApJ, 301, 355

Jenkins, E. B. & Shaya, E. J. 1979, ApJ, 231, 55

Jenkins, E. B. & Tripp, T. M. 2001, ApJS, 137, 297

Jiang, P., Ge, J., Zhou, H., Wang, J., & Wang, T. 2011, ApJ, 732, 110

Jorgenson, R. A., Murphy, M. T., Thompson, R., & Carswell, R. F. 2014, MNRAS, 443, 2783

Jorgenson, R. A., Wolfe, A. M., & Prochaska, J. X. 2010, ApJ, 722, 460

Joshi, R., Srianand, R., Noterdaeme, P., & Petitjean, P. 2017, MNRAS, 465, 701

Kacprzak, G. G. & Churchill, C. W. 2011, ApJ, 743, L34

Kacprzak, G. G., Churchill, C. W., Ceverino, D., et al. 2010, ApJ, 711, 533

Kalberla, P. M. W. & Kerp, J. 2009, ARA&A, 47, 27

Kanekar, N., Chengalur, J. N., & Lane, W. M. 2007, MNRAS, 375, 1528

Kanekar, N., Prochaska, J. X., Ellison, S. L., & Chengalur, J. N. 2009, MNRAS, 396, 385

Kanekar, N., Prochaska, J. X., Smette, A., et al. 2014, MNRAS, 438, 2131

Keenan, F. P., Dufton, P. L., McKeith, C. D., & Blades, J. C. 1983, MNRAS, 203, 963

Kennicutt, Jr., R. C. 1998a, ARA&A, 36, 189

Kennicutt, Jr., R. C. 1998b, ApJ, 498, 541

Kennicutt, Jr., R. C., Tamblyn, P., & Congdon, C. E. 1994, ApJ, 435, 22

Kim, T.-S., Partl, A. M., Carswell, R. F., & Müller, V. 2013, A&A, 552, A77

Krogager, J.-K., Fynbo, J. P. U., Møller, P., et al. 2012, MNRAS, 424, L1

Krogager, J.-K., Geier, S., Fynbo, J. P. U., et al. 2015, ApJS, 217, 5

Krogager, J.-K., Møller, P., Fynbo, J. P. U., & Noterdaeme, P. 2017, MNRAS, 469, 2959

Kulkarni, V. P., Fall, S. M., Lauroesch, J. T., et al. 2005, ApJ, 618, 68

Kulkarni, V. P., Khare, P., Péroux, C., et al. 2007, ApJ, 661, 88

Kulkarni, V. P., Meiring, J., Som, D., et al. 2012, ApJ, 749, 176

Kunth, D. & Bergeron, J. 1984, MNRAS, 210, 873

Lanzetta, K. M., Turnshek, D. A., & Wolfe, A. M. 1987, ApJ, 322, 739

Lanzetta, K. M., Wolfe, A. M., Turnshek, D. A., et al. 1991, ApJS, 77, 1

Law, D. R., Steidel, C. C., Erb, D. K., et al. 2009, ApJ, 697, 2057

Ledoux, C., Noterdaeme, P., Petitjean, P., & Srianand, R. 2015, A&A, 580, A8

Ledoux, C., Petitjean, P., Fynbo, J. P. U., Møller, P., & Srianand, R. 2006, A&A, 457, 71

Ledoux, C., Petitjean, P., & Srianand, R. 2003, MNRAS, 346, 209

Ledoux, C., Srianand, R., & Petitjean, P. 2002, A&A, 392, 781

Lee, K.-G., Bailey, S., Bartsch, L. E., et al. 2013, AJ, 145, 69

Lehner, N., Howk, J. C., Tripp, T. M., et al. 2013, ApJ, 770, 138

Lehnert, M. D., Nesvadba, N. P. H., Le Tiran, L., et al. 2009, ApJ, 699, 1660

Liu, X., Shapley, A. E., Coil, A. L., Brinchmann, J., & Ma, C.-P. 2008, ApJ, 678, 758

López, S., D'Odorico, V., Ellison, S. L., et al. 2016, A&A, 594, A91

Lusso, E., Worseck, G., Hennawi, J. F., et al. 2015, MNRAS, 449, 4204

Ma, J., Caucal, P., Noterdaeme, P., et al. 2015, MNRAS, 454, 1751

Ma, J., Ge, J., Zhao, Y., et al. 2017, MNRAS, 472, 2196

Madau, P., Pozzetti, L., & Dickinson, M. 1998, ApJ, 498, 106

Maiolino, R., Nagao, T., Grazian, A., et al. 2008, A&A, 488, 463

Mannucci, F., Cresci, G., Maiolino, R., Marconi, A., & Gnerucci, A. 2010, MNRAS, 408, 2115

Mannucci, F., Cresci, G., Maiolino, R., et al. 2009, MNRAS, 398, 1915

Martin, C. L., Shapley, A. E., Coil, A. L., et al. 2012, ApJ, 760, 127

Mather, J. C., Fixsen, D. J., Shafer, R. A., Mosier, C., & Wilkinson, D. T. 1999, ApJ, 512, 511

McDonald, P. & Eisenstein, D. J. 2007, Phys. Rev. D, 76, 063009

Ménard, B. & Chelouche, D. 2009, MNRAS, 393, 808

Miralda-Escudé, J., Cen, R., Ostriker, J. P., & Rauch, M. 1996, ApJ, 471, 582

Modigliani, A., Goldoni, P., Royer, F., et al. 2010, in Proc. SPIE, Vol. 7737, Observatory Operations: Strategies, Processes, and Systems III, 773728

Møller, P., Fynbo, J. P. U., & Fall, S. M. 2004, A&A, 422, L33

Møller, P., Fynbo, J. P. U., Ledoux, C., & Nilsson, K. K. 2013, MNRAS, 430, 2680

Møller, P., Warren, S. J., Fall, S. M., Fynbo, J. U., & Jakobsen, P. 2002, ApJ, 574, 51

Muecket, J. P., Petitjean, P., Kates, R. E., & Riediger, R. 1996, A&A, 308, 17

Murga, M., Zhu, G., Ménard, B., & Lan, T.-W. 2015, MNRAS, 452, 511

Nagamine, K., Springel, V., & Hernquist, L. 2004, MNRAS, 348, 435

Neeleman, M., Prochaska, J. X., Ribaudo, J., et al. 2016, ApJ, 818, 113

Neeleman, M., Wolfe, A. M., Prochaska, J. X., & Rafelski, M. 2013, ApJ, 769, 54

Nestor, D. B., Johnson, B. D., Wild, V., et al. 2011, MNRAS, 412, 1559

Nestor, D. B., Pettini, M., Hewett, P. C., Rao, S., & Wild, V. 2008, MNRAS, 390, 1670

Nestor, D. B., Rao, S. M., Turnshek, D. A., et al. 2002, in Astronomical Society of the Pacific Conference Series, Vol. 254, Extragalactic Gas at Low Redshift, ed. J. S. Mulchaey & J. T. Stocke, 34

Nestor, D. B., Turnshek, D. A., & Rao, S. M. 2005, ApJ, 628, 637

Noterdaeme, P., Laursen, P., Petitjean, P., et al. 2012a, A&A, 540, A63

Noterdaeme, P., Ledoux, C., Petitjean, P., et al. 2007, A&A, 474, 393

Noterdaeme, P., Ledoux, C., Petitjean, P., & Srianand, R. 2008, A&A, 481, 327

Noterdaeme, P., Ledoux, C., Zou, S., et al. 2018, ArXiv e-prints [[arXiv]1801.08357]

Noterdaeme, P., Petitjean, P., Carithers, W. C., et al. 2012b, A&A, 547, L1

Noterdaeme, P., Petitjean, P., Carithers, W. C., et al. 2012c, A&A, 547, L1

Noterdaeme, P., Petitjean, P., Ledoux, C., et al. 2010a, A&A, 523, A80

Noterdaeme, P., Petitjean, P., Ledoux, C., & Srianand, R. 2009, A&A, 505, 1087

Noterdaeme, P., Petitjean, P., Pâris, I., et al. 2014, A&A, 566, A24

Noterdaeme, P., Petitjean, P., & Srianand, R. 2015, A&A, 578, L5

Noterdaeme, P., Petitjean, P., Srianand, R., Ledoux, C., & López, S. 2011, A&A, 526, L7

Noterdaeme, P., Srianand, R., & Mohan, V. 2010b, MNRAS, 403, 906

O'Meara, J. M., Prochaska, J. X., Burles, S., et al. 2007, ApJ, 656, 666

O'Meara, J. M., Prochaska, J. X., Worseck, G., Chen, H.-W., & Madau, P. 2013, ApJ, 765, 137

Ouchi, M., Harikane, Y., Shibuya, T., et al. 2018, PASJ, 70, S13

Ouchi, M., Shimasaku, K., Akiyama, M., et al. 2008, ApJS, 176, 301

Ouchi, M., Shimasaku, K., Furusawa, H., et al. 2010, ApJ, 723, 869

Ouchi, M., Shimasaku, K., Okamura, S., et al. 2004, ApJ, 611, 660

Ozbek, M., Croft, R. A. C., & Khandai, N. 2016, MNRAS, 456, 3610

Pâris, I., Petitjean, P., Aubourg, É., et al. 2012, A&A, 548, A66

Pâris, I., Petitjean, P., Aubourg, E., et al. 2017a, ArXiv e-prints [[arXiv]1712.05029]

Pâris, I., Petitjean, P., Aubourg, É., et al. 2014, A&A, 563, A54

Pâris, I., Petitjean, P., Ross, N. P., et al. 2017b, A&A, 597, A79

Pei, Y. C. 1992, ApJ, 395, 130

Pei, Y. C., Fall, S. M., & Bechtold, J. 1991, ApJ, 378, 6

Péroux, C., Bouché, N., Kulkarni, V. P., York, D. G., & Vladilo, G. 2011, MNRAS, 410, 2237

Péroux, C., Storrie-Lombardi, L. J., McMahon, R. G., Irwin, M., & Hook, I. M. 2001, AJ, 121, 1799

Petitjean, P., Aracil, B., Srianand, R., & Ibata, R. 2000, A&A, 359, 457

Petitjean, P., Mueket, J. P., & Kates, R. E. 1995, A&A, 295, L9

Petitjean, P., Srianand, R., & Ledoux, C. 2002, MNRAS, 332, 383

Petitjean, P., Theodore, B., Smette, A., & Lespine, Y. 1996, A&A, 313, L25

Petitjean, P., Webb, J. K., Rauch, M., Carswell, R. F., & Lanzetta, K. 1993, MNRAS, 262, 499

Pettini, M., King, D. L., Smith, L. J., & Hunstead, R. W. 1997a, ApJ, 478, 536

Pettini, M., Shapley, A. E., Steidel, C. C., et al. 2001, ApJ, 554, 981

Pettini, M., Smith, L. J., Hunstead, R. W., & King, D. L. 1994, ApJ, 426, 79

Pettini, M., Smith, L. J., King, D. L., & Hunstead, R. W. 1997b, ApJ, 486, 665

Pontzen, A., Governato, F., Pettini, M., et al. 2008, MNRAS, 390, 1349

Popping, G., Somerville, R. S., & Trager, S. C. 2014, MNRAS, 442, 2398

Poznanski, D., Prochaska, J. X., & Bloom, J. S. 2012, MNRAS, 426, 1465

Prochaska, J. X. 1999, ApJ, 511, L71

Prochaska, J. X., Gawiser, E., Wolfe, A. M., Castro, S., & Djorgovski, S. G. 2003, ApJ, 595, L9

Prochaska, J. X., Herbert-Fort, S., & Wolfe, A. M. 2005, ApJ, 635, 123

Prochaska, J. X., O'Meara, J. M., Fumagalli, M., Bernstein, R. A., & Burles, S. M. 2015, ApJS, 221, 2

Prochaska, J. X., O'Meara, J. M., & Worseck, G. 2010, ApJ, 718, 392

Prochaska, J. X., Sheffer, Y., Perley, D. A., et al. 2009, ApJ, 691, L27

Prochaska, J. X. & Wolfe, A. M. 2009, ApJ, 696, 1543

Prochter, G. E., Prochaska, J. X., & Burles, S. M. 2006, ApJ, 639, 766

Quider, A. M., Shapley, A. E., Pettini, M., Steidel, C. C., & Stark, D. P. 2010, MNRAS, 402, 1467

Rafelski, M., Neeleman, M., Fumagalli, M., Wolfe, A. M., & Prochaska, J. X. 2014, ApJ, 782, L29

Rafelski, M., Wolfe, A. M., Prochaska, J. X., Neeleman, M., & Mendez, A. J. 2012, ApJ, 755, 89

Rahmani, H., Péroux, C., Turnshek, D. A., et al. 2016, MNRAS, 463, 980

Rao, S. M., Nestor, D. B., Turnshek, D. A., et al. 2003, ApJ, 595, 94

Rao, S. M. & Turnshek, D. A. 2000, ApJS, 130, 1

Rao, S. M., Turnshek, D. A., & Nestor, D. B. 2006, ApJ, 636, 610

Rauch, M., Haehnelt, M., Bunker, A., et al. 2008, ApJ, 681, 856

Rauch, M. & Haehnelt, M. G. 2011, MNRAS, 412, L55

Ribaudo, J., Lehner, N., & Howk, J. C. 2011, ApJ, 736, 42

Richmond, M. W., Treffers, R. R., Filippenko, A. V., et al. 1994, AJ, 107, 1022

Richter, P., Krause, F., Fechner, C., Charlton, J. C., & Murphy, M. T. 2011, A&A, 528, A12

Rosa-González, D., Terlevich, E., & Terlevich, R. 2002, MNRAS, 332, 283

Routly, P. M. & Spitzer, Jr., L. 1952, ApJ, 115, 227

Sánchez-Ramírez, R., Ellison, S. L., Prochaska, J. X., et al. 2016, MNRAS, 456, 4488

Sardane, G. M., Turnshek, D. A., & Rao, S. M. 2014, MNRAS, 444, 1747

Sardane, G. M., Turnshek, D. A., & Rao, S. M. 2015, MNRAS, 452, 3192

Sargent, W. L. W., Steidel, C. C., & Boksenberg, A. 1988, ApJ, 334, 22

Savage, B. D. & Sembach, K. R. 1991, ApJ, 379, 245

Schneider, D. P., Richards, G. T., Hall, P. B., et al. 2010, AJ, 139, 2360

Schulze, S., Fynbo, J. P. U., Milvang-Jensen, B., et al. 2012, A&A, 546, A20

Selsing, J., Fynbo, J. P. U., Christensen, L., & Krogager, J.-K. 2016, A&A, 585, A87

Sembach, K. R., Danks, A. C., & Savage, B. D. 1993a, A&AS, 100, 107

Sembach, K. R., Danks, A. C., & Savage, B. D. 1993b, A&AS, 100, 107

Shapley, A. E., Steidel, C. C., Erb, D. K., et al. 2005, ApJ, 626, 698

Sharma, M., Theuns, T., Frenk, C. S., & Cooke, R. J. 2018, MNRAS, 473, 984

Silva, A. I. & Viegas, S. M. 2001, Computer Physics Communications, 136 [astro-ph/0010533]

Silva, A. I. & Viegas, S. M. 2002, MNRAS, 329, 135

Simcoe, R. A., Sargent, W. L. W., & Rauch, M. 2004, ApJ, 606, 92

Slosar, A., Iršič, V., Kirkby, D., et al. 2013, , 4, 026

Smith, H. E., Jura, M., & Margon, B. 1979, ApJ, 228, 369

Snow, T. P. & McCall, B. J. 2006, ARA&A, 44, 367

Snow, T. P., Rachford, B. L., & Figoski, L. 2002, ApJ, 573, 662

Somerville, R. S., Popping, G., & Trager, S. C. 2015, MNRAS, 453, 4337

Songaila, A. & Cowie, L. L. 1996, AJ, 112, 335

Songaila, A. & Cowie, L. L. 2010, ApJ, 721, 1448

Srianand, R., Gupta, N., Petitjean, P., et al. 2012, MNRAS, 421, 651

Srianand, R., Petitjean, P., Ledoux, C., Ferland, G., & Shaw, G. 2005, MNRAS, 362, 549

Stecher, T. P. 1965, ApJ, 142, 1683

Steidel, C. C., Erb, D. K., Shapley, A. E., et al. 2010, ApJ, 717, 289

Steidel, C. C., Giavalisco, M., Dickinson, M., & Adelberger, K. L. 1996, AJ, 112, 352

Stengler-Larrea, E. A., Boksenberg, A., Steidel, C. C., et al. 1995, ApJ, 444, 64

Stewart, K. R., Brooks, A. M., Bullock, J. S., et al. 2013, Angular Momentum Acquisition in Galaxy Halos

Storrie-Lombardi, L. J., McMahon, R. G., Irwin, M. J., & Hazard, C. 1994, ApJ, 427, L13

Teyssier, R. 2002, A&A, 385, 337

Theuns, T., Leonard, A., Efstathiou, G., Pearce, F. R., & Thomas, P. A. 1998, MNRAS, 301, 478

Turnshek, D. A. & Grillmair, C. J. 1986, ApJ, 310, L1

Vanden Berk, D. E., Richards, G. T., Bauer, A., et al. 2001, AJ, 122, 549

Vernet, J., Dekker, H., D'Odorico, S., et al. 2011, A&A, 536, A105

Vestergaard, M. & Wilkes, B. J. 2001, ApJS, 134, 1

Vladilo, G. 1998, ApJ, 493, 583

Vladilo, G., Abate, C., Yin, J., Cescutti, G., & Matteucci, F. 2011, A&A, 530, A33

Vladilo, G., Centurion, M., Falomo, R., & Molaro, P. 1997, A&A, 327, 47

Vladilo, G., Centurión, M., Levshakov, S. A., et al. 2006, A&A, 454, 151

Vladilo, G., Molaro, P., Monai, S., et al. 1993, A&A, 274, 37

Vollmann, K. & Eversberg, T. 2006, Astronomische Nachrichten, 327, 862

Wakker, B. P. & Mathis, J. S. 2000, ApJ, 544, L107

Wang, J., Hall, P. B., Ge, J., Li, A., & Schneider, D. P. 2004, ApJ, 609, 589

Wang, T. G., Dong, X. B., Zhou, H. Y., & Wang, J. X. 2005, ApJ, 622, L101

Warren, S. J., Møller, P., Fall, S. M., & Jakobsen, P. 2001, MNRAS, 326, 759

Weatherley, S. J., Warren, S. J., Møller, P., et al. 2005, MNRAS, 358, 985

Weinberg, D. H., Davé, R., Katz, N., & Kollmeier, J. A. 2003, in American Institute of Physics Conference Series, Vol. 666, The Emergence of Cosmic Structure, ed. S. H. Holt & C. S. Reynolds, 157–169

Welty, D. E. & Hobbs, L. M. 2001, ApJS, 133, 345

Welty, D. E., Hobbs, L. M., & Kulkarni, V. P. 1994, ApJ, 436, 152

Welty, D. E., Morton, D. C., & Hobbs, L. M. 1996, ApJS, 106, 533

Weymann, R. J., Carswell, R. F., & Smith, M. G. 1981, ARA&A, 19, 41

Wild, V. & Hewett, P. C. 2005, MNRAS, 361, L30

Wild, V., Hewett, P. C., & Pettini, M. 2006, MNRAS, 367, 211

Wilkinson, D. T. 1987, in 13th Texas Symposium on Relativistic Astrophysics, ed. M. P. Ulmer, 209–218

Wiseman, P., Schady, P., Bolmer, J., et al. 2017, A&A, 599, A24

Wolfe, A. M., Briggs, F. H., & Jauncey, D. L. 1981, ApJ, 248, 460

Wolfe, A. M., Briggs, F. H., Turnshek, D. A., et al. 1985, ApJ, 294, L67

Wolfe, A. M. & Davis, M. M. 1979, AJ, 84, 699

Wolfe, A. M., Gawiser, E., & Prochaska, J. X. 2003a, ApJ, 593, 235

Wolfe, A. M., Gawiser, E., & Prochaska, J. X. 2005, ARA&A, 43, 861

Wolfe, A. M., Howk, J. C., Gawiser, E., Prochaska, J. X., & Lopez, S. 2004, ApJ, 615, 625

Wolfe, A. M., Prochaska, J. X., & Gawiser, E. 2003b, ApJ, 593, 215

Wolfe, A. M., Prochaska, J. X., Jorgenson, R. A., & Rafelski, M. 2008, ApJ, 681, 881

Wolfe, A. M., Turnshek, D. A., Smith, H. E., & Cohen, R. D. 1986, ApJS, 61, 249

Womble, D. S. 1993, PASP, 105, 1043

Womble, D. S., Junkkarinen, V. T., Cohen, R. D., & Burbidge, E. M. 1990, AJ, 100, 1785

Wright, A. E., Morton, D. C., Peterson, B. A., & Jauncey, D. L. 1979, MNRAS, 189, 611

Wu, X.-B., Wang, F., Fan, X., et al. 2015, Nature, 518, 512

Wucknitz, O., Wisotzki, L., Lopez, S., & Gregg, M. D. 2003, A&A, 405, 445

York, B. A., Kanekar, N., Ellison, S. L., & Pettini, M. 2007, MNRAS, 382, L53

York, D. G., Adelman, J., Anderson, Jr., J. E., et al. 2000, AJ, 120, 1579

Zafar, T., Péroux, C., Popping, A., et al. 2013, A&A, 556, A141

Zhang, Y., Anninos, P., & Norman, M. L. 1995, ApJ, 453, L57

Zheng, W., Kriss, G. A., Telfer, R. C., Grimes, J. P., & Davidsen, A. F. 1997, ApJ, 475, 469

Zhou, H., Ge, J., Lu, H., et al. 2010, ApJ, 708, 742

Zibetti, S., Ménard, B., Nestor, D. B., et al. 2007, ApJ, 658, 161

Zou, S., Petitjean, P., Noterdaeme, P., et al. 2017, ArXiv e-prints [[arXiv]1710.05369]

Zwaan, M. A., Meyer, M. J., Staveley-Smith, L., & Webster, R. L. 2005, MNRAS, 359, L30

Zwaan, M. A. & Prochaska, J. X. 2006, ApJ, 643, 675

Zych, B. J., Murphy, M. T., Hewett, P. C., & Prochaska, J. X. 2009, MNRAS, 392, 1429

Zych, B. J., Murphy, M. T., Pettini, M., et al. 2007, MNRAS, 379, 1409

Acknowledgements

• First of all I would like to thank my PhD supervisors Patrick Petitjean and Pasquier Noterdaeme, without your help, I would not be able to finish this PhD and thesis. Patrick, thank you for the continuous support of my PhD study and related research, and your strict requirement for me. Pasquier, thank you for all your ideas on coding, plotting and the scientific discussion, which gave me lots of inspiration.

• Thanks for my jury members who will be able to present in my defence. Roser Pello and Denis Puy, who reviewed my manuscript and gave precious comments and advises. The examiner Christophe Yeche and the president Marie-Christine Angonin.

• Thanks for all my collaborators: Cédric Ledoux, Jens-Kristian Krogager, Raghunathan Srianand, Hassan Fathivavsari, Thomas Krüler and Sébastian Lopéz.

• Thanks University of Pierre et Marie Curie, Sorbonne Université who fund my PhD. Ecolé doctoral 127 helps me with all the administrative processes.

• Thanks for the interesting discussion on science with JK, Sergei, Hassan, Hardi, Tilman, Jesse, Alba, Adarsh, Caterina, Patrick Boissé, while writing my thesis.

• Thanks JK, Sergei, Tilman, Jesse, Räphel, Clotilde, Valérie to cross-reading part of my thesis and gave me constructive advice.

• Thanks for all the people who took care me in the physical difficult time in the past a few months: Alba, Valérie, Chloé, Shanshan, Boyang, Oscar, Jesse, Doogesh, Tanguy, Yangmo, Matt.

• Thanks for all the lovely people at the third floor (the coolest floor!) in the last three years: best officemate Jesse brings a lot of fun and many help in Python plotting. Elisabeth, JK, Pasquier, Fréderic sometimes bring delicious sweets and cookie.

• Thanks for the useful advises from the anonymous referees of the paper.

• Thanks for all the PhD students with whom I spent happy three years with.

• Thanks for all the colleague, IT supporters, administrative people who gave me much help in the daily life.

• In the end, I would like to thank all my family and friends who always support me for my study and life.

List of Tables

List of Figures